# IRM “fingerprint” et Intelligence Artificielle pour la prise en charge des patients victimes d’un AVC

Thomas Coudert

THÈSE

Pour obtenir le grade de

Université Grenoble Alpes

# DOCTEUR DE L'UNIVERSITÉ GRENOBLE ALPES

École doctorale: PHYS - Physique
Spécialité : Physique pour les Sciences du Vivant
Unité de recherche: Grenoble Institut des Neurosciences

## IRM «fingerprint» et Intelligence Artificielle pour la prise en charge des patients victimes d'un AVC

## MRI 'Fingerprint' and Artificial Intelligence for stroke emergencies


Présentée par :
**Thomas COUDERT**


Direction de thèse :

| | |
|---|---|
| **Emmanuel BARBIER**<br>DIRECTEUR DE RECHERCHE, INSERM - Délégation Auvergne Rhône-Alpes | Directeur de thèse |
| **Thomas CHRISTEN**<br>CHARGE DE RECHERCHE, Université Grenoble Alpes | Co-encadrant de thèse |

Rapporteurs :

**Benjamin MARTY**
CHARGE DE RECHERCHE HDR, Institut de Myologie

**Meritxell BACH CUADRA**
MAITRE D'ENSEIGNEMENT ET DE RECHERCHE, University of Lausanne

Thèse soutenue publiquement le 27 novembre 2024, devant le jury composé de :

| | |
|---|---|
| **Olivier DETANTE,**<br>PROFESSEUR DES UNIVERSITES - PRATICIEN HOSPITALIER, Université Grenoble Alpes | Président du jury |
| **Benjamin MARTY,**<br>CHARGE DE RECHERCHE HDR, Institut de Myologie | Rapporteur |
| **Meritxell BACH CUADRA,**<br>MAITRE D'ENSEIGNEMENT ET DE RECHERCHE, University of Lausanne | Rapporteure |
| **Emmanuelle CANET-SOULAS,**<br>PROFESSEURE DES UNIVERSITES, Université Lyon 1 | Examinatrice |
| **Jonas RICHIARDI,**<br>SENIOR SCIENTIST, Lausanne University Hospital and University of Lausanne | Examinateur |
| **Florence FORBES,**<br>DIRECTRICE DE RECHERCHE, INRIA | Examinatrice |

# Contents

# Ethics statements

All human procedures were performed under the MAP-IRMaGe protocol guidelines (NCT05036629), validated by the CHU Grenoble Alpes, and coordinated by Dr.Arnaud Attyé.

All animal procedures conformed to French government guidelines and were performed under permits 380820 and A3851610008 (for experimental and animal care facilities) from the French Ministry of Agriculture (Articles R214–117 to R214–127 published on 7 February 2013), and in compliance with the ARRIVE guidelines (Animal Research: Reporting in Vivo Experiments).
All animal preparations were performed by an expert animal technician. Efforts were made to use animals from other experiments and retrospective data when possible to limit as much as possible this thesis' impact.

# List of Abbreviations

| | |
|---|---|
| **ASL** | Arterial Spin Labeling |
| **BiLSTM** | Bidirectional Long Short-Term Memory |
| **BOLD** | Blood Oxygen Level Dependent |
| **bSSFP** | balanced Steady-State Free Precession |
| **CA** | Contrast agent |
| **CBF** | Cerebral Blood Flow |
| **CBV** | Cerebral Blood Volume |
| **DE** | Differential Evolution |
| **DREAM** | Dual Refocusing Echo Acquisition Mode |
| **DSC** | Dynamic Susceptibility Contrast |
| **EM** | Expectation-Maximization |
| **ED** | Elliptical Distribution |
| **FA** | Flip Angle |
| **FISP** | Fast Imaging with Steady Precession |
| **fMRI** | functional MRI |
| **FWHM** | Full Width at Half Maximum |
| **GM** | Grey Matter |
| **GRE** | Gradient Echo |
| **GRU** | Gated Recurrent Unit |
| **HD-GMM** | High Dimensional Gaussian Mixture Models |
| **JSON** | JavaScript Object Notation |
| **LSTM** | Long Short Term Memory |
| **MCMRF** | Multi-Compartment Fingerprinting |

| | |
|---|---|
| **MRF** | Magnetic Resonance Fingerprinting |
| **MRI** | Magnetic Resonance Imaging |
| **MRvF** | Magnetic Resonance vascular Fingerprinting |
| **MWF** | Myelin Water Fraction |
| **PCA** | Principal Component Analysis |
| **R** | Mean vessel radius |
| **RF** | Radio-frequency |
| **RNN** | Recurrent Neural Network |
| **ROI** | Region Of Interest |
| **SE** | Spin Echo |
| **SENSE** | Sensitivity encoding |
| **sMRI** | Synthetic MRI |
| **SNR** | Signal to Noise Ratio |
| **$SO_2$** | Blood oxygen saturation |
| **SVD** | Singular Value Decomposition |
| **TE** | Echo Time |
| **TR** | Repetition Time |
| **USPIO** | Ultrasmall SuperParamagnetic Iron Oxide |
| **WM** | White Matter |

# General Introduction

## Stroke in the era of mechanical thrombectomy

Stroke, also known as cerebrovascular accident, is a critical medical condition characterized by a sudden disruption of blood flow to the brain, resulting in acute neurological deficits. This disruption can be due to either ischemia, caused by a blockage or narrowing of blood vessels, or hemorrhage, resulting from bleeding within the brain. The immediate consequences of a stroke can include loss of motor and sensory functions, speech difficulties, cognitive impairments, and in severe cases, death. In the EU, 1.1 million people suffer a stroke per year, representing about 9% of all deaths (Bejot et al. 2016; Wilkins et al. 2017). In terms of prevalence, nearly 12 million people in Europe live with the long-term effects of a stroke, which often include significant disabilities such as hemiplegia, speech difficulties, and cognitive impairments. Long-term stroke effects are directly related to the time during which tissues are deprived of oxygen.

Given the urgent need for rapid diagnosis and intervention, stroke represents a significant challenge for healthcare systems, demanding not only effective treatment strategies but also sophisticated imaging techniques to guide management and predict outcomes. Since 2015, several clinical studies (Warach et al. 2016), have shown the efficacy of new endovascular therapies (EVT) on the evaluation and treatment of stroke lesions. One of the key findings from these studies highlighted the critical role of brain imaging techniques in identifying patients who are most likely to benefit from treatment. Yet, this major improvement in care was mitigated by the low number of patients (≈10.5%) who could receive the treatment. The low rate was largely due to patients arriving at the hospital outside the eligibility period recommended by the guideline for receiving the treatment. Imaging in the acute phase of stroke must be conducted rapidly, as treatment efficacy is highest within a narrow time window, typically less than six hours after the onset of symptoms. This started to change in 2018 when several clinical trials showed that endovascular thrombectomy and intravenous thrombolysis could also be successful within 24 hours of stroke onset if advanced imaging protocols were used for patients' triage (Albers et al. 2018). These successful results support the rationale that cerebral physiology may be a better prognostic indicator of outcome rather than time alone and offer hope for a significant increase in the number of patients (≈30% of patients with unknown symptom onset time), better selection of therapies, and better prediction of stroke outcomes.

## What is the best imaging strategy for stroke emergencies?

While recent trials have underscored the necessity for robust, fast, and multiparametric imaging exams in stroke emergencies (Tsivgoulis et al. 2018), they also noted the limitations (need for contrast agent injection, low sensitivity and reproducibility, lack of consensus) of current imaging tools for the detection of brain tissue that may remain viable if blood flow can

be restored (*i.e.* the ischemic penumbra). However, the question of which imaging approach is best suited for stroke emergencies remains unresolved. On one hand, the first imaging modality typically used in patient management is computed tomography (CT), which is both fast (≈5-minute protocol) and widely accessible. However, there is a need to enhance the ability to detect ischemia and hemorrhages to improve patient triage (Donahue et al. 2018). A more precise evaluation of the ischemic penumbra is also crucial. This improved assessment could help estimate the time of onset in patients with unwitnessed strokes and potentially extend the therapeutic time window.

On the other hand, MRI allows the acquisition of quantitative information through quantitative MR imaging (qMRI) techniques like diffusion-weighted images (DWI, Nagaraja 2021) to detect the ischemic core and the use of multiple contrast mechanisms (FLAIR, perfusion (PWI, Demeestere et al. 2020), or possible new contrasts) to detect at-risk tissue. Additionally, $T_2^*$ imaging also helps in detecting microbleeds and chronic hemorrhagic changes that may influence stroke management and outcome. Furthermore, recent trials have demonstrated that ≈90% of patients clinically eligible for EVT can be scanned with MRI (main clinical restrictions remain restless or unstable patients) and that MRI-workflow process times are similar to those of CT scans (Provost et al. 2019).

**It thus appears that a very efficient exam for stroke emergencies would consist of an MRI protocol which (1) drastically reduces current MRI acquisition times (≈20-25min) (2) acquires more information about tissue microstructures (3) provides quantitative, standardized and summarized data within minutes.**

## Offering a paradigm shift in magnetic resonance imaging

Fulfilling all of the above requirements seems out of reach with our current MRI tools. Protocols that produce similar information to CT are already long for stroke emergencies (≈25 min protocol) as each estimate involves one independent MR sequence acquisition. A way to gain time is to reduce the images' spatial resolution but at the cost of degrading the quality of clinical diagnosis. In this context, collecting more information for imaging the penumbra while reducing the total acquisition time seems utterly difficult.

Fortunately, two complimentary and revolutionary concepts have emerged these last years in the field and could radically change the way we acquire and reconstruct MRI data.

### The concept of Magnetic Resonance Fingerprinting (MRF)

Introduced by Ma et al. 2013 in Nature, the MR Fingerprinting approach has been a great step toward unleashing the full power of MRI by allowing a single MR sequence to randomly excite tissue and be sensitive to multiple parameters at the same time. The MRF process involves fast undersampled high-resolution acquisitions with time-varying parameters defining the MRF sequence that produces temporal signal evolutions (or "fingerprints") in every voxel. These *in vivo* fingerprints are then compared to a large number of simulated signals obtained using combinations of *a priori* tissue parameters and stored in a "dictionary" database.

The values of the parameters corresponding to the closest simulated signals or "match" are then assigned to the associated voxels, producing multiple quantitative maps simultaneously. Figure .0.1 shows a schematic illustration of the standard MRF framework.

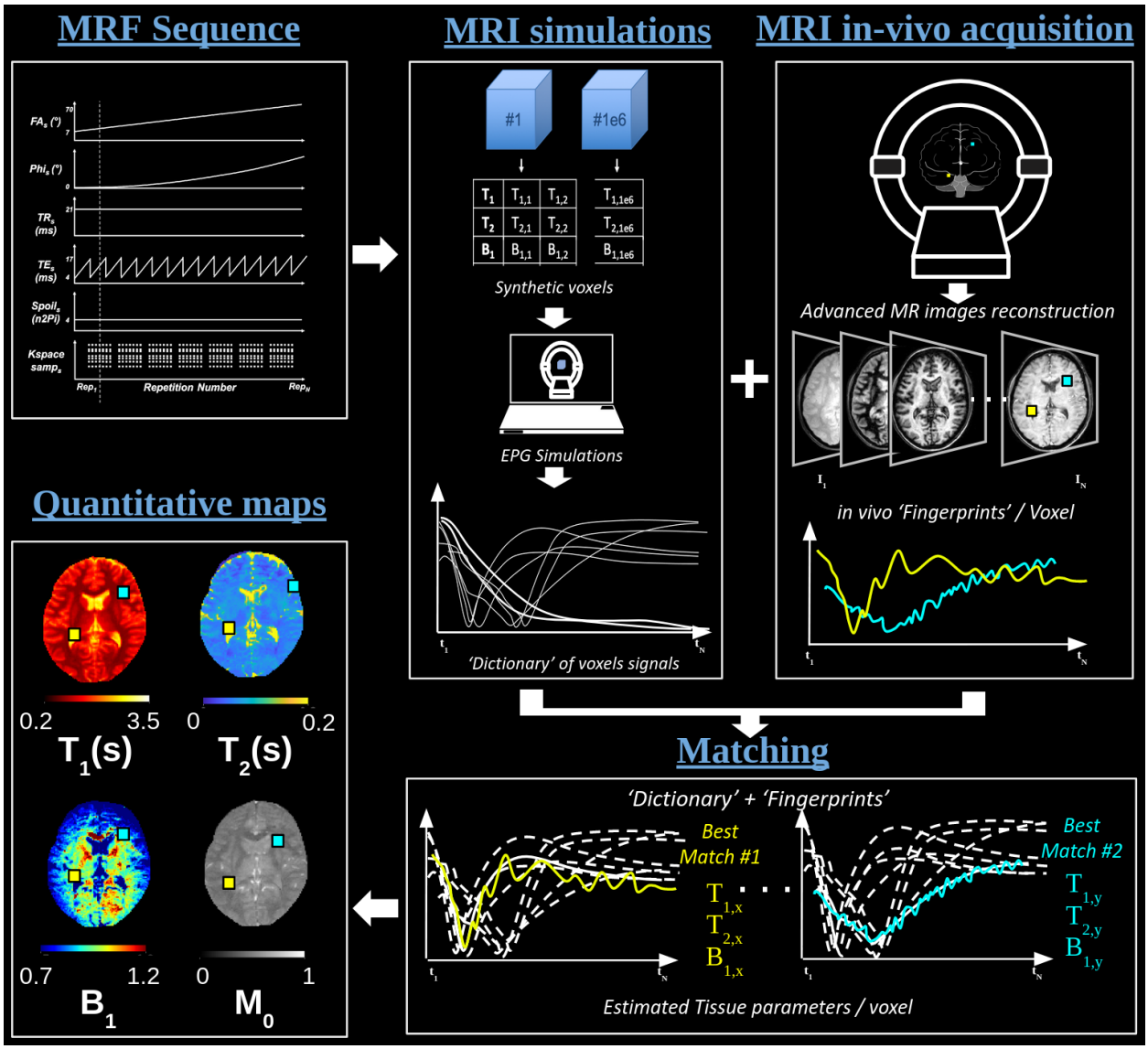


**Figure .0.1**: Illustration of the MRF framework. Data was obtained at 3T (Philips; IRMaGe) on a healthy volunteer.

With MRF, it is already possible to quantitatively map 3 parameters ($T_1$, $T_2$, proton density) of the whole human brain ($1mm^3$ spatial resolution) in the minute (Schauman et al. 2022. It is also possible to correct system imperfections (e.g. $B_1$ inhomogeneities) as well as some patient motions by including them in the numerical simulations and postprocessing pipelines. These types of acquisitions have now reached the clinic and could be applied to several organs and pathologies including stroke.

**It is yet important to realize that the MRF framework is not limited to a single excitation pattern (1 single MRF sequence) nor the measurement of the transverse**

**or longitudinal relaxation times ($T_1$, $T_2$).**

Indeed, an important feature of the MRF method is the inherent flexibility in the design of the protocols. In general MR, the type of estimated parameters, and the accuracy with which they are measured, highly rely on the designed scheme of the sequence. The key parameters defining an MR sequence include the flip angle (FA), which determines the rotation angle of the magnetization; the repetition time (TR), the time between successive RF pulses; the echo time (TE), the interval between the RF pulse and the signal measurement; and the RF phase, which controls the phase of the RF pulses. Adjusting these parameters allows to optimize the image contrast and the sensitivity to tissue parameters. Whereas a standard quantitative MRI sequence is usually made of a small number of pulses producing a small number of images (<20 for relaxometry measurements), MRF sequences can be easily defined by a high number of RF pulses (>200-2000). The MRF sequence parameters can arbitrarily change with time to enhance dictionary variance and so the sensitivity to different materials or tissues. As long as the sequence is sensitive to the parameters of interest, provides different fingerprints for different tissue types, and the MRF simulations are realistic enough to capture the signal variations, all sorts of MRF acquisition schemes can be proposed (Cohen et al. 2017a).

Following this line of thought, several teams have proposed to optimize MRF sequences in terms of acquisition time or robustness to several artifacts ($B_1$ in particular). Given the very large search space for MRF sequences, multiple automatic sequence optimization algorithms have been proposed. Other types of acquisition patterns have also been proposed to measure other effects such as $B_0$ inhomogeneities and corresponding $T_2^*$ information using TE variations (Wang et al. 2019). Using MR gradient variations, diffusion coefficient measurements have been reported, as well as quantification of blood flow in large blood vessels. Using an Arterial Spin Labeling acquisition scheme coupled with random changes in labeling times, an MRF ASL has also been proposed to provide CBF and MTT quantitative maps (MRF-ASL, Su et al. 2019).

For all of these approaches, the numerical models for MRF dictionary generation have been largely improved compared to classic single isochromat Bloch simulations. Going one step further, the Grenoble team has proposed to use simulations that contain 3D virtual representations of blood vessels to obtain simultaneous parametric maps that represent geometric structures and oxygenation of the microvascular system (See Figure .0.2). For the moment, the corresponding vascular MRF (or MRvF, Christen et al. 2014b) sequences have been short (<70 pulses) and simple (mainly TE variations), but combinations of acquisitions obtained before and after injection of an intravascular USPIO (Ultrasmall SuperParamagnetic Iron Oxide) contrast agent have led to promising results in both animals and human volunteers (Delphin et al. 2023).

Finally, it is worth mentioning that MRF can also provide standard MR-weighted images. Recent studies have explored the *intrinsic* contrast of acquired MRF time series images. This is particularly interesting as thousands of images can potentially be reconstructed from a single acquisition. For example, Gómez et al. 2019 have carefully designed the MRF acquisition parameters scheme to obtain $T_1$ or $T_2$ weighted images or angiographic-like

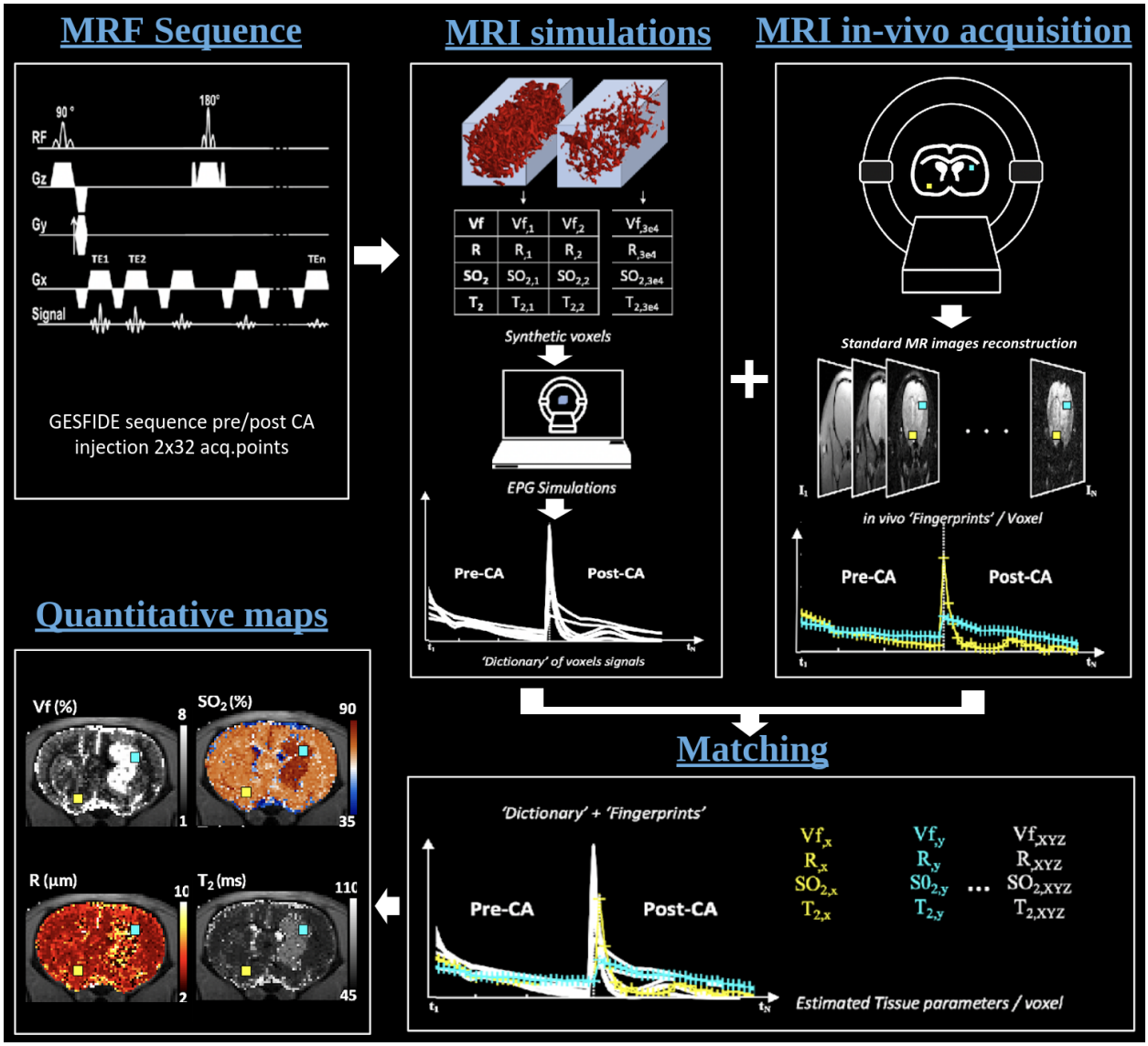


**Figure .0.2**: Illustration of the MRvF framework. Data was obtained at 4.7T (Bruker; IRMaGe) on a rat bearing a brain tumor.

projections on top of relaxometric maps. It is also possible to use the estimated quantitative maps to recreate (or synthetize) weighted images using postprocessing techniques.

## MRF current limitations

By taking advantage of the speed of the MRF approach, combined with the simultaneous acquisition of a large number of new parameter maps and contrasts, it can be easy to imagine a new type of MR protocol for acute stroke imaging. However, combining multiple MRF patterns into a single acquisition is not trivial. MRF works well when it is limited to a small number of estimated parameters (<3). But increasing the dimensions (>5) brings new technical challenges in computer power, storage memory (>Terabytes), and reconstruction times (>days) that become unrealistic even for research environments. A second challenge

for an MRF stroke exam is that the current MRvF framework for microvascular estimates relies on a contrast agent (ferumoxytol) that can only be used off-label for human studies in a few countries. More generally, the MRvF protocol involves administering a metal-based compound into the patient's bloodstream to enhance the sensitivity to the microvascular network. Even if CA is used in current stroke protocols for perfusion imaging, studies have already highlighted the potential risks of allergic reactions to Gadolinium compounds (see Costelloe et al. 2020; Iyad et al. 2023). Moreover, the effectiveness of contrast agents in highlighting ischemic brain tissue can vary based on factors like the timing of administration and the patient's physiological state, impacting the consistency and accuracy of quantitative measurements (Calamante et al. 2002; Ebinger et al. 2010). The increased cost and limited availability of contrast agents can further restrict their widespread application, particularly in resource-limited settings. Above all, the intravenous injection of CA during the protocol increases the duration of the exam. A contrast-free MRF exam would thus be preferable but new MRvF patterns need to be found.

## Emergence of Artificial Intelligence (AI) tools for MRI

Artificial Intelligence (AI), through deep learning (DL) and machine learning (ML) methods, has significantly advanced multiple aspects of MRI by enhancing image reconstruction, reducing scan times, and optimizing image analysis. For many years, numerous DL algorithms have proven extremely successful in different inverse problems of imaging (Heckel et al. 2024). Convolutional Neural Networks (CNN) and more recently vision models have impacted image reconstruction, and learning how to produce images from incomplete datasets is now a major area of MRI research. In Magnetic Resonance Fingerprinting (MRF), AI algorithms have transformed the traditional approach to generating tissue property maps. Instead of relying solely on computationally intensive dictionary matching, AI-driven methods can rapidly process MRF data to produce accurate maps of multiple tissue parameters, such as $T_1$ and $T_2$ relaxation times (Hoppe et al. 2018; Fang et al. 2019). Whereas some machine learning models have been applied for MRF signal representation (Boux et al. 2021), sequential deep learning models have been mostly used to learn complex patterns from MRF signals, enabling faster and more efficient reconstructions (Oksuz et al. 2018; Hoppe et al. 2019; Kang et al. 2023). Additionally, AI is now being used to optimize MRI acquisition patterns, allowing for more intelligent sampling strategies that further reduce scan times without sacrificing image quality (Perlman et al. 2022). Finally, by combining data from different acquisition methods, DL models can also generate synthetic contrasts, offering new insights into tissue characteristics without requiring additional scans or contrast agents (Preetha et al. 2021; Moya-Saez et al. 2021, see Figure .0.3). This integration of AI into MRI, particularly in MRF, is reshaping the field, enabling faster, more accurate, and less invasive imaging.

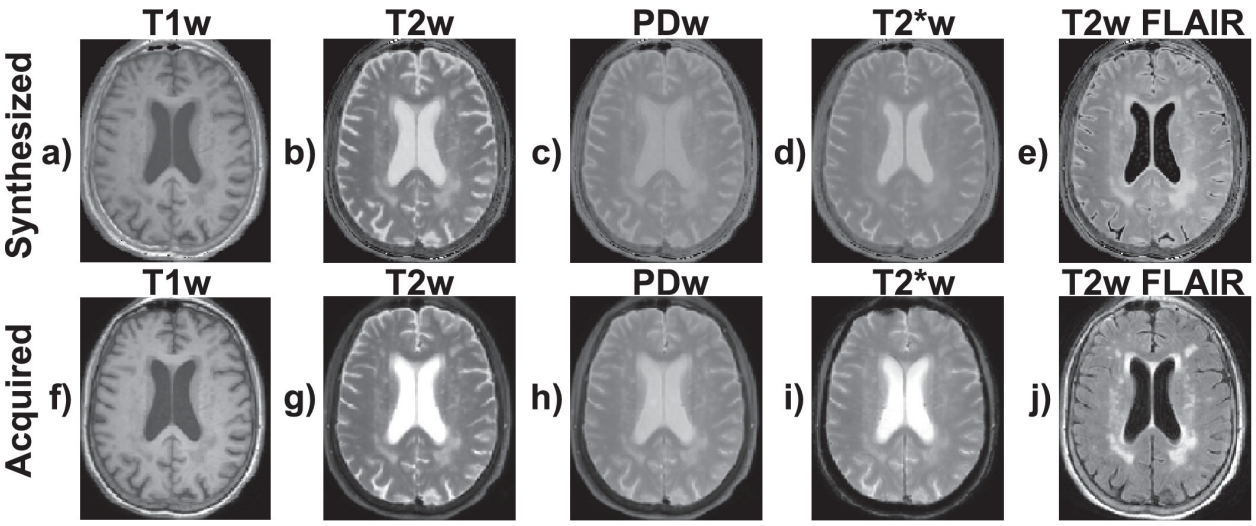


**Figure .0.3**: A representative axial slice of weighted images synthesized from one set of $T_1$, T2, and PD maps computed by a CNN and their corresponding acquired images. From Moya-Saez et al. 2021

# General project hypothesis

**We argue that MRF combined with recent AI solutions will enable the creation of true multiparametric and integrated MRI exams that are compatible with the demanding needs of stroke emergency workflows.**

# Thesis context and Objectives

The team develops and evaluates imaging methods for the study of cerebral pathologies and has internationally recognized expertise in the measurement of microvascular perfusion and quantitative multiparametric MRI. The laboratory is also part of the Multidisciplinary Institute in Artificial Intelligence (MIAI Grenoble Alpes 3IA) project that aims to conduct research in artificial intelligence. MRI scans are accessible on the IRMaGe imaging platform in Grenoble, which has 2 preclinical MR scanners as well as 1 clinical MR scanner dedicated to research (an ethics approval to perform MR exam on volunteers and an ongoing partnership with Philips on MRF developments). The team also works in close collaboration with mathematicians from INRIA Grenoble (Team Statify) and benefits from the expertise of neuroradiologists from Grenoble CHU and neurologists at the neurovascular unit specialized in new cellular therapies for stroke patients.

The present methodological work, funded by the ANR project "Magnetic Resonance Fingerprinting Unification for Stroke Emergencies (MRFUSE)", intended to develop flexible AI and MRF tools (simulations, acquisition, and reconstruction) that would lay the foundations for the design of efficient acute stroke protocols. These tools would be tested on human volunteers to prepare for further clinical studies.

**Our goals were to**

- **(1) be able to create fast (<6min vs 25min currently), efficient (>6 parameters in one acquisition), and robust MRF acquisition schemes that could replace current imaging solutions and offer a better selection of patients likely to benefit from treatments.**
- **(2) propose MRF modules for quantitative measurements of microvascular biomarkers without the need for contrast agent injection nor additional scan times. This could allow a better evaluation of tissues that can be saved, estimate the time of onset in patients with unwitnessed strokes, and better individualize treatments outside the current therapeutic window.**

# Manuscript organization

The present manuscript is organized into 5 chapters. The first two chapters of this thesis manuscript concentrate on technical developments and theoretical exploration, establishing the foundational concepts and hypotheses of this manuscript. These efforts serve as the basis for the following three chapters, which are transitioning into applied studies. All the relevant concepts and bibliographic references are introduced in each chapter.

Chapter I introduces a first approach for rapid stroke imaging utilizing MR Fingerprinting. It employs standard IR-spoiled MRF sequences to implement state-of-the-art MRF methods and tools, aiming to achieve fast, reproducible, and efficient relaxation time estimates. Building on these principles, it extends the application of relaxometry-based MRF to include quantitative intra-voxel property estimates and the generation of standard contrast images, providing insights into the microvascular structures of the human brain but with limited signal-to-noise ratio and potential noise confounders.

Chapter II addresses the limitations identified in Chapter I, and explores new MRF sequences to overcome the challenges of stroke imaging. We present a comparative analysis of spoiled and balanced gradient echo acquisitions, focusing on their sensitivity to magnetic field inhomogeneities. Based on these theoretical observations, and combined with the development of novel metrics for sequence sensitivity evaluation, we manually designed a new IR-balanced MRF sequence. This sequence showed promise in the *in vivo* estimation of brain microvascular characteristics without the need for contrast-agent injection.

Chapter III details an *in vivo* study conducted on human volunteers using the MRF sequences developed in Chapter II. Leveraging innovative MRF simulations that account for intra-voxel frequency distribution in MRF dictionaries, this chapter validates the potential of custom-designed bSSFP MRF sequences for high-resolution contrast-free relaxometry and microvascular measurements.

Chapter IV introduces two studies conducted to develop and validate advanced reconstruction methods designed to address the "curse of dimensionality" associated with the high-dimensional MRF techniques developed in Chapter III. The first method focuses on

novel subspace compression techniques for low-rank representation of MRF dictionaries, developed in collaboration with another Ph.D. student from INRIA. The second method named MARVEL, is a deep learning algorithm created in partnership with a postdoctoral researcher, serving as a surrogate of the traditional dictionary-matching approach for high-dimensional MR vascular Fingerprinting.

Chapter V finally proposes to explore the use of AI tools to accelerate the numerical simulations of water-diffusion and microvascular effects on MR signals evolution. To fasten microvascular simulations we proposed applying the method from Chapter III and we implemented a recurrent neural network for the quasi-instantaneous simulation of the water-diffusion effect. We present a detailed *in vivo* study validating the efficiency of the newly proposed methods on animal models in healthy and stroke conditions, imaged using the initial MRvF approach.

# Chapter I

# Implementation of an MRF spoiled sequence for standard relaxometry and contrasts imaging

This chapter presents our implementation of several tools dedicated to Magnetic Resonance Fingerprinting (MRF), including MR simulations, acquisition techniques, and reconstruction methods. These tools were initially chosen from the literature to address the challenges of stroke imaging, particularly the MRF sequence based on an FISP acquisition and a pattern previously proposed for fast and efficient relaxometry and contrast weighted estimates. We also implemented pipelines for slice profile and $B_1$ correction as well as dictionary compression for fast images and map reconstruction. Finally, we implemented and adjusted a Multicompartment MRF approach to provide initial estimates of cerebral blood volume without contrast agent injection.

All of these tools were tested in phantoms and a few human volunteers. In this chapter, we only present preliminary results intended to illustrate the methods. A complete validation study is not provided as it was quickly noticed that a new acquisition framework needed to be found if we were to complete all the objectives of the thesis (see Chapter II and following).

Part of these studies has been made in collaboration with Dr. Loic Legris, neuroradiologist and PhD student working on synthetic MRI in the context of MRF, and with Dr. Antoine Barrier, mathematician, working on advanced reconstruction tools for MRF.

## Contents

# I.1 Introduction

As introduced in the previous chapter, the MR sequence is a crucial element of the MRF framework as it defines the initial sensitivity of the protocol. There are infinite possibilities for the design of MRF fingerprint and finding an appropriate sequence for a particular application is not trivial. However, many previous studies have already looked for 'optimized' MRF sequences for brain relaxometry, either using manual designs or automated optimization algorithms. In particular, it has been noticed since the first MRF paper (Ma et al. 2013) that Spoiled Gradient echo sequences such as the Fast Imaging with Steady-State Imaging (FISP) sequence (first proposed by Jiang et al. 2015) were more robust and easier to implement than balanced SSFP sequences. Gómez et al. 2019 proposed a simple sequence design for rapid quantification of $T_1$ and $T_2$ relaxation times as well as simultaneous quantification and visualization of blood flow. The corresponding sequence parameters are shown in Figure I.1.1. It is interesting to note that the description of the sequence is different from standard MR sequences. Here the parameter trains (or temporal variations of parameters) are shown without describing the actual MR acquisition sequence (pulses and magnetic gradient shapes) used at each pulse number to create an image. For this particular MRF sequence, the variations of the parameters with pulse number are simple. Constant short TRs and corresponding short TEs are used during the entire train of 260 pulses. The phase of RF pulses does not change with time and only a linear ramp of FA introduces signal and contrast variations. An inversion pulse (not represented here) is also used at the beginning of the sequence to improve $T_1$ sensitivity.

In the context of this thesis, we used this basic MRF sequence to start our developments and decided to see if further optimization and modifications for stroke imaging should be made in a second step. This work presents results of interest for stroke patient management, especially concerning angiography-like projections from the signal intensity obtained in temporally resolved contrast images. Used under the MRF framework, we thought this sequence could provide accurate quantitative relaxometry maps as well as simultaneously provide vascular information according to its design.

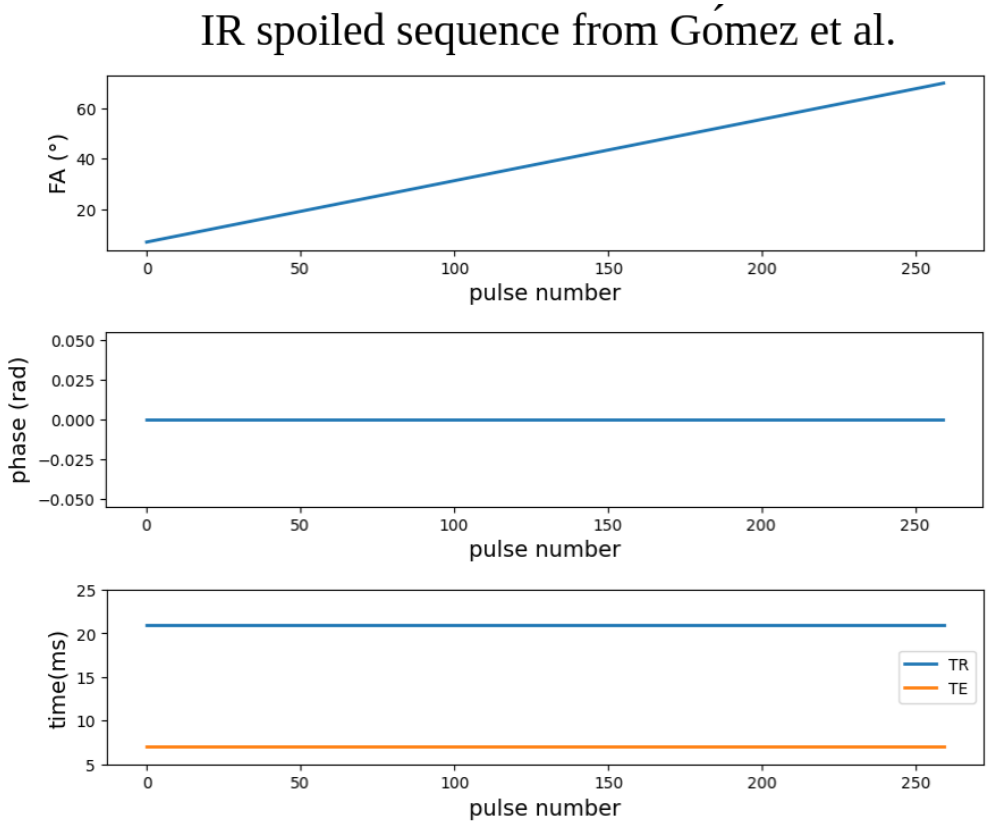


**Figure I.1.1**: Sequence parameters from the IR-spoiled sequence of Gómez et al. 2019.

## I.2 MRF relaxometry: standard methods

In this section, we introduce the basic MRF tools we have implemented for MRF simulations, acquisition, and reconstruction of relaxometry $T_1$, $T_2$ and $B_1$ maps.

### I.2.1 MRF Simulations

MRF dictionary simulations mostly rely on the numerical implementations of the equations introduced in the mathematical model presented in Bloch 1946. This rather simple simulation tool allows to the generation of an MRF dictionary for relaxometry ($T_1$,$T_2$) parameters and magnetic fields $B_1$ and $B_0$ shift estimates.

#### I.2.1.1 Bloch Equations Theory

Nuclei with a non-zero nuclear spin have a magnetic moment. These magnetic moments precess around the direction of a strong, constant, external magnetic field $\boldsymbol{B}$. This precession occurs at the Larmor frequency $\omega = \gamma\|\boldsymbol{B}\|$, where $\gamma$ is the gyromagnetic ratio, specific to the considered nucleus (42.58MHz/T for $^1$H, the most common element considered in MRI). In a volume element, the magnetic moments interact and partly align themselves along the external field. In addition, the nuclei distribute on different spin states ($-\frac{1}{2}$ and $\frac{1}{2}$ for $^1$H). These phenomena give rise to a polarization vector called the net magnetization $\boldsymbol{M}$. $\boldsymbol{M}$ is

aligned with $\boldsymbol{B}$ at equilibrium but can be tipped out of this state by a transverse magnetic field rotating at the Larmor frequency. $\boldsymbol{M}$ then precesses back to equilibrium, its transverse component decaying with a characteristic time $T_2$, and its longitudinal component recovering with a time $T_1$. The precession of $\boldsymbol{M}$ around $\boldsymbol{B}$ can induce a signal in an appropriate coil, which is the origin of the MR signal. A description of the temporal evolution of $\boldsymbol{M}$ was first given in Bloch 1946:

$$\frac{d\boldsymbol{M}}{dt} = \gamma(\boldsymbol{M} \times \boldsymbol{B}) - \frac{M_x}{T_2}\boldsymbol{x} - \frac{M_y}{T_2}\boldsymbol{y} + \frac{(M_0 - M_z)}{T_1}\boldsymbol{z} \tag{I.2.1}$$

where $\boldsymbol{M} = (M_x, M_y, M_z)$ and $\boldsymbol{B} = (B_x, B_y, B_z)$, in an orthonormal frame $(\boldsymbol{x}, \boldsymbol{y}, \boldsymbol{z})$. $T_1$ and $T_2$ are the longitudinal and transverse relaxation times, respectively. $M_0$ is the net magnetization at equilibrium.
When the main magnetic field is along $z$, one can separate the longitudinal ($M_\parallel$) and transverse ($M_\perp$) components of $\boldsymbol{M}$ with respect to $\boldsymbol{z}$:

$$\begin{aligned} M_\parallel(t+\delta t) &= M_\parallel(t) \cdot exp\left(\frac{-\delta t}{T_1(t)}\right) \; + \; M_0\left(1 - exp\left(\frac{-\delta t}{T_1(t)}\right)\right) \\ M_\perp(t+\delta t) &= M_\perp(t) \cdot exp\left(-i\gamma B_z(t)\delta t \; - \; \frac{\delta t}{T_2(t)}\right) \end{aligned} \tag{I.2.2}$$

Diffusion effects are neglected here.
Note the temporal dependence of $B_z$, which can be decomposed as

$$B_z(t) = B_0 + \Delta B_z(t) + G(t) \tag{I.2.3}$$

where $B_0$ is the applied field. $\Delta B_z$ represents the local off-resonance effect, which can be due, among other reasons, to inhomogeneities of $B_0$ and local tissue susceptibility. In the rest of this manuscript, these effects are sometimes called $B_0$ offset or $\delta f$ but rely on the same definition. $G(t)$ is the amplitude of an additional weak magnetic field that can be applied for imaging purposes. Only temporal considerations are presented here for the sake of simplicity, but there is of course a spatial dependence as well: the amplitude of the gradients, the field inhomogeneities, and the relaxation times may vary spatially in the imaged sample.
It is common to consider the evolution of $\boldsymbol{M}$ in a so-called "laboratory" frame that rotates at the Larmor frequency, to eliminate the rotation term $exp\,(-i\gamma B_0 \delta t)$.

There is of course no magnetization evolution without any initial perturbation. In practice, an RF pulse applied in the $(\boldsymbol{x}, \boldsymbol{y})$ plane tips $\boldsymbol{M}$ away from $\boldsymbol{z}$. A pulse can be seen as an instantaneous rotation in the so-called "hard pulse" approximation. For a pulse of flip-angle $\alpha$ and phase $\Phi$ with respect to $\boldsymbol{x}$ one multiplies $\boldsymbol{M}$ with:

$$R_\Phi(\alpha) = \begin{pmatrix} \cos^2\frac{\alpha}{2} & e^{2i\Phi}\sin^2\frac{\alpha}{2} & -ie^{i\Phi}\sin\alpha \\ e^{-2i\Phi}\sin^2\frac{\alpha}{2} & \cos^2\frac{\alpha}{2} & ie^{-i\Phi}\sin\alpha \\ -\frac{i}{2}e^{-i\Phi}\sin\alpha & \frac{i}{2}e^{i\Phi}\sin\alpha & \cos\alpha \end{pmatrix} \tag{I.2.4}$$

which is the result of $R_z(\Phi) \cdot R_x(\alpha) \cdot R_z(-\Phi)$, where $R_u$ denotes a rotation about any $u$ axis (Weigel 2015).

#### I.2.1.2 Matrix formulation for MRI simulations

The previous equations are easy to implement as matrix formulation to perform numerical simulations of the MR signal evolution. Relaxation and precession effects are computed as follows. Over a time period $\tau$:

- Any off-resonance effect, either local ($\Delta B$) or due to constant amplitude gradients (G), will rotate $\boldsymbol{M}$ around $\boldsymbol{z}$ by an angle

$$\varphi = 2\pi \cdot (\Delta B + G) \cdot \tau \tag{I.2.5}$$

- The relaxations are written as

$$\boldsymbol{A} = \begin{pmatrix} E2 & 0 & 0 \\ 0 & E2 & 0 \\ 0 & 0 & E1 \end{pmatrix} \cdot R_z(\varphi) \qquad \text{and} \qquad \boldsymbol{B} = \begin{pmatrix} 0 \\ 0 \\ 1 - E1 \end{pmatrix} \tag{I.2.6}$$

  where

$$\begin{aligned} E1 &= exp(-\tau/T_1) \\ E2 &= exp(-\tau/T_2) \end{aligned} \tag{I.2.7}$$

to eventually obtain $\boldsymbol{M}$ after a free precession over duration $\tau$:

$$\boldsymbol{M}(t+\tau) = \boldsymbol{A} \cdot \boldsymbol{M}(t) + \boldsymbol{B} \tag{I.2.8}$$

Computing the evolution of a single magnetization vector is usually not enough to accurately model a whole tissue voxel as the magnetic field inside the voxel is not homogeneous. Simulations have to be repeated for multiple isochromats, i.e. ensembles of spins processing at the same frequency. Choosing the number of isochromats is then a trade-off between computation cost and required precision.

#### I.2.1.3 Implementation

For the numerical simulations, we used a Python-Matlab in-house interpretation of the C implementation of Bloch's equations, originally developed by Prof. Dr. Brian Hargreaves at Stanford. In our code, the inputs of the simulation code are defined in a JSON (JavaScript Object Notation) file containing all the dictionary simulation mode parameters as well as sequence parameters: pulse number, spoil type, FA train, TR train, TE train, and RF phase train. JSON format allows the fast transmission of structured data. An example of a JSON configuration file is provided in figure I.2.1. An already simulated sequence can be used through its own JSON definition by setting the *input_seq* parameter to *True*. Many input arguments concerned optional simulation tools detailed further in this chapter.
Here is an overview of the main arguments and their use:

- *spoil*: FISP or bSSFP are strings used to precise the gradient readout of the sequence whether to be spoiled or balanced.

- the arguments from *n_ echoes* to *inv_ time* define the sequence or lead to an external input sequence file. It allows multi-echoes acquisition, inversion preparation pulse, phase cycling, etc...
- *SVD* and *SVD_ rank* are used for dictionary compression purpose (see Section I.4).
- the arguments from *gammalist* to the end define the dictionary parameters space, as well as advanced options in the dictionary that are detailed later in the manuscript (see Chapters II).

Aside from the main code, a high number of functions allows the generation of parameter trains either based on standard known evolutions such as B-spline FA train (Scope Crafts et al. 2022), linearly or quadratically cycling RF phase, or either completely tuned with specific values at each pulse.

```
{       "spoil": "FISP",
        "n_echoes": 1,
        "n_pulses": 260,
        "input_seq": false,
        "input_seq_path": "/path/for/sequence/input/file.json",
        "variableFA": true,
        "FA_train": "np.linspace(7, 70, n_pulses).reshape((1, n_pulses))",
        "TRtrain": "np.ones((1, N)) * 21",
        "TEtrain": "np.ones((1, N)) * 4 ",
        "name_seq": "_ref_phase_zero_",
        "phase": "quad",
        "phase_incr": 170,
        "inv_pulse": 1,
        "inv_time": "18",
        "SVD": false,
        "SVD_rank": 40,
        "commentaries": "This is an example JSON configuration file",
        "output_path": "/path/for/dictionary/saving/",
        "gammalist": "np.linspace(1, 20, 20)",
        "T1range": "[200, 3500, 20]",
        "T2range": "[10, 600, 20]",
        "B1range": "[0.7, 1.2, 10]",
        "param": "classic",
        "vasc": true,
        "grid": "regular",
        "slice_profile": false,
        "distrib": false,
        "distrib_path": "",
        "which_distrib": "",
        "bloch_based_dico": null   }
```

**Figure I.2.1**: Example of JSON input configuration file for numerical simulations.

The parameters of the dictionary are given as lists. The user can consider $T_1$, $T_2$, off-resonance $\delta f$, and $B_1$ (defined here as the ratio between the actual and nominal flip angle values). A mesh, following a sampling scheme specified in the argument *grid*, is created to obtain all the

combinations of the dictionary parameters, excluding cases where $T_2 > T_1$. All the cases are then treated in parallel using a Matlab `parfor`. All simulation parameters are saved along with the dictionary generated, allowing for robust tracking of the simulation parameters and easy reproducibility. The tool allows fast simulation of dictionaries from basic MR sequences, more complex ones from the literature, or completely free-designed sequences. In Figure I.2.2, signal entries from an MRF dictionary computed from the introduced sequence are shown. It illustrates the sensitivity of the sequence signal response to $T_1$,$T_2$ and $B_1$, where it can be seen that the signal evolutions are different in the different dimensions with clear differentiation between the fingerprints especially in the $T_1$ and $T_2$ dimensions.

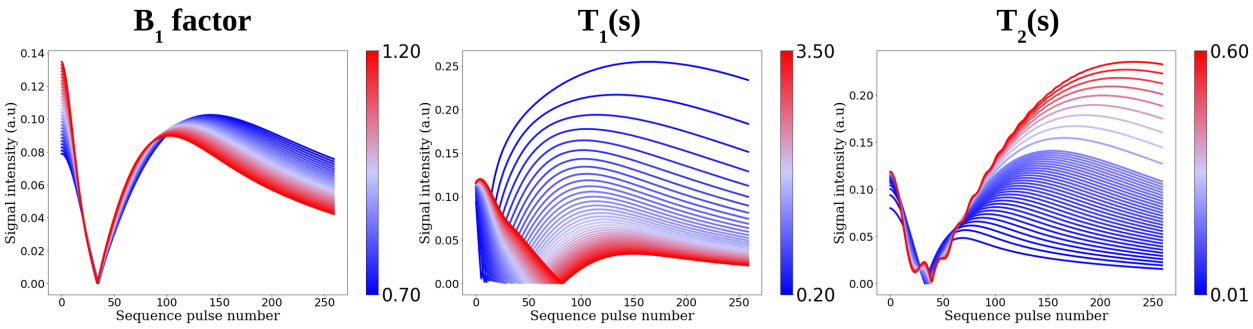


**Figure I.2.2**: MRF dictionary entries from the proposed spoiled sequence for different parameter values. In each plot, one parameter varies whereas the 2 others are fixed.

## I.2.2 MRF Acquisition

### I.2.2.1 Context: Philips Research collaboration

Our MR research facility is equipped with one 3T scanner dedicated to clinical research: Achieva 3.0T dStream Philips (Best, The Netherlands), quasar dual gradient, $\leq$40mT/m amplitude, and multiple head coils up to 32 channels. Philips does not offer a commercial MRF solution at the time being, but a research module is under development. We were granted access to this module through a research agreement with Philips Research (Philips GmbH, Innovative Technologies, Research Laboratories Hamburg) and the following section introduces the work done with this module.
The MRF patch is under development and can not be used under the certified software patch. Any acquisition performed with this patch is not intended for medical use. The images shown here were acquired from healthy volunteers and are printed with their agreement. All acquisitions were performed in agreement with the MAP-IRMaGe protocol (see ethics statement).

### I.2.2.2 Overview

MRF Parameters are passed through a structured CSV (comma-separated values) file, shown in Figure I.2.3. Lines starting with # are part of the file header. Philips uses these files both for dictionary simulation and acquisition. Part of the header lines are instructions for the simulator, which we do not have access to. Those of particular interest at acquisition time will be discussed below.
The last line of the header indicates the order in which the acquisition parameters are to be

```
# MRF sequence pattern
# created:  2020-10-27T15:35:27.829177
# revision:  336
# type:  generic
# class:  BlochGeneric
# length:  390
# repetition_delay (ms):  5000
# n_dummies:  0
# fixed_te:  0.0
# rf_pulse:  inv=inversion_nsls
# rf_pulse:  exc=am_sg_300_100_0
# rf_pulse:  t2prep=t2_prep_4
# mDIXON: no
# fa, tr, phase, te, aq, slice_profile_corr, spoil, rf_pulse
180.0,20,0.0,4,False,False,1.0,inv
5.0,15,0.0,4,True,False,1.0,exc
5.21809693683,15,0.0,4,True,False,1.0,exc
5.43577871374,15,0.0,4,True,False,1.0,exc
...
```

**Figure I.2.3**: CSV sequence description file for Philips scanners.

read. Most of their names are self-explanatory. Each line below corresponds to a so-called "block", lasting TR, with a pulse of flip angle FA that can be an excitation (`rf_pulse=exc`) or an inversion (`rf_pulse=inv`), an optional acquisition at TE (triggered by the `aq` boolean), and an optional spoiler of `spoil` $\times \pi$ across the voxel. The `slice_profile_corr` parameter is a flag for the simulator. These parameters are read at scan time. The module dynamically reads parameters from any CSV file stored in the proper directory, which allows for easy testing and session planning.

Additionally, a developed Philips MRF sequence based on an IR-FISP acquisition design is provided in the software. This sequence has been optimized by the Philips research team and involves compressed dictionary reconstruction directly on the software.

A large number of acquisition parameters can be set, taking advantage of many of the commercially available Philips tools. Acquisitions can be performed with a cartesian, spiral, or radial scheme. In the first case, a SENSE acceleration algorithm is available to speed up the acquisition. For the radial and spiral schemes, the number of spirals or spokes per image can be set to more than 1. It is worth noting that a $B_0$ pre-scan is performed before a spiral acquisition for deblurring.
These different schemes allow to explore the k-space within several trajectories. Each of these trajectories has pros and cons.

#### I.2.2.3 k-Space sampling

k-Space is a complex, multi-dimensional domain where the MR signal is stored during data acquisition. Each point in k-space corresponds to a specific spatial frequency component of the final image. The process of filling the k-space is governed by the magnetic field gradients, which dictate the path or trajectory followed during data collection. Different trajectories impact image resolution, acquisition time, and susceptibility to artifacts.

**Cartesian Sampling** Cartesian sampling is the most straightforward and traditionally used k-space trajectory in MRI. In this method, k-space is filled line by line in a rectilinear grid pattern. The gradients are applied in such a way that each line of k-space is sampled sequentially in a linear fashion, either in a row-by-row or column-by-column manner.

**Spiral Sampling** Spiral sampling involves collecting k-space data along a continuous spiral trajectory, most often starting from the center and moving outwards. This is achieved by applying oscillating gradient fields that trace a spiral path.

**Radial Sampling** Radial sampling (or spoke sampling) involves collecting data along spokes radiating out from the center of the k-space. Each spoke represents a line passing through the origin of k-space, with the gradients oscillating to acquire data along these radial lines.

Depending on the used trajectory, the reconstruction of the k-space data is more or less simple and can lead to artifacts and noisy reconstruction. In Figure I.2.4, we show different images and corresponding fingerprints obtained from the same volunteer using different k-space sampling schemes, with the spoiled sequence from Gómez et al. 2019. The matrix size is 256x256x1 with a voxel size of 0.78x0.78x3mm. The cartesian acquisition is undersampled with a compressed sense factor of 4, the spiral trajectory is made of 10 spiral arms among 25 interleaves, and the radial trajectory consists of 20 spokes. Whereas the cartesian acquisition (12 minutes) was 6 times longer than the spiral one (2 minutes), and 3 times longer than the radial one (4 minutes), the resulting fingerprints are smoother and less prone to temporal noise.

#### I.2.2.4 Outputs

At the end of the exam, data can be exported in several formats, among which the Philips proprietary format Par/Rec and the classical Dicom. Our image converter developed and maintained by O. Montigon from the IRMaGe facility (open source code available at https://github.com/populse/mri_conv) can deal with both formats, but dimensions are better managed when using the Philips format. In particular, when using Dicoms, 4D scans (3D spatial and temporal evolution) with only one slice are read as 3D scans in the current state of our tools. The Philips format was thus chosen for our experiments.

Finally, the output image is a 4D matrix format where the last dimension is the temporal dimension of length equal to the number of pulses in the input sequence.

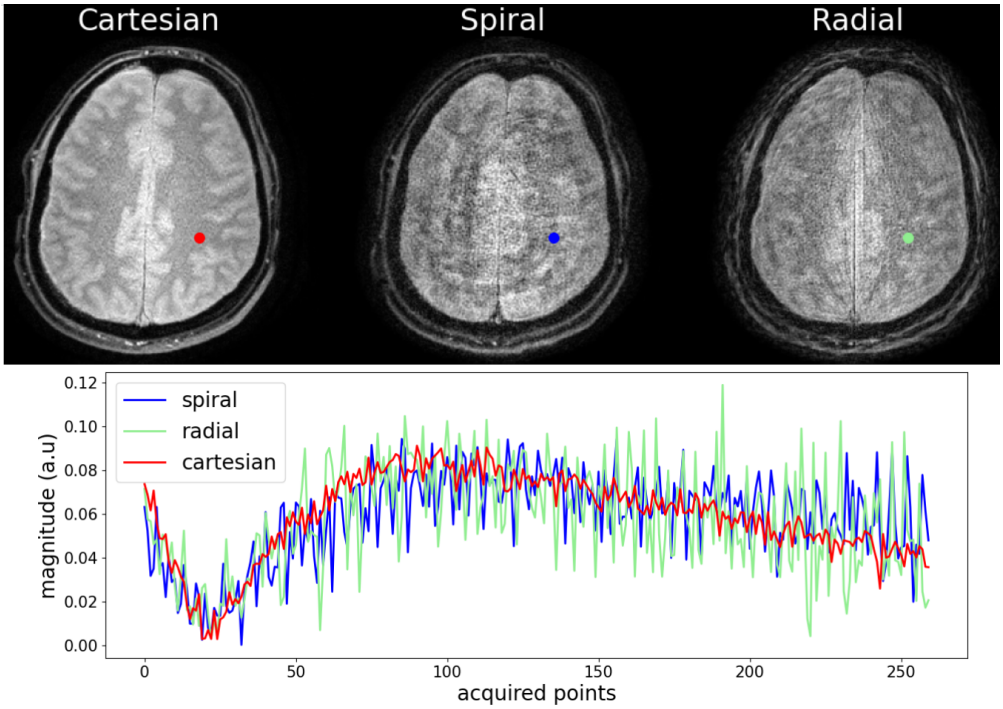


**Figure I.2.4**: Comparison of a fingerprint acquired with cartesian (red), spiral (blue), and radial (green) k-space sampling trajectory. The magnitude corresponds to that of the colored pixel, located with the same coordinate in each image. Images correspond to one acquisition point, here the first time point.

### I.2.3 MRF Reconstruction

After acquiring data on the scanner and performing simulations of the MRF dictionary based on the chosen sequence pattern, the last step of the MRF framework consists of the reconstruction of the parametric maps. This section details the implementation of our first reconstruction algorithm.

#### I.2.3.1 Principles

We initially used a standard approach for MRF reconstruction based on a dictionary-matching process, as described in Ma et al. 2013. The signal over time from each voxel of the 4D acquisition is matched to the signal of the MRF dictionary that maximizes the inner product, allowing for retrieval of the associated tissue parameters.

#### I.2.3.2 Implementation

During this thesis, we implemented a fast MRF reconstruction algorithm in Python using JAX library (https://github.com/google/jax). JAX provides a unified NumPy-like interface to computations that run on CPU, GPU, or TPU, in local or distributed settings. In our case, we used JAX to compute matrix operations between an MRF dictionary and an MRF acquisition on GPU to get high-speed reconstruction of MRF maps.

The algorithm takes as input a JSON file referencing the parameters of the reconstructions such as the path of the pre-computed MRF dictionary, the path of the MRF acquisition, and

an associated brain ROI to avoid unnecessary dot product computation outside the brain and save computation time. Options of the reconstruction algorithm are also detailed in the input JSON such as constrained matching, or compressed matching, which are described in the following subsections of this section.

There is also the possibility to produce a map of the matching product score, showing in each voxel the value of the highest product, possibly highlighting the weakness zone of the matching. The matched signal can also be stored for each voxel, generating a 4D volume that can be compared voxel by voxel with the acquisition. Figure I.2.5 provides an example of fingerprints acquired with the sequence introduced in this chapter in the grey and white matter parts of a human volunteer compared with their respective matched entry stored in the 4D 'matched volume' map.

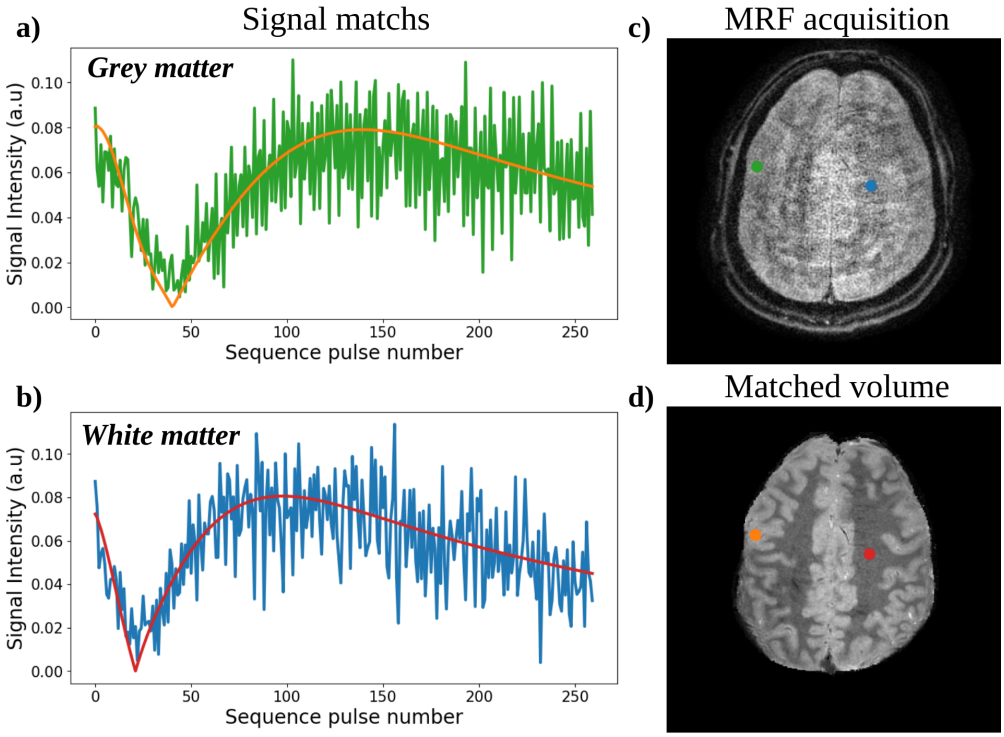


**Figure I.2.5**: Match results for fingerprints in the grey (a) and white (b) matter of the brain for the IR spoiled sequence under spiral acquisition. The signal locations are indicated on (c) a slice of the MRF acquisition and (d) a slice of the 4D matched volume map containing the matched dictionary entries, both shown at the first time point here.

Figure I.2.6 also shows an example of reconstructed relaxometry maps using the previously described code and the *in vivo* acquisitions from Section I.2.2.3 (Figure I.2.4) using different undersampled trajectories. On the first line, $T_1$ reconstructed maps are shown, on the second line, $T_2$ reconstructed maps are shown. Both parametric maps have been reconstructed through dictionary matching in a simulated dictionary using 30 $T_1$ uniformly distributed between 0.2 and 3.5s, and 30 $T_2$ uniformly distributed between 10 and 200ms. A reference $B_1$ map was used as a constraint (see Section I.3.2). We have also compared these results with the MRF Philips sequence (see Section I.2.2.2) in phantoms and volunteers. Actual validation results are provided in Chapter III. We observed similar parameter ranges in the

estimated relaxometry maps $T_1$ and $T_2$ (not shown), as well as the expected structure in the maps compared with standard literature results. Finally, Figure I.2.6 also confirms that undersampled (and thus artefacted) MRF acquisitions can actually provide decent parametric maps after matching.

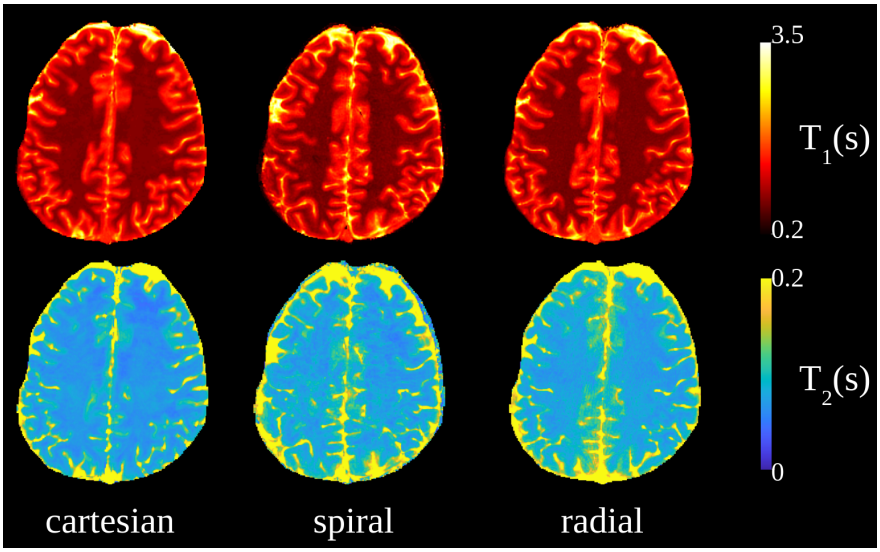


**Figure I.2.6**: Comparison of estimated MRF quantitative maps computed from a sequence acquired with cartesian (left column), spiral (middle column), and radial (right column) k-space sampling trajectory.

### I.2.4 Conclusion

In this section, we presented the MRF tools we have implemented in the lab for the acquisition and reconstruction of MRF estimate maps. Even if the first results show a promising estimation of relaxometry parameters compared to validated MRF sequences, these very first estimates are still limited because the simulations can suffer from other *in vivo* effects that need to be taken into account. Moreover, simple relaxometry maps don't provide enough information for stroke diagnosis in the clinic. In the rest of this chapter, we will explore MRF methods that have been shown to improve the accuracy of MRF relaxation times measurements, as well as advanced reconstruction methods for new parameter estimates and contras image generation.

## I.3 Correcting for scanner imperfections

Even if the standard relaxometry MRF method allows fast and accurate estimates of $T_1$, $T_2$ and $B_1$ maps, taking into account scanner imperfections in the simulations and reconstruction process has been shown to improve the accuracy of the estimates. We decided to implement two simple tools for RF slice profile and $B_1$ artifacts correction.

### I.3.1 Slice profile effect

In certain cases, the simple simulation models described above aren't sufficient to accurately represent the reality of an *in vivo* acquisition. Ideally, a slice in MRI should experience a uniform RF excitation throughout its thickness. However, in practice, the spatial excitation

of spins is a distribution ranging from the nominal flip angle (at the center of the slice) to largely reduced flip angles at the edges. This concept is illustrated in Figure I.3.1 for a truncated sinc pulse profile with two side lobes. The resultant change in signal across the thickness of a slice is termed the slice profile (SP).

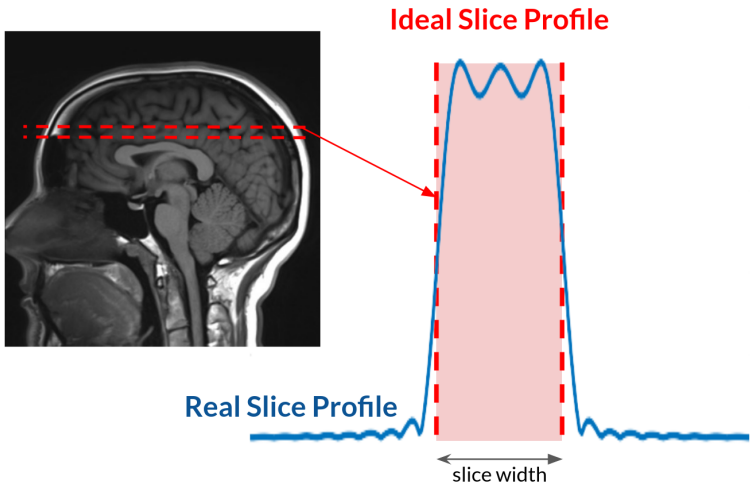


**Figure I.3.1**: Schematic illustration of the slice profile effect in an imaging slice.

As introduced by Ma et al. 2017 and deeply studied by Hong et al. 2017, the SP effect is one of the main causes of imperfection in MRF quantitative map reconstruction. Deviations between the actual and nominal flip angles due to the slice profile result in an error within the dictionary. The SP effects can be integrated into the simulation process by simulating the radiofrequency pulse profile in the dictionary.

We implemented such an approach by using a Matlab code developed in the lab that takes as input the pulse profile, the slice thickness, and the nominal desired FA value. It considers infinite relaxation time (*i.e* no relaxation occurs during the pulse duration), N spatial samples across the slice, and an extent of spatial sampling equal to 4 times the slice thickness. For each FA value of the FA train, the code uses the RF pulse profile, the slice section gradient, and the desired flip angle at each time point to represent how the magnetization vector evolves at different spatial positions across the imaged slice and evaluate the actual FA in each position (*i.e.* N spatial samples). Using this, we obtain a slice profile simulated with N isochromatic, then N flip angle values around the nominal flip angle derived from the profile. Each isochromat was then simulated independently for the whole sequence before averaging over the slice profile. By setting the *slice_profile* argument in the JSON input file (see Figure I.2.1), the dictionary simulations are repeated for each unique FA value of the slice profile and averaging according to this density. If the discretization of the profile is set to N=201 isochromatic, the simulation time is increased by a factor of 201/2 (symmetry of the profile) without parallel computation.

In Figure I.3.2, *in vivo* MRF results in one volunteer show that the SP is strongly correlated with the $B_1$ estimation, which makes sense as $B_1$ also relies on the FA actual value. For different types of sequences, the computed $B_1$ map is completely out of range without taking

into account the slice profile in simulations. It is worth noting that, in Figure I.3.2, the spoiled GRE sequence (middle) is designed with constant low flip angles which made the sequence less sensitive to SP effects than the advanced one (right) corresponding to the studied sequence with varying high flip angles.

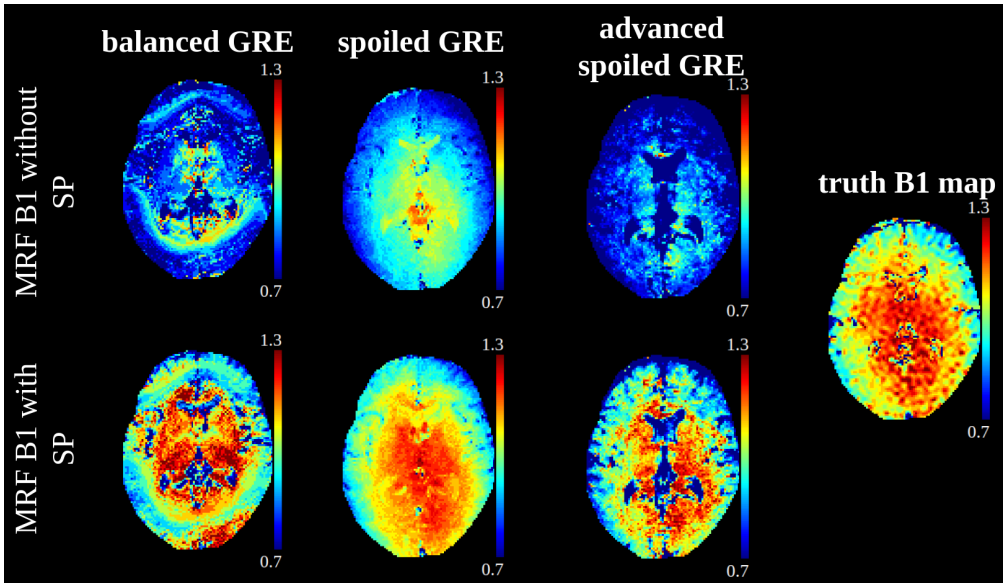


**Figure I.3.2**: Schematic illustration of the slice profile effect in an imaging slice. The three left columns represent the $B_1$ map derived from the MRF acquisition, without (top row) and with (bottom row) considering the SP in the dictionary. A $B_1$ map, acquired with a specific Philips sequence (DREAM, cf I.3.2 is displayed on the right column as reference.

In conclusion, even if incorporating the slice-profile effect greatly increases the simulation duration, it improves the quality of the reconstruction map.

### I.3.2 $B_1$ correction

As introduced in Section I.2.1.1, $B_1$ sensitivity is considered as a parameter dimension of the dictionary simulations, often with a range between 0.7 to 1.3. The actual flip angles are calculated as nominal flip angles multiplied by $B_1$. First MRF studies have shown that some sequences are more sensitive to the $B_1$ effect(notably when abrupt changes in flip angle are introduced as shown by Buonincontri et al. 2016) than others. The $B_1$ effect can be cross-related to other relaxometry effects such as $T_1$ as observed by Thomson et al. 2023, and MRF reconstruction could benefit from a $B_1$ correction technique (see Ma et al. 2017; Kang et al. 2023). $B_1$ correction means the acquisition of ground truth $B_1$ sensitivity maps that can be used during MRF matching protocol to constrain the matching space in the dictionary, reducing computing time and improving other parameters mapping. With standard MRI acquisition, it is also possible to acquire fast $B_1$ maps with dual refocusing echo acquisition mode (DREAM from Nehrke et al. 2012).

We implemented a $B_1$ correction technique by defining a path to a $B_1$-acquired map in the JSON input file of the reconstruction algorithm, to allow a constrained matching. Before dot-product computation, acquired $B_1$ values are processed such as:

- Spatial registration of the $B_1$ map to the MRF acquisition to ensure voxel-wise correspondence.
- Smoothing of the $B_1$ map to avoid inconsistency artifacts resulting from the acquisition.
- Assess $B_1$ map values to closest dictionary $B_1$ value to ensure correspondence between $B_1$ map and MRF dictionary simulations.

Then, for each $B_1$ value of the dictionary, the best match is computed between each acquisition voxel in a spatial mask corresponding to the processed $B_1$ map values, and the associated subpart of the dictionary. A schematic and simplified illustration of this process is shown in Figure I.3.3.

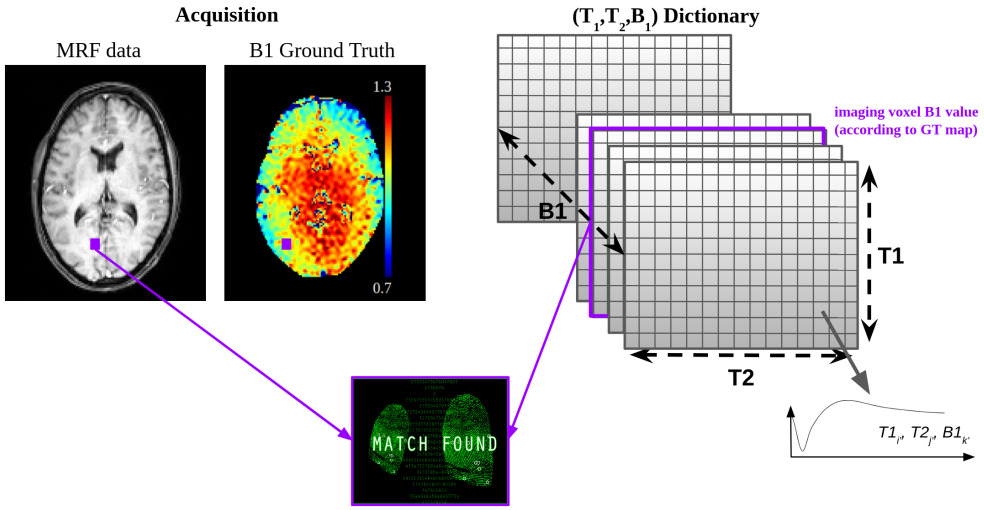


**Figure I.3.3**: Schematic illustration of the constrained matching using a $B_1$ ground truth map.

In the end, all spatial masks are joined together to reconstruct fully resolved quantitative maps constrained by the $B_1$ map.

Figure I.3.4 shows the impact of combining $B_1$-constrained reconstruction and SP simulation in one volunteer. Interestingly, $B_1$ constrained matching and slice profile effect are highly related. As introduced in Section I.3.1, the strong influence between SP and $B_1$ value is shown here because constraining matching without SP simulation degrades resulting maps. Both effects rely on the true pulse FA in the simulations and need to be combined to achieve the best results. One can observe that $T_1$ maps appear relatively insensitive to $B_1$ effect, while $T_2$ maps show greater dependence on the choice of the reconstruction mode.

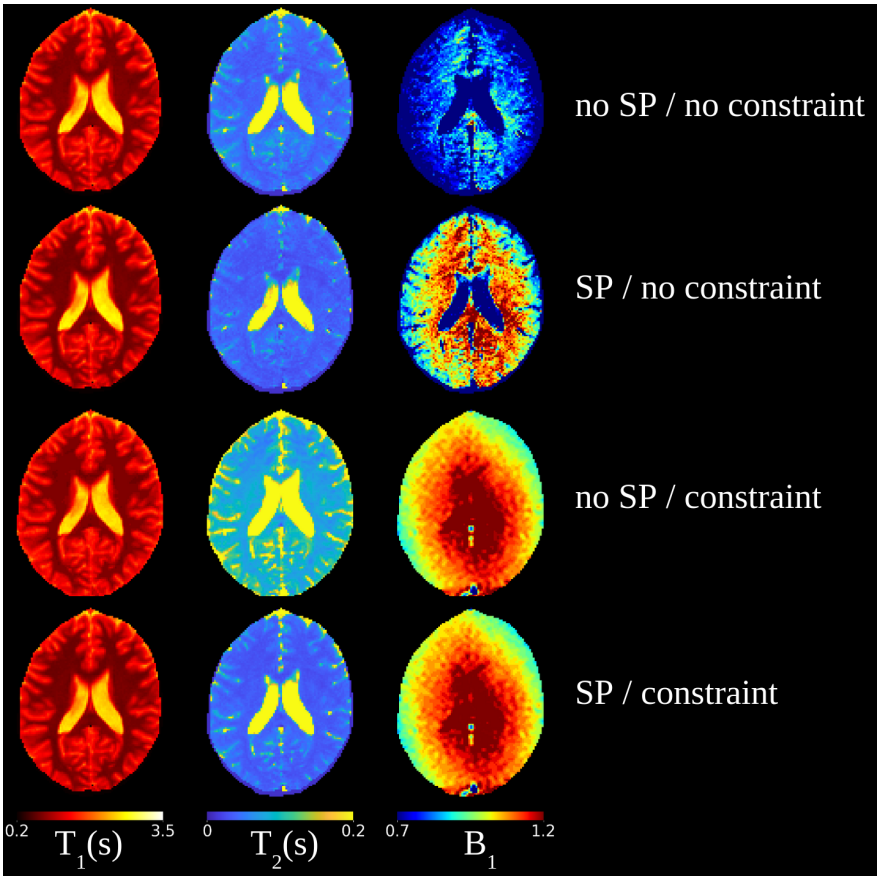


**Figure I.3.4**: *In vivo* reconstructed maps using or not using different combinations of slice profile correction and $B_1$ constraint matching. For the two last row, the $B_1$ map is the one used as a constraint.

## I.4 Accelerating the protocol using dictionary compression

When increasing the number of samples for each tissue parameter, or the number of parameters, the MRF dictionary gets larger and simulation easily leads to millions of signals, and then a large amount of data. Simulating a lot of these MRF dictionaries means storing gigabytes of signals. Moreover, heavy data means extensive loading and reconstruction times in the MRF protocol, especially if we add steps such as slice profile effects simulation. This is an important limit for the clinical translation of such a method. Facing these issues and inspired by McGivney et al. 2014, we have implemented a Singular Value Decomposition (SVD) compression of the dictionary in the time dimension. Considering the MRF dictionary of a sequence as a matrix of signal D of shape $(n_{signals}, n_{pulses})$. Using the SVD, we can write D as:

$$D = U\Sigma V^* \tag{I.4.1}$$

where $U \in \mathbb{C}^{n^2_{signals}}$ and $V \in \mathbb{C}^{n^2_{pulses}}$ and $\Sigma \in \mathbb{C}^{n_{pulses} \times n_{signals}}$ is a diagonal matrix containing the singular values. The columns of U are the left singular vectors and the columns of V are the right singular vectors.

By truncating $U$, $\Sigma$, and $V$ retaining only the first k vectors in each, a k-rank form of D could be computed. By calling the truncated right singular matrix $V_k$, a subspace dictionary could be obtained with the relation $D_k = D * V_k$ where $D_k \in \mathbb{C}^{n_{signals} \times k}$ where $D_k$ is a subspace representation of D in the "SVD" space of rank k. Figure I.4.1 shows an example of a dictionary projected in the low-rank space using an SVD on k=3 and k=10 temporal bases for the sequence from our sequence.

Using the k right singular vectors from $V_k$, it is possible to project the MRF acquisition in the same space as the dictionary and process to standard dictionary matching under the compressed domain. Dealing with such low-rank data reduces the RAM-loading time of the dictionary but also the matching time because the dot product is done in a smaller temporal dimension.

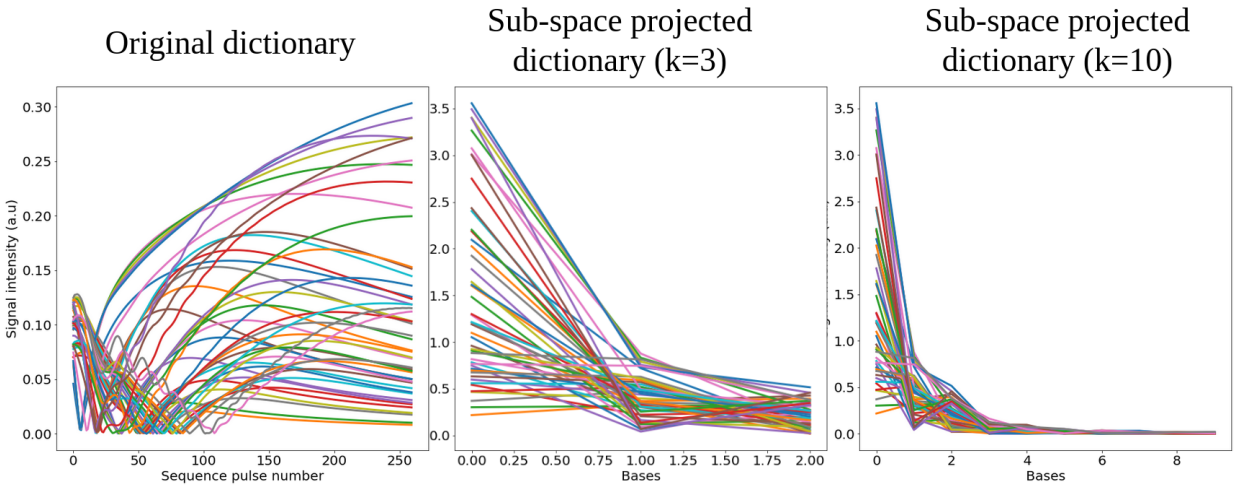


**Figure I.4.1**: MRF dictionaries in the compressed domain. On the left, is a selection of original fingerprints (260 pulses). Middle and right: the same fingerprints in the compressed domain, considering the first 3 ranks (middle) or the first 10 ranks (right) in the matrix $D$.

To validate our implementation, we computed different SVD subspaces of an MRF dictionary simulated from the studied sequence. The dictionary is simulated for 3 parameters $(T_1, T_2, B_1)$, and contains 490,000 entries. The SVD decomposition takes less than 10 seconds with the native implementation in Matlab. After the decomposition, two truncations are made resulting in a 3-base and a 10-base SVD dictionary.

Figure I.4.3 shows an example of reconstructed maps issued from both subspace dictionaries and compared with the original dictionary. As shown, the rank k which is the number of bases used in the subspace to temporarily describe the signal, needs to be set by finding a trade-off depending on the sequence used. This trade-off can be inferred from the shape of the projected dictionary. As seen in Figure I.4.1, the signal fades after 5 bases, suggesting that the information is mainly contained in the first 5 bases there. From our first experiments, we observed that the number of bases needed to produce parameter maps of sufficient quality as the original dictionary depends on the length of the sequence, but also the sensitivity of the sequence (spoiled VS balanced, see Figure I.4.2). There, it can be observed that the number of bases needed to transcribe almost all the information of the original signal is

higher for balanced sequences. These results have also been observed by McGivney et al. 2014. Moreover, as expected, the matching process is accelerated by approximately a factor of N/k for each reconstruction, where N is the sequence length.

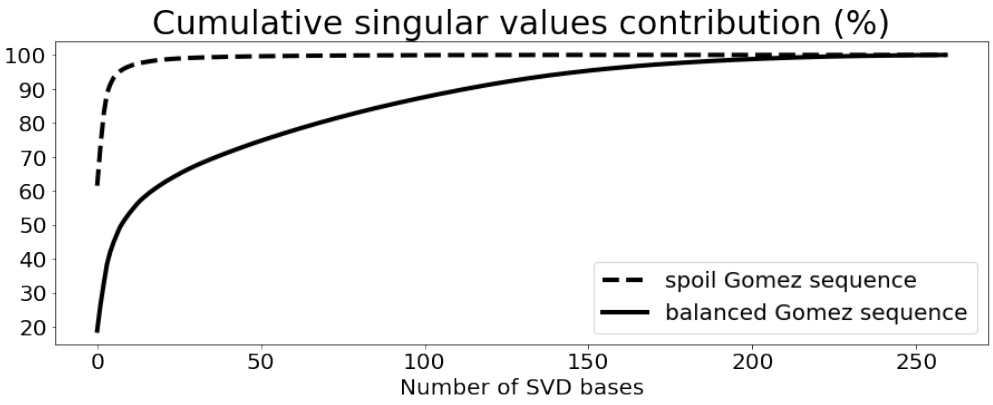


**Figure I.4.2**: Singular value contribution coefficients for two types of MR sequences readout.

We also conducted more experiments on heavier dictionaries with more than 20M entries and of 180Gb size for example. Whereas the SVD decomposition was longer to compute (approximately 200 seconds), our observations were similar since the sequence length and the parameter number are the same, suggesting that the number of required bases is more related to the sequence sensitivity than the dictionary parameters resolution.

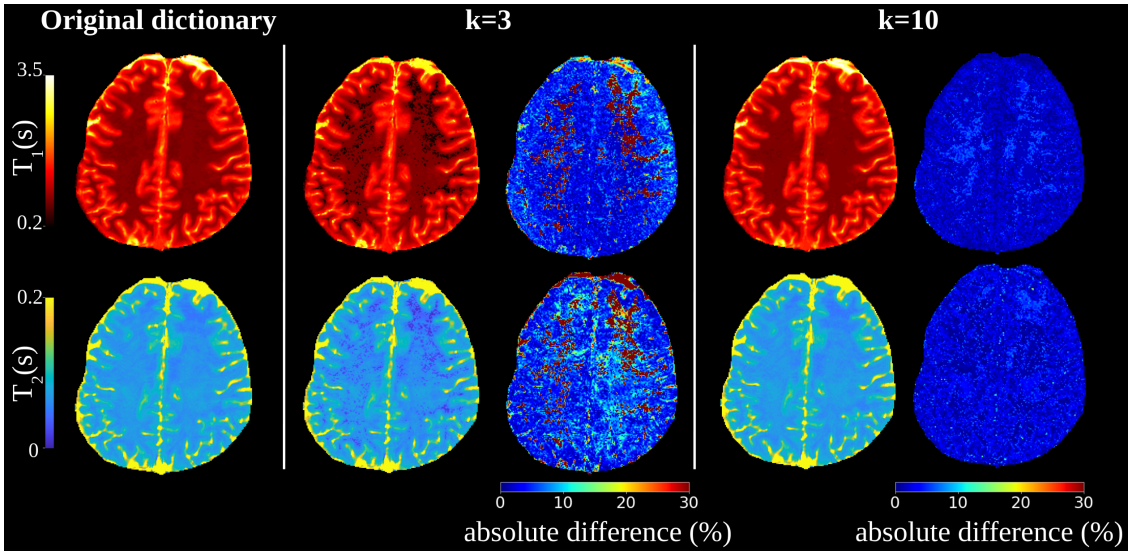


**Figure I.4.3**: *In vivo* reconstructed maps using SVD projected dictionaries with k=3 or k=10 bases. Absolute difference maps, computed between original dictionary maps and compressed ones, are shown.

To conclude, in the case of standard MRF relaxometry estimates, with spoiled MRF sequence and a small number of tissue parameters, the Singular Value Decomposition method seems to be an efficient compression method to reduce dictionary size and accelerate MRF reconstruction.

## I.5 Extending MRF for contrast images generation

In the previous sections, we showed the potential of the MR Fingerprinting framework for the estimation of quantitative relaxometry measurements in the human brain. However, stroke imaging also relies on contrast-weighted imaging such as FLAIR or $T_2^*$ MR images. This section explores how we could exploit MRF sequences to generate contrast images such as $T_1$w images.

### I.5.1 Sub-space reconstruction of undersampled data

As introduced previously, the IR spoiled sequence from Gómez et al. 2019 provides intrinsic contrast images in the time-resolved magnitude data acquired with the sequence ((Potentially 260 weighted images as it stands). However, in the context of MRF and undersampled acquisition as introduced in Section I.2.2.3, magnitude images are highly degraded by undersampling artifacts resulting from fast acquisition methods.

In Section I.4, we introduced SVD as a technique for low-rank compression of MRF signals in the temporal direction of the dictionary, to improve matching speed. In our team, Dr. Antoine Barrier works on low-rank methods for the reconstruction of undersampled MRF data. Among these low-rank methods, SVD has shown interesting results (see Assländer et al. 2018). SVD effectively smooths the acquired image while preserving essential structural information. This process not only reduces noise but also enhances the contrast, allowing for more accurate tissue characterization and improving the overall quality of the MRF reconstruction. Many methods of low-rank representation of acquired data have been explored in the k-space (Doneva et al. 2017; Zhao et al. 2018) mainly focusing on improving MRF reconstruction by denoising signal fingerprints resulting in the output of Fourier-based reconstructions of high-undersampled data.
Here, we implemented the tools developed by Dr. Barrier to reconstruct images from medium undersampled spiral acquisitions (10/25 interleaved). We used the same method as in Section I.4. But this time, we didn't aim to obtain a light dictionary of "shortened signals" using the contribution coefficients for matching but rather used the temporal basis obtained from the SVD decomposition (see an example in Figure I.5.1) to project the acquired fingerprint into a lower rank space, allowing to remove undersampling noise from the *in vivo* data. The results are the same as observed in Section I.4 where 90% of the information of the dictionary is concentrated in the first 5 bases for a spoiled MRF sequence. For the Gomez sequence and using a projection on 20 bases, nice contrast images can be retrieved from each time point.

Using the sequence from Gómez et al. 2019 that has been designed for contrast-enhanced acquisitions, and the low-rank approach allows us to obtain nice contrast images in the magnitude MRF data, using a projection of the acquired *in vivo* fingerprints on 20 bases as shown in Figure I.5.2.

We note that for higher undersampling factors, the results were not as good. This is probably because the reconstruction was made directly from the magnitude reconstructed images instead of raw k-space. Getting access to raw k-space data is in progress but was not achieved at the time of this manuscript, and we note that using magnitude images only, using low-

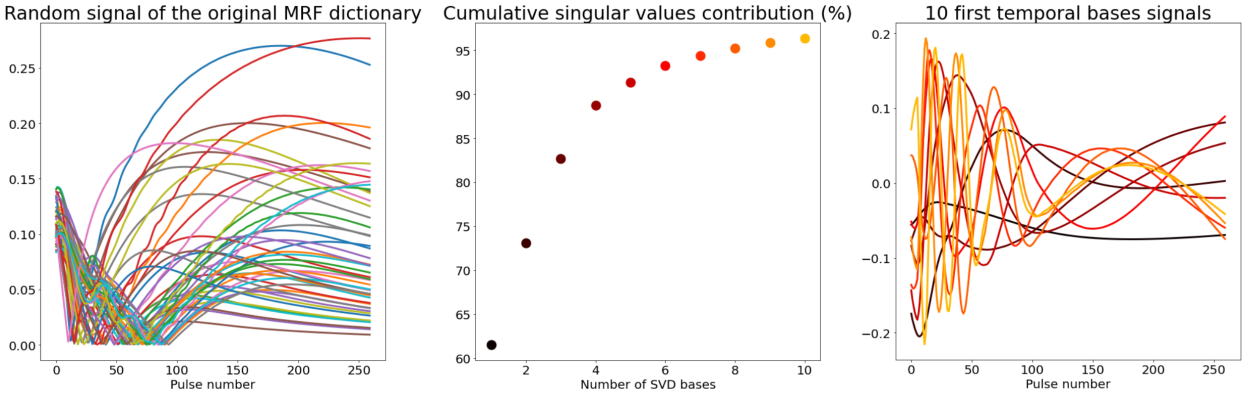


**Figure I.5.1**: 10 first SVD temporal bases (right) computed from an MRF dictionary (left) and their cumulative contribution (middle).

rank methods such as SVD for signal fingerprints isn't improving the MRF estimates. The undersampling factor threshold at which compression methods reach their limit is also the observed threshold at which the standard MRF reconstruction is distorted by undersampling noise (a detailed study of the impact of undersampling acquisition noise is provided in Section I.2.2.3).

Until the methods developed here can be applied to data in the k-space, this method can nevertheless be used to acquire contrasts similar to clinically weighted images, and angiography-like projections benefitted from the sequence design.

### I.5.2 Synthetic contrast generation

The information provided in the magnitude-image contrasts from the proposed sequence might not be sufficient to provide all the standard weighted images usually acquired during stroke exams. In that case, it might be possible to recreate weighted images directly from the estimated quantitative maps using a technique called synthetic MRI.

Synthetic MRI (sMRI) is a concept invented in the early 1980s (Bobman et al. 1985) when authors proposed some methods to retrospectively modify imaging parameters to generate new images corresponding to contrast-weighted MRI. Usually, the sMRI term (Hagiwara et al. 2017) is used for the synthesis of contrast-weighted images using quantitative relaxometry parameters, extracted from multi-contrast images (Ji et al. 2022). More recent techniques, made possible in particular by the arrival of artificial intelligence applied to imaging, allow the possibility of synthetic contrasts from another contrast-weighted image for example, corresponding to another type of sMRI and leading to confusion in the terminology. Figure I.5.3 proposes an overview of sMRI. Recently, sMRI has been developed using joint MRF and deep learning frameworks (Wang et al. 2022).

A recent algorithm proposed by Peretti et al. 2023 and called PySynth MRI has been provided with a user-friendly interface that generates many synthetic contrasts by computing a pixel-wise signal intensity as a function of input quantitative MRF maps of $T_1$, $T_2$ and Proton

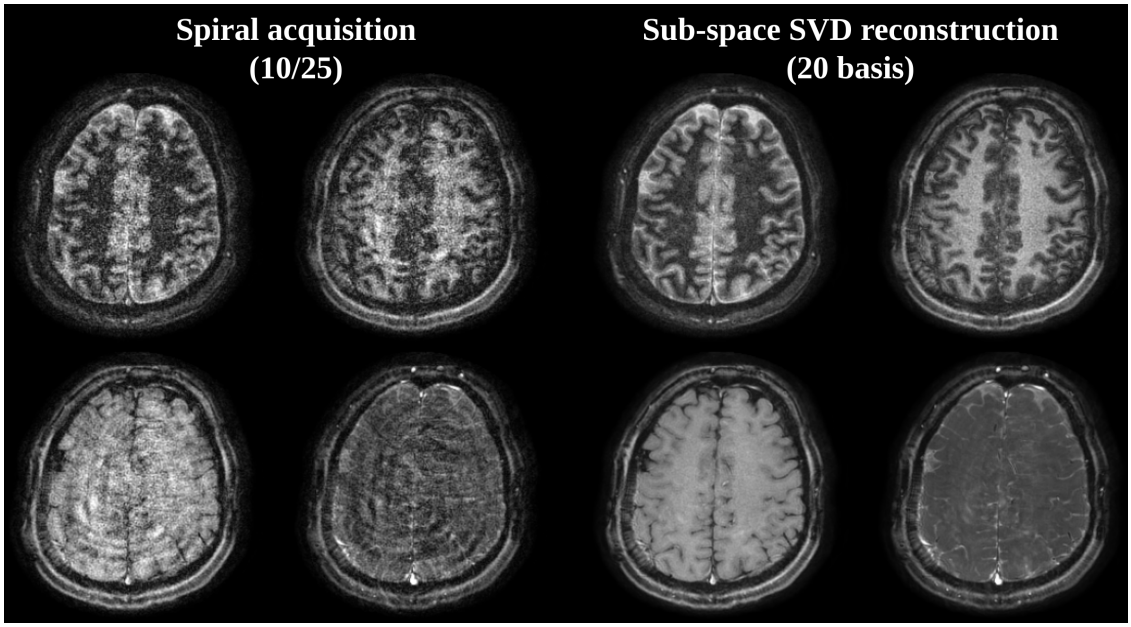


**Figure I.5.2**: Low-rank SVD reconstruction of spiral undersampled MRF data. On the left, random time point original images from an undersampled MRF spiral acquisition. On the right, the same time point images, denoised using the sub-space SVD reconstruction method, allowing the retrieval of contrast-weighted images. Images are shown for one slice of an healthy volunteer at 3T.

| Title | Equation | Description |
|---|---|---|
| **FSE** | $\mathrm{PD}\left(1-\exp\left(\frac{-\mathrm{TR}}{\mathrm{T_1}}\right)\right)\exp\left(\frac{-\mathrm{TE}}{\mathrm{T_2}}\right)$ | $T_2$w Fast Spin Echo |
| **GRE** | $\mathrm{PD}\left(1-\exp\left(\frac{-\mathrm{TR}}{\mathrm{T_1}}\right)\right)\exp\left(\frac{-\mathrm{TE}}{\mathrm{T_2}}\right)$ | $T_1$w Gradient Echo |
| **FLAIR** | $\mathrm{abs(PD)}\exp\left(\frac{-\mathrm{TSAT}}{\mathrm{T_1}}\right)\exp\left(\frac{-\mathrm{TE}}{\mathrm{T_2}}\right)\left(1-2\exp\left(\frac{-\mathrm{TI}}{\mathrm{T_1}}\right)\right)$ | $T_2$w Fluid Attenuated Inversion Recovery |
| **MP2RAGE** | $1-2\exp\left(\frac{-\mathrm{TI}}{\mathrm{T_1}}\right)$ | $T_1$w Magnetization-Prepared 2 RApid Gradient Echoes |
| **DIR** | $\mathrm{PD}\left(1-2\exp\left(\frac{-\mathrm{TI_2}}{\mathrm{T_1}}\right)+2\exp\left(\frac{-\mathrm{TI_1}+\mathrm{TI_2}}{\mathrm{T_1}}\right)-\exp\left(\frac{-\mathrm{TR}}{\mathrm{T_1}}\right)\right)\times\left(\exp\left(\frac{-\mathrm{TE}}{\mathrm{T_2}}\right)\right)$ | 3D Double Inversion Recovery |
| **TBE** | $\mathrm{PD}\left(1-2\exp\left(\frac{-\mathrm{TI}}{\mathrm{T_1}}\right)\right)\times\left(1-\exp\left(\frac{-\mathrm{TR}}{\mathrm{T_1}}\right)\right)\times\exp\left(\frac{-\mathrm{TE}}{\mathrm{T_2}}\right)$ | Tissue Border Enhancement |

**Table I.1**: Equations used for synthetic contrast generation in PySynth MRI.

Density (PD) and simulated scanner parameters chosen by the user via a graphical interface. I have collaborated with Dr. Legris to implement PySynth and obtain the first synthetic MR images using our IR-spoiled sequence and the reconstructed MRF quantitative maps. The following Table I.1 provides a list of the available contrasts as well as a description of how they are computed.

The key benefit of PySynth is that the code can be editable easily and new contrast can be computed based on other MRF-estimated maps added by the user. Bearing in mind the objective of the MRFUSE project, it could be very useful for stroke-relevant contrast image synthetisation using new estimated parameter maps. In Figure I.7.1, synthesized contrast images obtained with our sequence in a volunteer are shown in the bottom-right part. These results exhibit interesting contrasts but are still far from a clinically acceptable quality. A lot of work need to be done to improve the maps, probably by adding AI-powered tools in the

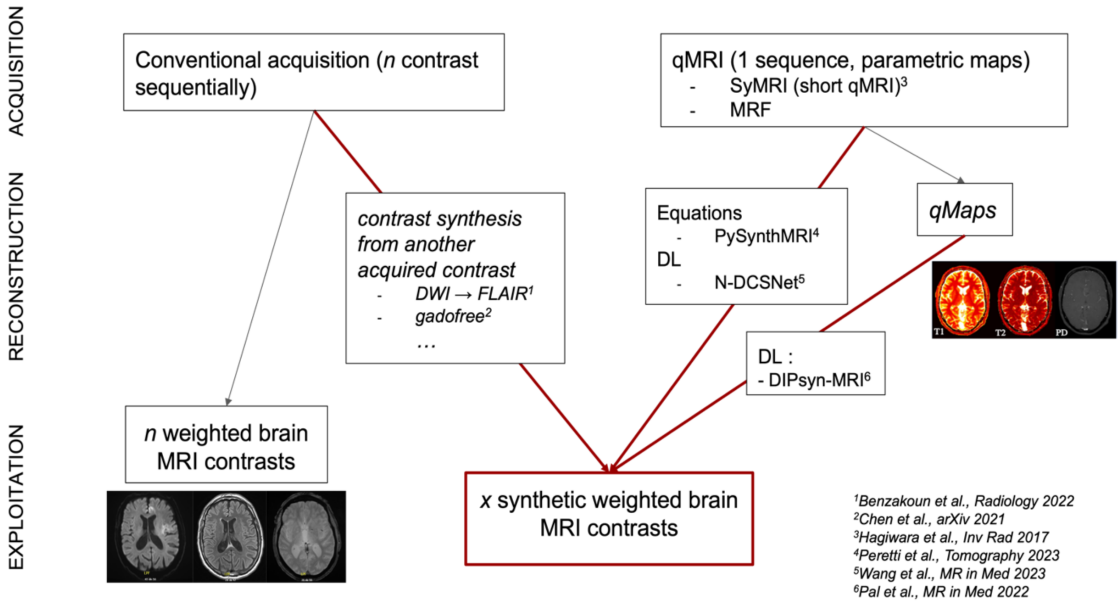


**Figure I.5.3**: Synthetic MRI overview. Courtesy of Dr. Loïc Legris.

synthesis process to improve the contrast generation adapted to the chosen MRF sequence.

## I.6 First estimates of intra-voxel properties using MCMRF

In practice, MRF relaxometry measurements can indicate abnormalities but do not fully capture the complexity of microstructural changes. This information is however crucial in the context of stroke imaging. Standard relaxometry MRF focuses on characterizing the properties of a single homogeneous compartment, assuming that the tissue or material being imaged has uniform relaxation properties. This model cannot accurately represent the reality where biological tissues and complex materials often consist of multiple compartments with different physical and chemical properties. Single-compartment models cannot accurately represent the reality of the structure of the human brain. In this section, we aim to extend the concept of Magnetic Resonance Fingerprinting to model and analyze tissues or materials with multiple distinct microenvironments, or compartments.

For this, we implemented tools for Multi-Compartment Fingerprinting (MCMRF). Even if the literature provides several names such as Multicompartment MRF (Tang et al. 2018, Multicomponent MRF (McGivney et al. 2018), Partial-Volume MRF (PV-MRF, see Deshmane et al. 2015), all rely on the same principles: Different tissues or components within a voxel are potentially separable in MRF because of their distinct signal evolutions. MCMRF consists of *a priori* choosing a few signal evolutions in a dictionary (and corresponding $T_1$,$T_2$ parameters) to construct a new dictionary using linear combinations of the signals with different weights. After matching, only the weights of the components in each voxel are estimated. Recently, new methods have used advanced component estimations models to automatically detect the principal source contributions in the MR signal without making prior assumptions about component relaxation time and expected number of compartments (Nagtegaal et al. 2023). The benefits of these multi-compartment approaches are that they rely on simple MRF sequences mainly used for relaxometry estimates. Applications of MCMRF are diverse. During this thesis, we quickly implement a simple multi-compartment model for MRF dictionary simulations using Python and our previously introduced simulations tool, and we apply it to two studies: Myelin Water Fraction (MWF) estimates in the human brain (Chen et al. 2019) and Cerebral Blood Volume (CBV) estimates.

**Myelin Water Fraction** As it was proposed by Chen et al. 2019, we used a three-compartment model including myelin water ($T_1$=130ms, $T_2$=20ms), intracellular/extracellular water ($T_1$=1300ms, $T_2$=130ms) and free water ($T_1$=4500ms, $T_2$=500ms). Weighted combinations of these three compartments were computed with a 1% resolution leading to a 5151 entries dictionary for our 3T application.

**Cerebral Blood Volume** We used the same implementation but we changed the values of relaxation time in the tissues. Inspire by Thomson et al. 2023, we chose a three-compartment model including an extra-cellular compartment ($T_1$=1110ms, $T_2$=80ms), intracellular blood ($T_1$=1600ms, $T_2$=300ms) and cerebrospinal fluid (CSF, $T_1$=3250ms, $T_2$=600ms). Values were chosen from literature and in-house measurements at 3T. No exchange was taken into account in the model.

In Figure I.6.1, we show the three signals associated with each compartment that were combined for the dictionary generation in both experiments.

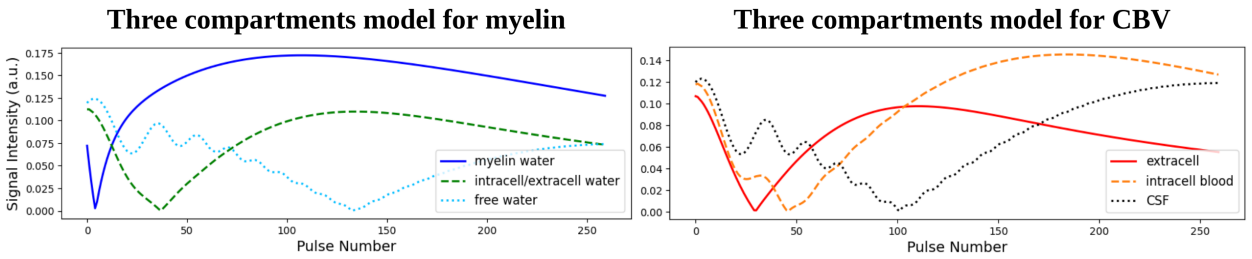


**Figure I.6.1**: Multi-component MRF results in an *in vivo* volunteer.

Figure I.6.2 shows the first results obtained in a volunteer for both studies applied on a *in vivo* cartesian sampled acquisition using the sequence from Gómez et al. 2019. Values are shown in % as the fraction of the compartment contribution in the tissue signal. Even with a simple model with no exchange, the first results are interesting. A high concentration of myelin is estimated in the white matter part of the brain as excepted by the literature (Fukunaga et al. 2010). Our results are consistent with Chen et al. 2019 who validated their methods against phantom experiments and literature references. Concerning blood volume, higher blood contributions are found in expected large vessel areas of the brain such as the sagittal sinus region. Moreover, a nice contrast between white matter and grey matter blood volume is seen and is consistent with the literature review (Bjørnerud et al. 2010; Knutsson et al. 2014; Leenders et al. 1990; Liu et al. 2017).

**Conclusion** Still relying on standard relaxometry MRF with spoiled sequences, multi-component MRF seems to offer information about sub-voxel tissue properties such as myelin or blood components in the imaging voxel. This information could provide a first approach to estimating, without contrast agent injection, vascular characteristics in the brain such as an approximation of the cerebral blood volume that could provide relevant insight into the human brain perfusion for stroke patients management.

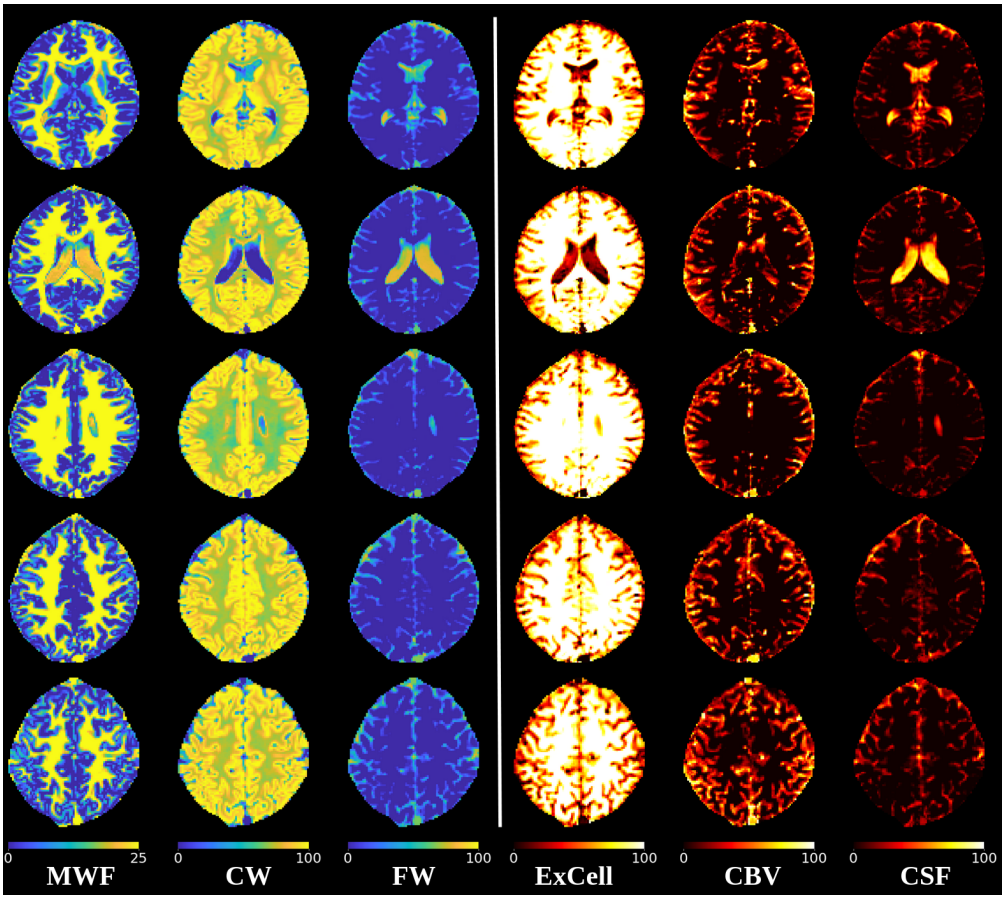


**Figure I.6.2**: Multi-component MRF results in an healthy volunteer at 3T.

## I.7 Conclusion

In this chapter, we presented the first MRF tools that we implemented for the simulation, acquisition, and reconstruction of ($T_1$,$T_2$,proton density) relaxometry maps using a standard MRF spoiled-GRE sequence. We showed that these MRF sequences could also provide contrast MRI images obtained either via low-rank artifact removal in magnitude MRF images or synthetic MRI contrasts from relaxation maps. Multi-compartment tools have also been implemented to try to provide initial estimates of intra-voxel contributions such as of myelin water or blood volume fractions. This pipeline could provide a first solution to the challenges raised by the MRFUSE project for the management of stroke patients. The combined results from a 2D MRF acquisition obtained in one volunteer are shown in Figure I.7.1 with apparent high-quality qualitative or quantitative images.

Although encouraging, this pipeline has yet several limitations. First, given the sequence design and the type of k-space sampling, the total acquisition time is already too long for emergency settings (2 minutes/slice). This could probably be improved using sequence optimization and advanced reconstruction of MRF maps using direct k-space data as it has been demonstrated in various recent studies that have reached whole brain acquisition time under a minute using sub-space reconstruction of 3D spiral acquisitions. As already

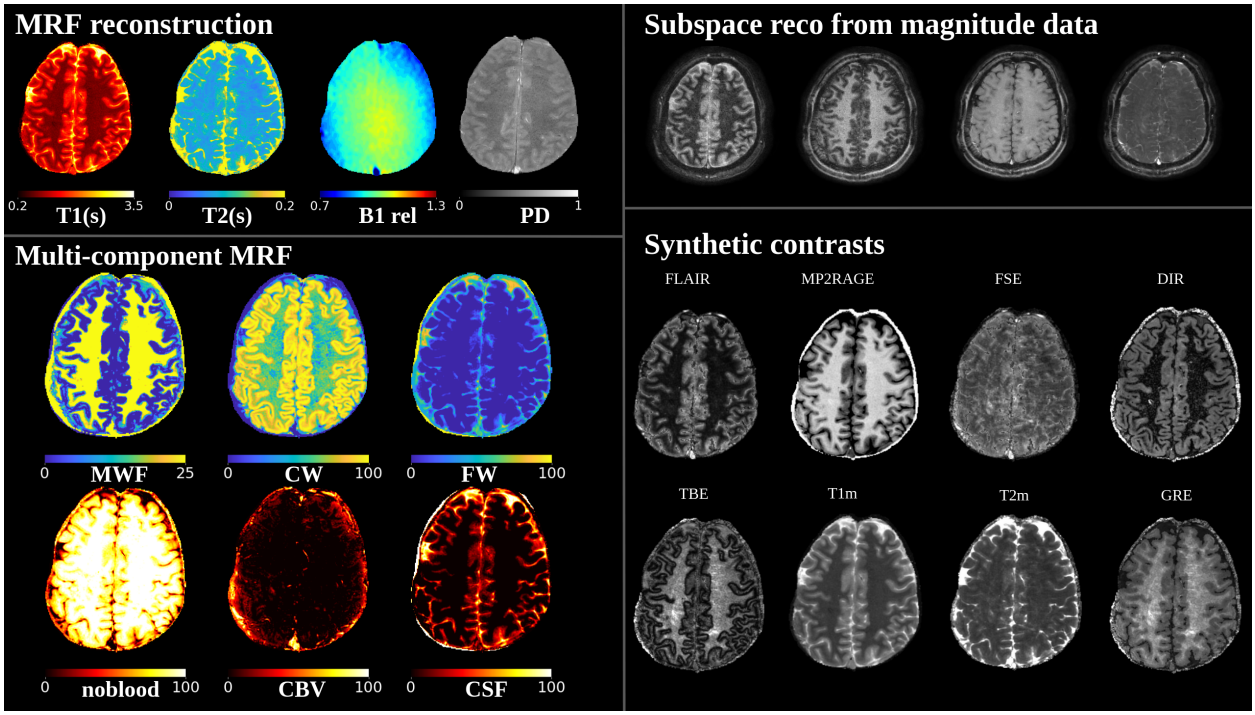


**Figure I.7.1**: Overview of the whole MRI maps (single slice) obtained from our pipeline. All the maps were reconstructed from a 2-minute acquisition at 3T without contrast-agent injection.

mentioned in this chapter, our synthetic contrasts obtained using physical models are also not satisfying for the moment. Again, recent advances in DL generation have shown better handling of partial volume effects and we could easily foresee an optimized sequence that will take into account the initial contrasts of the sequence to obtain important images for stroke protocols such as FLAIR or angiography.

The main issue with this current protocol remains with the ability to derive microvascular estimates from the sequence. Relying only on the averaged relaxometry properties of the tissues to quantify intra-voxel microvascular properties is difficult due to the small volume fraction occupied by the blood compartment (approx. 4%). A recent study from Thomson et al. 2023 proposed a contrast-free quantification method of CBV and intravascular water residence time using multi-compartment MRF (or partial-volume MRF, see Deshmane et al. 2015). They relied on $T_1$ and $B_1$ measurements, and a two-compartment model with exchanges between intra and extravascular pools. This is similar to our implementation except for the fact that we integrated $T_2$ measurements without modeling exchanges. Although results from both approaches are interesting in terms of contrast and large vessel visualization, it is clear that SNR is an issue in characterizing tissues with smaller CBV. Relying on a multi-compartment model also raises the question of the blood compartment homogeneity. It has been known for decades that blood relaxation highly depends on blood hematocrit and oxygenation. Thus, a unique couple of relaxation times will not be sufficient to capture the whole blood network and a possible intersection with another tissue component can be foreseen. Finally, relaxation times are also influenced by several factors including, water diffusion, or blood flow, making it even more difficult to isolate the vascular components'

contribution.

Given the 2 main objectives of our project, we concluded that instead of trying to optimize our protocol and thoroughly validate our initial results in a cohort of human volunteers, we would first explore and find new types of MRF sequences that could overcome these inherent limitations. This is the topic of the next chapter.

# Chapter II

# Towards non-contrast MRF sequences sensitive to vascular parameters

This chapter aims to improve the results obtained in the first chapter by looking at the quantification of the well-known BOLD effect with MRF rather than using simple $T_1$,$T_2$ measurements to estimate microvascular parameters. For this, different types of gradient-echo sequences are compared for their sensitivity to magnetic field inhomogeneities. An *in-silico* study is then conducted to manually find a sequence design that allows non-contrast estimates of the cerebral blood volume and averaged vessel diameters inside the MR voxels.

Part of this work was done during a 3 months Master's internship that I supervised.

## Contents

# II.1 Introduction

The previous chapter of this thesis examined the development and implementation of standard MRF tools to perform robust and fast relaxometric measurements as well as roughly characterize intra-voxel properties using $T_1$,$T_2$ multi-compartment models. As detailed in the previous discussion, it seems that these types of measurements alone are limited to microvascular quantification which is a crucial objective of our project.

In this chapter, we aim to overcome these limitations by integrating a new effect in our MRF framework: the well-known Blood Oxygen Level Dependent (or BOLD) effect. The BOLD contrast relies on magnetic susceptibility differences between oxygenated and deoxygenated blood, which disrupt the magnetic field within the imaging voxels. The underlying field inhomogeneities rely on the blood compartment properties and also on the spatial coherence of the microvascular structures, extending the effects beyond the immediate vicinity of the blood compartment, up to five times the diameter of the vessels. We hypothesized that this extended sensitivity to vascular geometry and function could be used to design a new method for non-contrast CBV and microvascular estimates with MRF.

In the first part, we aim to provide a better comprehension of the effect of the magnetic field inhomogeneities on the MR signal evolution of different types of MR sequences. To find suitable MRF sequences, we come back to two fundamental classes of fast MR gradient echo sequences:

**Spoiled GRE**: these sequences (such as the FISP sequence used in chapter I or the FLASH sequence) eliminate any residual of transverse magnetization before the next excitation pulse by using a combination of gradient spoiling (application of large magnetic field gradient in one or more spatial direction) and/or RF spoiling (application of different RF phases for each pulse. See later section in this chapter). The aim is to remove any coherent transverse magnetization, thus "spoiling" the residual signal from previous excitations. These types of sequences are usually used in BOLD functional MRI experiments using EPI readouts and for $T_2^*$ mapping when used with multiple echo times.

**Balanced GRE**: These sequences, also known as balanced steady-state free precession (bSSFP) sequences, store the transverse magnetization between pulses thus creating a steady-state condition where both longitudinal and transverse magnetization contribute to the signal. bSSFP are known for their high sensitivity to magnetic field inhomogeneities and have been occasionally used in fMRI experiments but their rather complex signal evolution and sensitivity to many other parameters has complicated their clinical usage. The effect of intravoxel $B_0$ inhomogeneities on bSSFP sequences has not been fully characterized in the literature.

We describe the general effect of $B_0$ inhomogeneities and BOLD effects on several sequences using a new framework based on the analysis of actual $B_0$ frequency distributions inside the voxels and the MR sequences response profiles (see explanations below). This allows a better understanding of the effect of realistic $B_0$ distributions on complex sequences such as bSSFP. This framework can also be used to quickly simulate MR signals and produce

MRF dictionaries that incorporate BOLD effects. In this chapter, we provide the general idea of the simulations but the details of the implementation will be given in Chapter III. We study and discuss the overall sensitivity of both types of sequences to magnetic field inhomogeneities for different acquisition parameters (TR, TE, FA, etc), in the transient and the steady state (*i.e.* the equilibrium after $5 \times T_1$ where the properties of the magnetization are unchanging with time) parts of the sequence.

In the second part, we focus our attention on bSSFP sequences and propose 2 metrics to manually find MRF-bSSFP sequences that could provide good sensitivity to CBV without contrast injection and could be played in our scanners.

## II.2 Theoretical study of magnetic fields inhomogeneities effects on MR signals evolution

### II.2.1 Basic Principles

In an MRI experiment, the nuclei in the body are exposed to a strong magnetic field, $B_0$. The magnetic moments of these nuclei align with the magnetic field and precess around the field direction at a specific frequency known as the Larmor frequency. The Larmor frequency, $\omega_0$, is given by:

$$\omega_0 = \gamma B_0 \tag{II.2.1}$$

where: $\gamma$ is the gyromagnetic ratio, a constant specific to the type of nucleus (for protons, $\gamma \approx$42.58MHz/Tesla).

$B_0$ inhomogeneities refer to deviations of the magnetic field from its ideal uniform value $B_0$. These deviations can be caused by imperfections in the magnet itself, but also by tissue biological properties as already mentioned in the introduction section and illustrated in Figure II.2.1 for voxels that contain paramagnetic cylinders ($\Delta\chi$=0.4ppm) placed in an external $B_0$=3T magnetic field. Magnetic field inhomogeneity maps can be derived from susceptibility distributions using the fast method proposed by Salomir et al. 2003.

A simple and common way to describe the effect of subvoxel $B_0$ inhomogeneities on the MR signal is to consider (1) the spatial variations of the fields (2) the corresponding Larmor frequencies and the local dephasing of the magnetization vectors, and (3) to compute the complex weighted sum of all spatial points to derive the total signal decay. In general, the extra dephasing effect due to $B_0$ inhomogeneities is represented as a new constant $T_2{}^*$ which replaces $T_2$ in the MR FID exponential decay. Yet, it is important to realize that this is only an approximation that supposes that the spins are static in the voxels, that the frequency distribution has a Lorentzian shape, and that a non-balanced GRE sequence is used.

In the present study, we tried to go beyond this simple representation and see if other types of signal evolutions can be observed in different MR sequences. In order to conduct our broader analysis, we chose to describe the effect of $B_0$ inhomogeneities and subsequent effects on MR

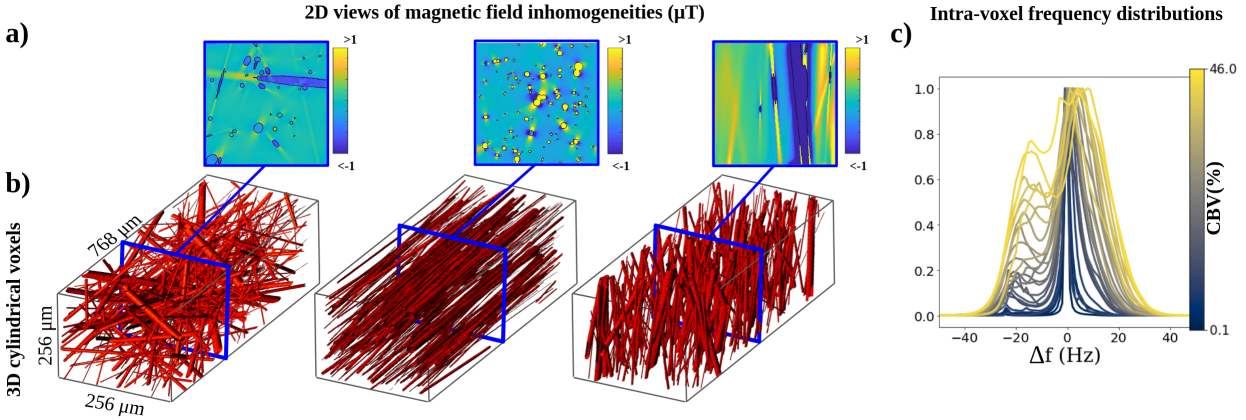


**Figure II.2.1**: Magnetic field simulations (a) in synthetic 3D-cylindrical vascular voxels (b) with fixed blood susceptibility value, leading to a set of intra-voxel frequency distributions (c). Panel c) corresponds to 100 simulated voxels (1 distribution/voxel). The color of the frequency distribution corresponds to the CBV of the voxel.

sequences with a new framework that allows fast evaluations in various conditions. First, as we considered that the effect of diffusion could be neglected, we forgot the spatial arrangement of the frequencies and focused only on the distribution of those values (see Figure II.2.1). Diffusion effects are weak for most short TR GRE sequences as shown in the next Chapter III. Second, we computed the response of an MR sequence for all individual frequency values in the histogram. This type of sequence frequency response function (or frequency response profile) is often used to study banding artifacts in bSSFP sequences but the combination of these types of profiles with actual subvoxel frequency histograms is omitted most of the time. Here we explicitly made that link and combined phase and frequency response functions at different echo times with the frequency histograms obtained from realistic magnetic field simulations to derive the temporal MR signal evolution (see Figure II.2.3 for example). This framework allowed us to quickly analyze different sequences in different modes and their sensitivity to different $B_0$ variations with or without contrast agent injection.

In the rest of this manuscript, the frequency response functions are represented as a function of the frequency offset (frequency difference between the radiofrequency synthesizer of a scanner and the local precession frequency of the magnetization) in Hertz. Unless mentioned overwise, response profiles are shown for standard tissue parameter values of grey matter ($T_1$=1300 ms, and $T_2$=80 ms) and in the steady-state conditions.

## II.2.2 Effects of magnetic field inhomogeneities on GRE spoiled sequences

Here we used our simulation pipeline to observe the response profiles and signal evolutions of GRE-spoiled sequences under various acquisition parameters.

### II.2.2.1 Influence of the acquisition parameters

**Flip Angle (FA) and Repetition Time (TR)** In Figure II.2.2, we compared the influence of acquisition parameters FA and TR on the shape of the response profile of a gradient spoiled sequence in the steady-state condition. We observed that the sequence exhibits a flat magnitude and a linear phase response profile for all the acquisition parameter values. The FA doesn't influence the phase response profile but the TR changes its periodicity. This was expected because the residual transverse magnetization is destroyed at the end of each TR, thus the dephasing acquired during one TR is not propagated into the next one.

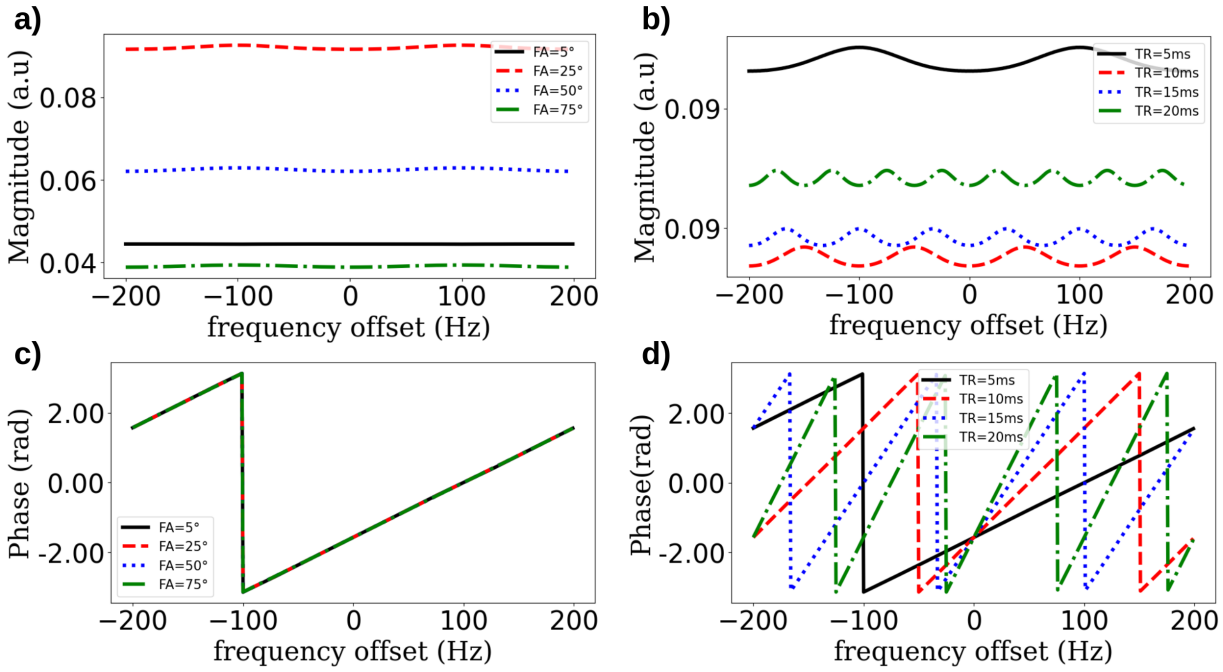


**Figure II.2.2**: Frequency response profile of a spoiled GRE sequence for different acquisition parameters. In a) TR is fixed at 5ms and in b) FA is fixed at 25°.

**Echo Time (TE)** In Figure II.2.3a, we show the known dependency of the response phase profile on TE values already demonstrated by Miller et al. 2003 where shifted TEs simply introduce a slight gradient in the off-resonance signal phase. Once again, the magnitude response profile is completely flat for every TE value. The profile amplitude decreases when the TE value increases as expected from the relaxation effect. This results in a quasi-mono-exponential signal decay at long echo times (small deviations at short echo times) when combined with a histogram of frequency distribution obtained from 20 voxel types.

**RF phase** In a spoiled GRE sequence, RF cycling involves varying the RF pulse phase to prevent coherent transverse magnetization buildup from previous excitations. This technique ensures that any residual transverse magnetization is effectively spoiled, allowing each excitation to start from a consistent magnetization state. SPGR sequences are a type of Gradient Spoiled GRE sequences with such additional RF spoiling. The RF cycling scheme is quadratic, typically expressed as:

$$\phi_n = \Delta\phi \times n^2 \tag{II.2.2}$$

where:

$\phi_n$ is the phase of the $n$-th RF pulse,
$\Delta\phi$ is the quadratic phase increment.

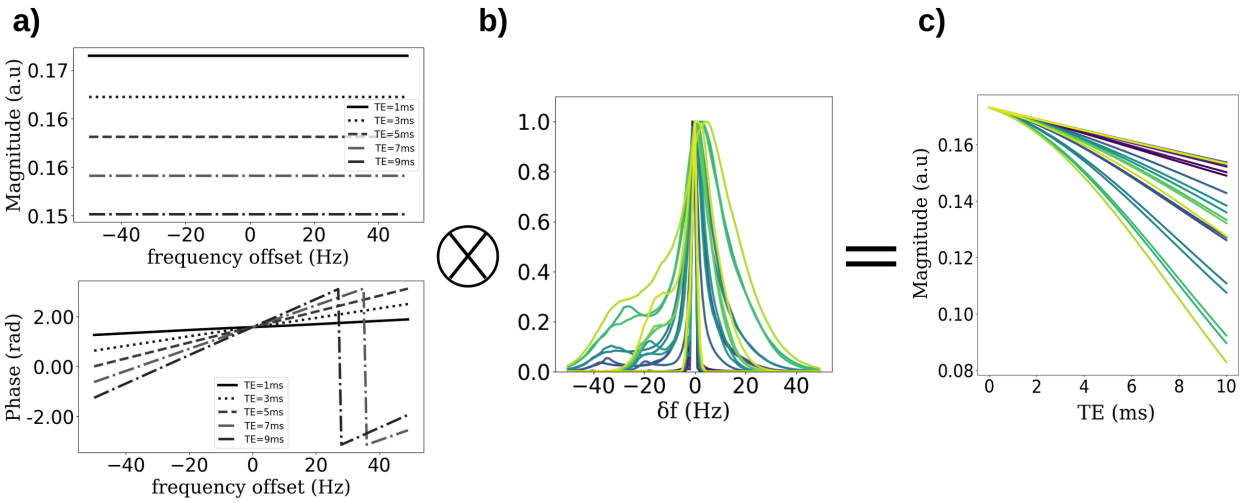


**Figure II.2.3**: Signal response of a spoiled GRE sequence to intra-voxel frequency distributions resulting from the convolution between the response profile for FA=10° and TR=10ms at several TE and the frequency distribution. The color code on the frequency distribution and on the signal as a function of TE corresponds to different CBV values.

We studied the response functions of such sequences in Figure II.2.4a. As shown, the magnitude response profile remains flat and the same slope is observed in the linear phase response for all RF cycling designs. The main effect of the RF increment is the steady state amplitude. Our simulations' results correspond to the expected steady-state amplitudes measured by Brown et al. 2014 for different phase cycling increments with a peak at 120°. Given the response profiles, quasi-exponential signal decays are also expected when these sequences are applied to 20 types of voxel.

**Time dependency** As already mentioned, the previous response profiles are shown when the sequences have reached their steady state. We also computed the same type of profiles for entire sequences (*i.e.* 1000 pulses). We can observe in Figure II.2.5 that the magnitude profile of a FISP sequence remains flat also in the transient state (0-100th pulse). This was also the case for all spoiled sequences.

Given the time-constant flat magnitude response profile, in a numerical phantom that contains a unique ($T_1$, $T_2$, $B_1$) values triplet and a gradient of frequency offset values (see Figure II.2.6a), the response of a spoiled GRE sequence will be completely homogeneous as shown by the numerical spatial simulations in Figure II.2.6b.

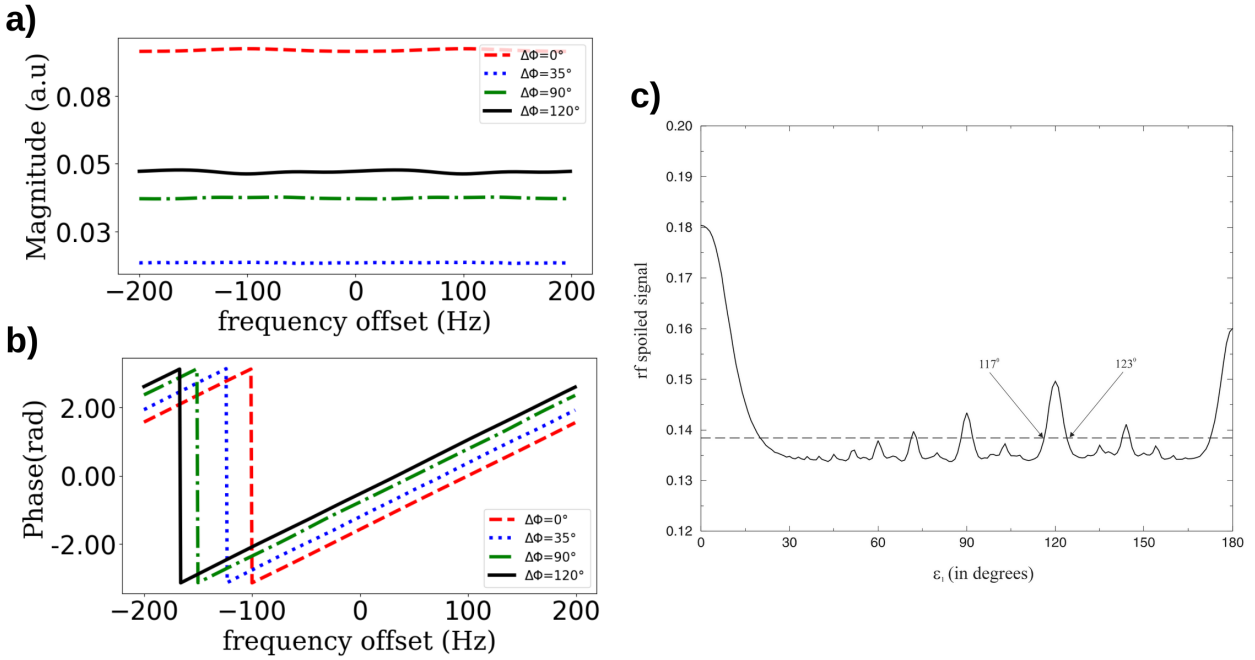


**Figure II.2.4**: Comparison of the frequency response profile of a GRE spoiled sequence for several RF phase designs. The graph in c) is from Brown et al. 2014.

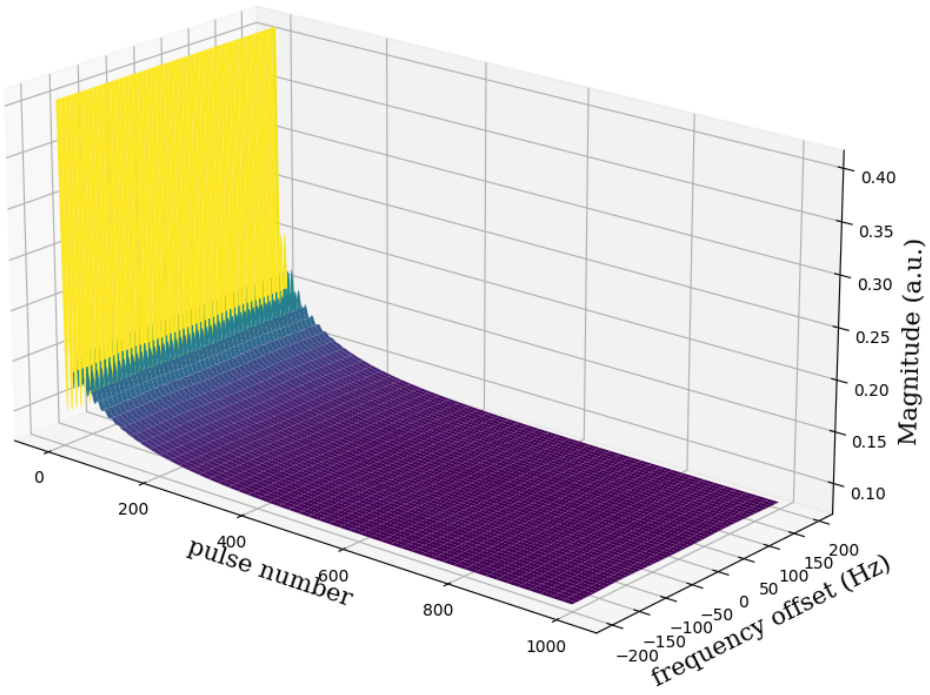


**Figure II.2.5**: Magnitude response profile of a GRE spoiled sequence through sequence pulse number. TR=5ms, FA=25°, no phase cycling.

### II.2.2.2 Conclusion

We observed that for spoiled GRE sequences, the signal decay response to different intra-voxel frequency distributions is always quasi-monoexponential. This is due to the flat magnitude

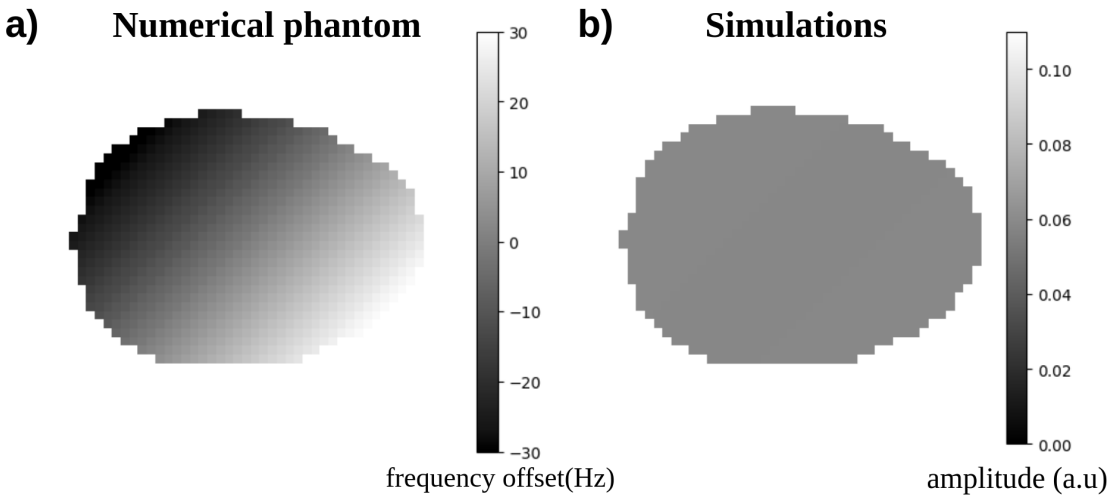


**Figure II.2.6**: Numerical spatial simulations of the response of a GRE spoiled sequence (b) to an inhomogeneous $B_0$ field phantom (a).

and linear phase response profiles obtained independently of the sequence parameters. A more complete figure in Chapter III shows that the response signals remain quasi-exponential and not unique for different intra-voxel frequency distributions. These types of signal evolutions are difficult to differentiate, making it hard to quantify the microvascular contributions under the MRF framework.

We should note that a more advanced analysis of the BOLD effect named quantitative BOLD (qBOLD) was proposed a few years ago (see review by Biondetti et al. 2023). This technique models the frequency distributions using statistical models of blood vessels represented as ensembles of isotropically oriented straight magnetic cylinders. By considering other signal contributions (large $B_0$ inhomogeneities, $T_2$), the slight deviations from monoexponential MR signal decay at short echo times (seen in our simulations) enable the separation of cerebral blood volume (CBV) and blood oxygen saturation ($SO_2$) contributions. However, this separation is feasible only at very high signal-to-noise ratios (SNR), and the cylinder model may not accurately represent all types of vascular structures.

On the other hand, many other standard MR imaging methods currently use spoiled GRE sequences for microvascular estimates. Yet, they always involve the injection of contrast agents (CA) such as Gadolinium-based compounds to enhance the magnetic susceptibility differences between blood and surrounding tissues. This induces a broadening of the intra-voxel frequency distributions and an increase in the distance between MR signals resulting from different microvascular contributions. This means, in terms of our framework, that instead of trying to create different types of signal variations (fingerprints) by changing the frequency response profiles with sequence parameters variations (which is not possible with spoiled GRE as seen in our study), these techniques induce different frequency histograms in the voxels using CA injections.

This is also the case with the initial MRvF (MR vascular Fingerprinting or MRvF Christen

et al. 2014b) approach described in the introduction chapter. Indeed, multi-echo spin- and gradient-echo sequences (non-balanced gradients) are used pre- and post-CA injection, allowing the estimation of CBV, mean vessel radius (R), and $SO_2$ within the MRF framework. The calculation of the frequency distribution is more realistic than the one used in qBOLD due to dictionaries that incorporate realistic biophysical representations of vascular networks. Additionally, the simulations account for the phase accumulation resulting from water diffusion. But the estimation of high-resolution maps of CBV, R, and $SO_2$ in rats and humans (Christen et al. 2014b; Lemasson et al. 2016) is only possible because combining pre- and post-contrast GESFIDE leverages the contrast-induced changes in susceptibility between the two states and not because of the intrinsic sensitivity of the MRF sequence pattern to frequency offsets.

The global conclusions of our observations are thus (1) that the use of MRF GRE spoiled sequence without a contrast agent for microvascular measurements is very difficult because these sequences always offer the same types of signal evolutions (exponential decay) that can lead to several identical fingerprints in the MRF dictionary. However, as demonstrated in multiple previous studies, when used in combination with CA injection, they allow the assessment of multiple microvascular parameters at the same time.

### II.2.3 Effects of magnetic field inhomogeneities on GRE balanced sequences

Balanced Steady-State Free Precession (bSSFP) MRI sequences are another type of GRE sequence that relies on the steady-state free precession (SSFP) theory introduced by Carr 1958. Unlike other non-balanced SSFP sequences which may allow the transverse magnetization to decay between pulses, bSSFP sequences employ balanced gradients. "Balanced" means that the net gradient-induced dephasing over a TR interval is zero (see Figure II.2.7). Because the gradients are balanced, no net phase is added to the magnetization by the end of the TR. The consequence is that the angle between the magnetization and the RF pulse depends only on the precession induced by off-resonance during the TR. Thus, by maintaining the phase coherence at each TR, only off-resonance effects cause phase variations and thereby signal alterations, making bSSFP sequences theoretically very sensitive to these field inhomogeneities.

In this section, we provide a comprehensive analysis of the sensitivity of the bSSFP signal response to acquisition parameters and tissue properties, offering a novel contribution, as this has not been explicitly explored in previous literature studies.

#### II.2.3.1 Influence of the acquisition parameters

**Flip Angle (FA) and Repetition Time (TR)** Through *in silico* numerical simulations of the MR signal, we compared the influence of acquisition parameters FA and TR on the shape of the response profile of the balanced sequence in the steady-state condition. In Figure II.2.8, we show the bSSFP magnitude and phase profile for some values of these parameters. In contrast with the observations made on spoiled-GRE sequences (see Figure II.2.2), the magnitude response profile is highly dependent on the FA and TR values of the sequence. It can be understood because the FA determines the amount of rotation of the spin dynamics whereas TR gives the amount of precession between two RF pulses and the amount

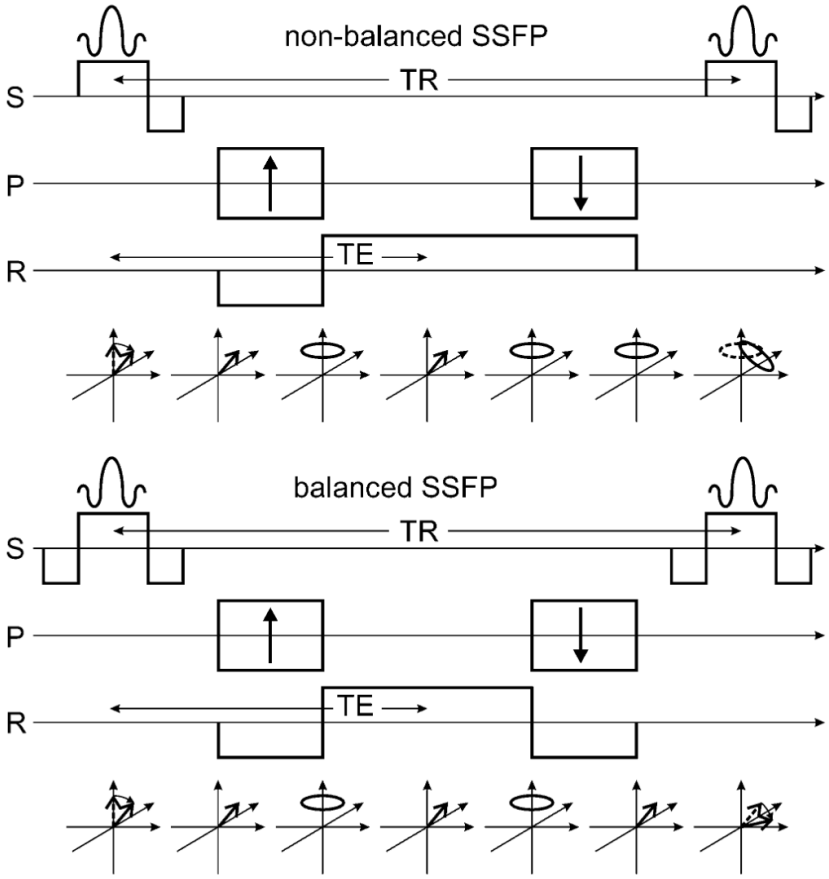


**Figure II.2.7**: Evolution of the magnetization within one TR period for a nb-SSFP (refocused FLASH) and a b-SSFP sequence, from Scheffler et al. 2003b

of magnetization decay and recovery. It is worth noting that, as for the spoiled sequences, the FA doesn't influence the phase response profile whereas the TR changes its periodicity. However, it can be observed that, in this case, the phase response profile isn't linear.

**Echo Time (TE)** We also conducted a study on the effect of the TE on the response profile of the balanced sequence. In Figure II.2.9a, we show the explicit dependency of the response phase profile on examples of TE values. The response profiles in both magnitude and phase results vary depending on TE and frequency offset. After averaging the complex signal according to frequency distributions ( II.2.9b), it results in magnitude signal responses in a wide variety of non-exponential shapes ( II.2.9c). One can observe that intra-voxel frequency profiles may be differentiated, even at short echo times. In Chapter III, other results of the magnitude signal responses are shown for several acquisition parameters.

**RF phase** In a standard bSSFP experiment, the RF pulses are typically repeated with a fixed phase. If the phase of the RF pulses is not varied, the signal amplitude will be nulled near the on-resonance frequency (*i.e.* zero frequency offset), as shown in Figure II.2.10 (blue line). These artifacts manifest as dark bands where the signal is null, resulting in poor image quality.

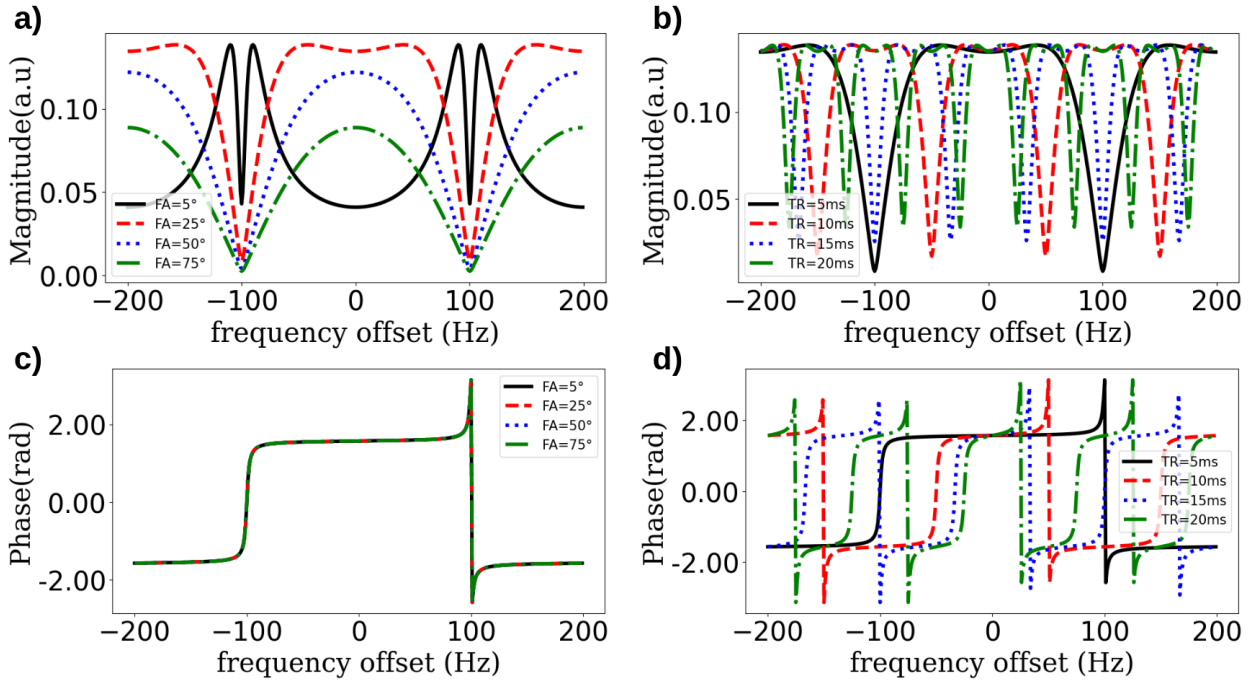


**Figure II.2.8**: Frequency profiles for a b-SSFP sequence, with an alternate 0-$\pi$ RF phase. In a) TR is fixed at 5ms and in b) FA is fixed at 25°

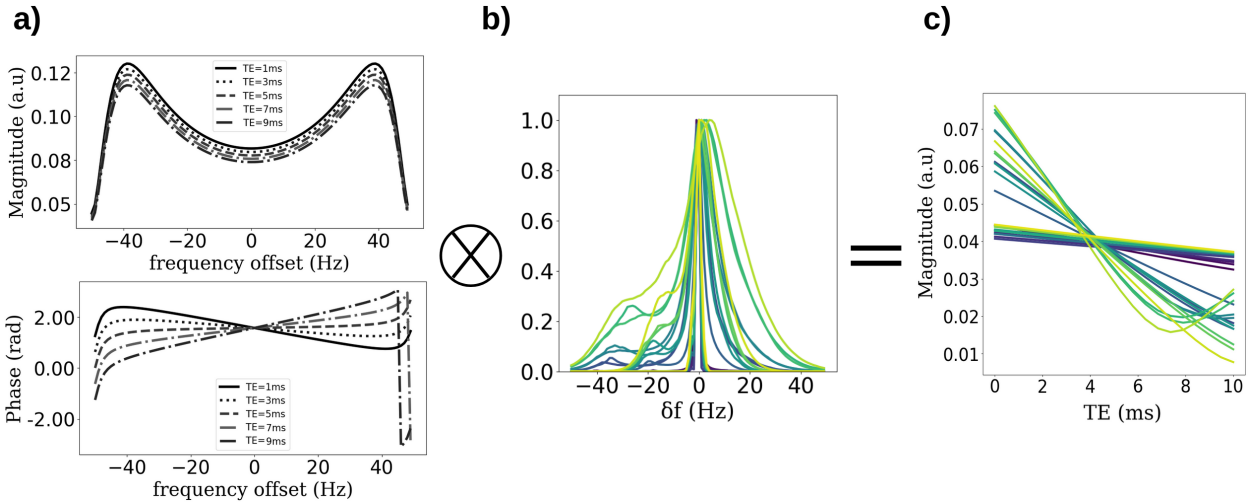


**Figure II.2.9**: Signal response of a bSSFP sequence to intra-voxel frequency distributions resulting from the convolution between the response profile for FA=10° and TR=10ms at several TE and the frequency distribution. The color code on the frequency distribution and the signal as a function of TE corresponds to different CBV values. A linear phase increment of 180° was used here.

To tackle this, the first papers (Scheffler et al. 2003b; Bieri et al. 2013) have proposed to alternate the RF phase between 0° and 180° (often referred to as the "0-$\pi$" alternation). This means that the phase of successive RF pulses is shifted by 180° relative to the previous pulse. The 0-$\pi$ RF phase alternation is a specific example of a broader category known as linear phase cycling. In linear phase cycling, the phase increment between successive RF

pulses is a constant value. For the 0-$\pi$ scheme, this increment is $\Delta\phi = 180°$. This results in a symmetric frequency response with a maximum intensity around the center frequency, minimizing artifacts caused by off-resonance effects because the "on-resonant" spins produce the highest signal (see Figure II.2.10, green line).

When different linear phase increments are used, a shift in the phase and magnitude response profiles of the bSSFP sequence are observed as shown in Figure II.2.10. Different linear increments alter the periodicity and location of signal nulls and peaks in the frequency domain, directly affecting the image quality and the localization of banding artifacts. This can be observed in Figure II.2.11 where we simulated the resulting signal of bSSFP sequences with different linear phase increments, on a numerical phantom where the off-resonance values vary along a gradient. Two pulses are shown, one at the beginning of the sequence (transient state) and one at the end (steady state).

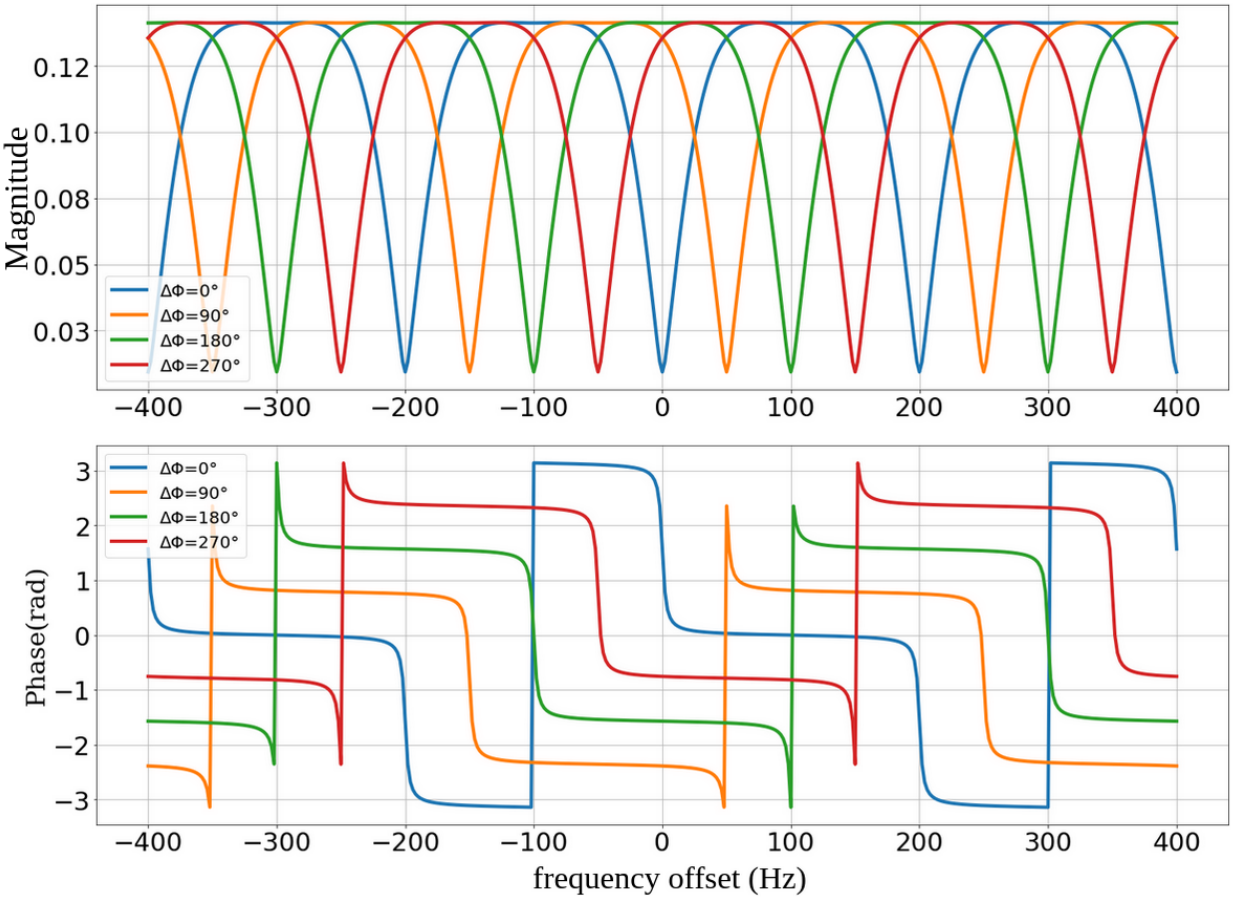


**Figure II.2.10**: bSSFP response profiles in magnitude (top) and phase (bottom) for different RF phase linear increments with FA=30°, TR=5ms, TE=TR/2.

It is worth noting that, in the phantom experiment of Figure II.2.11, the TR is long (21ms) so the banding artifacts are in the field of view no matter the phase increment. To tackle this, another technique to further reduce off-resonance artifacts in bSSFP MRI involves using several different linear phase increments across multiple acquisitions. Phase-cycled bSSFP (also known as multiple-acquisition bSSFP) consists of the acquisition of several bSSFP

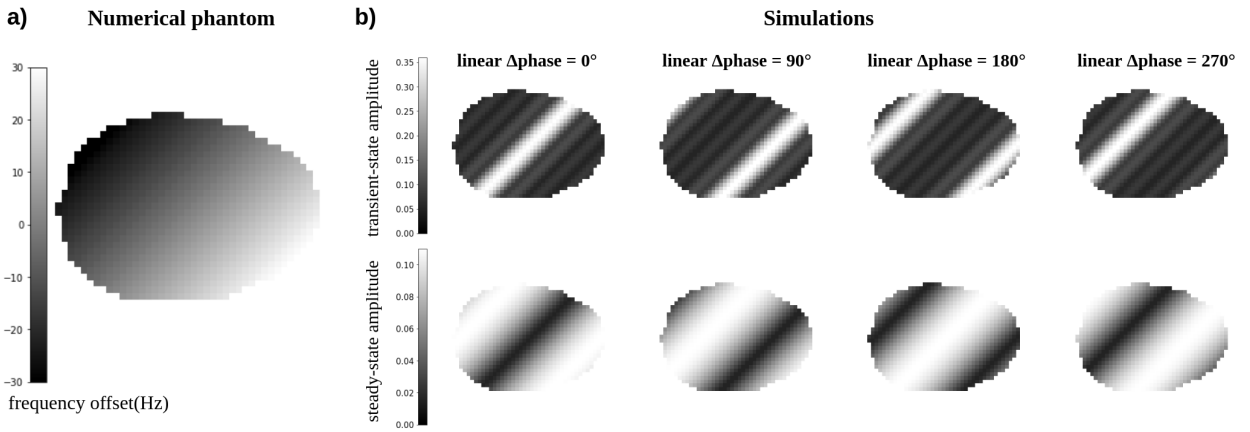


**Figure II.2.11**: Numerical simulations of the bSSFP images acquired for different RF phase increments (b) in a numerical phantom (a) where each voxel has a different frequency offset value that varies along a spatial gradient.

images with different radio frequency (RF) phase increments (*e.g.* $\Delta\phi = 0°/90°/180°/270°$) between subsequent RF pulses. A multitude of algorithms for the combination of these phase-cycled images have been proposed (Vasanawala et al. 2000; Hoff et al. 2024; Çukur et al. 2024), but the main principle is always the separate acquisition of multiple images. One classic and famous recombination method is the Maximum Intensity Projection which selects the highest intensity value from the set of phase-cycled images for each pixel position. This approach ensures that the most reliable signal from on-resonance frequencies is retained while minimizing the impact of off-resonance artifacts. The MIP technique leverages the redundancy of high-intensity signals across different phase-cycled acquisitions, effectively enhancing image contrast and reducing artifacts. This strategy is particularly useful in bSSFP imaging for achieving clearer and more homogeneous images, making it a valuable tool in both clinical practice and research. However, the multiple image acquisition limits these approaches with a long scanning time.

As for SPGR sequences (see section II.2.2.1), dynamic phase cycling has been introduced to overcome this limitation by replacing the linear phase increment with a quadratic phase increment. For example, Benkert et al. 2015 proposed a dynamically phase-cycled bSSFP by changing the phase cycle during the acquisition of each projection in radial imaging while Guo et al. 2020 used quadratic phase sequences with balanced gradients for fMRI applications. Both these works allow the removal of bSSFP banding artifacts in a single acquisition.

In the Equation II.2.2, the quadratic term ($\Delta\phi$) introduces a non-linear progression of phase shifts. As a result, the frequency response profile does not simply shift once and remain fixed; instead, it continuously evolves throughout the sequence. This continuous evolution distributes off-resonance effects over a wider frequency range, reducing the likelihood of artifacts becoming concentrated at specific frequencies by making the "bands" of the image move throughout the acquisition. Moreover, the non-linear progression of the phase shift increases the diversity of signal evolutions within the MRF sequence.

**Time dependency** Before reaching the steady state, the beginning of the sequence passes through a transient state, where the signal may oscillate wildly, its evolutions are way more complicated than in the steady state and harder to characterize. Figure II.2.12 shows the evolution of the bSSFP magnitude response profile through repetition pulses, highlighting the complexity of the transient state. It is also interesting to note that the first pulse of the sequence presents a flat frequency profile similar to the one obtained with a non-balanced sequence because there is no history of previous transverse magnetization at the beginning. Moreover, we see that the magnitude profile in the transient state is also very dependent on off-resonance frequencies and that the highest signal amplitude is not at the same frequency as in the steady state for the same sequence parameters. We also see that both states are influenced by the choice of the phase cycling scheme. In most standard bSSFP imaging, the transient state part of the signal is completely left out because of its complexity. In MR Fingerprinting, this difference in sensitivity between different parts of the sequence could be exploited to increase signal variability in the MRF dictionary (see Chapter III) by looking at both transient and steady-state signals.

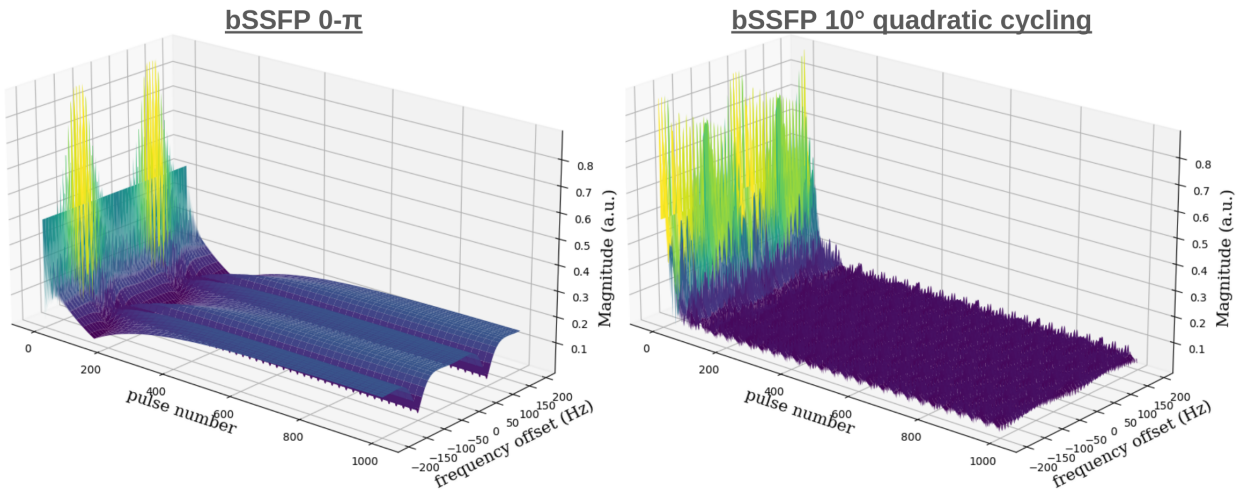


**Figure II.2.12**: Evolution of the magnitude response profile through pulse number for a b-SSFP sequence, with an alternate 0-$\pi$ RF phase (left) and a 10° quadratic cycling scheme (right), FA=25°, TR=5ms, and TE=TR/2.

### II.2.3.2 Influence of tissue parameters

In the optic of using bSSFP within an MRF approach, it is also important to evaluate the influence of other tissue parameters than the intra-voxel magnetic field distributions such as the relaxation times $T_1$ and $T_2$.

For this, we simulated MR signals resulting from a balanced sequence for several relaxometry values. Figure II.2.13 shows that tissues with different $T_1$ and $T_2$ show different frequency responses, meaning that the MR signal response of a bSSFP sequence is also sensitive to the tissue properties, motivating the use of balanced sequence for MRF.

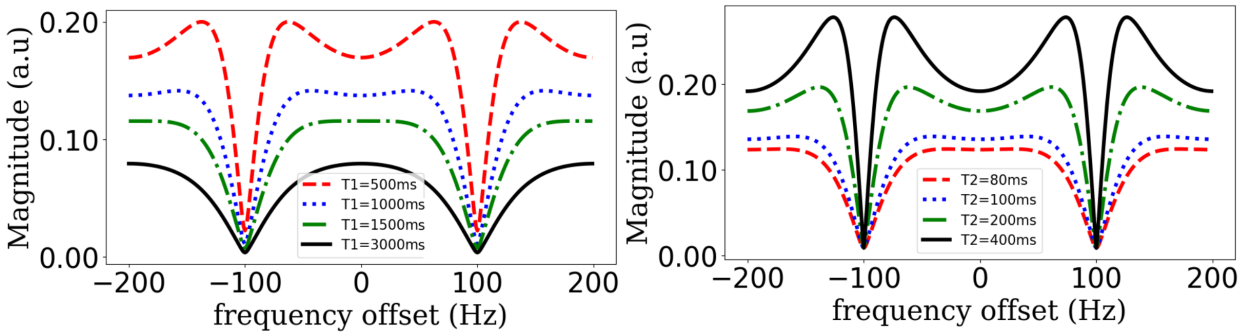


**Figure II.2.13**: Magnitude response profile for a b-SSFP sequence for different tissue parameters, with an alternate 0-$\pi$ RF phase, FA=25°, TR=5ms, and TE=TR/2. For $T_1$ plot (left), $T_2$=80ms and for $T_2$ plot (right), $T_1$=1300ms.

### II.2.3.3 Conclusion

Changing the parameters of the sequence seems to change the response profile of the bSSFP sequence and so signal time evolutions. Moreover, this signal response profile is also very sensitive to tissue parameters such as $T_1$ and $T_2$. The dependency of the signal amplitude to frequency offset make the response signal very sensitive to intra-voxel frequency distribution (*i.e.* magnetic field inhomogeneities).

In the first description of MRF by Ma et al. 2013, the sequence used was an IR-bSSFP sequence with pseudo-random TR and FA trains and an alternating 0-$\pi$ RF phase. After that, bSSFP sequences were abandoned in favor of GRE-spoiled sequences whose low sensitivity to off-resonance limited artifacts and produced better results. Recently, the bSSFP sequence design has been exploited again in MRF experiments relying on their high sensitivity to off-resonance as proposed by Guo et al. 2020 that introduced Oscillating Steady-State Imaging (OSSI), a novel functional MRI method designed to improve signal-to-noise ratio (SNR) and provide high-resolution imaging, by carefully designing the RF phase cycling.

Following this, Wang et al. 2019; Boyacioglu et al. 2020 proposed a modified MRF technique that uses a quadratic RF phase (qRF-MRF) to simultaneously measure $T_2^*$ in addition to $T_1$, $T_2$, $M_0$ and $\delta f$ parameter maps (see Figure II.2.14). As previously mentioned in this chapter, $T_2^*$ is an approximate of the response of an MR sequence if considering Lorentzian frequency distribution. Here the same approximation was made for $\delta f$ but the signal evolutions are not necessarily exponential with TE.

Without needing long echo times, nor necessarily multiple echo times given the time evolutions, we have shown the superior sensitivity of balanced GRE sequences compared to spoiled GRE sequences without contrast agent injection. Moreover, the sensitivity of balanced sequences to the acquisition parameters as well as the tissue parameters, make this type of sequence a candidate of choice for the contrast-free MRF estimation of magnetic field inhomogeneities and so microvascular properties of the human brain such as CBV or R. However, this high sensitivity implies a careful design of the sequence parameters to maximize the accuracy of the MRF estimates.

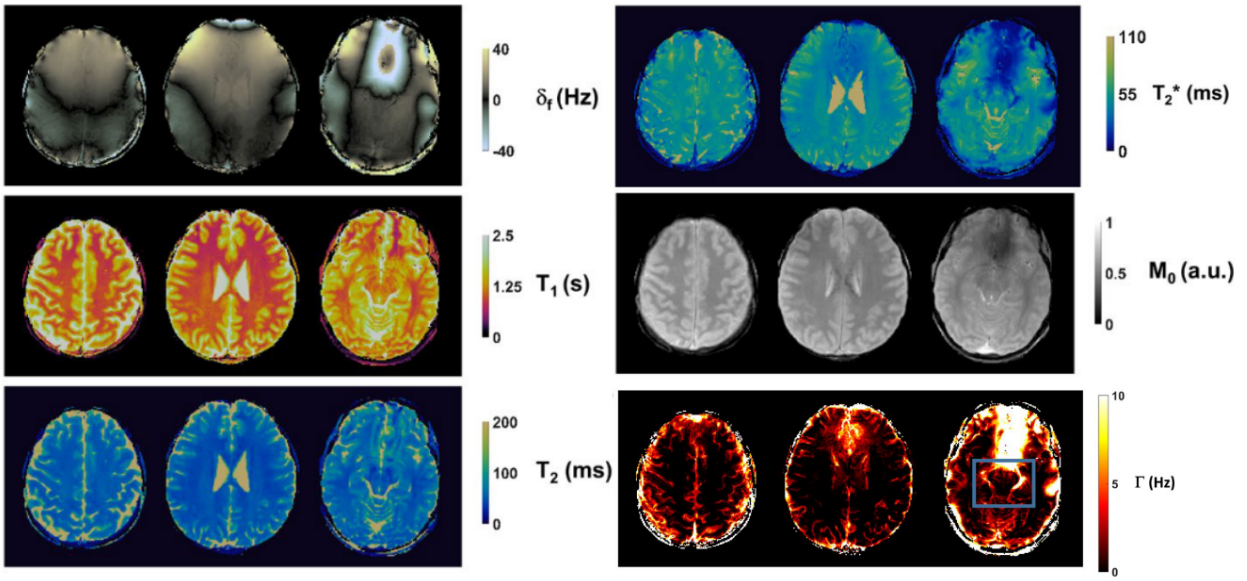


**Figure II.2.14**: Representative *in vivo* tissue property maps measured with the qRF-MRF method, adapted from Wang et al. 2019.

## II.3 *In silico* research of MRF-bSSFP sequences for non-contrast microvascular estimates

In the last few years, optimization of MRF sequences has become an important focus point in the MRF community. Already introduced at the beginning of MRF, it is well known that the design of the sequence acquisition pattern highly influences the accuracy and the rapidity with which the estimates are obtained. As shown previously, the TR, the FA, and the RF phase of the sequence highly influence the bSSFP profile and thus the sensitivity of the sequence. Since there is *a priori* no requirement on the design of the parameters trains in an MRF experiment, there are a lot of degrees of freedom in the design of the sequence, and by changing the acquisition parameters we could improve the sensitivity of the signal to the desired tissue properties.

When the estimated parameters are numerous and the simulations time-consuming, as is the case for magnetic field inhomogeneities representation, automated optimization faces several limits and the implementation of the adapted algorithm is not trivial.

In the following section, we propose to use multiple *in silico* simulations with varying acquisition parameters to identify trends in the bSSFP sequence that could enhance the sensitivity of bSSFP sequences to intra-voxel frequency distributions. As the optimization of conventional quantitative MRI sequences and MRF sequences for relaxometry measurements has been deeply studied, we already know how to get a good design for $T_1$ or $T_2$ estimates. Given the high dimension of our optimization problem, we will thus focus on CBV and R estimates. As CBV and R are both related to the frequency distribution shape and therefore cannot be separated, the encoding capability of R is implied in the encoding in the CBV

dimension here.

## II.3.1 Developments of metrics to evaluate sequence encoding capabilities

To design a bSSFP pattern, one has to find a way of quantifying its sensitivity to the parameters of interest, often characterized as the encoding capability of the sequence. As already explained by Ma et al. 2013, sensitivity to tissue parameters in an MRF approach is improved when signals with different parameters are more unique (ideally, orthogonal to each other). Based on this, we developed two in-house metrics inspired by the literature.

### II.3.1.1 Inner-product approach

The cost function proposed by Cohen et al. 2017a in their optimization problem is a dictionary-based evaluation of the encoding capability of the sequence. In the simple form proposed by Cohen, this function relies entirely on the variance in the MRF dictionary, without discrepancy between parameters or any integration of possible noise artifacts in the *in vivo* acquired signals that will be matched. We tried to use this very simple inner-product approach as a metric for our study using the following algorithm:

- Generate MRF dictionary for chosen sequence parameters: D($T_1$,$T_2$,$B_1$,$\delta_f$,CBV,R).
  - ◇ Extract sub-dictionary with all parameters fixed but the parameters of interest: d($T_{1i}$,$T_{2i}$,$B_{1i}$,$\delta_{fi}$,CBV,R).
  - ◇ Compute the matrix $h = d \times d^T$
  - ◇ Compute a matrix using the distance between parameters of interest in the dictionary

$$D_{\text{diff}} = \begin{bmatrix} 0 & \theta_1 - \theta_2 & \cdots & \theta_1 - \theta_n \\ \theta_2 - \theta_1 & 0 & \cdots & \theta_2 - \theta_n \\ \vdots & \vdots & \ddots & \vdots \\ \theta_n - \theta_1 & \theta_n - \theta_2 & \cdots & 0 \end{bmatrix}$$

    where $\theta$ is the parameter of interest, here $\theta$=(CBV,R) and n is the number of values of the parameters of interest in the dictionary.
  - ◇ Weight $h$ by the distance matrix: $h = h \times D_{\text{diff}}$
  - ◇ Let A be the set of all off-diagonal elements of h. A = $\{h_{ij} \mid 1 \leq i, j \leq n,\ i \neq j\}$

$$\mu = \frac{1}{n^2 - n} \sum_{i \neq j} h_{ij} \tag{II.3.1}$$

$$\sigma = \sqrt{\frac{1}{n^2 - n} \sum_{i \neq j} (h_{ij} - \mu)^2} \tag{II.3.2}$$

  - ◇ $\mu$ and $\sigma$ rely on the similarity between signals for different (CBV,R) values and aim to be minimized.
- Repeat this process 50 times by randomly changing the combination of non-interest parameter values in sub-dictionary d.
- Compute the mean and standard deviation across all combinations.

This computation allows a very fast and straightforward evaluation of the variance along the parameter of interest dimension in a dictionary. However, it is limited because it doesn't introduce any noise in the process. We tried to add noise in the dictionary before computation but depending on the Signal-to-Noise Ratio (SNR), it disturbs the metrics of the variance and sometimes falsely "improves" the distance between signals leading to false evaluations of the sequence parameters.

#### II.3.1.2 Monte Carlo approach

To make the metric more realistic and closer to *in vivo* real encoding capability, we introduced a second approach inspired by Sommer et al. 2017 based on a Monte-Carlo (MC) process as follows:

- Generate MRF dictionary for chosen sequence parameters: D($T_1$,$T_2$,$B_1$,$\delta_f$,CBV,R).
  - ◇ Extract 50 dictionary entries equally distributed in the whole parameter space (Sobol distribution, Sobol' 1967).
  - ◇ Add adapted noise to the 50 selected entries.
  - ◇ Match the 50 entries into the original dictionary D.
  - ◇ Let $\theta_{\text{expected}}$ be the expected tissue parameters associated to each noisy entry and $\theta_{\text{matched}}$ be the tissue parameters obtained after matching. For each noisy signal $i$ (where $i = 1, 2, \ldots, 50$), the matching error $E_i$ is given by:

$$E_i = \frac{|\theta_{\text{expected},i} - \theta_{\text{matched},i}|}{\theta_{\text{expected},i}}$$

    The mean matching error $\mu_E$ is computed as:

$$\mu_E = \frac{1}{50} \sum_{i=1}^{50} E_i$$

    The standard deviation of the matching error $\sigma_E$ is computed as:

$$\sigma_E = \sqrt{\frac{1}{50} \sum_{i=1}^{50} (E_i - \mu_E)^2}$$

- Repeat this process 2000 times with randomized noise.
- Compute the mean and standard deviation reconstruction error over all repetitions.

By using this metric, we have access to an estimate of the reconstruction error for each parameter of the dictionary that can be weighted depending on the chosen parameters and relies on a variety of realistic noises given the randomness induced by the Monte Carlo process. In the rest of this study, we choose to approximate the noise resulting from the undersampling of the k-space during the acquisition by a Gaussian-distributed noise.

#### II.3.1.3 Conclusion

Based on a literature review adapted for our microvascular estimation methods, we have implemented two metrics that capture the encoding capability of MRF sequence for microvascular estimates (CBV, R). On the one hand, the *inner-product approach* allows very

rapid estimation involving a limited number of simulations but is focused on the variance in the CBV dimension and introduces no notion of acquisition noise. On the other hand, the *Monte-Carlo method* is more realistic, allowing the introduction of configurable undersampling noise, and produces a more general overview of the estimation error made on each parameter.

We hypothesize that the first metric will allow a fast sorting of possible optimal parameter directions in a large parameters search space whereas the second one will be more designed for fine-tuning the acquisition parameters or in the case where there are fewer values to be tested. We thus used these tools to study different types of MRF acquisition schemes and find possible MRF sequence candidates for our project.

### II.3.2 Influence of FA schemes

In MRF relaxometry, the design of the FA train is important as it directly influences the accuracy and efficiency of tissue property quantification. The FA train determines the sequence of flip angles applied during the MR acquisition, which affects the signal evolution and, consequently, the ability to distinguish between different tissue types. MRF literature agrees that a time-constant FA train highly limits the sensitivity of an MRF sequence (Assländer 2021) and there is a need for a time-varying FA train design that would produce more distinct signals for different tissues.

The optimization work made by Gómez et al. 2019 and used in the first Chapter suggests that a flip angle ramp from 7° to 70° over 260 repetitions, preceded by an inversion pulse, presents an optimal design to increase the contrast sensitivity of spoiled sequences. We tried to use the same FA train within a bSSFP design and compared it with other FA train designs shown in II.3.1. When computing the similarity score (from II.3.1.1) on the designed sequence, the time constant FA train (II.3.1a) returns a score of more than 99%, indicating a high similarity between the signal in the MRF dictionary. The five remaining FA trains return similarity scores between 97.6 and 97.8%, indicating that the variance in the associated MRF dictionaries is higher. From these results, and focusing on CBV estimates, we deduced that the FA train will not be the most important parameter to optimize, since it is time-varying.

### II.3.3 Influence of RF phase cycling schemes

Using the definition of the linear and quadratic cycling above, several phase increments have been tested with the metrics defined in II.3.1. As shown in Figure II.3.2, no matter the linear phase increment, the similarity score between two dictionaries, computed with the inner-product approach (II.3.1) is approximately the same. As the linear phase increment shifts the magnitude response profile, the overall similarity score through all off-resonance frequencies doesn't change. As it can be seen in Figure II.3.3, by looking precisely at both metrics values for different off-resonance frequencies (*e.g.* evaluating the encoding capability in a subset of the dictionary for a fixed off-resonance value), the mean score is always the same and the worst score values are just shifting along the frequencies axis as the magnitude response profile is also shifting. These very low score frequencies are not suitable because their presence comes from banding artifacts that we want to remove during MRF reconstruction. However, these results validate that our metrics are quantitatively related to the variance of

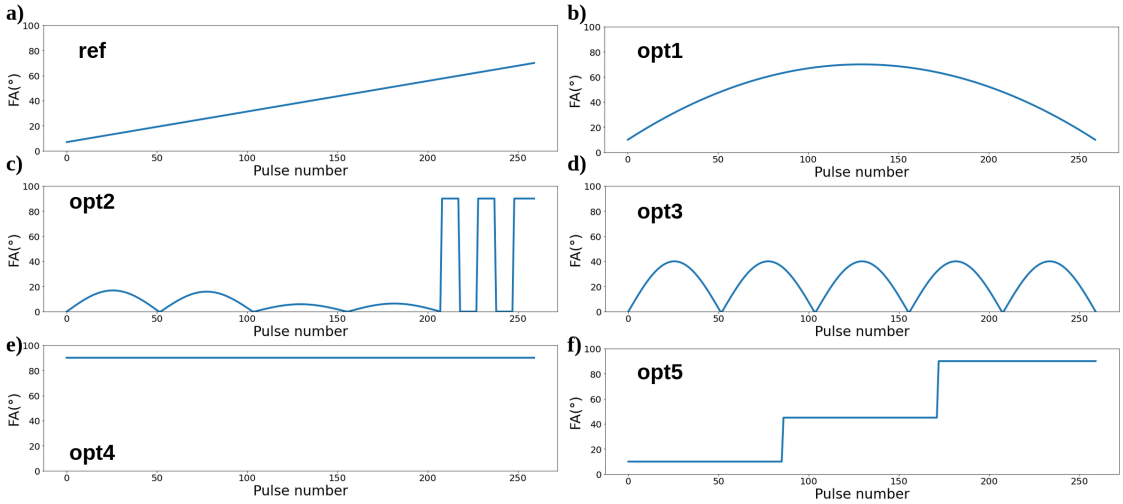


**Figure II.3.1**: Flip Angles train used for our comparison study where TR is time-constant and fixed at 9ms, the RF phase is quadratically cycled with a 10° increment.

the signal at specific parameter space regions of the dictionary.

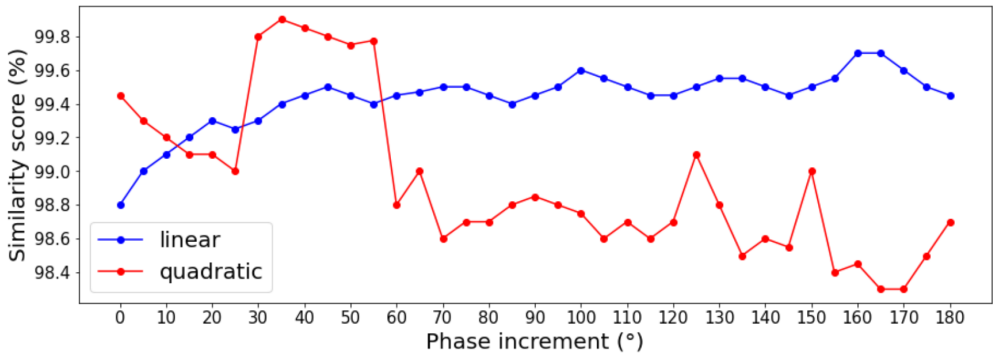


**Figure II.3.2**: Inner-product evaluation of bSSFP sequence with linear (blue) or quadratic (red) RF phase cycling. The resulting similarity score is plotted in % from 0 to 180° by 5° steps.

Facing this, a quadratic phase increment that will continuously shift the profile in time during the acquisition seems to help increase the score as shown in Figure II.3.4 where the error on CBV estimation is measured with the MC metric. Some quadratic phase increments lead to better overall encoding capability estimation than others such as increments around 10°. Interestingly, when taking into account noise in more realistic metrics, the results are not exactly on the same trend as with the inner-product approach in Figure II.3.2. Moreover, Figure II.3.5 shows that the encoding capability of the bSSFP sequence is better distributed through the whole frequency range, when the phase is quadratically cycled than when it is linear, especially in the case of the MC metric.

From this study, we concluded that a quadratic phase cycling bSSFP with a specific increment of 10° is an interesting candidate for our study of CBV estimations.

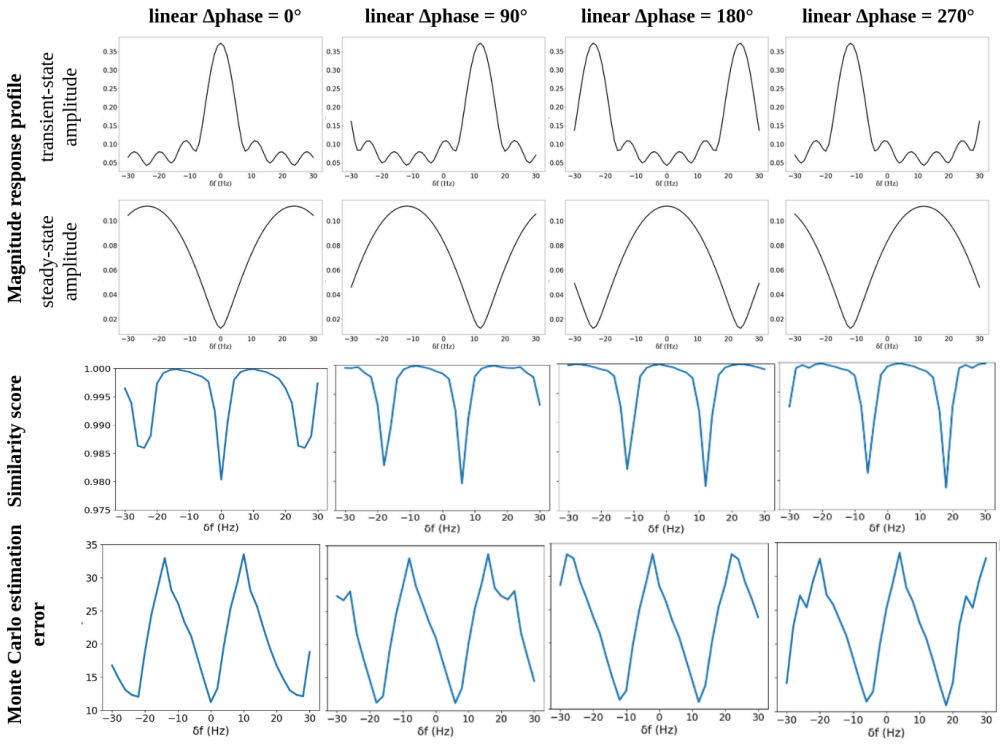


**Figure II.3.3**: Encoding capability evaluation of bSSFP sequence with several linear phase increments. The absolute Similarity Score and the Monte-Carlo error in % are compared with the magnitude and phase response profile of 4 different sequences with several RF phase linear increments. This highlights the frequency-dependence of the proposed metrics.

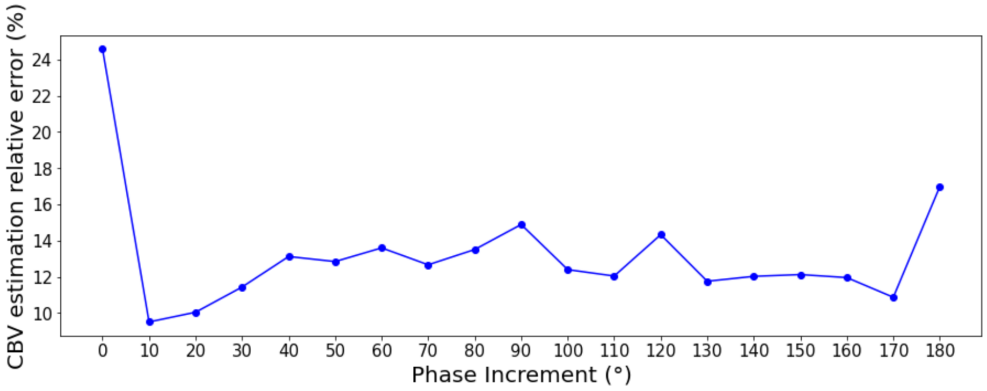


**Figure II.3.4**: Monte-Carlo error (%) on the CBV estimation made with bSSFP sequences with several quadratic phase increments, from 0 to 180° by 10° steps.

## II.3.4 Influence of TR schemes

Trying to optimize sequence sensitivity as well as the sequence length could be done by designing an appropriate TR train. As the width of the banding artifacts is inversely proportional to the TR in a bSSFP sequence, TR is usually kept short so that the acquired signal is within the passband of the frequency spectrum. However, as we can choose a quadratically cycling RF phase design, it opens the door to longer TR values without risking

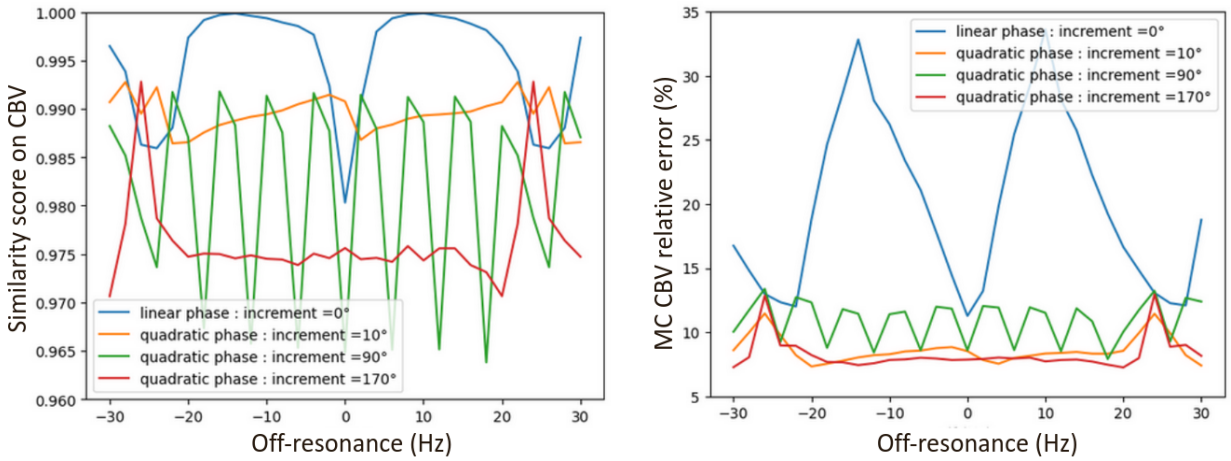


**Figure II.3.5**: Encoding capability estimation with the two introduced metrics for different phase cycling schemes. Similarity score (left) and Monte Carlo relative error (%) are plotted along off-resonance values in Hz.

being affected by banding artifacts. Nevertheless, the metrics evaluations over TR values seem to enhance sequence encoding capability (see II.3.6) when TR is short. However, *in vivo* acquisition are limited by readout time and acquisition window duration, and too short TR would lead to shorter k-space trajectory time, decreasing the quality of the acquisition. There is an important trade-off in the design of the sequence between the theoretical sensitivity and what is adapted to a real acquisition with the readout sampling constraint. Moreover, by keeping TR constant, we mitigate the sensitivity of the sequence to noise and undersampling artifacts that have been observed in purely random TR train design (Ma et al. 2013).

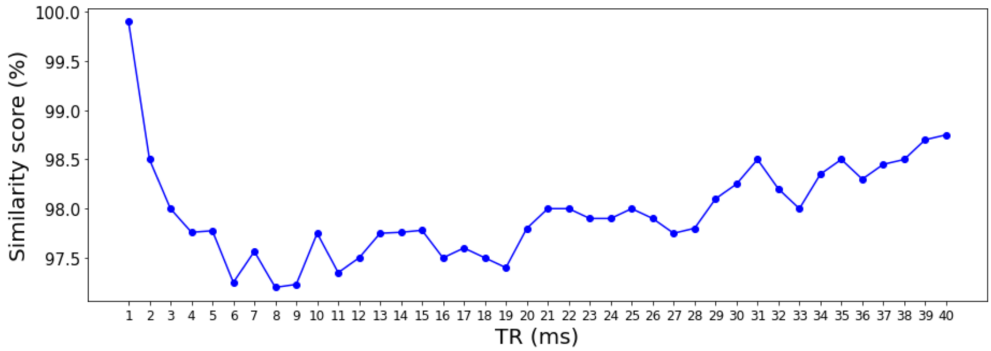


**Figure II.3.6**: TR train comparison with the similarity score metric, FA is linearly increased from 7° to 70°, the RF phase is quadratically cycled with a 10° increment.

## II.3.5 Influence of TE schemes

As shown in Figure II.3.7, TE directly influences the phase response profile of the bSSFP sequence and thus the signal response. Moreover, as introduced by Scheffler et al. 2003a, at TE=TR/2 and for specific sequence parameters, the bSSFP sequence signal can in some cases produce spin echo-like behaviors that reduce the sensitivity to off-resonance frequency, also shown in our study in next Chapter III. Thus, proper TE optimization enhances the contrast

between different tissues, facilitating more accurate differentiation and quantification of tissue parameters such as $T_1$, $T_2$, and off-resonance frequency. Moreover, a multi-echo approach could theoretically help capture this signal phase response variability and enhance sequence sensitivity. Figure II.3.8 shows that using a 3-echoes acquisition instead of a single-echoes one could improve the sensitivity of the bSSFP sequence to off-resonance frequency according to the similarity score, for certain FA trains. However, as for TR, the readout timing constraints of MRI machines reduce the potential number of echo times (TEs) that can be acquired within each TR, for a satisfying acquisition resolution. For example in Figure II.3.8c), the "long" position setup of the echoes is not feasible due to the short time between the last echo and the end of the pulse. This limitation forces a compromise in the design, potentially reducing the richness of the signal evolution data that can be captured.

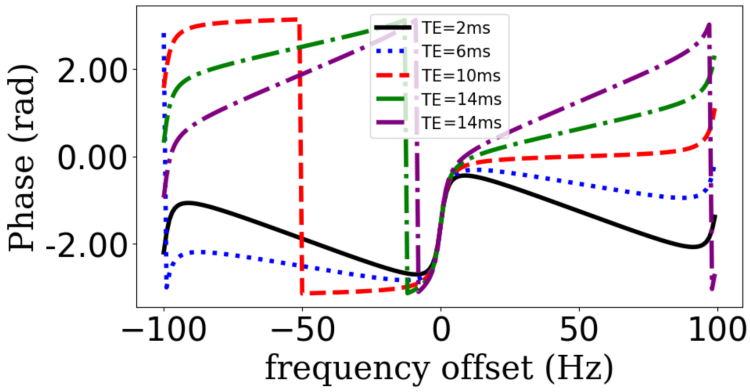


**Figure II.3.7**: TE effect on the bSSFP phase profile. The phase response profiles of five bSSFP sequences with different echo times are compared.

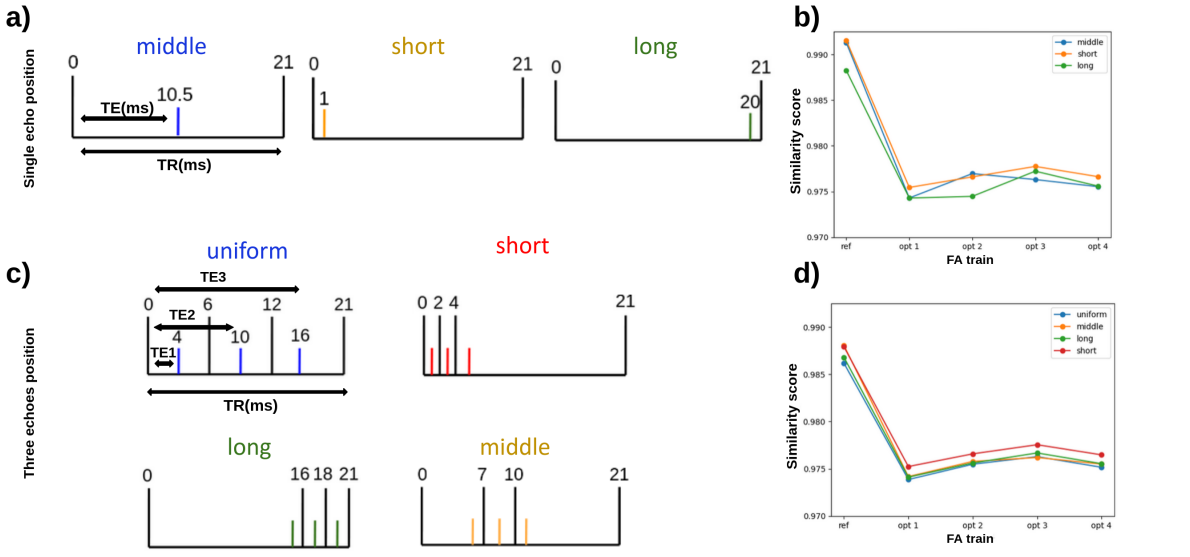


**Figure II.3.8**: Echoes duration effect on the similarity score of a bSSFP sequence for different FA train designs. In the case of a single echo placement (a), Similarity Scores computed from the five FA designs are shown in (b) for three options. In the case of triple echo acquisitions (c), results are shown in (d) for four options.

As a result, while the theoretical benefits of a short TR and multiple echo times are clear, the

practical constraints of current MRI technology require a careful balancing act in designing TR and TE parameters to optimize the performance of MRF-bSSFP sequences.

### II.3.6 Conclusion

Based on our analysis, we concluded that the optimal design of a bSSFP sequence for microvascular properties estimates should contain :

- a quadratically cycled RF phase with an increment of 10° or 170° at each repetition.
- a time-varying flip angle. We decided to use the 7°-70° linear increasing FA train, with an inversion pulse at the beginning. Based on this design, we decided that the length of the sequence would be made of 260 repetition pulses.
- a trade-off between short TR times and multiple echoes acquisition.

Figure II.3.9 proposes a possible design of an MRF sequence for the non-contrast estimation of brain microvasculature.

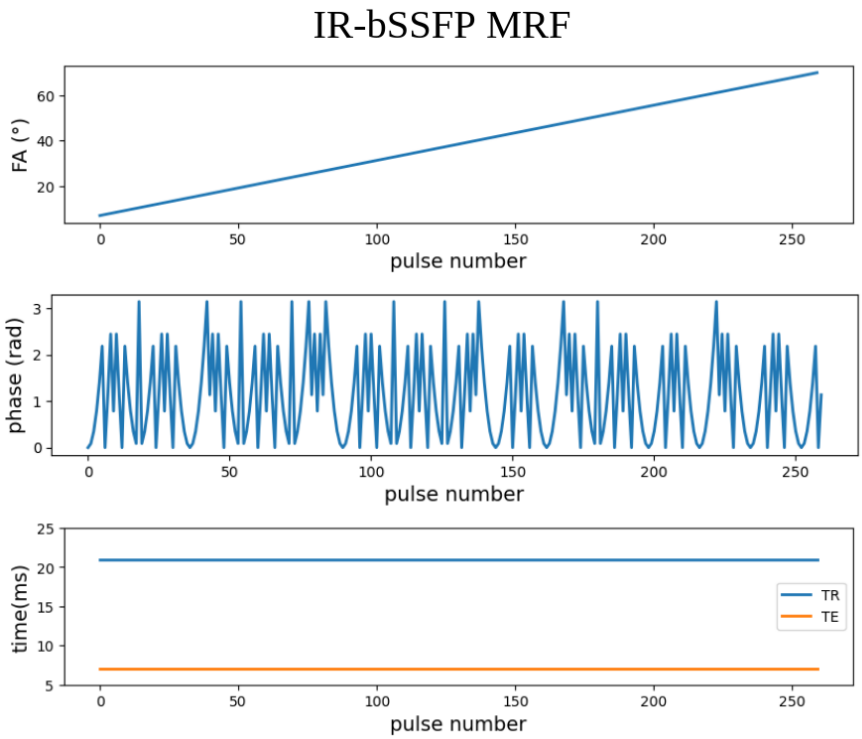


**Figure II.3.9**: Proposed IR-bSSFP sequence parameters, manually designed for MRF estimates of relaxometry as well as microvascular tissue parameters. RF phase is plotted modulo $\pi$ radians.

## II.4 *In vivo* practical limitations and other influences

In the previous section, we designed an optimal bSSFP sequence acquisition scheme. However, in the scanner, we know we will face constraints due to the hardware limitations of the MRI machine. In this section, we aim to evaluate the *in vivo* feasibility of the optimized design

from the previous section. As in the previous Chapter I, we used the MRF Philips software and we designed our sequence using CSV files as input of the acquisition protocol. We tested our sequences in phantoms and human volunteers and showed only the *in vivo* results.

As already introduced in Section I.2.2.3 of Chapter I, an important limitation is the time taken and the way to collect k-space data. How k-space is sampled during MRI acquisition directly affects the quality, speed, and nature of the resulting images. Even if the cartesian sampling is easy to implement and less susceptible to imperfections of the imaging gradients, the sequential filling of k-space can be time-consuming, depreciating this method in most of the MRF community where the scan time must be as short as possible. Some work has tried optimized trajectories such as the pseudorandom cartesian trajectory (Jiang et al. 2024) but standard MRF protocol relies on spiral (Ma et al. 2013; Jiang et al. 2015; Buonincontri et al. 2017; Chen et al. 2016; Hamilton et al. 2017) or radial (Assländer et al. 2017; Cloos et al. 2016) sampling trajectories.

On the Philips MRI software, these three trajectories are available but only the cartesian trajectory allows the acquisition of multiple echoes after one excitation pulse.

### II.4.1 Test of cartesian MRF-bSSFP acquisitions

In our first experiments, we focused on validating the behavior of bSSFP acquisitions on our scanner, using cartesian trajectory.

**Single echo experiments with different phase cycling schemes** We designed three sequences with a simple acquisition pattern: a FISP sequence (non-balanced), a bSSFP sequence with a zero constant RF phase, and a bSSFP sequence with the standard 0-$\pi$ alternating scheme. The FA and the TR were kept constant at 40° and 10ms with TE=TR/2. We used a cartesian k-space sampling trajectory with a compressed-sense factor of 3. In Figure II.4.1, we show the *in vivo* results in one volunteer of this experiment in the form of magnitude images at different time points of the acquisition, as well as magnitude and phase steady-state response profiles computed from simulations. As expected, the balanced sequence with no phase cycling exhibits strong banding artifacts (blue arrow) compared to the non-balanced acquisition. Adding an RF phase cycling with a 180° linear increment (or 0-$\pi$ alternate) shifts the magnitude response profile and thus the passband (grey rectangle) position along the frequency offset values, helping remove banding artifacts in the observed FOV for a 2D one slice acquisition. Keeping the pass-band in the observed range of frequency offset is often more difficult for multi-slices acquisition. It is worth noting that small banding artifacts (green arrow) remain in the transient part of the sequence where we have detailed before that the response profile is different from the steady state part.

In the following figure II.4.2, *in vivo* fingerprint signal examples, from the same volunteer, are shown, which look typical of bSSFP signal with the oscillatory pattern at the beginning of the sequence and the reach of a steady state.

According to our previous observations, the sequence RF phase must to be quadratically cycled. As introduced in section II.3.3, this dynamic cycling of the phase should make the

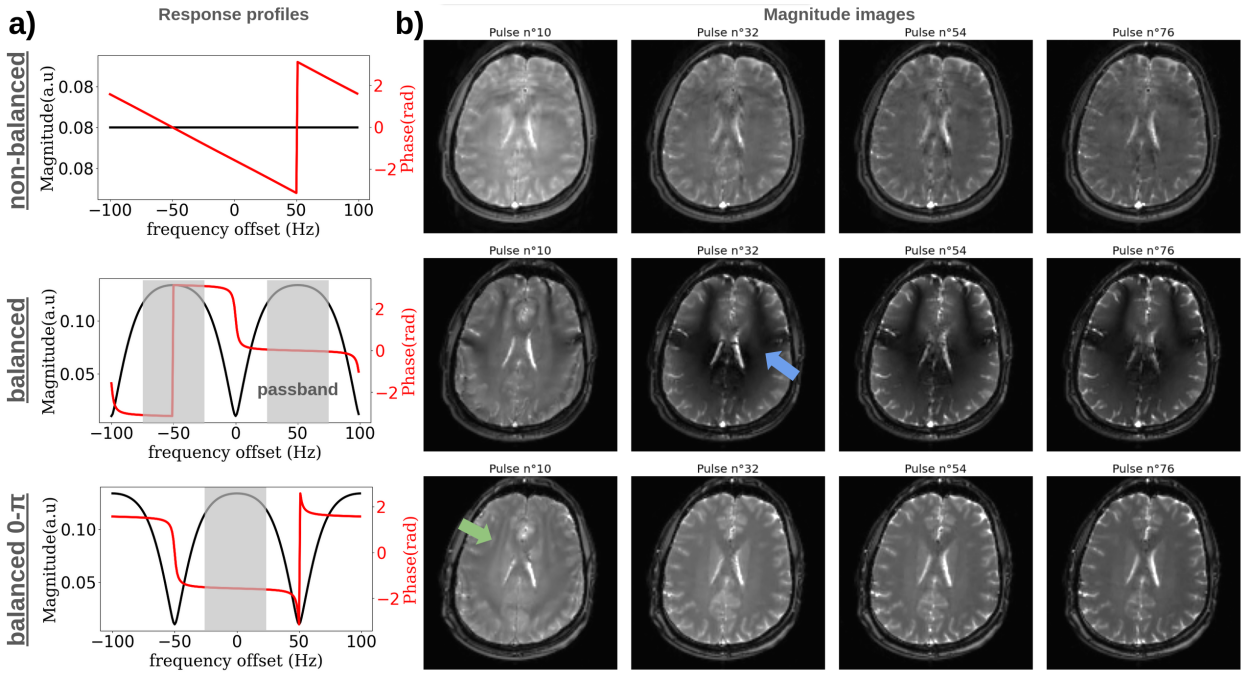


**Figure II.4.1**: *In vivo* acquisition of non-balanced and balanced MRF sequence in one healthy volunteer. a) Expected steady-state response profile from *in silico* simulations. b) Acquired *in vivo* magnitude images at different pulses of the MRF acquisitions.

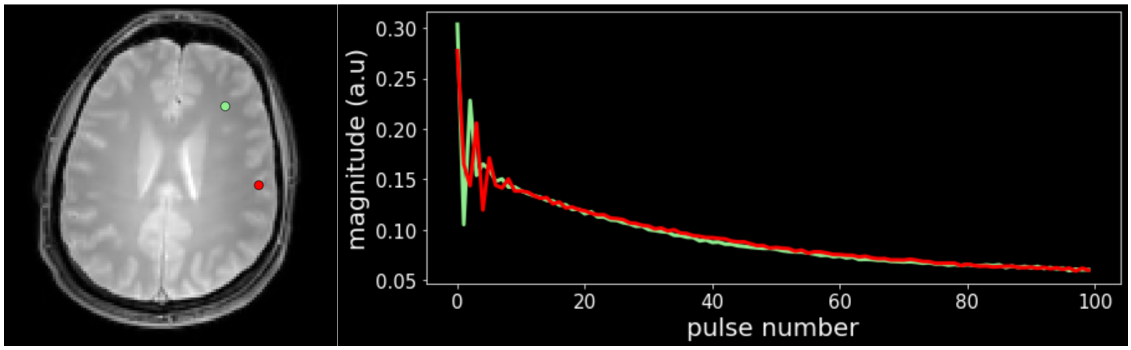


**Figure II.4.2**: *In vivo* signals of a balanced MRF sequence, without phase cycling, in a white matter voxel (green) and a grey matter voxel (red), extracted from acquisition on one healthy volunteer, with a high-sampled trajectory.

profile shift according to simulations, meaning that the off-resonance bands of the image will shift too. In Figure II.4.3, two acquisitions are compared: a bSSFP sequence with no phase cycling and a bSSFP sequence with a 10°-increment quadratic phase cycling. As expected, it can be observed that the off-resonance bands are moving from one acquisition time (or pulse number) to the other.

**Multi echoes experiments** In Coudert et al. 2022a, we conducted a small study using a multi-echoes version of the designed bSSFP sequence using a cartesian trajectory with a compressed sense factor of 3. Facing the high scanning time, we used a small resolution

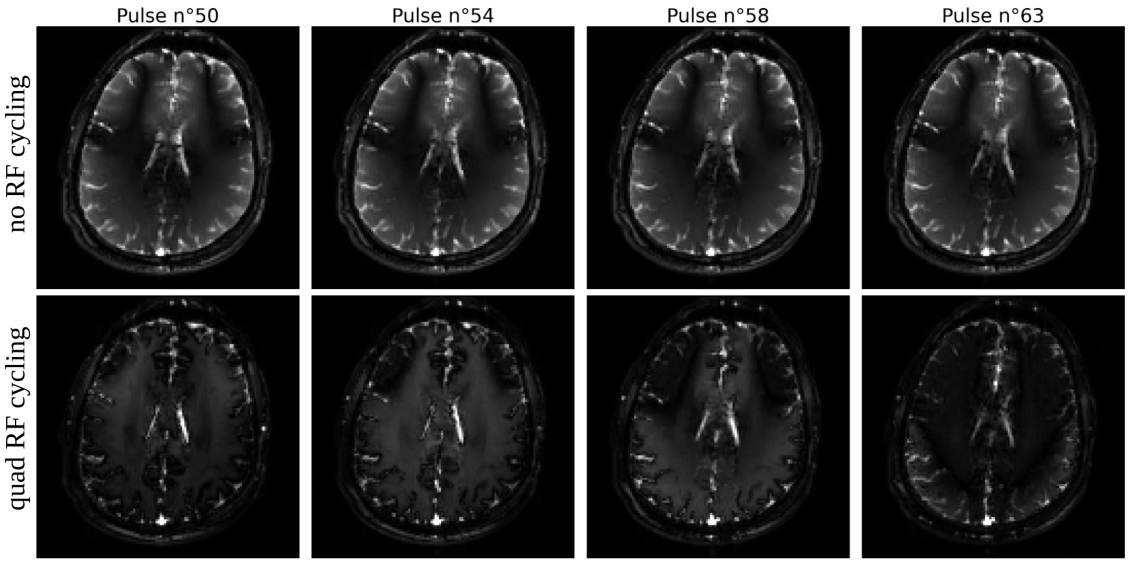


**Figure II.4.3**: *In vivo* acquisition of balanced MRF sequence without (above) and with (below) RF phase cycling. MRF images were acquired on one healthy volunteer and plotted for several pulse numbers.

acquisition with a matrix size of 128x128x1 and a voxel size of 1.56x1.56x3.00 $mm^3$. Figure II.4.4b shows an example of the acquired fingerprint in a GM voxel. As we acquired 3 echoes between each pulse rather than one, the signal is of length 3×pulses number, meaning here 3×260=780 time points. With this, we had access to the signal decay evolution between two pulses as shown in the zoom part of the fingerprint (Figure II.4.4c), giving more information about tissue properties as the TE influences the bSSFP response profile as shown before. We also show 3 acquired images, highlighting large contrast variations between repetitions and echoes in Figure II.4.4a. As the sequence length is short, we had a 6-second delay between sequence repetitions to ensure fully relaxed magnetization and avoid signal saturation that would drift the measured fingerprint away from our theoretical MRF dictionary simulations (see more details in II.4.2.1). This led to an acquisition time of around 8 minutes per slice.

However, low-resolution MRF can decrease the quality of microvascular estimates through partial volume effects. When upgrading the matrix size to 256x256 in the axial plane, the k-space sampling time will be multiplied by 2. Keeping the same 6-second delay as the previous study will lead to a scan time of 12 minutes per slice. This is not suitable for fast MR Fingerprinting estimation as desired.

**Compressed Sense effect** To accelerate the acquisitions, we tried to increase the compress sense factor. However, reaching reasonable scanning time implies very high compressed sense factors that made blurring artifacts in the acquired image. These artifacts are clear in Figure II.4.5 where *in vivo* results of a multi-slice acquisition using a cartesian undersampling scheme with a compressed sense (CS) factor of 10 versus a compressed sense factor of 3, are shown. We have observed that these artifacts degrade the quality of the resulting computed maps.

This brings us to the need for a more efficient k-space trajectory such as radial or spiral sampling.

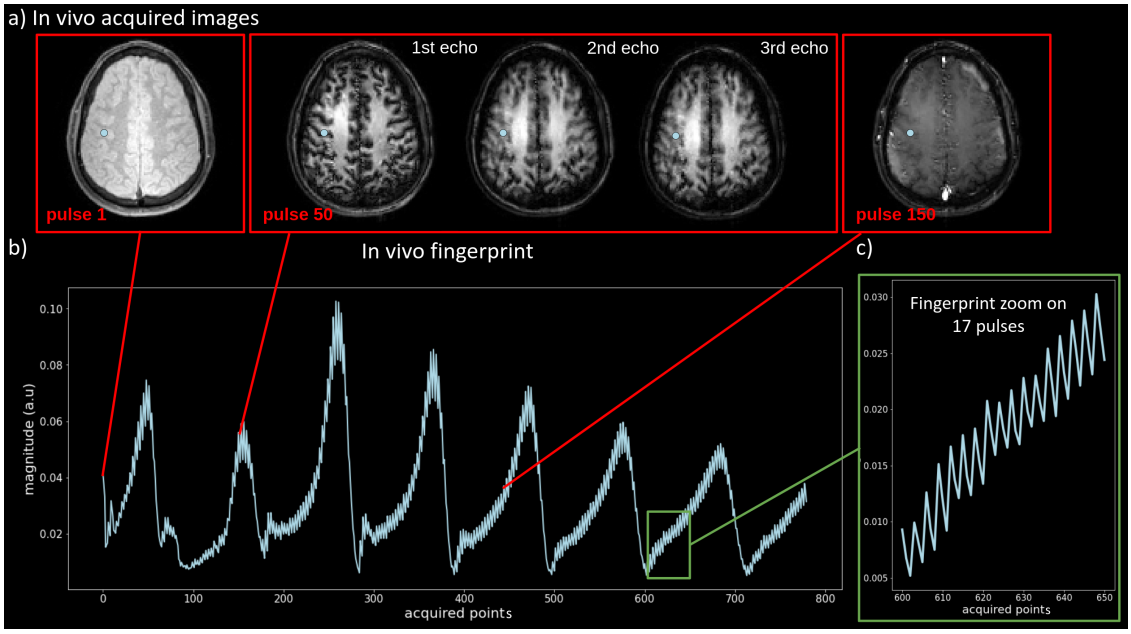


**Figure II.4.4**: *In vivo* fingerprint of a quadratic phase cycled multi-echoes bSSFP (b) and the corresponding magnitude images at some time points (a). A zoomed view of the signal with the multi-echoes is shown in (c). Adapted from Coudert et al. 2022a.

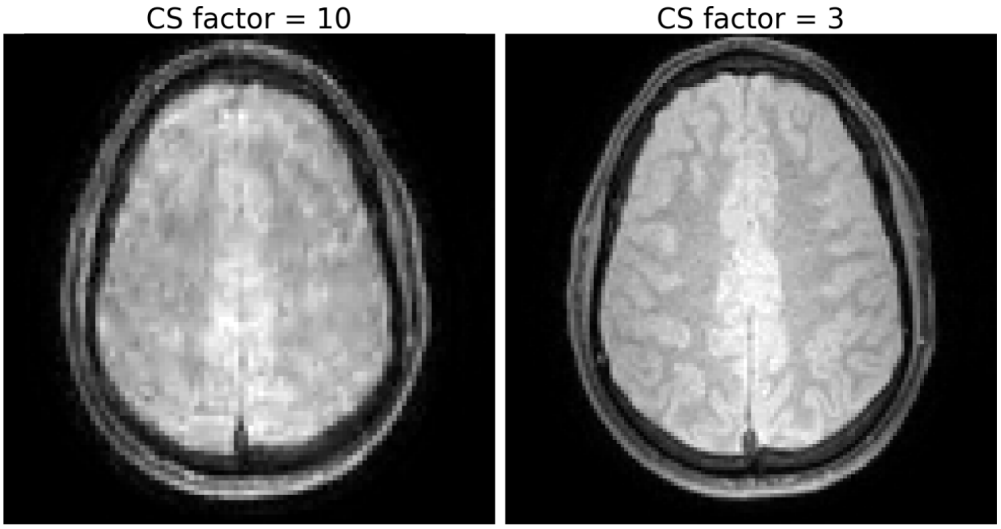


**Figure II.4.5**: Comparison of cartesian acquired images for two compress sensing factors (CS=10 on the left and CS=3 on the right) on the same healthy volunteer.

## II.4.2 Tests of spiral MRF-bSSFP acquisitions

As illustrated in Figure I.2.4 Chapter I, spiral and radial trajectories produce undersampling noise in the time-resolved fingerprint, but the matching process reconstruction outpass this and the estimated maps are of the same quality as with cartesian trajectory, in scan time of 2 minutes for spiral acquisition (10 spiral over 25 interleaves) and 4 minutes for radial acquisition (20 spokes over 256) compared to the previously recorded time of 12 minutes for

one cartesian acquired slice of size 256x256. The drawbacks are that multi-echoes spiral and multi-echoes radial acquisitions are not provided by the MRI software.

Facing this, we decided to focus on higher resolution acquisition in shorter scan times using a spiral undersampling trajectory. According to observed *in vivo* acquisition protocol constraints, TR was set constant at 21ms and TE at 4ms allowing acquisition windows of more than 10ms, mitigating undersampling artifacts in the acquisition and improving the smoothness of the signal fingerprints.

**Spiral undersampling factor** To choose the optimal undersampling factor using a spiral trajectory, we conducted an *in silico* study of the impact of the noise added in the signal under the Monte-Carlo metric evaluation (see section II.3.1). The noise added here was an aliasing noise defined as follows for a signal X and a desired t-SNR (temporal Signal to Noise Ratio, usually used to measure SNR in fMRI time series, see Triantafyllou et al. 2005; Welvaert et al. 2013):

$$\mathbf{N} \sim \mathcal{N}(0, \sigma)$$

where $\mathbf{N}$ is drawn from a normal distribution with mean $\mu = 0$ and standard deviation $\sigma$ calculated as:

$$\sigma = \sqrt{\frac{\overline{\mathbf{X}}^2}{\text{t-SNR}}}$$

where $\overline{\mathbf{X}}$ represents the mean of the signal $\mathbf{X}$, and t-SNR is the temporal signal-to-noise ratio.

The Figure II.4.6 shows the results. For relaxometry parameters ($T_1$, $T_2$) the effect of the t-SNR on the estimation error is mitigated which confirms our observations in Chapter I but the quality of the estimation of the parameter of interest which is the CBV is highly impacted. The CBV estimation relative error exceeds 35% for very low t-SNR.

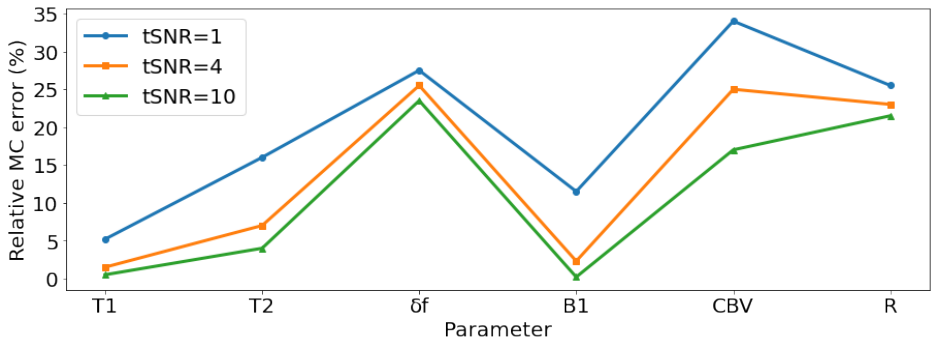


**Figure II.4.6**: Comparison of the estimation error measured with the MC approach for different t-SNR values used to generate the artificial noise in the process. Three experiments were made using the same input bSSFP sequence.

*In vivo* experiments presented in Figure II.4.7 show that increasing the spiral undersampling factor (i.e reducing the number of acquired spirals per image for the same number of interleaves) decreases the overall t-SNR in the brain area. According to the observation made *in silico*, this will reduce the quality of our MRF estimations.

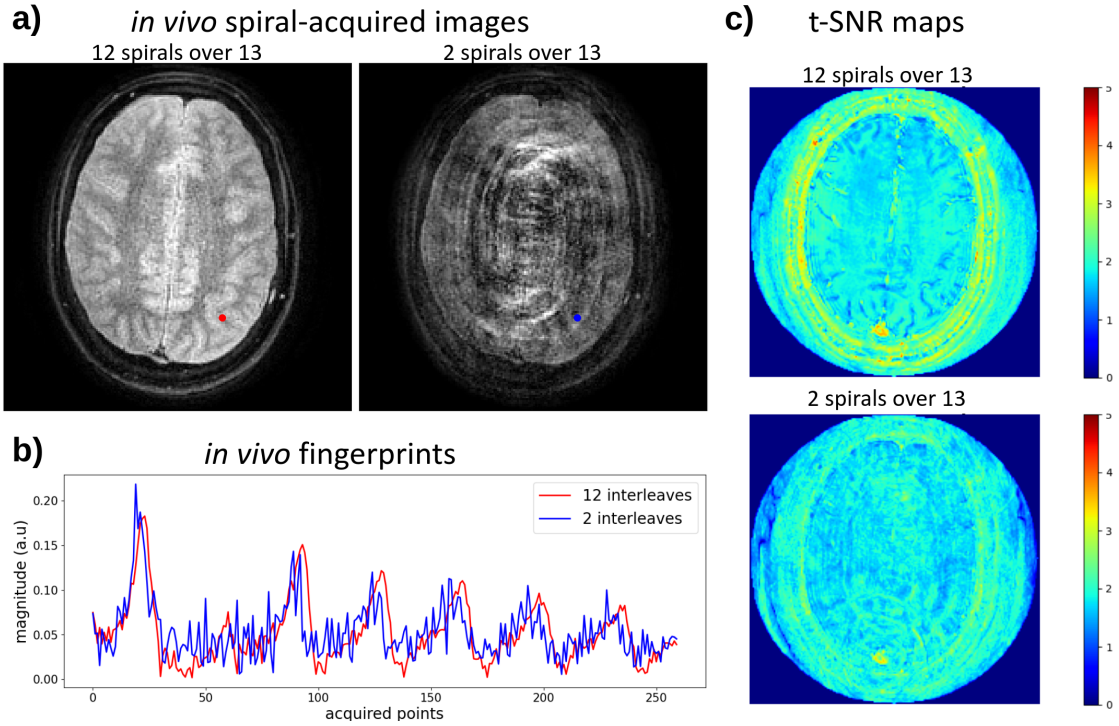


**Figure II.4.7**: a) *In vivo* acquisitions using spiral trajectory with different undersampling factors b) corresponding *in vivo* fingerprints in a voxel c) corresponding computed t-SNR maps.

In the rest of this manuscript, we decided to pursue our study keeping a low spiral undersampling factor (12 spiral arms over 13 interleaves) that still presents a good trade-off between MRF image t-SNR and short scan time.

### II.4.2.1 Multi-shot imaging

In multishot spiral imaging in MRI, if the delay between two shots (sequence repetitions) is too short, the spins may not fully return to equilibrium, leading to incomplete relaxation. This incomplete recovery can result in saturation effects, where the signal from the tissue is reduced in subsequent measurements, affecting the image contrast and signal-to-noise ratio (SNR). A delay between sequence repetitions is thus necessary.

In standard multi-slice imaging (*M2D* mode on Philips software), we can set this delay manually in the sequence definition to ensure fully complete relaxation even with short-duration sequences. However, following the idea of acquiring as many slices as possible in a short acquisition time, using multi-slice interleaved imaging (*MS* mode on Philips software) is a technique that can be used to take advantage of long delays between sequence repetitions in MRI. In multi-slice interleaved imaging, slices are acquired in an interleaved order rather than sequentially. By interleaving slices, the time required for $T_1$ relaxation can be effectively utilized. While the spins in one slice are relaxing, the scanner is acquiring data from another slice. This way, the overall TR for each slice is effectively increased without prolonging the total scan time. This helps avoid saturation artifacts while optimizing acquisition duration.

However, our first tests, in phantoms and humans, comparing *M2D* with delay and *MS* with several slice imaging showed different results in the obtained fingerprints. In the latter case, the measured fingerprints don't match our numerical simulation and the reconstruction leads to bad estimates of every tissue parameter. We suspect that this could result from a $B_0$ drift artifact, but in the interest of getting a viable sequence quickly for our first proof of principle, we decided to go with the *M2D* mode four our multi-slice and multi-shot spiral acquisition. This implies the use of a 6-second delay between sequence repetitions leading to a scanning time of 2 minutes per slice. Note that using an interleaved *MS* mode acquisition, we could reduce this time by a factor of 2 with the same spiral undersampling pattern.

## II.5 Conclusion

In this chapter, we have shown the potential of bSSFP-type sequences for microvascular and relaxometry estimates in the human brain according to a *in silico* study of the manifest sensitivity of these sequences to magnetic field inhomogeneities. Compared to MRF-standard spoiled GRE sequences, the balanced sequences response signal is highly sensitive to the intra-voxel frequency offset distribution without the need for contrast agent injection during the acquisition. We designed possible candidates according to theoretical *in silico* studies and the constraints of our current hardware and software options. In the literature, the sensitivity of the bSSFP signal response to acquisition parameters and tissue properties has not been clearly addressed yet.

In the next chapter, we will detail the numerical simulation process that allows the representation of intra-voxel field inhomogeneities contribution in the computed MR signals for the MRF dictionary generation. Using the optimized acquisition sequence and undersampling parameters derived from our *in silico* observations, we conducted an *in vivo* study on 6 healthy volunteers to validate our hypothesis.

# Chapter III

# First study of combined relaxometry and contrast-free cerebral microvascular estimates in human volunteers using balanced Steady-State Free Precession MR Fingerprinting

This chapter presents the work submitted in *Magnetic Resonance in Medicine* on the 7th of August 2024, where I am the first author. The content of this paper has been slightly adapted to fit within the broader narrative of this thesis, ensuring continuity and coherence with the preceding and following chapters. While the core findings and analyses remain unchanged, minor adjustments have been made to align the structure and formatting with the overall manuscript. This integration highlights the relevance of the study within the context of the thesis, reflecting its contribution to the overarching research objectives.

This study proposes a novel, contrast-free Magnetic Resonance Fingerprinting (MRF) method using balanced Steady-State Free Precession (bSSFP) sequences for the quantification of cerebral blood volume (CBV), vessel radius (R), and relaxometry parameters ($T_1$, $T_2$, $T_2^*$) in the brain. An *in vivo* study on human volunteers is described in this chapter.

## Contents

# III.1 Introduction

Estimations of brain microvascular properties (blood volume, blood flow, microvessel diameter, capillary transit time, etc.) are crucial for diagnosing, staging, and evaluating therapies in various pathologies like stroke and tumors (van Dijken et al. 2017; Shiroishi et al. 2015; Demeestere et al. 2020). A common MR method to assess microvascular properties is the Dynamic Susceptibility Contrast (DSC) approach which relies on MR signal variations following an intravenous injection of gadolinium (Gd) based contrast agents (CA). The CA induces magnetic susceptibility differences between the blood compartment and the surrounding tissues. This leads to broadening the distributions of MR frequencies inside the imaging voxels, and a corresponding reduction of gradient echo (GRE) signal intensities proportional to the voxel blood volume in the absence of large vessels (see Troprès et al. 2015). Simple biological models can be used to retrieve cerebral blood flow (CBF) or mean arterial transit time (MTT) and more advanced models can estimate capillary transit times and maximum oxygen extraction fraction (OEF, Jespersen et al. 2012). Interestingly, signal magnitudes from spin echo (SE) sequences are also reduced due to water diffusion effects. Combining GRE and SE signal variations can provide information sensitive to microvessel density and size as shown by Stadlbauer et al. 2017; Emblem et al. 2013. Absolute quantification of vascular parameters using DSC is however difficult (Willats et al. 2013). It requires estimations of local Arterial Input Functions (AIF) and signal deconvolutions. The main drawback of DSC is the use of bolus of CA which not only limits spatial resolution due to the need for dynamic measurements but also increases the risk of nephrogenic systemic fibrosis and potential gadolinium retention in brain or kidney tissue as detailed by Iyad et al. 2023.

Several methods based on the Blood Oxygen Level Dependent (BOLD) effect have been proposed to avoid CA injection (Christen et al. 2012; Biondetti et al. 2023). Many studies have used $T_2^*$ maps as surrogates for blood volume and/or oxygenation estimates. These maps are computed by considering Lorentzian frequency distributions inside the voxels and corresponding mono-exponential signal decays from multi-echoes GRE sequences. These baseline maps are however not fully reliable as many non-vascular effects ($T_2$, shim) also contribute to the signal decay which often deviates from the simple exponential model. A more advanced analysis of the baseline BOLD effect, named quantitative BOLD has also been proposed (He et al. 2007; Christen et al. 2014a; Christen et al. 2010). It relies on modeling the frequency distributions using statistical models of blood vessels represented as ensembles of isotropically oriented straight magnetic cylinders. Accounting for other signal contributions, small deviations from monoexponential MR signal decay at short echo times allow the separation of cerebral blood volume (CBV) and blood oxygen saturation ($SO_2$) contributions. This is however possible only at very high SNR and the cylinder model might not be able to represent all types of vascular structures as suggested by Sedlacik et al. 2010. Recently, interesting results have been reported on non-contrast blood volume and blood arrival estimates using either internal resting-state fluctuations by Christen et al. 2015 or externally controlled gas challenges to mimic boluses of paramagnetic blood. However, these approaches also suffer from low SNR and thus low spatial resolution.

Most of the previous MR studies designed for microvascular estimates have been based on

GRE sequences. It has been known for decades that other types of sequences are more sensitive to frequency shifts. In particular, the balanced steady-state free precession (bSSFP) sequences have a signal response (magnitude and phase) that highly depends on the frequency offset $\delta f$ as demonstrated by Scheffler et al. 2003b; Miller 2012. In comparison, the frequency response functions of GRE are always flat in magnitude and linear in phase. When measuring with a bSSFP sequence the signal from a voxel that contains a large distribution of resonance frequencies, the variations often deviate from exponential decay and can in some cases produce spin echo-like behaviors (Scheffler et al. 2003a; Leupold 2018). Moreover, the bSSFP response functions are known to depend on the sequence parameters and to differ between transient and steady states. It is thus possible to induce changes in signal evolution by changing the flip angle (FA) or repetition time (TR) rather than trying to modify the *in vivo* distributions of frequencies using CA injection. The high sensitivity of bSSFP to microvascular properties has already been observed in several BOLD fMRI experiments (Miller 2012). However, it is also clear that quantitative estimates from bSSFP-type sequences are difficult to obtain as the signals also depend on various non-vascular parameters including $T_1$, $T_2$, or $B_1$.

The Magnetic Resonance Fingerprinting (MRF, Ma et al. 2013) framework was proposed 10 years ago to allow the extraction of multiple parameters simultaneously from complex MR sequences in their transient states. Matched to a dictionary of signals obtained *in silico*, even highly undersampled images can produce reliable quantitative relaxometry maps. bSSFP type sequences have been analyzed in the first MRF study to produce $T_1$, $T_2$, $M_0$, and $\delta f$ maps. However, FISP (Fast Imaging with Steady Precession) GRE sequences have since been preferred because of lighter dictionary generation and analysis. Two recent studies from Wang et al. 2019; Boyacioglu et al. 2020 have proposed to analyze bSSFP sequences for additional $T_2^*$ estimates using Lorentzian intra-voxel frequency distributions in the dictionaries. In parallel, the MRF framework has also been used to assess vascular properties. An ASL-based sequence combined with MRF (MRF-ASL, Su et al. 2019) has shown promising results on CBF and bolus arrival time (BAT) estimations validated against DSC MRI. Additionally, multi-echo spin- and gradient-echo sequences acquired pre and post-CA injection allow the estimation of CBV, mean vessel radius (R), and $SO_2$ within the MRF framework (MR vascular Fingerprinting or MRvF, Christen et al. 2014b). Compared to standard relaxometry MRF, these sequences provide only a few fully sampled images but the dictionaries involve realistic biophysical representations of the vascular networks. The magnetic field perturbations due to the magnetic susceptibility distributions and the phase accumulation due to water diffusion are also computed. In that case, high-resolution maps of CBV, R, and $SO_2$ have been obtained in rats and humans by Christen et al. 2014b; Lemasson et al. 2016.

The current chapter hypothesizes that bSSFP sequences, used in an extended High-Dimensional MRvF framework, can provide quantitative maps of $T_1$, $T_2$, $T_2^*$, $M_0$, $\delta f$, CBV, and microvascular properties without CA injection. We studied the sensitivities of GRE and bSSFP sequences *in silico* and proposed an MRF-bSSFP candidate for vascular estimates. We compared the results obtained in human volunteers using large multidimensional dictionaries generated from Lorentzian distributions of magnetic field or frequency distributions based on 3D vascular voxels, either artificially generated (standard approach using cylinders) or segmented from microscopy datasets (as recently proposed by Delphin et al. 2024).

# III.2 Methods

## III.2.1 Two-step MRF Dictionary generation

Standard MRF dictionaries describing signal evolutions of unbalanced GRE sequences usually contain 3 dimensions ($T_1$, $T_2$, $B_1$) as in the work proposed by Jiang et al. 2015. To represent the resonance frequency shift sensitivity, dictionaries that describe bSSFP sequences need to take into account an extra dimension that describes the intra-voxel average frequency offset ($\delta f$). We first generated such a base dictionary $\text{Dico}_{\text{base}}$($T_1$, $T_2$, $B_1$, and $\delta f$) using in-house Python+Matlab code derived from a reference Bloch simulator for standard relaxometry sequences, initially implemented by Dr. Brian Hargreaves at Stanford. Simulations were performed at 3.0T with 20 $T_1$ values (0.2 to 3.5s), 20 $T_2$ values (10 to 600ms), 10 $B_1$ values (0.7 to 1.2) and frequency offset $\delta f$ values (from -50 to 49 Hz with an increment of 1 Hz), keeping only signals for which $T_1 > T_2$, resulting in a 390,000 entries dictionary.

New dimensions need to be added to the dictionary when accounting for $T_2^*$ or microvascular effects. In the first approximation, the influence of blood vasculature on signal evolutions can be seen through the changes in the voxel frequency shift distributions caused by magnetic sources (see Miller et al. 2008). While it is possible to compute the corresponding voxel spatial magnetic field distributions and to sum the MR signals to come from multiple spatial locations (Christen et al. 2014b), a faster solution needs to be proposed when the dictionaries also contain multiple relaxometry parameters and thus hundreds of millions of simulated signals. If the influence of water diffusion is low (see Figure III.2.1), the voxel spatial frequency distributions can be simplified and it is possible to focus on the shapes of the frequency histograms only.

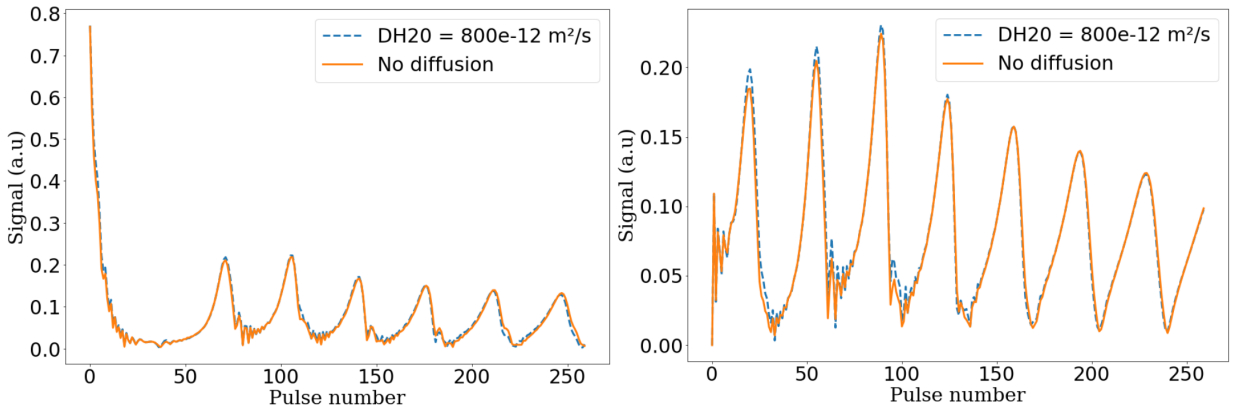


**Figure III.2.1**: Water diffusion effects on signals responses of the proposed MRF-bSSFP. $T_1$=1.6s, $T_2$=0.2s, $B_1$=0.7, $\delta f$=5Hz, $SO_2$=50%, CBV=3%, R=5$\mu$m (left) and $T_1$=1.1s, $T_2$=0.11s, $B_1$=1.0, $\delta f$=25Hz, $SO_2$=80%, CBV=5%, R=5$\mu$m (right).

Following the work of Wang et al. 2019, a $T_2^*$-like behavior, sensitive to microvascular properties, may simply be obtained by recombining several complex signals from the base dictionary according to the histogram of intra-voxel frequency values. Our $\text{Dico}_{\text{base}}$ was simply weighted by pre-computed intra-voxel frequency distributions in a range of $\Delta f$ frequencies

centered on $\delta f$ values (see Figure III.2.2). We evaluated four methods: standard Lorentzian distributions and 3 approaches based on the simulation of an intravoxel microvascular network, with increasing biophysical complexity, as detailed below. These distributions were defined by specific parameters $\theta$ that can then be estimated in the MRF framework by matching into a new dictionary which depends on $(T_1, T_2, B_1, \delta f, \theta)$ as detailed in Figure III.2.3.

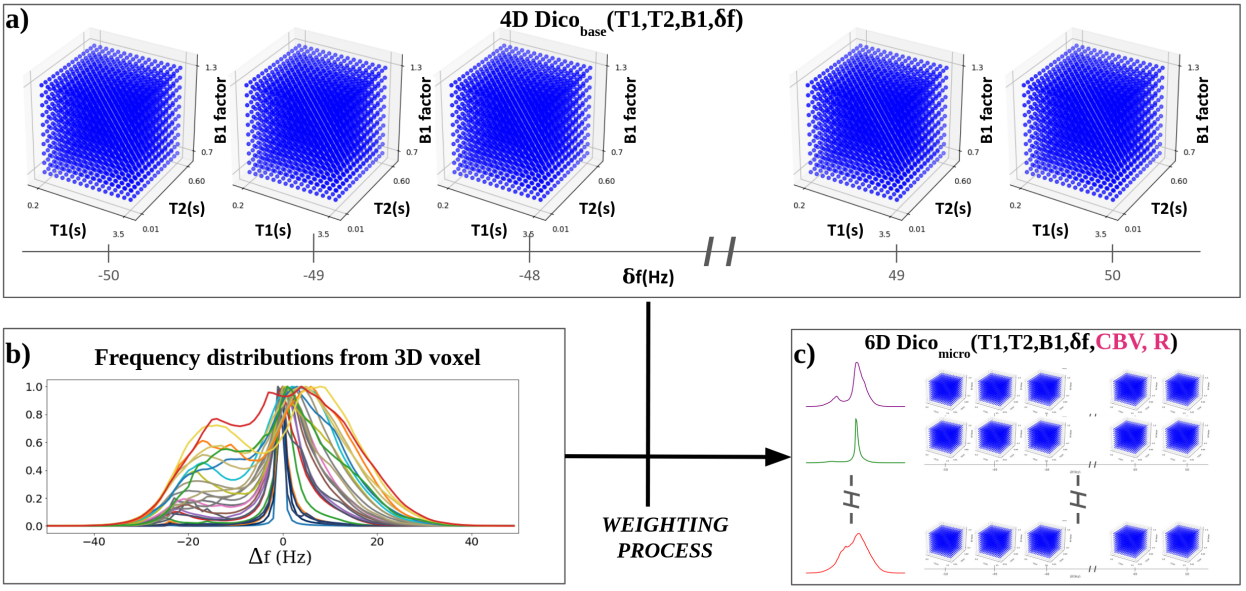


**Figure III.2.2**: Two-step MRF simulations process. a)Simulations of a standard 4D Bloch dictionary with ($T_1$,$T_2$,$B_1$,$\delta f$) parameters grid. b)Use of frequency distributions from 3D voxels to weight the 4D dictionary resulting in a 6D dictionary (here shown for example at df=0Hz) (c) with CBV and R dimensions related to the 3D frequency distributions.

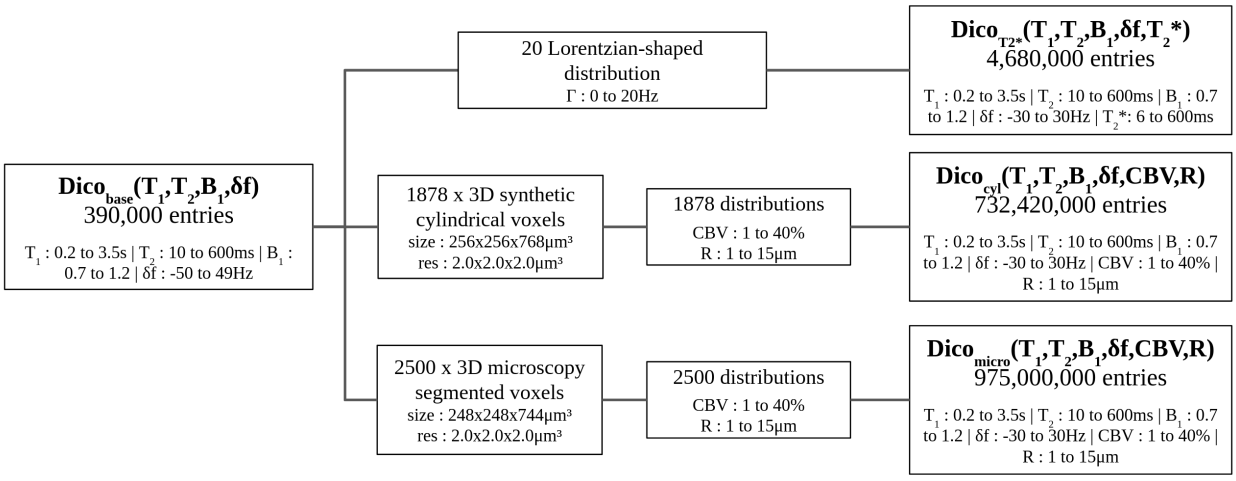


**Figure III.2.3**: Simulation parameters for the three dictionaries presented in the Methods section.

### III.2.1.1 Lorentzian frequency distributions for $T_2^*$ estimates ($Dico_{T_2^*}$)

It is common to consider that the intra-voxel frequency distribution has a Lorentzian shape. This shape was chosen such that a monoexponentially decaying transverse signal evolution

would be produced from a GRE sequence. This approximation defines the $T_2^*$ relaxation time which corresponds to the width of the distribution (or the time constant of the exponential signal decay of unbalanced multi-gradient echo sequences). Here, we followed the work of Wang et al. 2019, by modeling the intra-voxel frequency distribution with probability density function given by:

$$L(\Delta f, \Gamma, \delta f) = \frac{\frac{\Gamma}{2}}{(\Delta f - \delta f)^2 + (\frac{\Gamma}{2})^2} \tag{III.2.1}$$

where $\Delta f$ is the frequency-dependent signal values of the $\text{Dico}_{\text{base}}$, $\delta f$ the mean frequency of the voxel and $\Gamma$ the full width at half maximum of the distribution (ranging from 0 to 20 Hz with an increment of 1 Hz). Using the two-step dictionary generation process described above, an expanded dictionary that depends on $(T_1, T_2, B_1, \delta f, \Gamma)$ is obtained by weighting each complex signal contribution by the spin density at the corresponding frequency.

This dictionary can be then interpreted as $\text{Dico}_{T_2^*}(T_1, T_2, B_1, \delta f, T_2^*)$ by using:

$$\frac{1}{T_2^*} = \frac{1}{T_2} + \pi\Gamma \tag{III.2.2}$$

To ensure fully defined distributions in the convolution process only values in the range -30 Hz $< \delta f <$ 30 Hz were used in the expanded dictionary, leading to a total number of 4,680,000 entries.

#### III.2.1.2 Realistic frequency distributions for vascular estimates

The *in vivo* intra-voxel magnetic field distribution is usually more complex than a Lorentzian distribution. It is possible to compute the magnetic field distributions produced by 3D vessel structures using a fast Fourier-based approach (Salomir et al. 2003; Marques et al. 2005). We did this using MRVox (Pannetier et al. 2013), an in-house Matlab simulation tool. The corresponding $\delta f$ distributions thus depend on vascular characteristics such as CBV, R, $SO_2$. The simulations of the distributions were made with a main magnetic field of 3.0T oriented in the Z direction, with the $SO_2$ in each voxel set at 70% and the micro-vascular hematocrit fraction at 0.85×42% as suggested by Sakai et al. 1985.

**3D cylindrical voxels ($\text{Dico}_{\text{cyl}}$)** Straight cylinders are common approximations for blood vessel shapes in MR simulations. We thus generated 3D voxels containing multiple straight cylinders with variable radii, using Matlab. 2500 combinations of (CBV, R) were chosen, with manually distributed ranges for each parameter, where the mean radius R was set as the center of a Gaussian distribution of vessel radii in a given voxel, resulting in 1878 3D voxels taking into account that the geometrical constraints of the cylinder generation can not always accommodate all (CBV, R) combinations. Vessels were isotropically oriented in 60% of the voxels and anisotropically oriented along $B_0$ and in the transverse plane in 20% each. After validating that the voxel size does not significantly influence the distribution of the intra-voxel magnetic inhomogeneities as long as the size ratios between the axes and their orientation were respected (see Figure III.2.4), the voxel size was fixed at 256x256x768$\mu$m$^3$ with a 2.0x2.0x2.0$\mu$m$^3$ resolution for vascular structures simulations. From these 3D voxels,

magnetic field distributions were computed using a Fourier transform detailed in Salomir et al. 2003 (see Figure III.2.5). The corresponding 1878 frequency distributions were then used to expand the 390,000 entries $\text{Dico}_{\text{base}}$ dictionary, leading to a 732,420,000 entries vascular dictionary $\text{Dico}_{\text{cyl}}(T_1, T_2, B_1, \delta f, CBV, R)$. Only $-30$ Hz $< \delta f <$ 30 Hz values were used for matching in the expanded dictionary, with simulations computed on the fly during the matching process for efficiency.

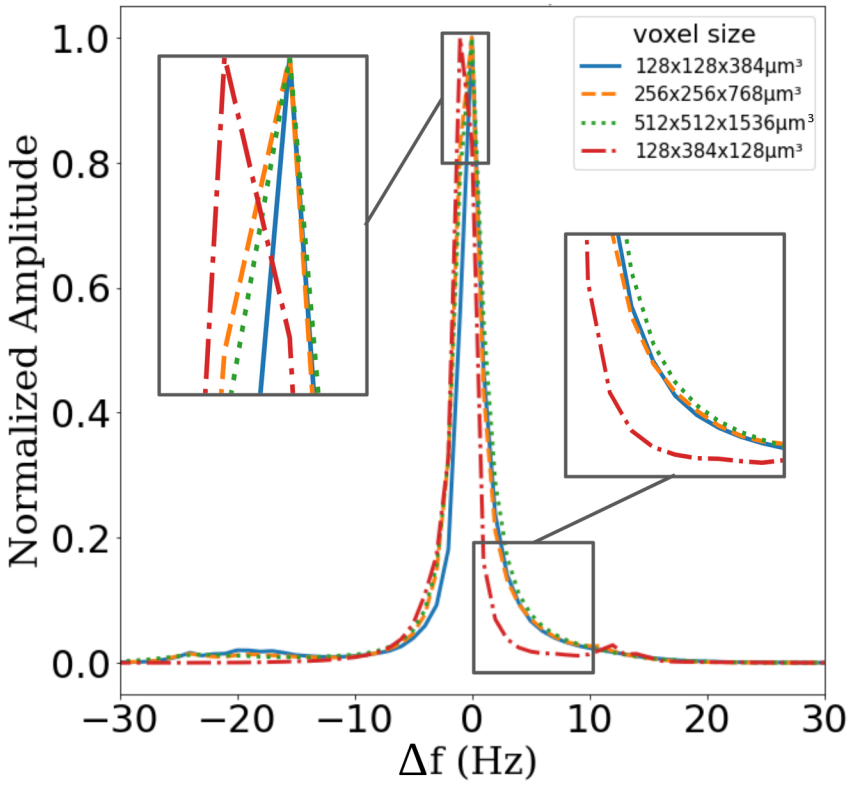


**Figure III.2.4**: Intra-voxel frequency distribution for a synthetically generated voxel with cylindrical vessels, for $SO_2$=60%, CBV=5%, and R=6$\mu$m. Each line corresponds to a different voxel size.

**3D microscopic voxels** ($\text{Dico}_{\text{micro}}$) As described previously by Delphin et al. 2023, it is possible to use microscopy-derived vascular networks as input for the magnetic field simulations. Here we used 2500 3D voxels segmented from multiple open-access datasets of whole brain, healthy mouse vascular networks as a basis to create a dictionary of signals with 3D-resolved MR simulations (see Figure III.2.5). The voxel size is 248x248x744$\mu$m$^3$ with a 2.0x2.0x2.0$\mu$m$^3$ resolution. The voxels were chosen among a dataset of 30,000 segmented voxels such that the (CBV, R) values distribution was as close as possible to the 3D cylindrical voxels (CBV, R) distribution. At the end, the $\text{Dico}_{\text{micro}}(T_1, T_2, B_1, \delta f, CBV, R)$ contains 975,000,000 entries and only $-30 < \delta f <$ 30 Hz values were used for matching.

**Rectangular distributions for additional contributions** bSSFP sequences are very sensitive to $B_0$ variations and other sources of field inhomogeneities can influence the final vascular estimates. To consider this effect in our reconstructions, we also convolved each of the 2500 microscopic distributions with seven rectangular-shaped distributions with different

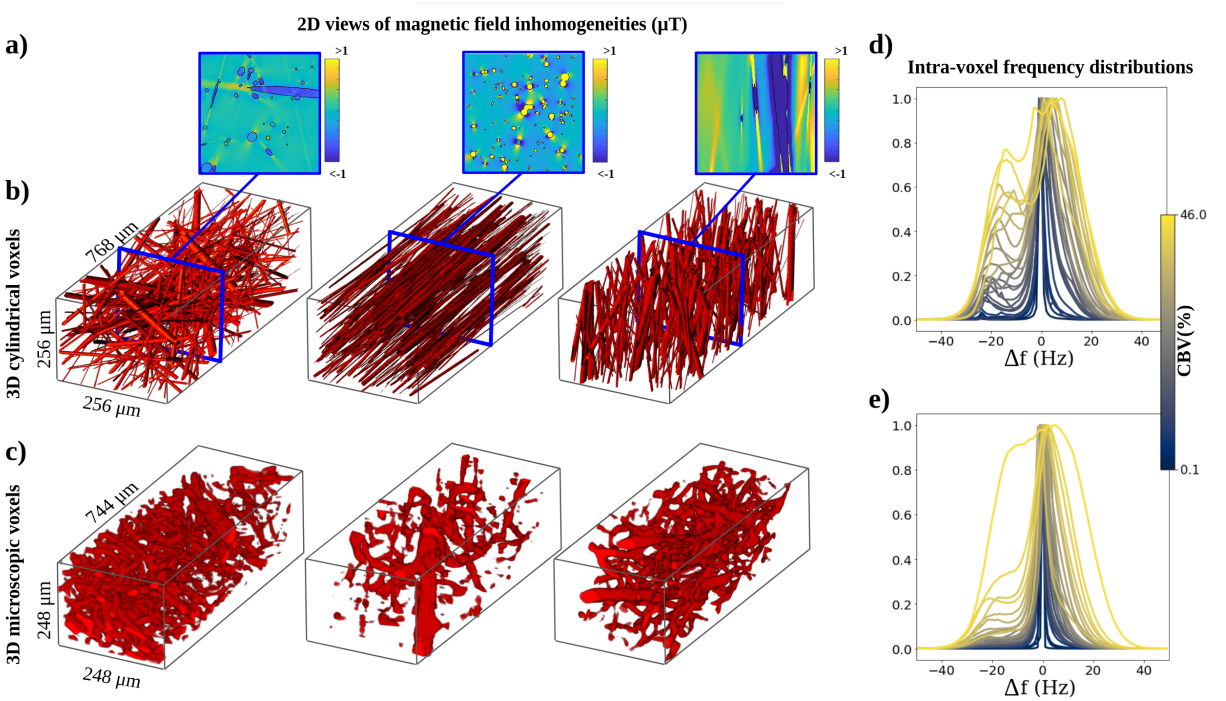


**Figure III.2.5**: Magnetic field simulations (a) in vascular voxels with fixed blood susceptibility value, leading to a set of intra-voxel frequency distributions: using synthetic 3D-cylindrical vascular voxels (b, d) and using microscopy-segmented 3D vascular voxels (c, e). For the distributions, color code corresponds to (CBV,R) and is mainly influenced by changes in the CBV which varies between 0.1 and 46%.

widths representing spatial linear gradients across the voxel (Figure III.3.9c-e). This finally leads to 17,500 distributions with a new dimension ("$B_0$ gradient") in the convoluted dictionary, determining the width of the additional top-hat function, and ranging between $10^{-5}$ and $10^{-2}$ T m$^{-1}$. Given the large size of the final dictionary (6,825,000,000 entries), the matching process was constrained here by a ground truth $B_1$ map acquired on the same subject to reduce computation cost as it was introduced by Ma et al. 2017.

## III.2.2 *In silico* study

We used our dictionary simulations to compare *in silico* the $B_0$ inhomogeneity sensitivity of FISP and bSSFP sequences. Different sets of sequence parameters were used for FISP-type sequences to look at multi-echoes signal decay in response to frequency distributions obtained with and without contrast agent (CA) contribution(III.2.6. In the latter case, the magnetic susceptibility of the blood compartment at equilibrium was set to 5.5 ppm. The frequency distributions were computed from 27 3D vascular voxels with varying $SO_2$, CBV, R values, at 3 Tesla, with a blood hematocrit fraction of $0.85 * 42\%$ and no water diffusion effect. To examine bSSFP-type sequences' sensitivity to non-contrast frequency distribution, varying sequence parameters were also used to simulate multi-echo signal decay, and both the transient-state and steady-state parts of the signal were studied. In every case, the magnitude and phase frequency response profiles were also calculated (at an echo time of TR/2).

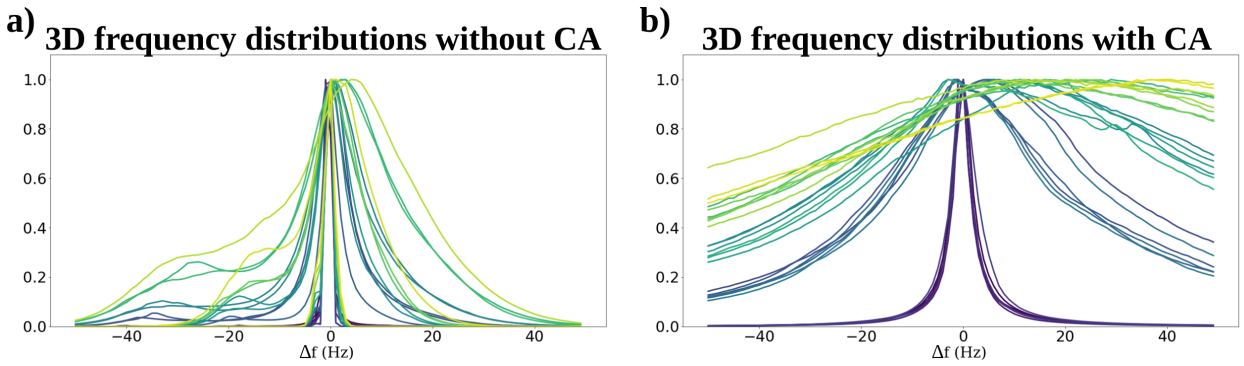


**Figure III.2.6**: Intra-voxel frequency distributions computed from synthetic cylindrical voxel without (a) and with (b) the presence of USPIO contrast agent. Distributions are plotted after normalization to enhance figure readability.

### III.2.3 MR Data Acquisition

*In vivo* acquisitions were realized on 6 healthy volunteers (28.0±5.5 years old, 3 males and 3 females) using a 32-channel head receiver array on a Philips 3T Achieva dStream MRI at the IRMaGe facility (MAP-IRMaGe protocol, NCT05036629). This study was approved by the local medical ethics committee and informed consent was obtained from all volunteers prior to image acquisition. The proposed MRF-bSSFP sequence was based on an IR-bSSFP acquisition. 260 repetitions were acquired (TR=21 ms, TE=7 ms) with FA linearly increasing from 7° to 70° as suggested by Gómez et al. 2019 and a quadratic phase cycle of 10° increments with additional $(0, \pi)$ cycling between subsequent acquisitions.

For our proof of principle study, the acquisitions were performed using constant density spiral sampling (12 interleaves out of 13), matrix size=192x192x4, voxel size=1.04x1.04x3.00mm$^3$ for a total scan duration of 2 minutes per slice. For comparison, an MRF IR-spoil sequence from Gómez et al. 2019 was used to acquire $T_1$, $T_2$, and $M_0$ quantitative maps. For $T_2^*$ validation, a standard multi-echo GRE (MGRE, TR=70 ms, 10 echoes $TE_1$=3.8 ms and $\Delta TE$ = 6.4 ms) sequence was acquired. Finally, an anatomical $T_1$w MRI (spin-echo sequence with FA=90° and TR=600ms, a matrix size of 512x512x327 with a slice thickness of 0.55mm and a spatial resolution of 0.447x0.447mm$^2$) was acquired and used for regions of interest (ROIs) delineation.

In one subject, the MRF-bSSFP sequence was also acquired with cartesian sampling (compressed sense factor of 4) and high resolution in 2D to reduce shim and partial volume effects with a matrix size of 256x256x1 and a voxel size of 0.78x0.78x3.00mm$^3$, leading to a total scan time of 12 minutes. Additionally, a DREAM (Nehrke et al. 2012) sequence was applied to obtain a reference $B_1$ map.

### III.2.4 MR Data Processing

All processing was performed with Python. An MRF standard dictionary-based matching method was used. The dot product of each acquired fingerprint with the whole dictionary was computed and the entry yielding the highest value was kept as the best match. Due

to constraints in computational power and storage size, the matching process was batched over the acquisition size and also over the number of signals of the dictionary in the case of convolved dictionaries by convolving distribution on the fly (see Section III.2.1). Combining simulations and matching, for a 4-slices acquisition with the resolution detailed in Section III.2.3, the reconstruction process takes about 2 hours on a single NVIDIA Quadro RTX 8000 with 48Go of memory using the JAX library. Concerning reference acquisitions, $T_2^*$ values were derived from exponential fitting to the MGRE signal decay. $T_1$ and $T_2$ quantitative reference values were computed by a classical matching approach using a Bloch-simulated dictionary with the same ($T_1$, $T_2$, $B_1$) ranges as the $Dico_{base}$ in Section III.2.1.

### III.2.5 Image analysis

MRF $T_1$, $T_2$ and $T_2^*$ values for the grey matter (GM) and the white matter (WM) regions were calculated from automated ROIs generated using the Otsu's thresholding method (Otsu 1979) in Matlab using anatomical $T_1$WI as reference. CBV and R values for the GM, and WM regions were computed using the same method, and values inside the superior sagittal sinus (SS) vein were also computed from manual ROI validated by a neuroscientist. The reference ROI values for relaxometry estimates were computed for the MR reference sequences described in Section III.2.3. The accuracy and precision of the proposed method were assessed by comparing relaxometry $T_1$&$T_2$ quantitative estimates with acquired validation maps from IR-FISP MRF, using Bland-Altman analysis. Result maps were smoothed with a Gaussian filter (with a Gaussian kernel of standard-deviation $\sigma$=0.4 pixel) before computation only to improve plot clarity in Figure III.3.7c,e.

## III.3 Results

### III.3.1 *In silico* study

In Figure III.3.1a, we show the frequency distributions obtained in voxels with realistic microvascular networks with different CBV, R, and $SO_2$ properties. The distributions from the same voxels containing the contrast agent are represented in Figure III.3.1b, highlighting peak broadening. Color code corresponds to (CBV,R,$SO_2$) and is sorted by CBV values. As expected, the frequency magnitude response profile of the spoiled sequence is flat for every set of sequence parameters (TR, FA)leading to quasi-mono-exponential decays in multi-echo FISP sequences. With CA, signal changes at longer echo times reveal CBV differences. Note that distributions for the CA injection case are highly truncated on the fixed frequency range. Figure V.2.2, Chapter V shows a larger representation of these distributions.

In contrast, bSSFP signal profiles vary with sequence parameters. Figure III.3.2 shows that, even with fixed TR and FA, the profile differs between transient and steady states. For non-contrast distributions from Figure III.2.6, signals may increase with echo time rather than decrease monotonically. Certain parameter combinations may produce spin echo-like signals at different echo times, and high flip angles can cause significant signal variability even at short echo times. The transient state is represented by looking at echoes between two pulses at the very beginning of the sequence, while the steady state is assumed for echoes

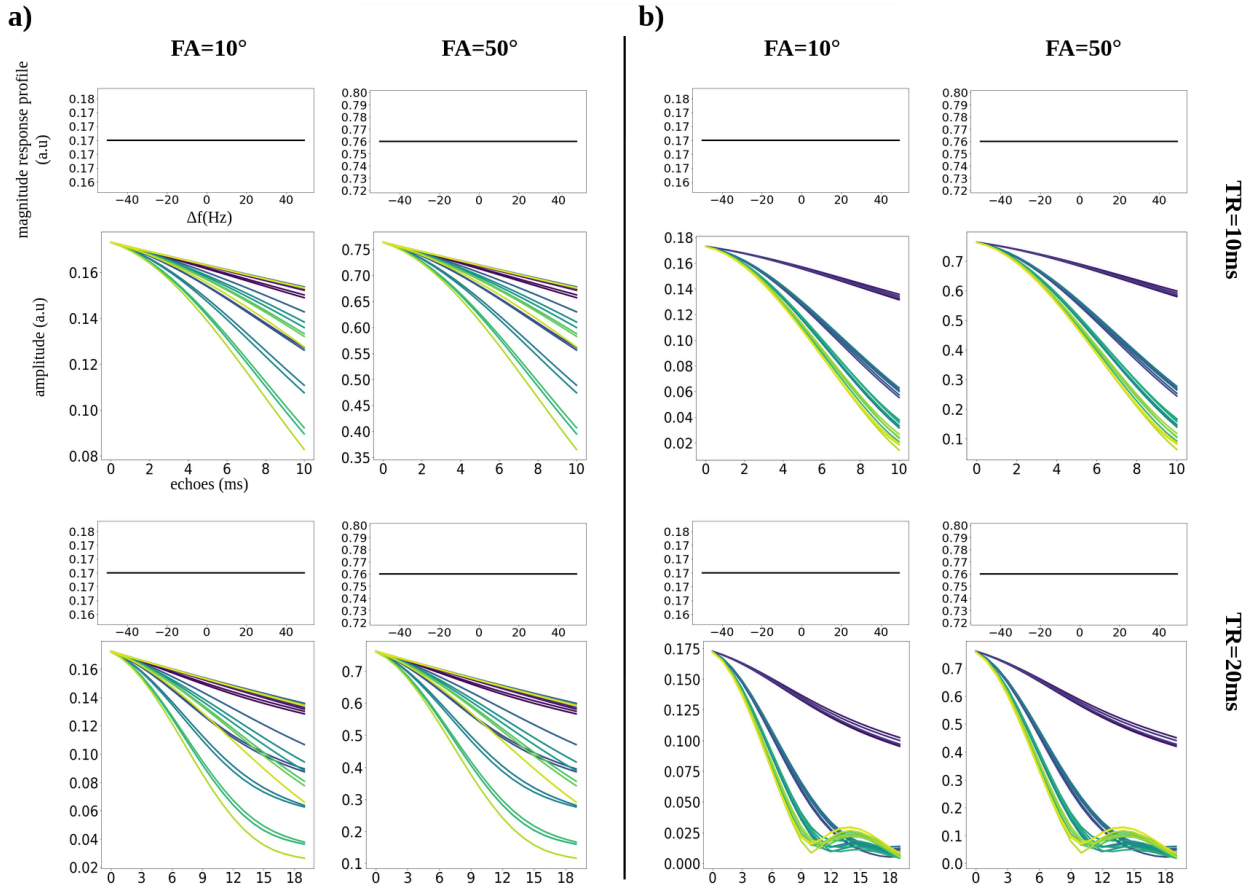


**Figure III.3.1**: *In silico* study of the FISP signal response to different intra-voxel frequency distributions. The magnitude response profile and signal decays associated with 3D frequency distributions are shown without CA in a) and with CA in b). The magnitude response profile is shown for TE = TR/2 for TR=10ms and TR=20ms, and average tissue properties of grey matter at 3T (GM, $T_1$= 1300 ms, and $T_2$= 80 ms) and for $\delta f$=0Hz. The color code is primarily related to the CBV value.

between two pulses after an important number of TRs depending on the sequence parameters.

The previous observations led to the design of the single echo, short TR, MRF-bSSFP sequence that includes FA variations within transient and steady-state sections. This design enhances sensitivity to frequency distributions by allowing response profile variations over the signal acquisition time. Figure III.3.3 shows signal entries from subsections of the $\text{Dico}_{\text{micro}}$ computed with the proposed sequence. Variations in signal evolution are evident with parameter changes, and different panels show limited cross-talk between parameters. Notably, changes in CBV cause distinct signal variations not captured by sensitivities to $T_1$, $T_2$, $B_1$ or $\delta f$.

## III.3.2 *In vivo* acquisitions

Figure III.3.5 shows examples of *in vivo* MRF signals obtained in GM, WM, and SS regions in one healthy volunteer. Three magnitude images showing changes in contrast and bSSFP banding artifacts obtained at different pulse numbers are also shown. Figure III.3.5c shows

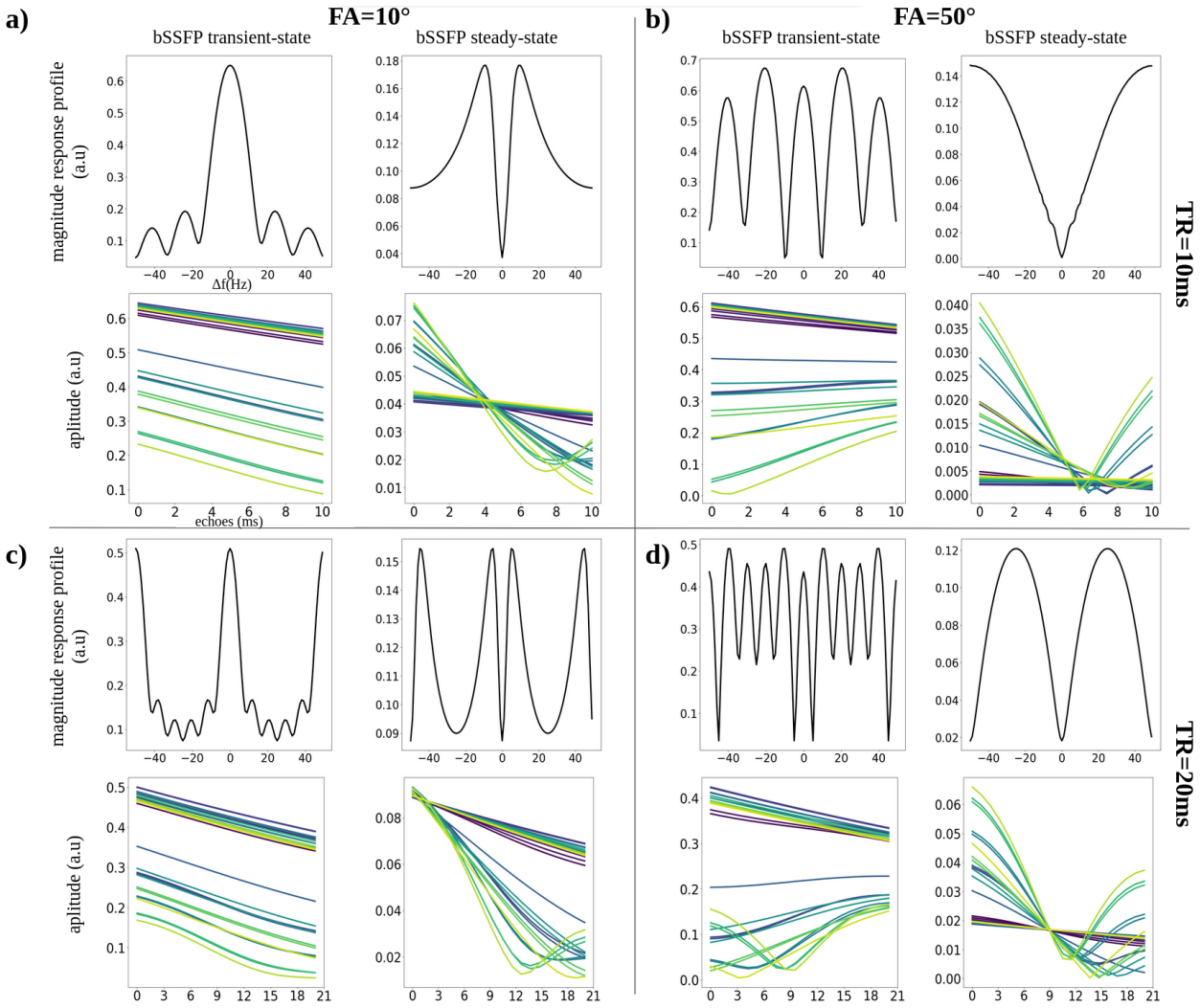


**Figure III.3.2**: *In silico* study of the bSSFP response signal to the intra-voxel frequency distributions without contrast agent. Magnitude response profiles as well as sequence signal decays are shown for different sets of sequence parameters, for TE = TR/2, and average tissue properties of grey matter at 3T (GM, $T_1$= 1300 ms, and $T_2$= 80 ms) and for $\delta f$=0Hz.

the magnitude image at first pulse $TR_0$ to localize the ROIs. The frequency distributions obtained after MRF matching and the associated (CBV, R) values are given. More estimated frequency distributions are shown in Figure III.3.4. Notably, the superior sagittal sinus vein shows a clearly different signal evolution as well as a larger matched frequency distribution with high estimated CBV and R values.

Figure III.3.6 shows results obtained with the MRF-bSSFP sequence in another subject. Different dictionaries including increasingly realistic frequency distributions were used for the reconstructions. This highlights the sensitivity of the sequence to the frequency dimension, showing that $T_1$ and $T_2$ maps are not well estimated with unique $\delta f$ values. $T_2{}^*$ maps and better $T_2$ estimates are obtained when considering Lorentzian distributions. CBV and R values are obtained when considering vascular distributions with differences between the cylinder and realistic microscopy distributions. A clear contrast between CBV values in

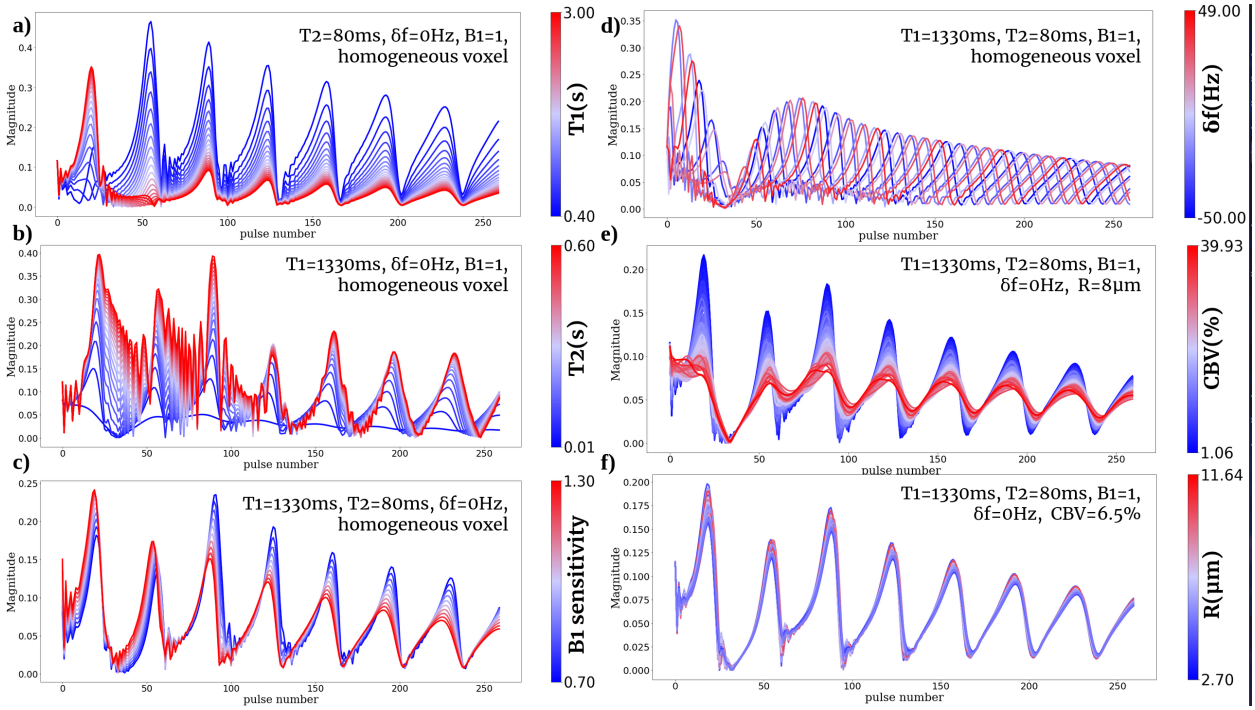


**Figure III.3.3**: Sets of representative dictionary entries. For $T_1$, $T_2$, $B_1$, and $\delta f$ properties (a,b,c,d) the signal responses are plotted for a voxel devoid of the vasculature (single intra-voxel frequency, i.e. Dirac distribution). Only 1 of the 4 dictionary properties is varied whereas the remaining 3 are fixed. For CBV, and R properties (e,f), 1 of the 6 dictionary properties is varied whereas the remaining 5 are fixed.

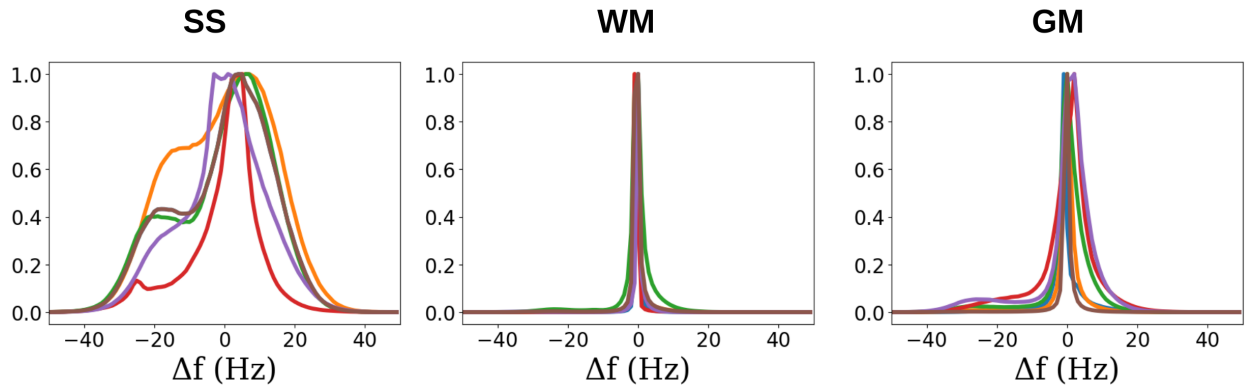


**Figure III.3.4**: *In vivo* matched results of intra-voxel frequency distributions (associated with CBV and R values) in anatomic ROIs for one subject. SS=Sagittal sinus, WM=White Matter, GM=Grey Matter.

GM and WM can be observed. Larger CBV and R values are also found in large blood vessels such as the SS. Using realistic microscopy distributions, R values are lower than using cylinders and in the range of physiological values.

Relaxometry maps derived from the reference MRF IR-FISP sequence and our proposed MRF-bSSFP sequence are compared in Figure III.3.7 a and b respectively, in which 4 slices of one subject are shown. Scatter plots and results from voxel-wise Bland Altman (BA) analyses are shown in (Figure III.3.7c and e respectively). The dotted blue lines indicate the

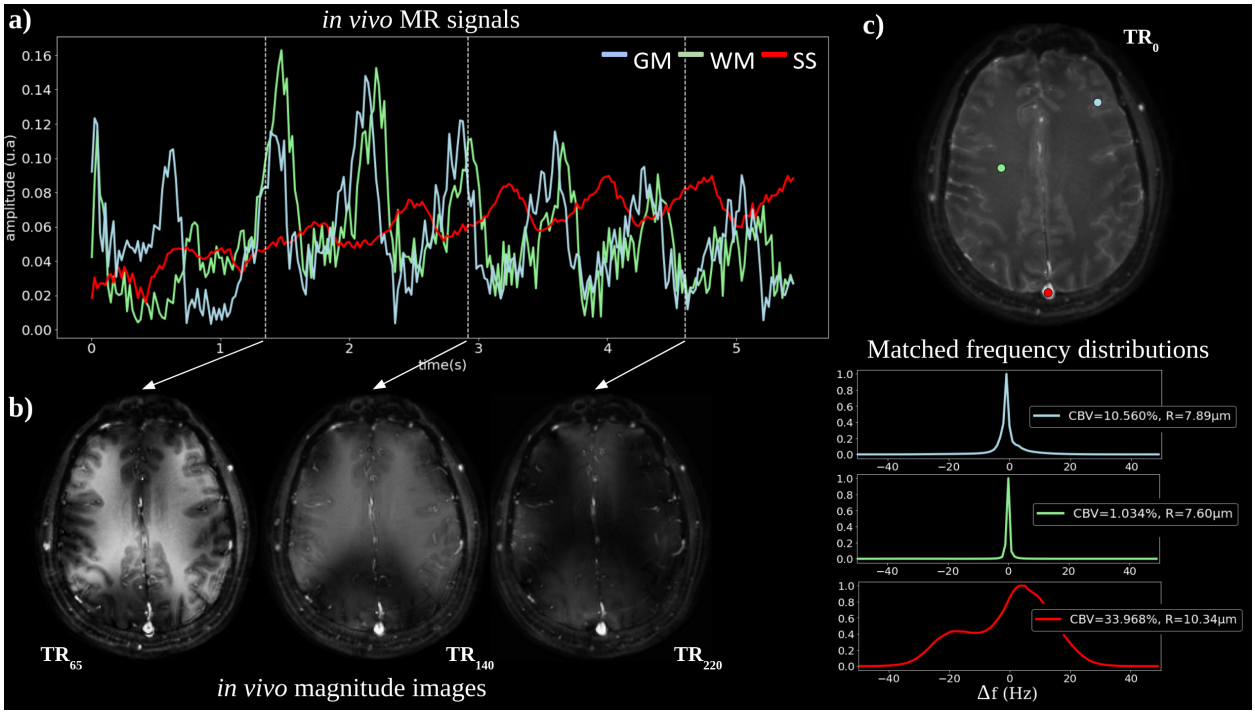


**Figure III.3.5**: a) Example of in-vivo MR signals in grey matter (blue), white matter (green), and sagittal sinus (red) regions in one healthy volunteer. b) Magnitude images from in-vivo acquisition for different times of the sequence. c) Matched frequency distributions for the 3 tissue signals located by dots on the $TR_0$ magnitude image above.

95% limits of agreement, and the solid green line indicates the mean bias. The scatter plot comparing $T_1$ values shows a strong correlation with data points clustering around the line of identity (red dashed line). This indicates that $T_1$ values from both sequences are generally in good agreement. Higher dispersion around the line of identity is seen in the upper limits of the $T_2$ scatter plot which suggests differences in the quantitative maps for high $T_2$ values as pointed out in Figure III.3.7d. Better delineation of the ventricles regions is observed with the MRF-bSSFP sequence. This is also shown by the noticeable spread around the bias in the BA plots for high $T_2$ estimates in both WM and GM. CBV maps show degraded quality with possible shim and spiral artifacts when approaching deeper brain regions. Large vascular structures are however still visible.

The ROI analysis for the 6 volunteers is summarized in Table III.1(mean ± standard error of the mean, N=6). Reference values obtained using the MRF IR-FISP sequence ($T_1$,$T_2$) and the MGRE sequence ($T_2^*$) are given for comparison. Ranges of values found in the literature are also given. The average measured GM/WM ratio for the CBV measurement over the six healthy volunteers is 1.91±0.31. Quantitative maps obtained for one slice of the six healthy volunteers are shown in Figure III.3.8. Literature values for $T_1$ and $T_2$ come from Wansapura et al. 1999; GJ et al. 2005; Lu et al. 2005; Jiang et al. 2015; Ma et al. 2013. Literature values for $T_2^*$ come from Ni et al. 2015; Peters et al. 2007. Literature values for CBV and R measurements come from Bjørnerud et al. 2010; Knutsson et al. 2014; Leenders et al. 1990; Liu et al. 2017; Uh et al. 2009; Sakai et al. 1985; Delphin et al. 2023.

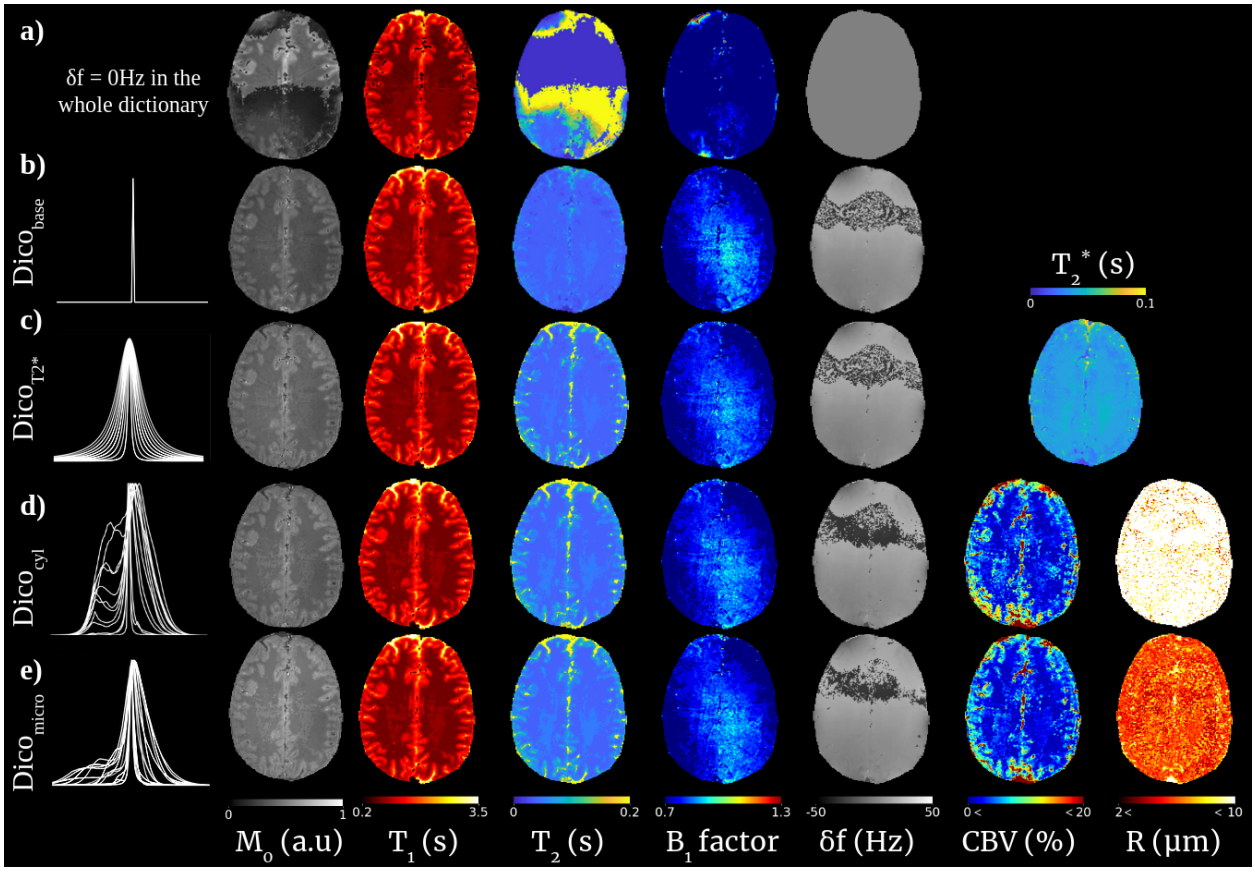


**Figure III.3.6**: Matching results for our MRF-bSSFP sequence with 5 different MRF dictionaries: a) defined on ($T_1$,$T_2$,$B_1$) parameters grid. b) defined on ($T_1$,$T_2$,$B_1$,$\delta f$) parameters grid. c) defined on ($T_1$,$T_2$,$B_1$,$\delta f$) parameter grid + Lorentzian distributions for $T_2^*$ estimate. d) defined on ($T_1$,$T_2$,$B_1$,$\delta f$) parameters grid + frequency distributions from 3D cylindrical vascular model. e) defined on ($T_1$,$T_2$,$B_1$,$\delta f$) parameters grid + 3D frequency distributions from microscopy vascular model.

**High resolution maps and other contributions** In Figure III.3.9a, we show the results obtained from the high-resolution cartesian MRF acquisition. The CBV map can be compared with and without taking into account an additional $B_0$ gradient dimension in the dictionary (see Section III.2 and Figure III.3.9b). Clear differences are observed in the white matter region and are highlighted by the black arrows. It is worth noting that the highest $B_0$ gradient values are mainly localized in the white matter region of the brain. Examples of magnetic fields' 2D $B_0$ spatial distributions and corresponding frequency distributions obtained in voxels containing vascular networks and one $B_0$ gradient are shown in Figure III.3.9c. Note that in Figure III.3.9b, only CBV and $B_0$ gradient estimates are shown, but the extended method allows the simultaneous estimate of $T_1$, $T_2$, $B_1$, $\delta f$, R, CBV, and $B_0$ gradient external contribution as well as $T_2^*$ maps if using the Lorentzian dictionary.

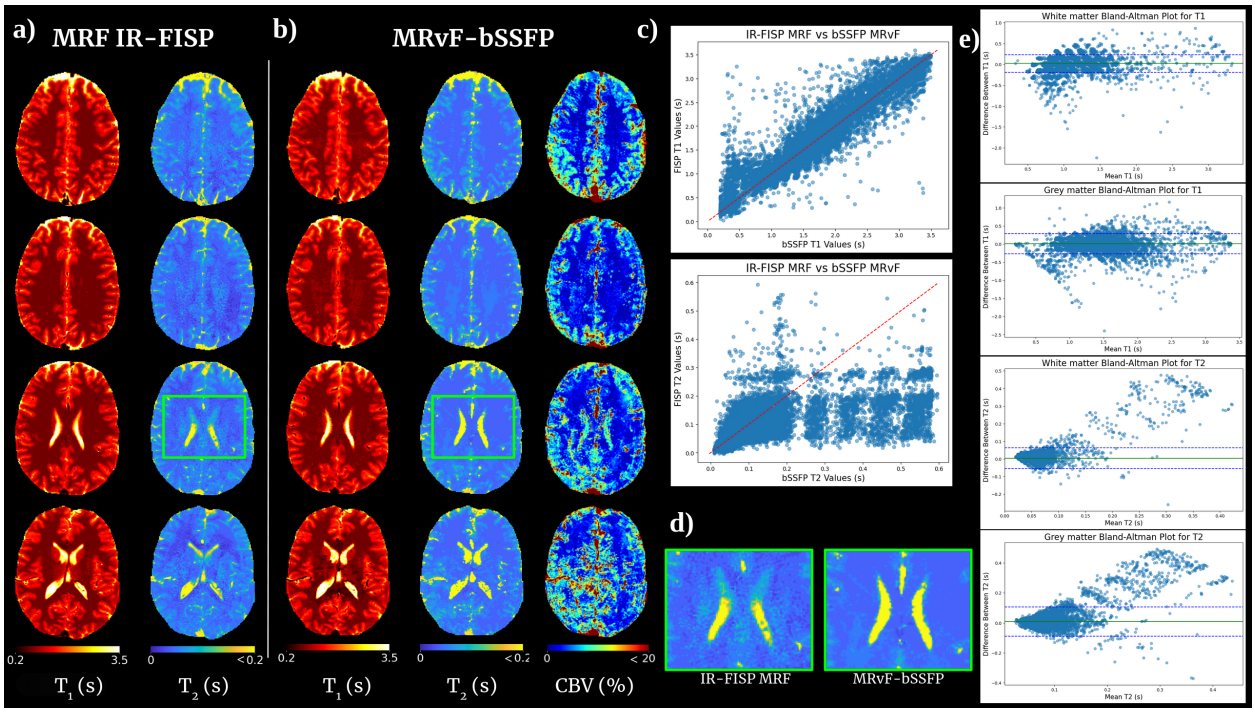


**Figure III.3.7**: Comparison between ($T_1$,$T_2$) estimates from standard MRF IR-FISP sequence (a) and our approach based on MRF-bSSFP (b). c) in-vivo results comparing MRF IR-FISP and MRF-bSSFP for all pixels $T_1$and $T_2$values. d) Focus on the ventricles regions in the $T_2$ estimates. e) Bland-Altman plots..

| Parameter | Tissue | MRF-bSSFP | References[1,2] | Litterature |
|---|---|---|---|---|
| $T_1$(ms) | WM | 943 ± 63 | 919 ± 44 | ∼ 790 – 1080 |
| | GM | 1334 ± 37 | 1341 ± 46 | ∼ 1180 – 1820 |
| $T_2$(ms) | WM | 47 ± 5 | 46 ± 3 | ∼ 56 – 84 |
| | GM | 68 ± 7 | 64 ± 4 | ∼ 70 – 130 |
| $T_2^*$(ms) | WM | 37 ± 2 | 49 ± 2 | ∼ 45 – 48 |
| | GM | 37 ± 2 | 51 ± 2 | ∼ 42 – 52 |
| CBV(%) | WM | 4.72 ± 0.87 | — | ∼ 1.7 – 3.6 |
| | GM | 8.65 ± 1.38 | — | ∼ 3.0 – 8.0 |
| | SS | 36.70 ± 2.87 | — | — |
| R($\mu$m) | WM | 5.85 ± 0.07 | — | 6.8 ± 0.3 |
| | GM | 6.27± 0.21 | — | 7.3 ± 0.3 |
| | SS | 10.20 ± 0.44 | — | — |

[1] $T_1$ and $T_2$ reference values were estimated from an MRF IR-FISP sequence.
[2] $T_2^*$ reference values were exponentially fitting from a multi-echo GRE sequence.

**Table III.1**: Region of interest analysis for *in vivo* $T_1$, $T_2$, $T_2^*$, CBV and R values.

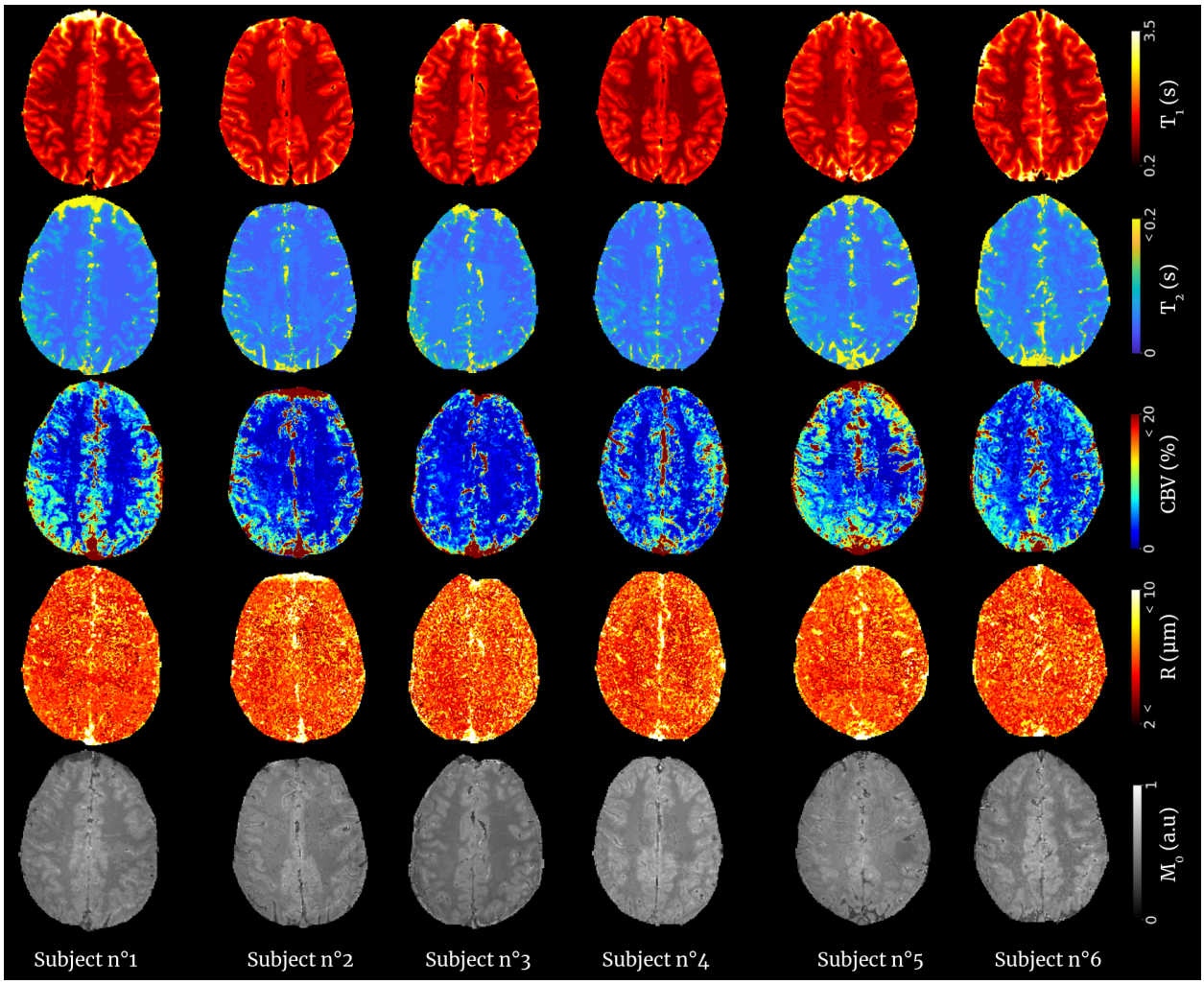


**Figure III.3.8**: *In vivo* quantitative maps for the 6 healthy volunteers of our study.

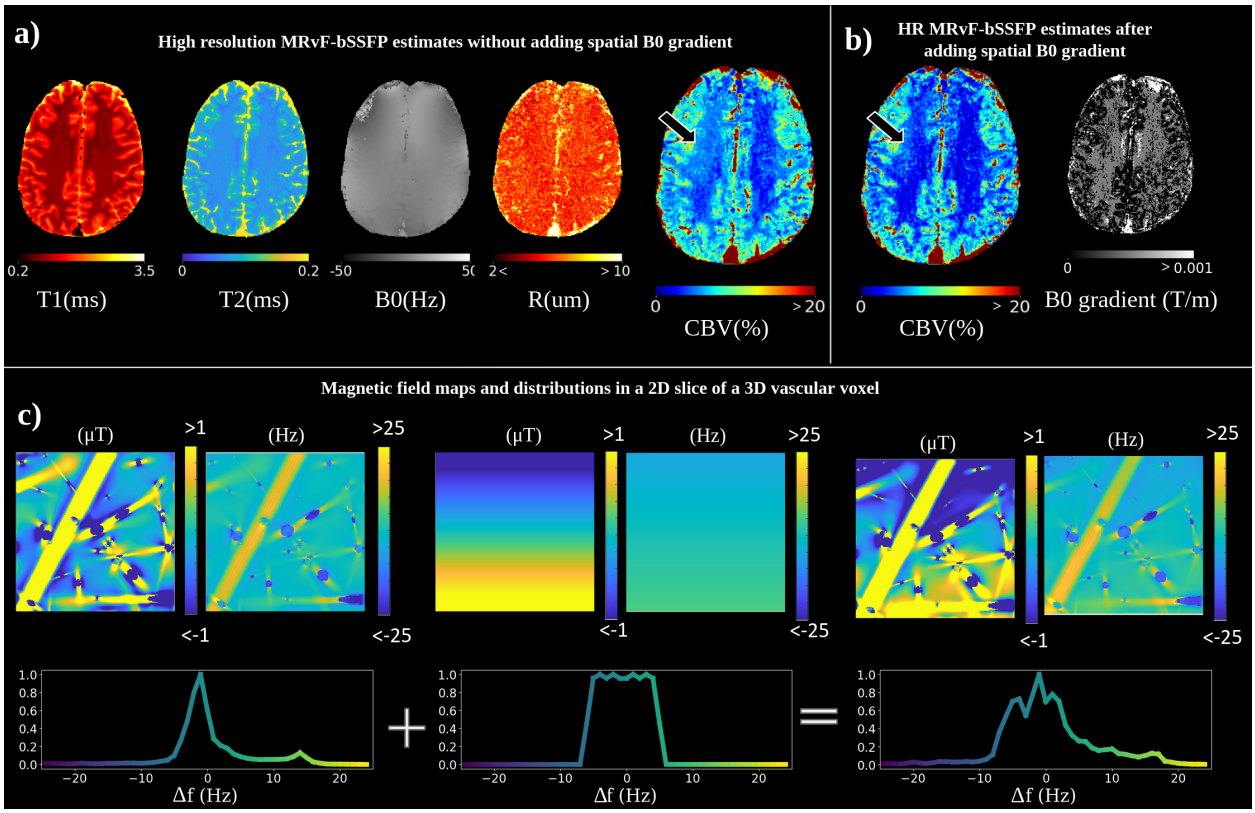


**Figure III.3.9**: a) MRF-bSSFP estimates for the 2D cartesian acquisition using intra-voxel magnetic field distributions where only blood vessels contribute to field inhomogeneities (c). Convoluting top-hat function on frequency distributions accounts for spatial $B_0$ gradient in the X-direction. Adding function FWHM parameters in the dictionary allows the estimates of this spatial $B_0$ gradient strength as shown in b).

## III.4 Discussion and Conclusions

In this work, we proposed a new contrast-free method for the simultaneous quantification of relaxometry, magnetic fields, and microvascular parameters using the sensitivity of bSSFP sequences to sub-voxel frequency distributions in both transient and steady-state regimes. Because numerous parameters can influence these MR signals, we analyzed our results using a High-Dimensional version of the MRF framework, using dictionaries that include simulations on realistic microvascular networks. Our preliminary results obtained in 6 healthy subjects compare well with standard MRF FISP $T_1$ and $T_2$ estimates and are in the range of reported relaxometry literature values. Strong contrast between CBV estimates in WM and GM and a CBV ratio of 1.91 between these regions were expected (Bjørnerud et al. 2010; Knutsson et al. 2014; Leenders et al. 1990; Liu et al. 2017; Uh et al. 2009; Sakai et al. 1985). Large values of CBV and R in voxels containing known large blood vessels are also encouraging. Results show good reproducibility of our findings across multiple subjects (see Figure III.3.8).

However, $T_2^*$ estimates using the MRF-bSSFP methods are higher than the $T_2^*$ values obtained using MGRE sequences, and quantitative values of CBV are on the high end of reported literature. Comparison of our technique against DSC in healthy tissues and lesions will be needed, although quantitative estimates of CBV using Gd injection might also be overestimated as shown by Wirestam et al. 2010. Pre-clinical studies in animal models of stroke or tumor could also be conducted, allowing comparison with steady-state perfusion measurements obtained with Ultra Small Particle of Iron Oxide (USPIO) CA as well as comparison with subsequent histological analysis (Valable et al. 2008). Changes in response to $CO_2$ gas challenges could also be used to induce temporal variations of CBV and oxygenation values.

Several optimizations are foreseeable. The model for MRvF simulations could be improved by adding additional magnetic field susceptibility sources. We already observed that simple additions of linear gradients in the dictionary had an impact on the vascular estimates. This could correspond to shim artifacts or the presence of myelin sheath in WM as it is suggested in Figure III.4.1 where we provide a comparison between "external $B_0$ gradient" maps and Myelin Water Fraction maps obtained using multi-compartment MRF using the reference spoiled sequence (see Chapter I). Myelin fibers are known to contribute to the magnetic susceptibility of tissues and thus modify the underlying magnetic field distribution (Chen et al. 2013; M et al. 2021). Intra-voxel frequency shifts can vary across different brain regions and have an impact on bSSFP frequency response profile asymmetries as shown by Miller et al. 2010. It could be possible to improve the simulations using higher-order shims and representations of microstructures in the virtual voxels. In the same way, nonheme iron in deep GM could be included. The vascular simulations could also be improved by considering realistic 3D networks from human brains and additional estimates such as vessel orientation and density could be considered.

Finally, dictionary matching could be improved by taking into account the actual RF pulse profile in the simulations. It has been shown in Ma et al. 2017; Buonincontri et al. 2016, and in the Chapter I of this manuscript, that including the slice profile effects in the dictionary simulations highly improves reconstructed maps quality for FISP-based sequences. This

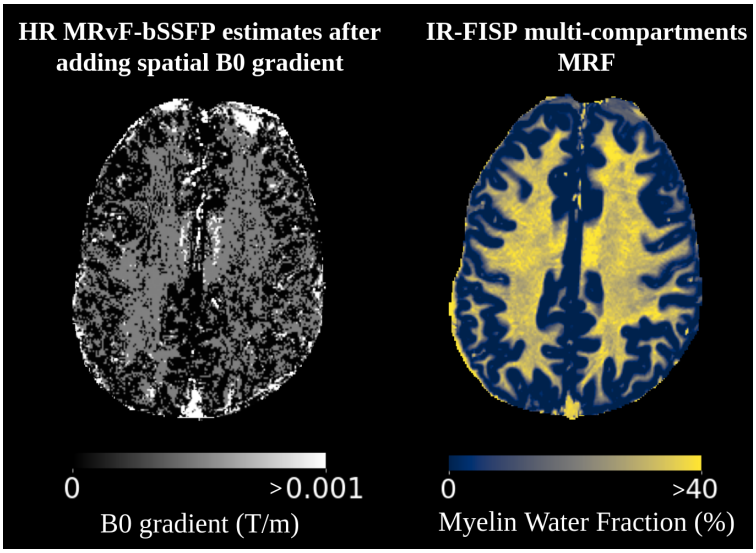


**Figure III.4.1**: Comparison between estimated $B_0$ gradient map from our proposed method and an MWF quantitative map computed with MC-MRF. Acquisitions have been made in 2D for one healthy volunteer.

could enhance the measurement of relaxometry parameters as well as intra-voxel parameters. In Figure III.4.2 and Table III.2, we show the impact of taking this slice profile effect into account before the convolution process. While interesting results can be observed on the $T_2^*$ maps compared to the 2D multi-echo GRE reference, the effect is only partially corrected as the bSSFP slice profile also depends on off-resonance as demonstrated by Staehle et al. 2008. Correctly incorporating RF profiles in our simulations would thus require a new type of efficient dictionary generation.

**Table III.2**: Region of interest analysis for *in vivo* $T_2^*$ values with and without SP effect simulations.

| Parameter | Tissue | No Slice Profile | Slice Profile | Reference |
|---|---|---|---|---|
| $T_2^*$ (ms) | WM | $37 \pm 2$ | $47 \pm 4$ | $49 \pm 2$ |
| | GM | $37 \pm 2$ | $51 \pm 3$ | $51 \pm 2$ |

$T_2^*$ reference values were exponentially fitting from a multi-echo GRE sequence.

Another way to improve the method is to work on data acquisition. In our proof of principle study, a 2D acquisition with high k-space sampling was chosen to avoid strong image artifacts. Long delays had to be put at the end of each spiral interleave to ensure the returns to equilibrium. A 3D version of the sequence with single shot acquisition would be much faster and would also avoid the need for above mentioned fastidious slice profile corrections. Yet, finding a better MRF acquisition pattern is not trivial given the high number of dimensions. Automatic procedures might be required (Lee et al. 2019; Cohen et al. 2017a; Coudert et al. 2022b; Jordan et al. 2021) and these algorithms could focus on optimized RF phase evolution that has already been shown to have a large impact in FISP sequences for diffusion or $T_1$ estimates. The influence of TR or the addition of multiple echoes could also be explored to

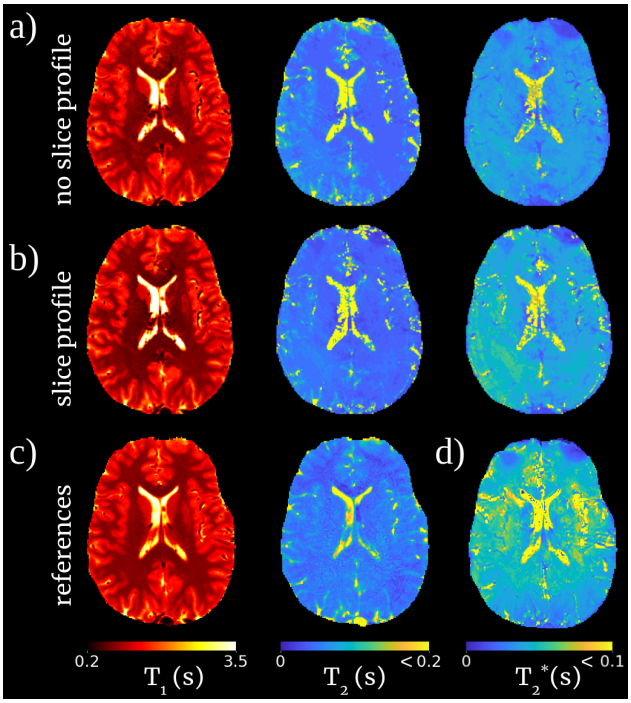


**Figure III.4.2**: *In vivo* 2D quantitative maps of one healthy volunteer of our study. The simulations for the matched dictionary have been made without slice profile (a), with slice profile (b), and are compared to the reference MRF-FISP sequence (c) and the fitting from an MGRE (d).

improve frequency distribution (see Schäper et al. 2022) or blood oxygenation sensitivities. However, one has to pay attention to the evolution of TR and FA which can also increase the sensitivity to water diffusion or magnetization transfer effects. In our first design, these contributions were minimized (III.2.1) using short TR, short TE, and low FA and allowed fast simulations that neglected the spatial arrangement of intra-voxel magnetic fields.

Given the potential new simulation models that would lead to larger dictionaries and longer MRF patterns for undersampled acquisition sequences, this High-Dimensional MRF reconstruction process might have to switch from simple dot product matching to deep learning reconstruction with data compression (Zhao et al. 2018). Yet, it has been shown that subspace reconstruction of bSSFP sequences is not trivial (McGivney et al. 2014), and special DL network architectures might be needed to handle the nonlinear signal variations and large dimensions of the dictionaries as proposed by our team (see Barrier, Antoine and Coudert, Thomas et al. 2024). Better reconstructions could also be obtained by using the complex data as input of the DL network (Lu et al. 2022) as the phase information in bSSFP experiments has been shown to influence the frequency profile asymmetry of the sequence as shown in Plähn et al. 2024.

It is important to note that, in this study, we were mainly focusing on deoxygenated blood, as the BOLD effect is primarily sensitive to changes in deoxyhemoglobin. By focusing on deoxyhemoglobin, our results rely on venous CBV, excluding arterial contributions. Once properly validated, our method could help clinical investigations of several cerebrovascular pathologies including stroke, or cancer.

# Chapter IV

# Development of Artificial Intelligence tools for High-Dimensional MRF reconstructions

This chapter introduces advanced reconstruction methods developed during this thesis to manage the curse of dimensionality brought by High-Dimensional MRF. Relying on the optimized sequence design and the new reconstruction methods proposed in the previous chapters, two methods are introduced.

First, a dictionary compression method with an advanced low-rank representation of the MRF dictionaries has been developed in collaboration with Geoffroy Oudoumanessah, PhD student, and statistician in the Statify team (INRIA). This work led to the preparation of a conference paper: Cluster Globally, Reduce Locally: Scalable Efficient Dictionary Compression for Magnetic Resonance Fingerprinting where the statistical material and methods were the focus of Geoffroy. It will be submitted at the *2025 IEEE 22nd International Symposium on Biomedical Imaging (ISBI)* and extended for submission as a research paper in *Annals of Applied Statistics* where I am the second author.

Second, an advanced deep-learning reconstruction method that surpasses traditional dictionary matching and has led to an accepted paper in the *Medical Image Computing and Computer Assisted Intervention (MICCAI) 2024* conference, as a co-primary author with Dr. Antoine Barrier, postdoctoral student in the team, and mathematician. This paper named MARVEL: MR Fingerprinting with Additional micRoVascular Estimates using bidirectional LSTMs will also be published in the *Springer Lecture Notes in Computer Science (LNCS)* after the meeting.

## Contents

# IV.1 Introduction

In the previous chapters of this manuscript, we showed the potential of the use of MR Fingerprinting methods combined with bSSFP sequences for the estimations of relaxometry tissue parameters as well as microvascular properties in the human brain, without the need for contrast agent injection.

As detailed in Chapter III, these estimates imply the generation of billion-entries MRF dictionaries. For sequences with hundreds of time points, it means a storage capacity of more than the terabyte to store the dictionary and an incredibly time-consuming reconstruction process implying memory-greedy operations. To tackle this, our first approach implies an on-the-fly process where the dictionary search is made in a batched subdictionary that is simulated during the reconstruction process and accounts for only a few intra-voxel distributions. In the end, the best-matched result overall subdictionaries is kept for each *in vivo* fingerprint. A schematic illustration of this process is shown in Figure IV.1.1.

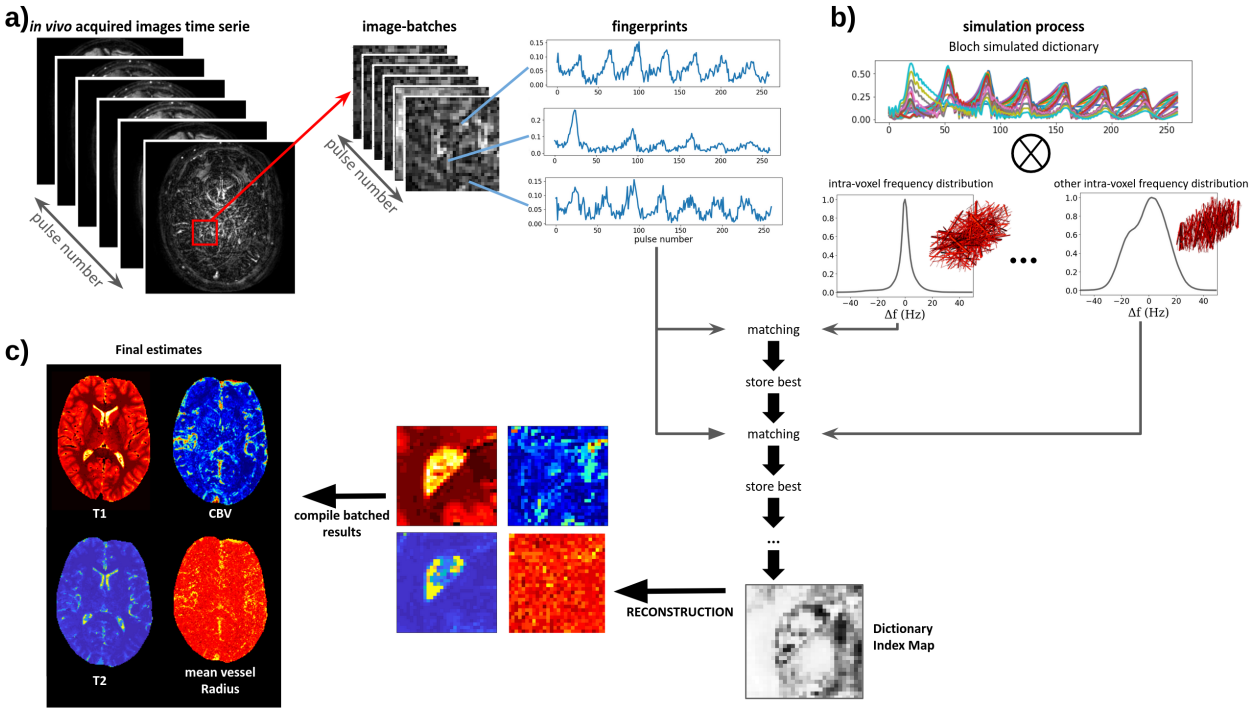


**Figure IV.1.1**: Schematic illustration of the on-the-fly matching/simulating process. a) *in vivo* acquisition images are batched and time-resolved fingerprints are extracted b) *in silico* simulations are computed using few intra-voxel frequency distributions at the same time. The Bloch dictionary convolved with distributions is then used for matching with the fingerprints, resulting in an indexes map that is used for the reconstruction of c) batched parameters maps that are compiled to retrieve full maps.

This innovative MRF reconstruction method reduces memory capacity needs by never computing the whole billion-entries dictionary in one go. Still, it greatly increases reconstruction time and limits clinical applications as numerical simulations imply computing resources.

In this chapter, two families of advanced reconstruction methods are proposed to overcome these limitations. On the one hand, the first solution focuses on the reduction of the

dictionary dimension using a low-rank representation of the dictionary space, reducing memory requirements and accelerating the matching process. As a proof of concept, this part is focused on $T_2^*$ estimates considering Lorentzian frequency distributions (see Chapter III) but the extension to microvascular estimates is rather straightforward and will be explored in the future. On the other hand, recent advances propose the use of deep learning surrogates for both simulations and matching processes allowing direct reconstruction of acquired images into parameter maps, providing very fast inference in a computing-cheap fashion. We developed a Bidirectional Long Short-Term Memory (BiLSTM) network for the direct estimation of relaxometry and microvascular parameters from bSSFP *in vivo* fingerprints.

## IV.2 A machine learning model for large dictionaries compression

### IV.2.1 Introduction

As shown in previous chapters of this manuscript, MRF relies on large signal dictionaries, often requiring dimensionality reduction for practical use. Standard compression methods, such as SVD (see Chapter I Section I.4), have been successfully applied to spoiled FISP sequences, reducing dictionary size by projecting signals into a low-dimensional subspace without compromising map quality. However, sequences like bSSFP are sensitive to numerous tissue parameters, demanding a larger number of bases for accurate signal projection, as noted by McGivney et al. 2014 and confirmed in our experiments. This makes traditional SVD computationally expensive, especially for large dictionaries, as highlighted by Yang et al. 2018, who proposed randomized SVD to address memory constraints. Other approaches, such as non-Euclidean analyses of dictionary spaces (Li et al. 2023), further improve dimensionality reduction.

While dictionary compression techniques have made strides in reducing size, the computational complexity of matching remains a significant barrier to clinical implementation. One approach to tackle this involves partitioning the dictionary into clusters before reducing the dimension, as shown by Cauley et al. 2015, who used K-way clustering followed by Principal Component Analysis (PCA) within each cluster. This reduces the matching complexity by first identifying the signal's cluster, and then applying a cluster-specific projection. More recently, Ullah et al. 2023 proposed a faster matching strategy by applying clustering and using GPUs for dictionary matching, although challenges persist when dealing with large numbers of parameters.

Whereas reducing the dimension of high-dimensional dictionaries often assumes that most of the information in the signals can be captured and represented in a single lower-dimensional subspace, more flexible approaches, such as mixtures of factor analyzers (MFA, McLachlan et al. 2003) and mixtures of PPCA (MPPCA, Tipping et al. 1999), allow for different dimensional subspaces to capture signal variability. High-Dimensional Gaussian Mixture Models (HD-GMM, Bouveyron et al. 2014) generalize these models by clustering the data into multiple subspaces of varying dimensions, enabling simultaneous compression and clustering. However, these methods are often designed for batch data, making them inefficient for

large-scale MRF dictionaries due to hardware limitations. Approaches like down-sampling risk losing important information, while incremental methods, also referred to as online, allow for sequential processing of data in smaller groups, as seen in SHASTA-PCA (Gilman et al. 2023) and reviewed by Balzano et al. 2018. However, incremental methods for mixture models are less developed, even if a preliminary attempt for an incremental MPPCA can be found in Bellas et al. 2013.

In this work, considering dictionaries both large in size and dimension, our proposal is twofold. Building on HD-GMM, we showed how they can simultaneously compress and cluster large-scale high-dimensional MRF dictionaries. We then derived a new incremental (or online) algorithm, based on a principled Expectation-Maximization (EM) framework (McLachlan et al. 2008), to learn such a model from very large data sets. We demonstrated the effectiveness of our approach on MRF reconstruction, showing results comparable to the high-dimensional dictionary matching referred to as *full-matching* in the next sections. This approach allows us to exceed the resolution and size used in current implementations and to reconstruct a larger number of MR parameter maps with improved accuracy, making the clinical application of MRF closer. In line with Golbabaee et al. 2019, we also proposed to enhance previous work by Boux et al. 2021, training multiple clustered GLLiM models on the clustered dimensionally reduced dictionary with HD-GMM, demonstrating that combining our model with regression models improves MRF reconstruction methods.

## IV.2.2 Material and methods

### IV.2.2.1 HD-GMM model

**Identifying group-wise subspaces.** The HD-GMM model assumes that observations are *i.i.d.* realizations of a random variable $\mathbf{y}$, which follows a Gaussian mixture model (GMM) with $K$ components:

$$p(\mathbf{y};\boldsymbol{\theta}) = \sum_{k=1}^{K} \pi_k \mathcal{N}_M(\mathbf{y};\boldsymbol{\mu}_k,\boldsymbol{\Sigma}_k), \tag{IV.2.1}$$

where $\mathcal{N}_M$ denotes the $M$-dimensional Gaussian distribution with mean $\boldsymbol{\mu}_k$, covariance $\boldsymbol{\Sigma}_k$, and $\pi_k$ the mixture weight.

Similarly to what has been introduced in Chapter I Section I.4, since most parameters are contained in the covariance matrices, efficient parameter reduction can be obtained using the eigendecomposition $\boldsymbol{\Sigma}_k = \boldsymbol{D}_k \boldsymbol{A}_k \boldsymbol{D}_k^T$, where $\boldsymbol{D}_k$ is the orthonormal $M \times M$ matrix containing the eigenvectors $\{\boldsymbol{d}_1, \ldots, \boldsymbol{d}_M\}$ of $\boldsymbol{\Sigma}_k$, and $\boldsymbol{A}_k$ is a diagonal matrix containing its eigenvalues, for cluster $k$.

In HD-GMM, each $\boldsymbol{A}_k$ consists of only $d_k + 1$ different eigenvalues:

$$\boldsymbol{A}_k = \mathrm{diag}(a_{k1}, \ldots, a_{kd_k}, b_k, \ldots, b_k),$$

with $a_{kj} > b_k$, for $j = 1 : d_k$, where $d_k \in \{1, \ldots, M-1\}$ is the number of dominant eigenvalues for cluster k, that can vary between clusters but fixed in our work to a user-decided dimension $d$.

The HD-GMM model reduces the complexity of the covariance matrix by assuming that the data in each cluster $k$ lies primarily in a lower-dimensional subspace, spanned by the first $d$ eigenvectors (which correspond to the eigenvalues $a_{k1},\ldots,a_{kd}$). In directions orthogonal to this subspace (i.e., in the less significant dimensions), the model assumes that the variance is isotropic—meaning it is the same in all those directions.

This isotropic assumption simplifies the model significantly by treating the remaining dimensions equally. Since the remaining directions are assumed to have the same variance (isotropy), the eigenvalues corresponding to those dimensions are set equal to $b_k$. This isotropic assumption is a common simplification in high-dimensional models where we aim to capture the primary variance and treat the residual noise as uniform. When $b_k$ is negligible, this parameterization implies that the noise variance is contained in a subspace $\mathbb{E}_k^{\perp}$, orthogonal to a group-specific subspace $\mathbb{E}_k$, parameterized by the $d$ eigenvectors associated with the first $d$ eigenvalues $\{a_{k1},\ldots,a_{kd}\}$. The subspace $\mathbb{E}_k$ captures the main cluster shape (see Figure IV.2.1 for an illustration).

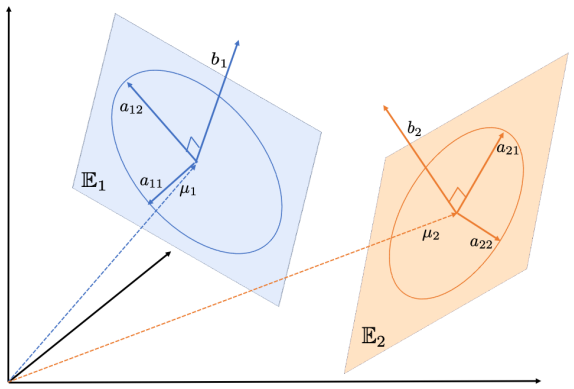


**Figure IV.2.1**: HD-GMM schematic illustration, from the original space of dimension $D = 3$, $K = 2$ clusters of dimension $d = 2$ are computed.

The model parameters are then $\boldsymbol{\theta} = \{\boldsymbol{\theta}_k, k = 1 : K\}$, where $\boldsymbol{\theta}_k = \{\pi_k, \boldsymbol{\mu}_k, \boldsymbol{A}_k, \boldsymbol{D}_k\}$ for each cluster. These can be estimated using an EM algorithm (Bouveyron et al. 2007). When $d \ll M$, significant computational gains can be achieved.

In the EM, there are two steps:

- In the E step, we compute the expected log-likelihood of the data given the current model parameters. This quantity implies the computing of a distance which is rather expansive because it implies the computation of every eigenvalue of $\boldsymbol{A}_k$.
- In the M step, we update the parameters (means, covariances, and mixing coefficients) to maximize the likelihood computed in the E step.

To deal efficiently with the distance needed for the computation of the log in the E step, we focused on a reduced-dimensional representation. Let $\widetilde{\boldsymbol{D}}_k$ consist of the first $d$ columns of

$\boldsymbol{D}_k$, supplemented by $(M-d)$ zero columns, and $\overline{\boldsymbol{D}}_k = (\boldsymbol{D}_k - \widetilde{\boldsymbol{D}}_k)$ is the remaining features. Then, the projections of $\mathbf{y}$ on $\mathbb{E}_k$ and $\mathbb{E}_k^{\perp}$ are defined as:

$$P_k(\mathbf{y}) = \widetilde{\boldsymbol{D}}_k \widetilde{\boldsymbol{D}}_k^T(\mathbf{y} - \boldsymbol{\mu}_k) + \boldsymbol{\mu}_k,$$

$$P_k^{\perp}(\mathbf{y}) = \overline{\boldsymbol{D}}_k \overline{\boldsymbol{D}}_k^T(\mathbf{y} - \boldsymbol{\mu}_k) + \boldsymbol{\mu}_k.$$

The distance could then be written in the form:

$$\begin{aligned}(\mathbf{y} - \boldsymbol{\mu}_k)\boldsymbol{D}_k \boldsymbol{A}_k^{-1} \boldsymbol{D}_k^T(\mathbf{y} - \boldsymbol{\mu}_k) =& (\mathbf{y} - \boldsymbol{\mu}_k)^T \widetilde{\boldsymbol{D}}_k \boldsymbol{A}_k^{-1} \widetilde{\boldsymbol{D}}_k^T(\mathbf{y} - \boldsymbol{\mu}_k) \\ &+ (\mathbf{y} - \boldsymbol{\mu}_k)^T \overline{\boldsymbol{D}}_k \boldsymbol{A}_k^{-1} \overline{\boldsymbol{D}}_k^T(\mathbf{y} - \boldsymbol{\mu}_k) \\ =& \|\boldsymbol{\mu}_k - P_k(\mathbf{y})\|^2_{\widetilde{\boldsymbol{\Sigma}}_k^{-1}} + \frac{1}{b_k}\|\mathbf{y} - P_k(\mathbf{y})\|^2, \end{aligned} \tag{IV.2.2}$$

where $\|.\|^2_{\widetilde{\boldsymbol{\Sigma}}_k^{-1}}$ is the norm defined by $\|\mathbf{y}\|^2_{\widetilde{\boldsymbol{\Sigma}}_k^{-1}} = \mathbf{y}^T \widetilde{\boldsymbol{\Sigma}}_k^{-1} \mathbf{y}$ with $\widetilde{\boldsymbol{\Sigma}}_k^{-1} = \widetilde{\boldsymbol{D}}_k \boldsymbol{A}_k^{-1} \widetilde{\boldsymbol{D}}_k^T$.

Equation (IV.2.2) uses the definitions of $P_k$ and $P_k^{\perp}$, along with the fact that $\|\boldsymbol{\mu}_k - P_k^{\perp}(\mathbf{y})\|^2 = \|\mathbf{y} - P_k(\mathbf{y})\|^2$. The formula effectively calculates how far $\mathbf{y}$ is from the mean $\boldsymbol{\mu}_k$ of the $k$-th Gaussian component, adjusted for the covariance structure of the Gaussian.

By breaking down the distance calculation into a sum of two terms, one related to the projection and one to the residual distance, we simplified the problem by focusing only on the most important features (in $\widetilde{\boldsymbol{D}}_k$). This reduces the amount of computation required and speeds up the process because (IV.2.2) does not depend on $P_k^{\perp}$ and thus does not require computing the last $(M-d)$ columns of $\boldsymbol{D}_k$, the eigenvectors associated with the smallest eigenvalues. Similarly, determinants can be efficiently computed as:

$$\log(|\boldsymbol{\Sigma}_k|) = \sum_{j=1}^{d} \log(a_{kj}) + (M-d)\log(b_k).$$

Determinants help us understand the volume of the space covered by the Gaussian.

This parameterization allows for the efficient handling of high-dimensional data. However, it does not provide a lower-dimensional representation of the data. While such a reduced-dimensional representation may not always be needed, it can be crucial when dealing with hardware or software limitations. Originally, HD-GMM was not designed for this situation.

The next paragraph describes how HD-GMM can be further exploited as a dimensionality reduction technique.

**Cluster-wise dimension reduction.** As clustering models, HD-GMM provides a probability $r_k(\mathbf{y})$ that any possible observation $\mathbf{y}$ is assigned to cluster $k$ for each $k = 1 : K$. Denote $\widetilde{\boldsymbol{D}}_k^*$ as the $M \times d$ matrix built with the first $d$ columns of $\boldsymbol{D}_k$, orthonormal vectors by construction.

A reduced-dimensionality representation $\widehat{\mathbf{y}}_k$ of $\mathbf{y}$ can then be obtained, for each of the $K$ different subspaces, by computing the scalar products of a centered $\mathbf{y}$ with the columns of $\widetilde{\boldsymbol{D}}_k^*$. This results in:

$$\widehat{\mathbf{y}}_k = S_k(\mathbf{y}) = \widetilde{\boldsymbol{D}}_k^{*T}(\mathbf{y} - \boldsymbol{\mu}_k),$$

while its reconstruction $\widetilde{\mathbf{y}}_k$ in the original space is given by:

$$\widetilde{\mathbf{y}}_k = \widetilde{\boldsymbol{D}}_k^* \widehat{\mathbf{y}}_k + \boldsymbol{\mu}_k.$$

In practice, it is reasonable to use as a reduced-dimensionality representation of $\mathbf{y}$ only the one corresponding to the most probable group $k$, *i.e.*, with the highest $r_k(\mathbf{y})$. This means we first determined which cluster is most likely for $\mathbf{y}$ and then used the reduced-dimensionality representation for that specific cluster.

In this setting, HD-GMM acts as a divide-and-conquer paradigm by initially clustering the data into $K$ clusters and then performing cluster-specific data reduction:

- *Divide Step*: Data (MRF dictionary signals for example) is clustered into K groups. This clustering helps in applying dimensionality reduction more effectively within each cluster, rather than trying to reduce dimensions for the entire high-dimensional dataset at once.
- *Conquer Step*: For new observations, the cluster assignment probabilities are used to determine the most appropriate reduced-dimensionality representation. This approach minimizes the loss of information because each cluster's reduced representation is optimized for that specific cluster.

However, for subsequent processing (such as MRF dictionary matching for example), it is important to keep track of clustering information for each observation. The reduced representations cannot be pooled back together, as they are likely to become indistinguishable across clusters. As summarized in Algorithm 1, each reduced cluster needs to be matched separately. This algorithm details the process with its application on MRF dictionary reduction.

**Algorithm 1** Divide & Conquer high dimensional regression of large data volumes

1: **Clusterisation and dimensionality reduction of the dictionary:** MRF dictionary of signals $\mathbf{X}_N = \{\mathbf{x}_i\}_{i=1:N}$, with associated tissue parameters $\mathbf{Y}_N = \{\mathbf{y}_i\}_{i=1:N}$, with $\mathbf{y}_i \in \mathbb{R}^D, \mathbf{x}_i \in \mathbb{R}^N, D \gg 1, N \gg 1$

2: **Online HD-GMM:** $\mathbf{X}_N$ is divided into $K$ clusters, of dimension $d < D \implies$ cluster assignment probabilities and cluster-wise projections of the MRF dictionary signals in the maximum probability cluster$(\mathbf{r}, \mathbf{S}) = \{r_k(\cdot), S_k(\cdot)\}_{k=1:K}$

3: **Cluster-wise reductions:** Compute $(\boldsymbol{r}, \boldsymbol{S})$ with the signals from the MRF acquisition $\widetilde{\mathbf{X}}_M = \{\widetilde{\mathbf{x}}_i\}_{i=1:M}$, $\widetilde{\mathbf{x}}_i \in \mathbb{R}^D$ to obtain the projection $\widehat{\widetilde{\mathbf{X}}}_k$ for each cluster $k \in 1:K$, as done for the MRF dictionary.

4: **Hierarchical Matching based on the clusters:** For each cluster $k \in 1:K$, for $\widehat{\widetilde{\mathbf{x}}}_i \in \widehat{\widetilde{\mathbf{X}}}_k$ compute idx $= \arg\max_{\widehat{\mathbf{x}} \in \widehat{\mathbf{X}}_k} \widehat{\widetilde{\mathbf{x}}}_i \cdot \widehat{\mathbf{x}}$ (standard MRF matching with inner-product approach, between compressed signal) and set $\widetilde{\mathbf{y}}_i = \mathbf{Y}_N[\text{idx}]$ to retrieve matched tissue parameters

5: **return** the matched parameters for the acquisition and **reconstruct** the MRF maps.

**Incremental learning for high-dimensional MRF dictionaries.** In handling large datasets, particularly in high-dimensional settings like high-dimensional Gaussian Mixture Models (HD-GMM), direct optimization can be challenging due to memory constraints. To address this, incremental learning techniques are employed, which process data in smaller, manageable batches rather than all at once.

*We are not going to detail the advanced computation between this, but only want to notice that this problem has been tackled by the INRIA Statify team and Geoffroy Oudoumanessah to handle large MRF dictionaries.*

An incremental variant of the Expectation-Maximization (EM) algorithm, known as online EM (In handling large datasets, particularly in high-dimensional settings like high-dimensional Gaussian Mixture Models (HD-GMM), direct optimization can be challenging due to memory constraints. To address this, incremental learning techniques are employed (Fort et al. 2020; Nguyen et al. 2020; Oudoumanessah et al. 2023), which process data in smaller, manageable batches rather than all at once. An incremental variant of the EM algorithm, known as online EM (Cappé et al. 2009), is particularly useful here. This method updates the model parameters as new data arrives, making it feasible to handle very large datasets efficiently.

By leveraging the exponential family form of the Gaussian mixture model, which simplifies the update process, and using specialized optimization techniques (like Riemannian optimization) for high-dimensional parameter updates, the online EM algorithm effectively manages large-

scale data while maintaining computational efficiency. This approach ensures that we can process and learn from high-dimensional MRF dictionaries.

#### IV.2.2.2 Application to MR Fingerprinting

**MRF acquisition** *In vivo*, acquisitions were performed on one healthy volunteer using a 32-channel head receiver array on a Philips 3T Achieva dStream MRI at the IRMaGe facility (MAP-IRMaGe protocol, NCT05036629). This study was approved by the ethics committee and informed consent was obtained from all volunteers before image acquisition. The imaging pulse sequence was based on the optimal MRF-bSSFP design from Chapitre III. 260 repetitions were acquired (TR=21 ms, TE=4 ms) with FA linearly increasing from 7° to 70° and a quadratic phase cycle of 10° increments with additional $(0, \pi)$ cycling between subsequent acquisitions. For our proof of principle study, the acquisition was performed using cartesian sampling with compressed sense factor or 3, matrix size=256x256x1, voxel size=0.78x0.78x3.00mm$^3$ for a total scan duration of 12 minutes per slice.

In an extended paper, we also applied the proposed method on the same 6 healthy volunteers as in Chapter III, where data were acquired under spiral undersampling. However, the method was modified and improved, notably regarding the dimensions of the obtained clusters. This is considered out of the scope of this manuscript and will not be detailed here.

**MRF dictionary** In this study, we used the two-step dictionary generation process from Chapter III using Lorentzian off-resonance frequency distributions to obtain the $T_2{}^*$ parameter dimension in the final expanded dictionary. Simulations were performed at magnetic field of strength of 3.0T with 20 $T_1$ values (0.2 to 3.5s), 20 $T_2$ values (10 to 600ms), 10 $B_1$ values (0.7 to 1.2) and frequency offset $\delta f$ values (from -50 to 49 Hz with an increment of 1 Hz), keeping only signals for which $T_1 > T_2$, resulting in a $390,000$ entries dictionary. Then, 20 Lorentzian distributions of full width at half maximum (FWHM) varying between 1 and 20 Hz were used for the weighting, leading to a total of 4,680,000 entries (*i.e.* series of 260 time-points) after the selection of signals in the range $-30 < \delta f < 30$Hz.

**Model selection and initialization** All processing was performed with Python using the JAX library. The only two hyperparameters we needed to set in the HD-GMM are the number of components in the mixture $K$ and the desired dimension vector $\boldsymbol{d}$. Usually, for mixture models, the number of components is selected using the Bayesian Information Criterion (BIC) Schwarz 1978, which requires running multiple models with varying $K$ values and finding the elbow or the minimum of the BIC curve. The desired dimension vector $\boldsymbol{d}$ is automatically set later during the initialization of the parameters which makes the number of components $K$ the only parameter that the user needs to set prior to the online-EM algorithm. In our case, the BIC gives $K = 30$ and $d = 10$. For initializing our EM algorithm, we used the heuristic mentioned in Hong et al. 2021 Section 3.5, which provides good performance for our approach too.

**Reconstruction** Once the model is trained, we compressed the dictionary from 20Gb of signal with a dimension of 260 to 400Mb of signal with a dimension of $d = 10$. Consequently, this compressed dictionary was used for efficient matching according to Algorithm 1 for

reconstructing MRF data. As the acquired *in vivo* fingerprints were also passed through the compression algorithm, they were assigned to one of the clusters of the low-rank dictionary space. This pre-clusterization already sorts the fingerprints according to the signal shape, providing supplementary information, and allowing a hierarchical matching of the MRF data in each cluster. This accelerates the matching process in the same fashion as the $B_1$ constraint MRF method proposed in Chapter I Section I.3.2 of the manuscript.

In this study, *full matching* maps were used as reference maps, although it has obvious limits in terms of hardware and robustness to noise.

Finally, we also tried to reconstruct MRF data based on the DRONE model (Cohen et al. 2017b), a 4-layer fully connected NN -initially developed for small-dimension relaxometry MRF- and with a combination of the HD-GMM reduction and the Bayesian learning model referred to as GLLiM Boux et al. 2021; Deleforge et al. 2015. The GLLiM model corresponds to a regression model for which a number of Gaussian components need to be chosen and is set to $K_g = 50$.

### IV.2.3 Results

Reconstructed maps results are shown for reduced dictionary representations, using either SVD with $d = 10$ (Figure IV.2.2 line 2) or HD-GMM with $d = 10$ and $K = 30$ (Algorithm 1, lines 2-3 and Figure IV.2.2 line 4). Machine learning-based reconstructions are also shown in Figure IV.2.2 line 3 and 5 respectively.

Figure IV.2.3 completes the comparison with absolute error maps with respect to the full matching, for $T_2^*$.

Figures IV.2.2 and IV.2.3 clearly show that both SVD and DRONE provide unsatisfying maps, *e.g.* for $T_2$ and $T_2^*$. The HD-GMM approach is visually similar to full matching. Its combination with GLLiM provides close to full matching and more spatially homogeneous maps, despite some remaining "shim" artifacts that we interpreted as learning bias due to the high cross-correlation between $\delta f$ nominal value and the resulting $T_2^*$ value. A zoom on $T_1$ maps is provided for comparison in Figure IV.2.4, where the small artifacts in the matching-based map, due to the high undersampling of the MR acquisition, are smoothed with learning.

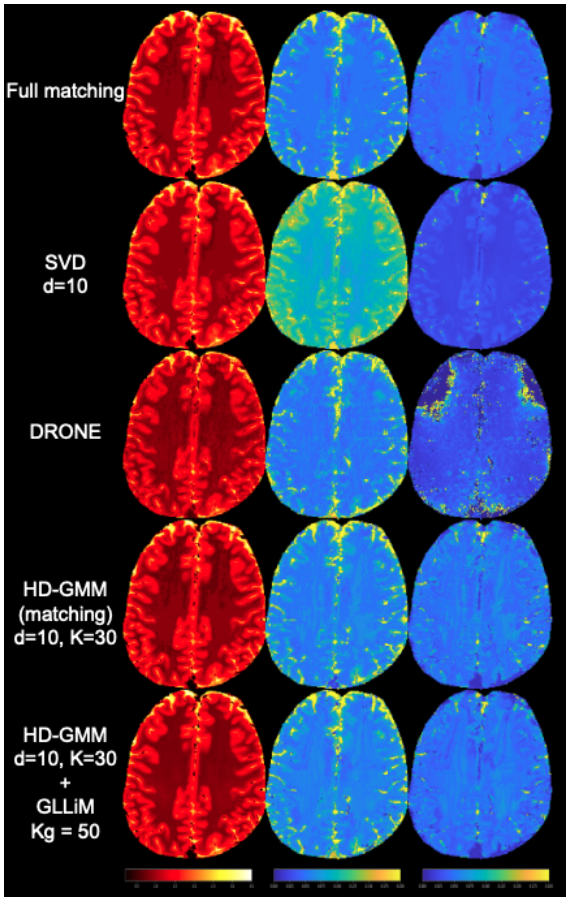


**Figure IV.2.2**: $T_1$, $T_2$, $T_2^*$ reconstructed maps (columns) using matching in original MRF dictionary (first line), SVD compressed (second) or HD-GMM compressed (fourth). Machine learning reconstructed maps are also shown, using DRONE (third line) or the previously proposed GLLiM method (last line).

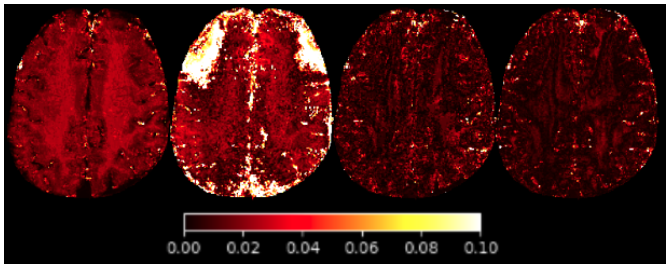


**Figure IV.2.3**: $T_2^*$ absolute error maps, for SVD, DRONE, HD-GMM and HD-GMM + GLLiM ($d = 10$, $K = 30$, $K_g = 50$).

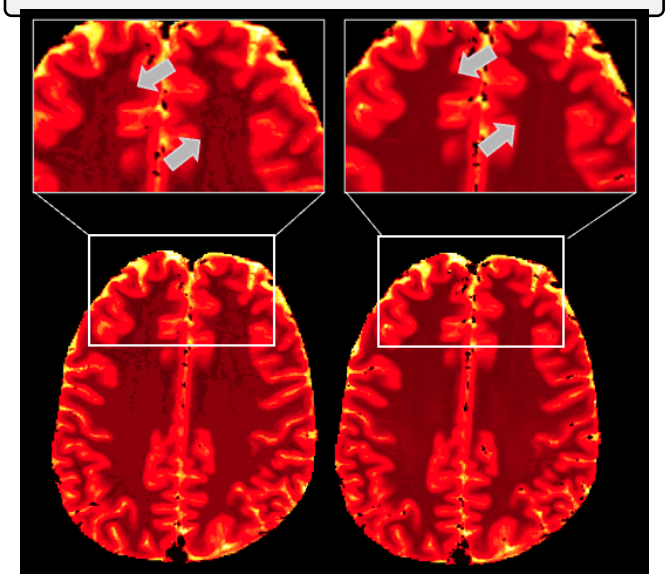

**Figure IV.2.4**: $T_1$ map homogeneity of HD-GMM + GLLiM (right) *vs* full matching (left).

HD-GMM's superior performance is underlined quantitatively in Table IV.1 where the Mean Absolute Error (MAE), over all voxels, with respect to full matching is shown for all 5 parameters. In Table IV.1, MAEs are computed with respect to imperfect still noisy full matching maps, which explains why the GLLiM variant of HD-GMM does not provide the lowest MAE despite more satisfying maps in terms of spatial homogeneity.

| Method | $T_1$ (s) | $T_2$ (s) | $T_2^*$ (s) | $\delta f$ (Hz) | $B_1$ sensitivity |
|---|---|---|---|---|---|
| DRONE Cohen et al. 2017b | 0.14 | 0.022 | 0.096 | 5.0 | 5.5 |
| SVD McGivney et al. 2014 | **0.056** | 0.047 | 0.018 | 1.4 | 0.1 |
| HD-GMM + matching | 0.058 | **0.016** | **0.010** | **1.0** | **0.04** |
| HD-GMM + GLLiM Deleforge et al. 2015; Boux et al. 2021 | 0.081 | 0.019 | 0.012 | 1.3 | 0.05 |

**Table IV.1**: MAEs over voxels, with respect to full matching, for DRONE, SVD ($d = 10$), and HD-GMM ($d = 10$, $K = 30$, $K_g = 50$). Best values in bold.

Another quantitative comparison is provided in Table IV.2, with $T_1$, $T_2$, and $T_2^*$ mean values over voxels, respectively in white and grey matter ROIs, delineated on $T_1$ maps. When compared to ranges in healthy subjects as provided in Wang et al. 2019, HD-GMM variants show more in-range values than most other methods. In Python with Jax library, full matching takes 11s, SVD matching takes 4s and the HD-GMM variants take less than 0.4s on Nvidia V100 GPU. On an Apple M2 Pro CPU, full matching takes 1 to 2 hours, while HD-GMM variants take only 2min.

| Parameter | ROI | Full matching | SVD | DRONE | HD-GMM | HD-GMM+GLLiM | Literature Wang et al. 2019 |
|---|---|---|---|---|---|---|---|
| $T_1$(ms) | WM | $868 \pm 2$ | $905 \pm 2$ | $850 \pm 2$ | $847 \pm 2$ | $834 \pm 1$ | 690-1100 |
| | GM | $1373 \pm 7$ | $1400 \pm 7$ | $1272 \pm 6$ | $1360 \pm 7$ | $1337 \pm 7$ | 1286-1393 |
| $T_2$(ms) | WM | $49 \pm .1$ | $87 \pm .2$ | $50 \pm .2$ | $55 \pm .2$ | $55 \pm .2$ | 56-80 |
| | GM | $73 \pm 1$ | $118 \pm 1$ | $77 \pm 1$ | $81 \pm 1$ | $81 \pm .1$ | 78-117 |
| $T_2^*$(ms) | WM | $46 \pm .1$ | $23 \pm .5$ | $29 \pm 24$ | $51 \pm .2$ | $51 \pm .2$ | 45-48 |
| | GM | $46 \pm .4$ | $30 \pm .4$ | $27 \pm 33$ | $55 \pm .6$ | $51 \pm .1$ | 42-52 |

**Table IV.2**: Mean $T_1, T_2, T_2^*$ values in white (WM) and grey (GM) matter ROIs. Out-of-range values in orange and red, red is further out.

### IV.2.4 Discussion

In conclusion, this work introduces a robust and innovative approach to enhancing the practicality and efficiency of Magnetic Resonance Fingerprinting (MRF) by developing a novel framework that significantly reduces the complexity and computational demands typically associated with high-dimensional MRF signal processing. The proposed method employs the new framework of High-Dimensional Gaussian Mixture Models (HD-GMM) in conjunction with an incremental learning algorithm. Additionally, the clustering structure of HD-GMM allows for greater dimensionality reduction with the same level of information loss, which is particularly crucial in clinical settings where the high computational cost and time required for processing MRF data have been significant barriers to its widespread adoption.

An ongoing work aims to extend this method to other types of Elliptical Distributions than only Gaussian Distributions, and it has been shown to improve the reconstruction results especially when dealing with highly noised MRF data such as spiral undersampled acquisitions. This work is in writing in collaboration with the Statify Team to be published in *Annals of Applied Statistics* with me as second author.

# IV.3 A deep Learning surrogate for MRF reconstructions

## IV.3.1 Introduction

In the last few years, numerous studies in the MRF literature have explored the use of neural network-based surrogates for MRF reconstruction, highly improving parameter map reconstruction speed compared to standard dictionary matching. Neural networks can serve as surrogates by learning the mapping between acquired MR signals and the corresponding tissue parameters directly from training data, eliminating the need for dictionary matching. The major part of this work focused on a parameter estimation to limited $T_1$ or $T_2$ using FISP-type sequences (Cohen et al. 2017b; Hoppe et al. 2018; Hoppe et al. 2019; Oksuz et al. 2018; Fang et al. 2020; Cabini et al. 2024). There are some traces of deep learning work using bSSFP MRF (Soyak et al. 2021). However, the number of estimated parameters is still limited to three and the sequence design is rather simple regarding the sequence encoding capability. As shown by Barbieri et al. 2021, when the sensitivity of the designed sequence implies an increased number of estimated parameters, standard neural network approaches highly suffer from the curse of dimensionality, and state-of-the-art predictive models need to be redesigned.

In this section, we propose to analyze the MRF signal coming from the proposed MRF-bSSFP sequence designed for the simultaneous quantification of parameters including vascular microstructures (CBV, R), relaxometry maps ($T_1$, $T_2$) and magnetic field maps ($B_1$, $B_0$ or corresponding frequency shift $\delta f$).

In this work, our approach relies on:

1. A fast MR vascular Fingerprint simulation tools accounting for intra-voxel frequency inhomogeneities detailed in Chapter III.
2. A Bidirectional Long Short-Term Memory (BiLSTM, Graves et al. 2005b) network used as a surrogate of the matching reconstruction process.

LSTMs (Long Short-Term Memory) are a type of recurrent neural networks (RNN) designed to capture long-range dependencies in sequences. These types of networks have shown promise in modeling sequential data, making them suitable for analyzing MRF temporal signals (Hoppe et al. 2019; Cabini et al. 2024). If the input sequence to an LSTM is reversed, a reverse-LSTM processes it in the opposite direction, capturing the dependencies that occur from the end of the sequence to the start. However, since certain dependencies may exist in both directions, only processing the sequence in one direction (forward or reverse) might not capture all the important context. Bidirectional LSTMs (Bi-LSTMs, Graves et al. 2005a) were introduced to address this limitation by combining a forward LSTM (which processes the sequence from start to end) with a reverse LSTM (which processes it from end to start). This allows the model to capture dependencies in both temporal directions, making it particularly useful for time series data where context from both the past and future is important for accurate predictions (Siami-Namini et al. 2019).

Through an *in vivo* study on healthy human volunteers, we aimed to compare three LSTM

network training approaches to identify the one that will be the more appropriate for the MRF reconstruction of microvascular quantitative maps.

## IV.3.2 Material and methods

This section describes the material and methods used for our experiments. We provide the open-source associated code that can be found at https://github.com/nifm-gin/MARVEL.

### IV.3.2.1 Dictionary simulation and matching process

As a reference, a standard dictionary-matching process was used to provide quantitative parameter maps of relaxometry ($T_1$, $T_2$, $M_0$), magnetic fields ($B_1$, $B_0$) and microvascular properties (CBV, R). The material and methods for the simulating and matching tools have already been described in the first chapters of this manuscript (see Chapters I and III) and are not going to be repeated here. However, for this study, we used direct simulations of the entire dictionary, reaching the limits of memory and computation. This approach ensures fairness when compared to the deep-learning method, as we aimed to work within a clinically feasible context.

We used here only 300 intra-voxel frequency distributions computed from microscopy-issued vascular structures, resulting in a final "reference" dictionary containing 7,344,400 entries with a file size of already 29.4 Gb.

### IV.3.2.2 Deep Learning Reconstruction

We introduced a deep learning reconstruction framework to overcome the limits of dictionary-matching in high dimensions and allow the computation of quantitative parameter maps in a reasonable time for clinical applications. We chose an LSTM network. These types of networks have shown promise in modeling sequential data, making them suitable for analyzing MRF temporal signals Siami-Namini et al. 2019. The structure of the proposed network is shown in Figure IV.3.1.

We trained separately three models: an LSTM, a reverse LSTM, and a bidirectional LSTM. The training was combined with on-fly simulations of the train dataset dictionary to avoid storing it entirely. We used Tensorflow Keras to implement and train the network. In Keras, a BiLSTM can be implemented using the `Bidirectional` wrapper around an LSTM layer.

**Training strategy** As training a network to simultaneously estimate 6 MRI parameters requires a large number of microvascular parameters value to learn the diversity of brain vascularization, the needed training dataset (*i.e* MRF dictionary) would be too large regarding the storage capacity of an average modern computer.

To overcome this, and inspired by the "on-the-fly" simulation/matching process introduced in Chapter III, we used a fixed pre-computed Bloch dictionary of ($T_1$, $T_2$, $B_1$, $\delta f$). At regular training steps, we used a random intra-voxel frequency $\delta f$ distribution to weight the Bloch dictionary and derive an updated dictionary where signals evolution is modified and

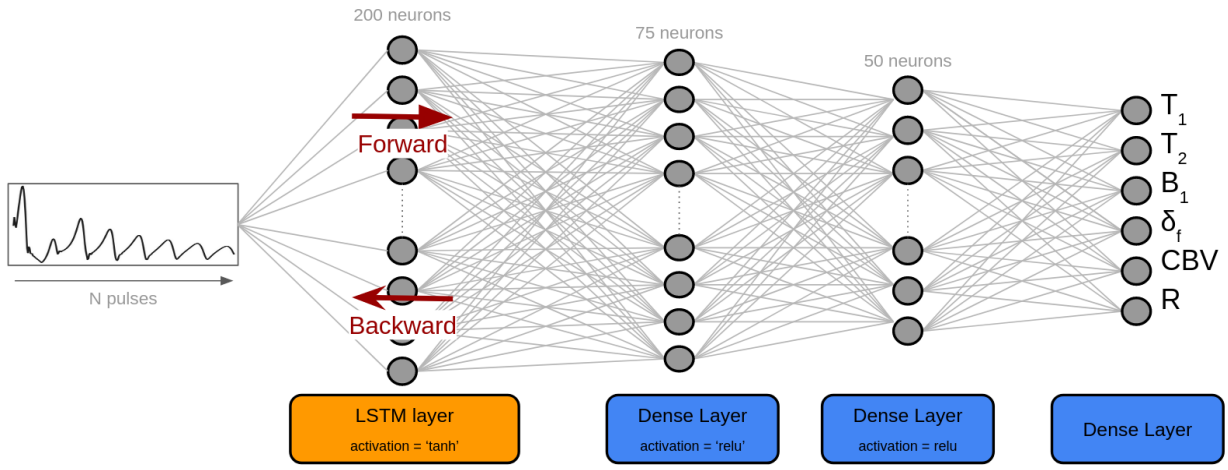


**Figure IV.3.1**: Schematic illustration of the BiLSTM network structure. The red arrows illustrate the bi-directional process happening through the LSTM layer.

representative of this intra-voxel distribution related to a chosen microvasculature. We detail the training procedure below.

We generated the base dictionary with 1,000,000 signals associated to 10,000 triplets $(T_1, T_2, B_1)$, pseudo-randomly picked into $[0.2\,s, 3.5\,s] \times [0.01\,s, 0.6\,s] \times [0.7, 1.2]$ using a Sobol (Sobol' 1967) distribution, and to 100 $\delta f$ values (from -50 to 49 Hz with an increment of 1 Hz). The increasing number of signals in this dictionary used for convolution, compared to the matching case (with 43,000 entries), is made possible by the online update of the vascular expanded dictionary, which prevents the dictionary size from exploding when adding microvascular parameters.

Before training, we computed (as detailed in Chapter III) a set of 28,000 frequency distributions of voxels with different vascular parameters CBV and R. Then, during training and at every 5 epochs, we generated a new training batched dictionary by randomly associating, to each set of parameters $T_1$, $T_2$, $B_1$, $\delta f$, a couple (CBV, R) of vascular parameters among our 28,000 distributions, using the updating procedure explained above.

To increase the robustness of the learning against noisy undersampled acquisitions, we added a centered Gaussian noise to signals of the vascular dictionary during training, with variance randomly chosen such that the resulting SNR is uniform in the range $[1, 20]$. This choice of a wide SNR range is motivated by previous studies (Barbieri et al. 2021 and Section II.4.2) and the aim of considering acquisitions with significant SNR variations (see next section). Note that the on-fly weighting of the pre-computed Bloch dictionary explained above is quite fast in Python (about $\sim 45\,s$) and can be parallelized with the network training so that the online update of the dataset allows for a drastic increase in the number of training signals while not increasing the training time.

We used the Adam optimizer with the Mean Squared Error (MSE) loss and an initial learning rate of $10^{-3}$, reduced by a factor of 0.8 every 5 epochs.

#### IV.3.2.3 MR data acquisition

*In vivo* acquisitions were realized on 3 healthy volunteers with a Philips 3 T Achieva dStream MRI at the IRMaGe facility (MAP-IRMaGe protocol). The proposed MRF sequence was based on the MRF-bSSFP of Chapter III. 260 repetitions were used (TR = 21 ms), with Flip Angle (FA) linearly increasing from 7° to 70° as suggested in Gómez et al. 2019, and a quadratic phase cycle of 10°. To compare the robustness of the model against under-sampling noise, one acquisition was performed using Cartesian sampling (matrix size: $256 \times 256 \times 1$; voxel size: $0.78 \times 0.78 \times 3.00\,\text{mm}^3$) with a scan time of 12 minutes per slice, and the two other acquisitions were performed using a spiral trajectory (matrix size: $192 \times 192 \times 3$; voxel size: $1.04 \times 1.04 \times 3.00\,\text{mm}^3$) with 12 acquired shots and a scan time of 2 minutes per slice. Yet, the $k$-space undersampling scheme used in spiral scanning induces significant noise on the acquired signals. A sequence with the same parameters scheme, except the application of a spoiling gradient in the slice selection direction, was also acquired in one volunteer (spoiled GRE sequence). This sequence was used as a reference to show the ability of simple networks to reconstruct 3-dimensional relaxometry MRF maps.

#### IV.3.2.4 Image analysis

MRF $T_1$and $T_2$ values for the grey matter (GM) and the white matter (WM) regions were calculated from automated ROIs generated using the Otsu's thresholding method (Otsu 1979) in Matlab using anatomical $T_1$WI as reference. CBV and R values for the GM and WM regions were computed using the same method, and values inside the superior sagittal sinus (SS) vein were also computed from manual ROI validated by a neuroscientist. Reference literature values come from Wansapura et al. 1999; Hasan et al. 2012; Gelman et al. 2001; Stikov et al. 2015; Delphin et al. 2024; Ito et al. 2004.

### IV.3.3 Results

Quantitative parameter maps obtained in one volunteer using Cartesian acquisition are given in Figure IV.3.2. Relaxometry maps ($T_1$, $T_2$, $B_1$) obtained with the standard spoil sequence and reconstructed with the LSTM network (first row) are of high quality, suggesting that a standard LSTM approach is adapted for low dimensional MRF acquisitions reconstruction. In the second row, results from standard dictionary-matching on the bSSFP sequence (reconstruction time 2223 s) show noisier maps but also provide frequency and microvascular maps with the right contrasts and global values in the expected ranges.

The third and fourth rows show the reconstructed maps from a standard and a reverse LSTM network. As can be seen, the predicted maps are degraded and artefacted. However, in the last row, the proposed BiLSTM network can provide high-quality maps for all the parameters (under a reconstruction time of 3.5 s). In particular, the CBV and R maps exhibit expected high values where large vessels are located.

This can also be observed in Table IV.3, where ROIs estimates values for several methods are shown. Measured values that are the closest to references are presented in **blue**. The ones

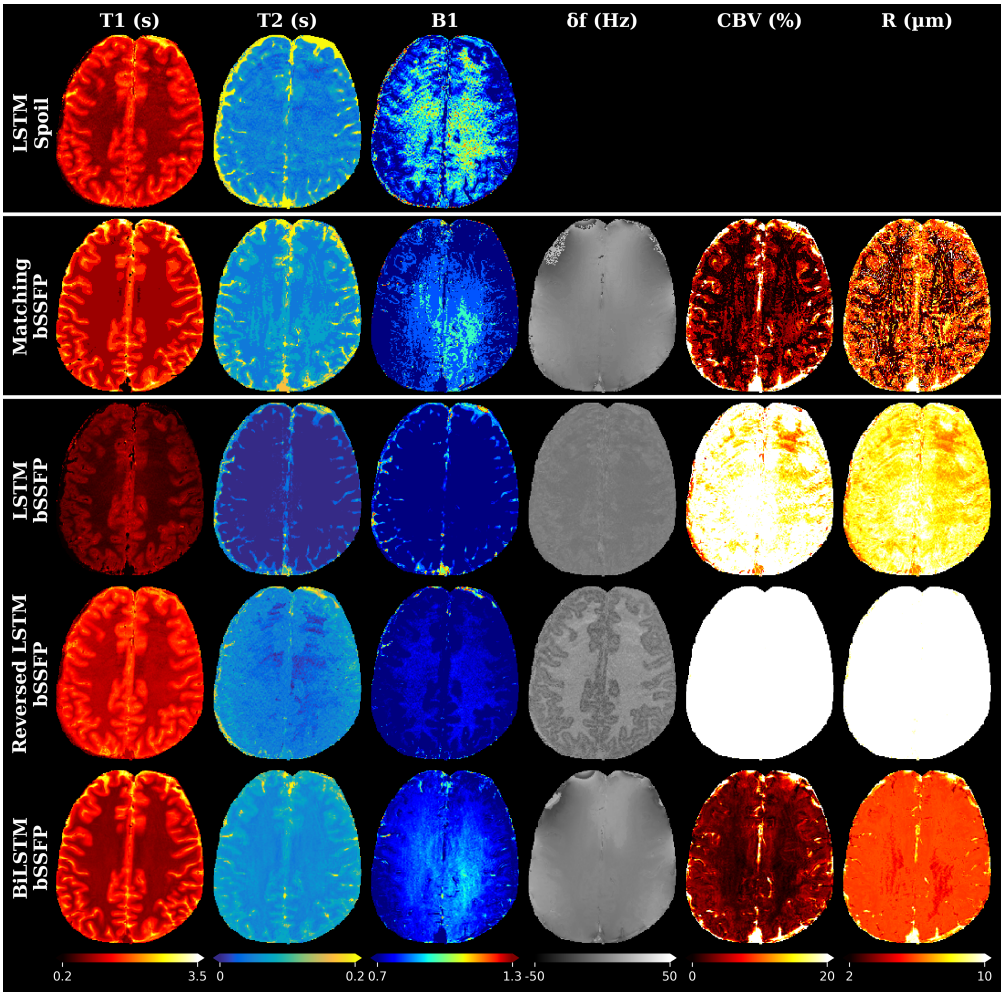


**Figure IV.3.2**: Parameter maps of the Cartesian acquisitions obtained with the BiLSTM reconstruction methods on one healthy volunteer. (Note that the slice position slightly differs between the Spoil and bSSFP acquisitions).

reconstructed by the BiLSTM are closer to results obtained in previous literature studies[1] and give a grey/white matter ratio of CBV values close to 2.

Additionally, parametric maps obtained in one slice of the second volunteer using the spiral scheme acquisition are presented in Figure IV.3.3. Standard matching and BiLSTM reconstruction are compared and suggest that the network can adapt to a different type of space sampling and SNR. Histograms of values are also provided to highlight the discretized *versus* continuous value distributions between the two approaches. BiLSTM results for all slices of the 2 volunteers using the spiral acquisition are given in Figure IV.3.4.

## IV.3.4 Discussion

In this study, we showed the possibility of quickly analyzing MRF data containing multiple dimensions including microvascular properties. This was done using a combination of fast and

[1]CBV and R values from the literature were obtained using contrast agent injection.

**Table IV.3**: ROIs estimates of $T_1$, $T_2$, CBV and R. Best values compared to literature.

| Parameter | Tissue | LSTM | Rev. LSTM | BiLSTM | Matching | Literature |
|---|---|---|---|---|---|---|
| $T_1$ (ms) | WM | $538 \pm 121$ | $1119 \pm 177$ | **$823 \pm 55$** | $931 \pm 46$ | $\sim 690 - 1100$ |
| | GM | $674 \pm 202$ | $1440 \pm 261$ | **$1320 \pm 339$** | $1381 \pm 380$ | $\sim 1286 - 1393$ |
| $T_2$ (ms) | WM | $0.5 \pm 6$ | $37 \pm 15$ | **$54 \pm 5$** | $50 \pm 13$ | $\sim 56 - 80$ |
| | GM | $8 \pm 22$ | $53 \pm 21$ | $69 \pm 21$ | **$80 \pm 70$** | $\sim 78 - 117$ |
| CBV (%) | WM | $19.8 \pm 4.5$ | $40.0 \pm 0.4$ | **$2.0 \pm 0.9$** | $2.0 \pm 5.0$ | $\sim 1.7 - 3.6$ |
| | GM | $22.2 \pm 5.3$ | $39.8 \pm 1.2$ | **$3.9 \pm 3.4$** | $1.49 \pm 1.9$ | $\sim 3 - 8$ |
| | Sag sinus | $19.5 \pm 8.5$ | $37.3 \pm 4.2$ | $21.2 \pm 7.3$ | $28.2 \pm 8.8$ | |
| R (µm) | WM | $8.2 \pm 0.8$ | $10.0 \pm 0.0$ | **$5.6 \pm 0.3$** | $4.2 \pm 2.3$ | $6.8 \pm 0.3$ |
| | GM | $8.5 \pm 0.9$ | $10.0 \pm 0.0$ | **$5.8 \pm 0.5$** | $5.4 \pm 2.2$ | $7.3 \pm 0.3$ |
| | Sag sinus | $7.8 \pm 1.3$ | $10.0 \pm 0.2$ | $8.8 \pm 1.5$ | $10.1 \pm 2.2$ | |

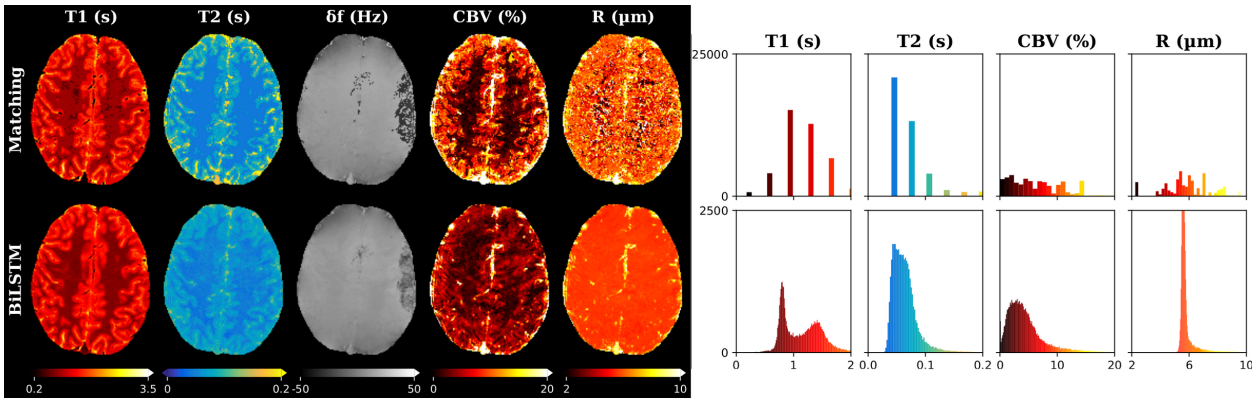


**Figure IV.3.3**: Parameter maps of one slice of a volunteer of the bSSFP spiral acquisition obtained with dictionary-matching and our BiLSTM network, and associated histograms.

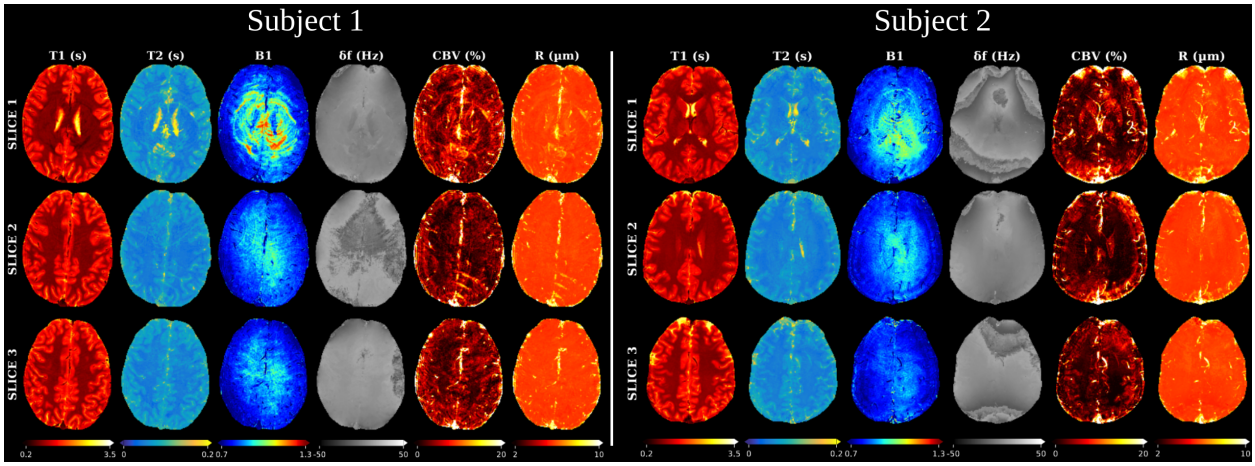


**Figure IV.3.4**: BiLSTM reconstructions of the spiral acquisition for two healthy volunteers. Computed in 3.5 s.

light realistic simulations and the use of Bidirectional LSTMs. Our first results on healthy volunteers are encouraging especially for the CBV maps that show a nice contrast between white matter, grey matter, and blood vessels and present similar values to those usually obtained using Gadolinium injections or positron emission tomography (PET). Quantitative validation of our method against standard Dynamic Susceptibility Contrast (DSC) MRI

analysis in healthy volunteers is limited due to the required injection of contrast agent. However, further analyses and comparisons with reference methods should be conducted in patients to validate the whole approach.

It is worth noting that the standard LSTM and the reverse LSTM show two completely different behaviors. LSTMs are designed to retain important information over time, but in long sequences, earlier information can still be diluted or lost as the model focuses more on recent inputs. As the sequence used here and its sensitivity to tissue parameters, have been widely studied during this thesis, we know that the encoding of the different parameters is more or less important depending on the parts of the sequence signal response. We hypothesize that this could explain why an uni-directional network isn't able to capture all the information of the signal for every parameter and why the Bi-directional approach works much better.

However, although the results are promising and the grey/white matter ratio of 2 obtained by our BiLSTM network in the CBV maps is expected in the human brain, it seems that the network reconstruction tends to smooth the parameter maps. This effect might be minimized by optimizing the MRF acquisition sequence with automatic procedures to improve the initial sensitivity to the (vascular) parameters. The numerical simulations could also be improved by using input frequency distributions computed from more realistic and diverse vascular vessel geometries, and by adding other sources of magnetic susceptibility to our model, such as myelin fiber structures. The use of a reference $B_1$ map could also help improve the reconstruction accuracy.

In addition, other solutions can be foreseen to enhance the reconstruction pipeline. The network structure could be further improved to handle longer fingerprints and the training step could contain additional undersampling noise to improve reconstruction from spiral acquisitions.

Finally, the results of the $T_2$ estimates in the grey matter seem to be underestimated compared to the matching procedure and the expected literature ranges. As it has been designed by Gómez et al. 2019 for the FA train, and according to our observations on the signal evolution in the dictionary simulated from our MRF-bSSFP sequence (see Chapter III), most of the $T_2$ sensitivity of the sequence is concentrated in the middle part of the signal. Similarly to what has been observed for the single-direction LSTM in this study, the middle part of the signal could be forgotten during training leading to misestimation of the $T_2$ values. This hypothesis makes us think that the learning of the signal representation could be enhanced by splitting the signal in both parts and learning with both parts in a bidirectional fashion. Moreover, temporal compression methods such as those introduced in Section IV.2 could also be applied to the MRF dictionary before training to help the LSTM networks capture long-term dependencies more effectively.

## IV.4 Conclusion

In this chapter, we proposed two advanced reconstruction methods to overcome the curse of dimensionality for high-dimensional MR Fingerprinting. Whereas the first one introduces a low-rank compression method for reducing matching costs in heavy MRF dictionaries, the second one proposes to bypass the matching process by using a BiLSTM neural network as a surrogate for the identification of each tissue parameter for the acquired fingerprints. The first method is however still limited by the number of low-rank projections needed to sufficiently depict the signal evolution and not decrease matching accuracy. The extension from $T_2^*$ application to microvascular estimates or new parameters such as brain oxygenation could also be challenging. The second method's results are promising but the length of the sequence seems to limit the capacity of the neural network to capture the encoding of every parameter in the signal evolution.
From this, we think that combining both methods to train a BiLSTM neural network under a low-rank representation of the MRF dictionary could highly improve our previous results and bridge the gap between our methods and the clinical application. This is an ongoing work that we aim to conduct and publish in the following months.

As it stands, both of these approaches nonetheless increase the potential applications of our MRF-bSSFP sequence in the management of stroke patients. It might also be possible to extend the method to measure other microstructural parameters such as brain oxygenation without complexifying the dictionary-matching process nor increasing computation time by training again the low-rank projection model and the reconstruction neural network.

# Chapter V

# Fast AI-powered simulations of water-diffusion and microvascular effects

This chapter presents a new method for the fast simulations of water-diffusion and microvascular MRF dictionaries. Our new simulation pipeline relies on our previous work using voxel frequency distributions combined with a deep-learning model for proton diffusion estimates. Powered by a deep-learning model, we propose a new MRF simulation tool that highly speeds up dictionary generation compared to existing methods.
Given the lack of current MRvF data acquired in stroke patients that could be used to validate our new approach, we relied here on retrospective data acquired in the lab in healthy and stroke animal models.
This study was fully conducted during my thesis and designed to be published soon as the primary author.

## Contents

# V.1 Introduction

In the previous chapters of this manuscript, we proposed a new MRF method relying on an innovative bSSFP sequence for the simultaneous and fast high-resolution quantification, without contrast agent, of tissue parameter maps such as $T_1$, $T_2$, R, and CBV, which are essential for perfusion imaging and stroke diagnosis. However, while these parameters are critical for assessing blood flow and vascular characteristics, they do not fully capture the complexity of stroke pathology. Stroke imaging poses unique challenges due to the complexity of tissue damage, where both perfusion and diffusion play crucial roles in understanding the underlying pathology. Water diffusion, representing the random motion of water molecules within tissues and quantified via the apparent diffusion coefficient (ADC), is crucial for detecting early ischemic changes, as it directly reflects cellular integrity and the restriction of water movement in damaged tissues. Similarly, Oxygenation Saturation ($SO_2$), through its influence on the blood-oxygen-level-dependent (BOLD) effect, could provide vital information about tissue viability and metabolic status, yet it was not included in the previous approach. The absence of these parameters limits the ability to comprehensively differentiate between ischemic and hemorrhagic strokes and to fully assess tissue viability, which is essential for accurate diagnosis and treatment decisions in stroke management.

Classically, imaging diffusion and measuring ADC is made by applying a series of diffusion-weighted MRI sequences and analyzing the signal attenuation due to water diffusion in different directions. $SO_2$ is typically measured using pulse oximetry, but accurately quantifying oxygenation with MRI is challenging due to the complex relationship between the MRI signal and multiple factors which all influence the magnetic properties of blood. Without contrast agent injection, incorporating it into the MRF framework is nontrivial due to this complex interplay between oxygenation, blood volume, and field inhomogeneities.

With the help of a contrast agent, our lab has however proposed an MR vascular Fingerprinting method (MRvF, Christen et al. 2014b) that allows the simultaneous quantification of CBV, R, $T_2$ and $SO_2$. Recently, this method has been improved by the use of realistic microvascular models, to produce such quantitative estimates in tumor animal models (Delphin et al. 2024). This study relied on data acquired in the lab using a Gradient Echo Sampling of the FID and SE (GESFIDE) sequence acquired pre- and post-USPIO contrast agent injection. The results have been validated against an analytical model, previous histological analyses, and oxygenation ($pO_2$) measurements made with optic fiber probes (see Figure V.1.1). In this study, the water diffusion effect was taken into account in the simulation using MRVox (Pannetier et al. 2013), a Matlab in-house simulation tool, using an Apparent Diffusion Coefficient (ADC) to 850 $\mu m^2/s$ as a trade-off between healthy and tumoral tissues. Initially, the MRVox software was developed for the accurate simulations of MR signals, considering the susceptibility effects resulting from the microvasculature and the effect of water diffusion. This was made using small simulation time steps (<0.5ms) and costly matrix computation, that led to high simulation times (>days for realistic MRvF dictionaries). Thus, previous studies were limited to the generation of small-scale MRF dictionaries (with tens of thousands of entries) on a distributed parameter grid. The reconstruction process was then performed using machine learning methods (see Boux et al. 2021). This approach limited the accuracy of parameter estimates and the performance of the machine learning models which has been

observed to decline as the number of parameters increases.

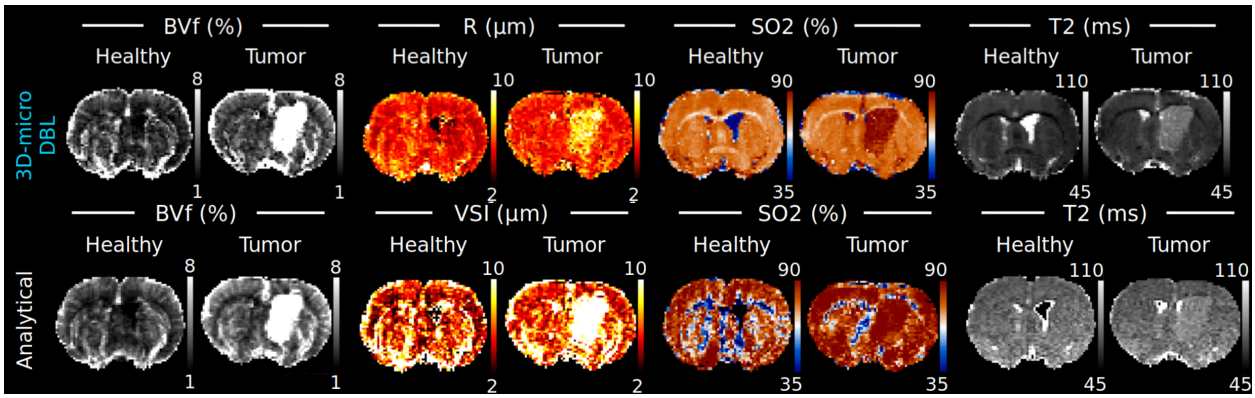


**Figure V.1.1**: Parametric maps obtained through DBL-MRvF using microscopy-derived simulations for healthy and tumoral tissue, from Delphin et al. 2024.

In this work, we proposed to fasten the actual MRVox simulation protocol to allow the generation of larger MRF dictionaries that could improve the accuracy of the estimates. Moreover, given the context of this thesis, we aimed to extend the application of the proposed methods to stroke animal models. To achieve this, our approach was two-fold:
First, we used the proposed two-step MRF simulation process that we have presented in Chapter III, powered with newly segmented microvascular voxels, to fasten the basic microvascular simulations made with MRVox and simulate MRvF dictionaries in the order of minutes.
Second, we aimed to replace the actual time-consuming water-diffusion effect simulations made with MRVox. Recurrent Neural Networks (RNNs) are commonly used for time sequence generation as they can capture temporal dependencies. When the signal sequences are long, RNNs can struggle with long-term dependencies in the signal. More advanced architectures like LSTM networks have been developed, using gating mechanisms to better manage long-range dependencies in sequences. However, LSTM comes with increased complexity due to its more intricate structure. In a recent study, Liu et al. 2021 used a Gated Recurrent Unit (GRU) RNNs, for the fast modeling of spoiled GRE sequence signals trained from Bloch equations for ($T_1$, $T_2$) MRF estimates. GRU RNNs offer a simpler alternative to LSTMs by combining the forget and input gates into a single gate, providing a balance between performance and computational efficiency. We hypothesized that this kind of architecture could also be used to model the effect of water diffusion on an input MR signal without diffusion, for specific tissue parameters.

Given the lack of MRF data from stroke patients to validate our approach, we chose to use retrospective data acquired in the lab in a rat model of permanent ischemia to conduct our *in vivo* study. As evoked earlier, compared to the previous chapters of this manuscript, these data were acquired using a GESFIDE sequence. The main difference with the proposed MRF-bSSFP sequence is in the length of the sequence (here the fingerprints are made of 64 time points) and a slightly different parameter sensitivity that results here from the concatenation of a pre and a post-CA signal. The proposed method should however be

generalizable to other MRF sequences than the GESFIDE one.

## V.2 Methods

### V.2.1 Animal models

**Healthy model** Wistar rats (N=8, 268±23g) were imaged with the described MR protocol and served as healthy animal models in this study.

**Stroke model** Sprague Dawley rats (n=13) underwent permanent focal brain ischemia induced by intraluminal occlusion of the right middle cerebral artery. Briefly, the right carotid arterial tree was isolated. A cylinder of melted adhesive (length 2mm; diameter 0.38mm) attached to a nylon thread (diameter 0.22mm) was advanced from the lumen of the external carotid artery into the internal carotid artery up to 5mm after the external skull base. Rats were imaged by MRI 60 minutes after the occlusion. 4 animals died during the surgery. The Stroke group is therefore composed of N=9 animals (365±18g).

### V.2.2 MRI acquisition

MRI was conducted with a horizontal bore 4.7 T Biospec animal imager (Bruker Biospin, Ettlingen, Germany) with an actively decoupled cross-coil setup (body coil for radiofrequency transmission and quadrature surface coil for signal reception) and Paravision 5.0.1. GESFIDE sequence (TR=4000 ms, 32 gradient-echoes, Spin-Echo=60ms; voxel size=$234\times234\times800\mu m^3$, 5 slices, FOV = $30 \times 30$ $mm^2$) was acquired before and after the manual injection of the ultrasmall superparamagnetic iron oxide nanoparticles (USPIO) P904 (200 µmol/kg body weight; Guerbet, Roissy, France). A three-minute delay after the first injection was applied before starting the second GEFIDSE acquisition.

### V.2.3 Dictionary simulations

For all experiments, simulations were performed at 4.7T. Each signal simulations were made separately for the pre and post-USPIO contrast-agent parts of the MR signal. In the latter case, the magnetic susceptibility of the blood compartment at equilibrium was set to 3.5 ppm.
For the microvascular components, 3D microvasculatures were segmented from microscopy-imaged voxels of a mouse brain. The microscopy dataset is the same as the one introduced in Chapter III, segmentation was however improved with an advanced segmentation model by a PhD student of the team, using the VesselExpress software (Spangenberg et al. 2023). To achieve a great diversity of voxels, representing healthy and pathological vascular networks, two types of data augmentation were performed and illustrated in Figure V.2.1: dilation, using two different structuring elements: a 3x3x3 cube and a sphere with a radius size of 2 (left panel); and merging, where two or more segmented MR-size voxels were superimposed (right panel). In the end, it resulted in 45,000 segmented voxels from which structures can be selected and associated with several $SO_2$ values of our choice to generate the dictionaries of this study. The number of voxels used for the generation of each dict is given in each section.

For every dictionary in the subsequent experiments, $T_2$ values were added after the microvascular simulation by multiplying each GESFIDE signal by exponential functions with different $T_2$ values.

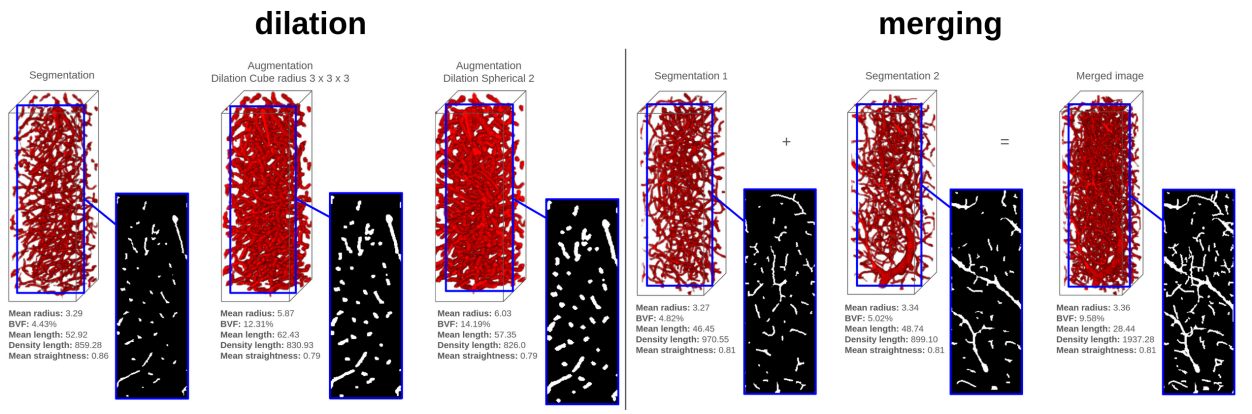


**Figure V.2.1**: Microvascular voxel data augmentation. Example of dilation process (left) and merging process (right). Courtesy of Maitê Silva Martins Marçal.

### V.2.3.1 Fast simulations of MRvF dictionaries without diffusion effects

First, we proposed to compare two simulation models for the generation of MRvF dictionaries with CBV, R, $SO_2$ and $T_2$ tissue parameters. On one side, we computed a reference MRvF dictionary using the MRVox software, on the other side, we proposed to apply the new methods proposed in Chapter III of this manuscript, which we called here the "Distributions" method.

**MRVox simulations** We used the MRVox software to accurately simulate the MR signals resulting from the application of a GESFIDE sequence on 20,000 microvascular voxels chosen in the already introduced dataset and characterized by a certain blood volume (CBV), mean vessel radius (R), and mean oxygenation saturation ($SO_2$). This resulted in a 20,000-entry MRF dictionary.

**Distributions simulations** We used our in-house two-step dictionary generation process (see Chapter III for a detailed methodology of this method). 20,000 voxels were used with assigned CBV, R, and $SO_2$ values. From these values, we derived 20,000 intra-voxel magnetic field inhomogeneity distributions. Examples of the computed distributions are shown in Figure V.2.2 with and without the presence of contrast-agent. These distributions, sampled every 1Hz between $-200$ and $+200$Hz were then used to account for magnetic field inhomogeneities effects on Bloch computed MR evolutions, for the pre-CA and the post-CA parts of the GESFIDE signal response (32 acquisitions points in each part).

### V.2.3.2 Fast simulations of the water diffusion effect in MRvF dictionaries

In the standard MRVox approach, the effect of water diffusion is modeled by the convolution of a Gaussian kernel and can be hindered by cell and vessel compartment walls updating the MR signal evolutions for very small time step, which is highly time-consuming and

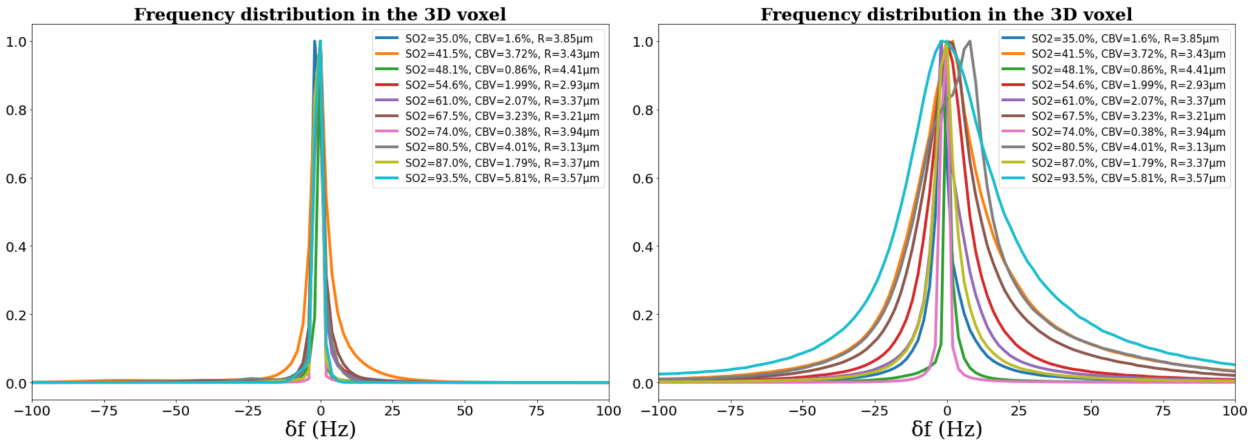


**Figure V.2.2**: Intra-voxel frequency distributions without (left) and with (right) contrast agent. The distributions are derived from intra-voxel magnetic field inhomogeneities maps, computed from 3D microvasculature with fixed oxygenation. Simulations were made at 4.7T. For the computation with contrast agent, the magnetic susceptibility of the blood compartment at equilibrium was set to 3.5 ppm

limits the generation of MRF dictionaries with a sufficient number of signal entries. Yet, the effects of water diffusion that we have observed on the GESFIDE signals are mainly a shape modification between the signal without and the signal with diffusion.

We implemented and trained a GRU RNN to model the water diffusion effect on MR signals as a surrogate for the conventional process. To ensure proper validations, the standard MR simulations, with and without diffusion, were conducted using the MRVox software as a reference, independently of the "Distributions" method also proposed in this study.

**Network** The model follows a GRU RNN architecture with a single output dimension representing the magnetization vector. The network input is a signal without water diffusion effects, and a set of ($SO_2$, CBV, R) tissue parameters values. The network processes batches of 5 signals, while the RNN layer contains 32 units. An Adam optimizer, a popular gradient-based optimization algorithm, is used to optimize the model, using a Mean Squared Error (MSE) loss. Learning rate adjustments are handled such that the learning rate reduces when the validation loss plateaus, using a factor of 0.8 and patience of 20 epochs. Additionally, a minimum learning rate of $1e^{-6}$ is enforced to prevent it from diminishing to very small values. Model checkpoints are saved based on the training loss, with the best model retained in an HDF5 file named according to the experiment setup. Early stopping is employed with a patience of 15 epochs, halting the training process if the validation loss does not improve, to prevent overfitting. Together, the callbacks ensure efficient training while avoiding overfitting and dynamically adjusting the learning rate based on performance trends.

**Training set** The model was trained on an NVIDIA GeForce RTX 3060. As for the simulation process, the signals were split into pre- and post-part, and the network was trained in two separate models. In the same way, the prediction is made for pre and post-CA parts of the signals that are then concatenated. The training set was made of 20,000 signals simulated using the MRVox software for the GESFIDE sequence described previously. The signals were

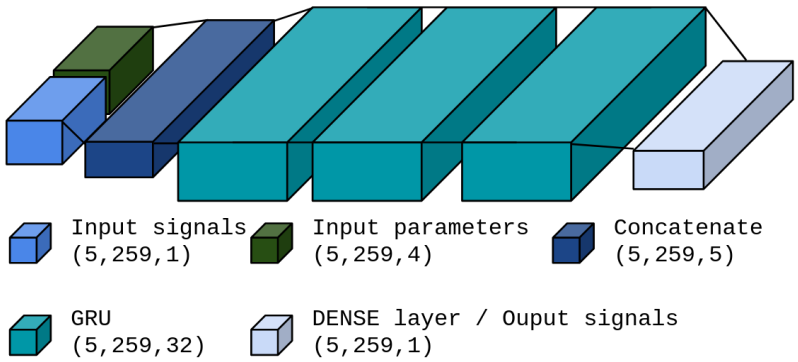


**Figure V.2.3**: Schematic representation of the RNN model used in this study assuming a batch size of 5 signals.

simulated once without diffusion effect, and then with diffusion effect to serve as ground truth. For the diffusion, the ADC was fixed to 850$\mu m^2$/s. $SO_2$ values were distributed along a Sobol repartition. In contrast, CBV and R were chosen from realistic 3D microvasculature voxel (as detailed in Chapter III of this manuscript for human experiments).

**Testing set** The testing of the model was made on 2,000 signals not used for training. As for the training set, these 2,000 signals were simulated with and without diffusion to serve as a ground truth for evaluating the model.

### V.2.3.3 Combining both methods for large MRF dictionaries simulations

As the final contribution of this study, we combined the fast simulations of MRvF dictionary for CBV, R, $SO_2$ and $T_2$ using the "Distribution" methods, with water diffusion effect representation using the proposed GRU RNN. We named the combined protocol, MR-WAVES (MR Water-diffusion And Vascular Effect Simulations).

On one side, validation dictionaries were computed using 2,000 microvascular voxels, resulting in 2,000 intra-voxel frequency distributions from which we computed 2,000 MR signals. We then used our neural network to represent the diffusion effect in this 2,000-entry dictionary, by inferring the no-diffusion signals and their associated tissue parameters. For comparison, we used the 2,000-entry dictionaries computed previously (1) from MRvox with diffusion and (2) from Mrvox without diffusion and inferred by the RNN for diffusion.

Finally, we used 45,000 microvascular voxels and associated for each voxel, two different $SO_2$ values, resulting in 90,000 intra-voxel frequency distributions from which we computed 90,000 MR signals. We then used our neural network to represent the diffusion effect in this 90,000-entry dictionary, by inferring the no-diffusion signals and their associated tissue parameters.

### V.2.4 MRF reconstruction

For the fast simulation without diffusion, MRF parameters maps were reconstructed using GESFIDE data acquired on the healthy animals. For the fast simulation with diffusion, and the combination of both methods, MRF parameters maps were reconstructed using both healthy and stroke animals data. In all of the proposed experiments, the MRF reconstruction relied on a standard dictionary-matching process as already detailed in the previous chapters of this manuscript.

### V.2.5 Statistical Analysis

Simulations results were evaluated by computing the Normalized Root Mean Squared Error (NRMSE) between both dictionaries' entries across the whole parameter space, in each experiment. The resulting parametric maps were analyzed through the evaluation of the relative difference between reconstructed maps with both methods and a Bland-Atlman analysis over all animals of the groups.

## V.3 Results

### V.3.1 Fast simulations of MRvF dictionaries without diffusion effects

Considering that the magnetic field distributions have been precomputed, the 20,000 entries using the "Distributions" method were computed in 400 seconds, compared to the 84,000 seconds required for the MRVox dictionary, demonstrating a 200-fold acceleration. The mean NRMSE across the entire parameter space was 0.53%, indicating a high agreement between the two simulation algorithms. Figure V.3.1 shows a detail of the measured NRMSE across the parameter space.

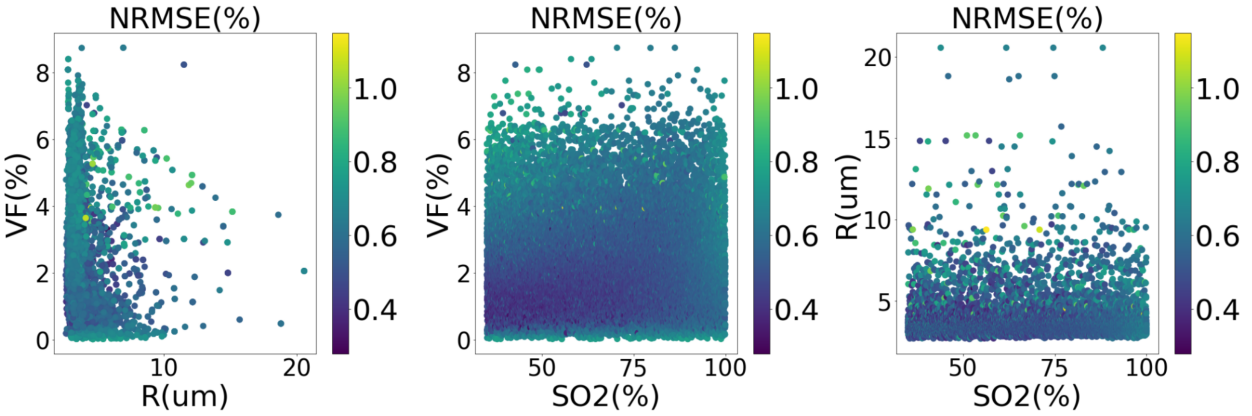


**Figure V.3.1**: NRMSE between whole signals (pre and post-CA concatenation) from the Distribution methods and signals from MRVox, plotted across the 3D parameters space (CBV, R, $SO_2$) before adding the $T_2$.

Using MRI GESFIDE data acquired on the 8 healthy animals, we reconstructed MRF parameters maps of (CBV, R, $SO_2$ and $T_2$) in 20 seconds of matching time per animal, using dictionaries computed with both methods (MRVox vs Distribution). In Figure V.3.2, we show

examples of reconstructed MRF maps for two healthy animals of our study, comparing the reconstruction made with $Dico_{mrvox}$ and our proposed method $Dico_{distrib}$. Relative difference maps are shown on the bottom line. It is interesting to note that in the second animal (right panel), the main error in mean radius (R) maps results from imperfect shimming areas of the acquisition, near the sinuses. Density histograms of the relative difference across the voxels of the slices are also shown. For each of the presented histograms, we measured that approximately 45% of the voxels was under 2% relative difference between both methods.

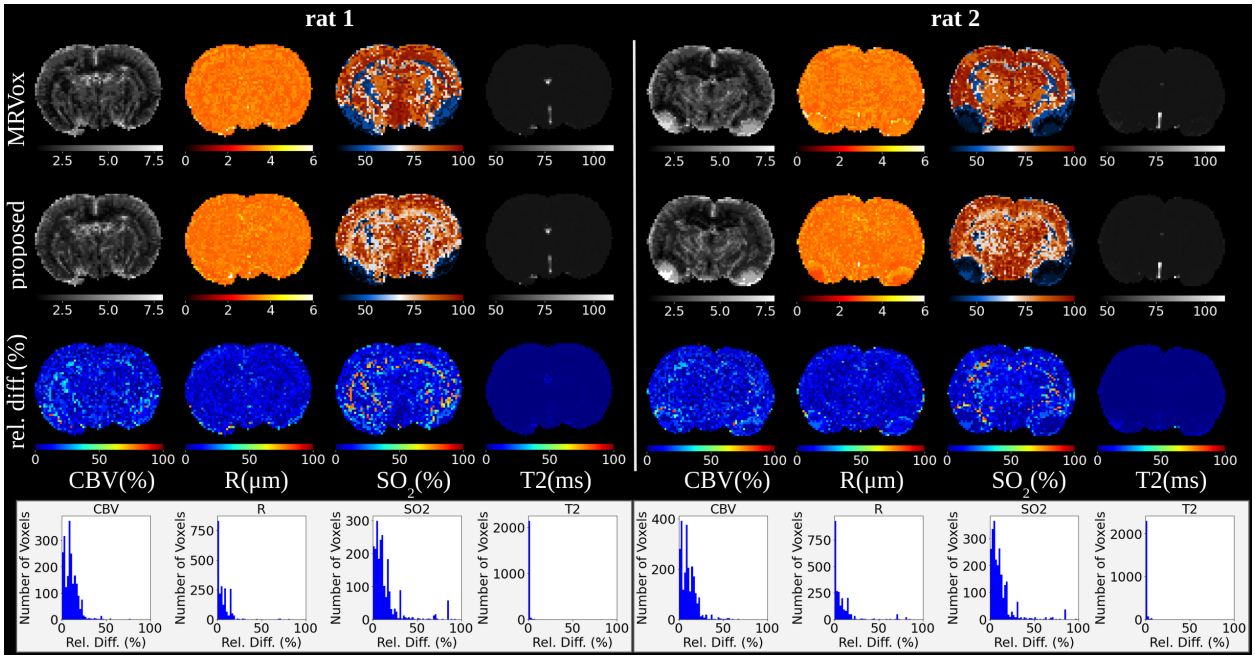


**Figure V.3.2**: Illustration example comparing MRF reconstruction maps using dictionary computed from both simulations methods on one slice, for two animals. First line: MRVox dictionary; middle line: proposed Distribution methods; last line: relative difference maps in %, threshold below 100%. Below the maps, detailed histograms of the density of relative difference values are shown for each parameter map.

In Figure V.3.3, a Bland-Altman analysis is shown for each reconstructed parameter map across the three previously manually drawn ROIs. The Bland-Altman plots show excellent agreement for all the estimated parameters in the whole brain as well as in the cortex and striatum areas separately. Each point corresponds to one rat in the plot. A small bias (red line) close to 0 and narrow spreads of the points indicate that both methods agree with low variability across animals. Some outliers points (*i.e.* outside of the limits of agreement: blue lines representing the mean±1.96*std of the differences) however suggest that for some subjects, there may be significant differences between both methods.

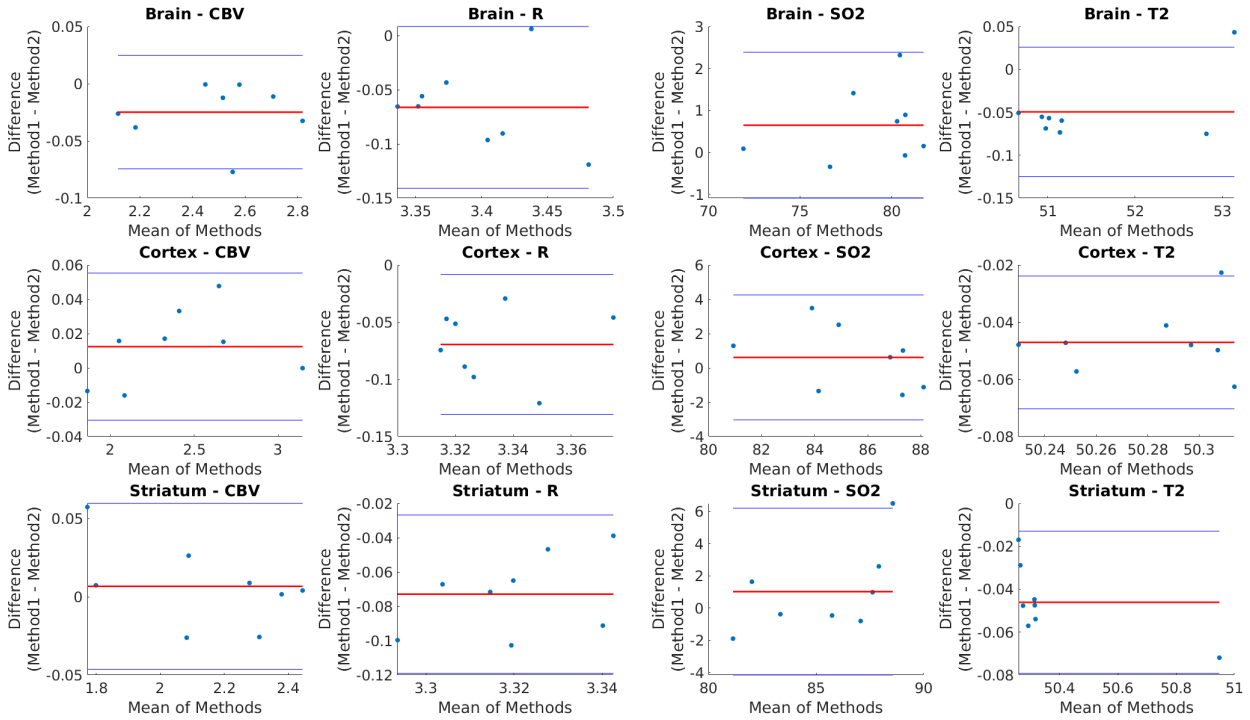


**Figure V.3.3**: Bland-Altman plots assess the differences in CBV, R, $SO_2$ and $T_2$ reconstructed using Distribution method and MRVox.

### V.3.2 Fast simulations of the water diffusion effect in MRvF dictionaries

Using the dataset of 20,000 training entries, the training on the GRU RNN lasted approximately 300 seconds. For the 2,000 testing signals, the prediction time was just 3 seconds. Figure V.3.4 illustrates examples of predicted signals, comparing them with both the input signals (without diffusion) and the expected ground truth for the pre and post-diffusion sections.

Figure V.3.5 presents the normalized root mean square error (NRMSE) calculated between the 2,000 predicted signals and their corresponding ground truth across the parameter space. The overall error is low (<5%) and uniformly distributed across different parameter values. However, notable exceptions are observed for signals corresponding to large vessels (R>15µm or CBV>5%), where the error is highest. These cases could be considered outliers, as such values are uncommon in healthy rat brains.

First, we reconstructed MRF quantitative parameters maps of CBV, R, $SO_2$ and $T_2$ from GESFIDE data on the healthy animals cohort. The parameters maps were reconstructed: (1) with a 2,000-entry MRF dictionary simulated without diffusion effect (2) with a 2,000-entry MRF dictionary with diffusion computed in MRVox, and (3) with a 2,000-entry MRF dictionary with diffusion with the proposed RNN. In Figure V.3.6, we show an example of the results on one slice from one of the 8 healthy animals. The relative difference maps highlight the similarity between the results using both simulation methods.

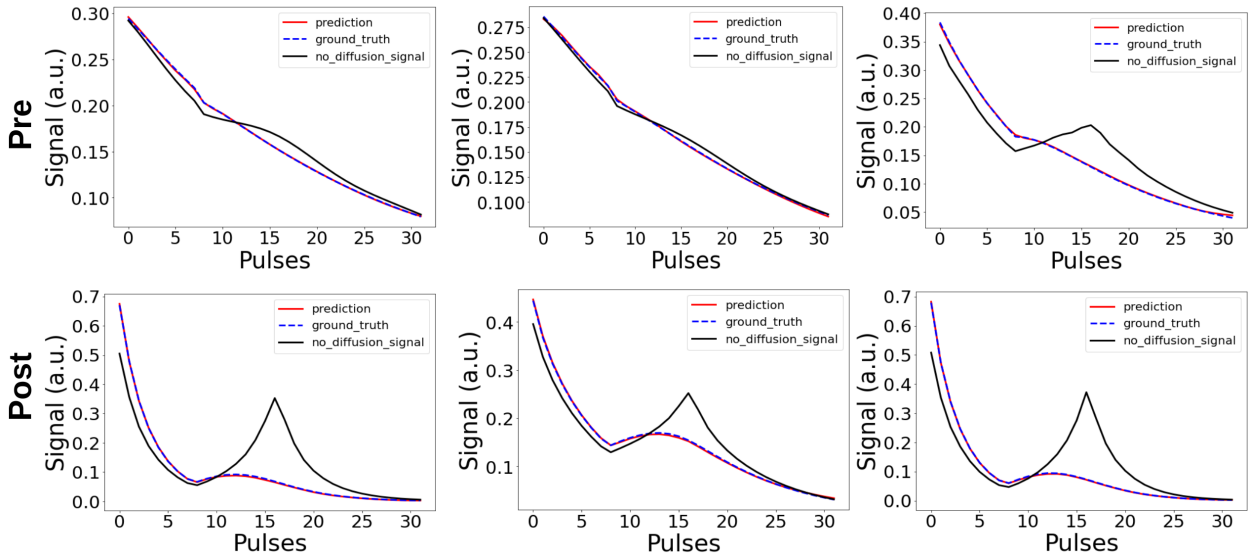


**Figure V.3.4**: Examples of signal predictions from the RNN model with the pre (first line) and the post-CA (last line) of the signals. RNN prediction: red, no diffusion reference: MRVox, ground truth: MRVox. Left column: CBV=3.97%, R=3.27µm, $SO_2$=84.14%. Middle column: CBV=2.53%, R=4.23µm, $SO_2$=85.01%. Right column: CBV=3.79%, R=3.44µm, $SO_2$=36.46%. As RNN inference is made before $T_2$ relaxation representation, here $T_2$=100ms everywhere.

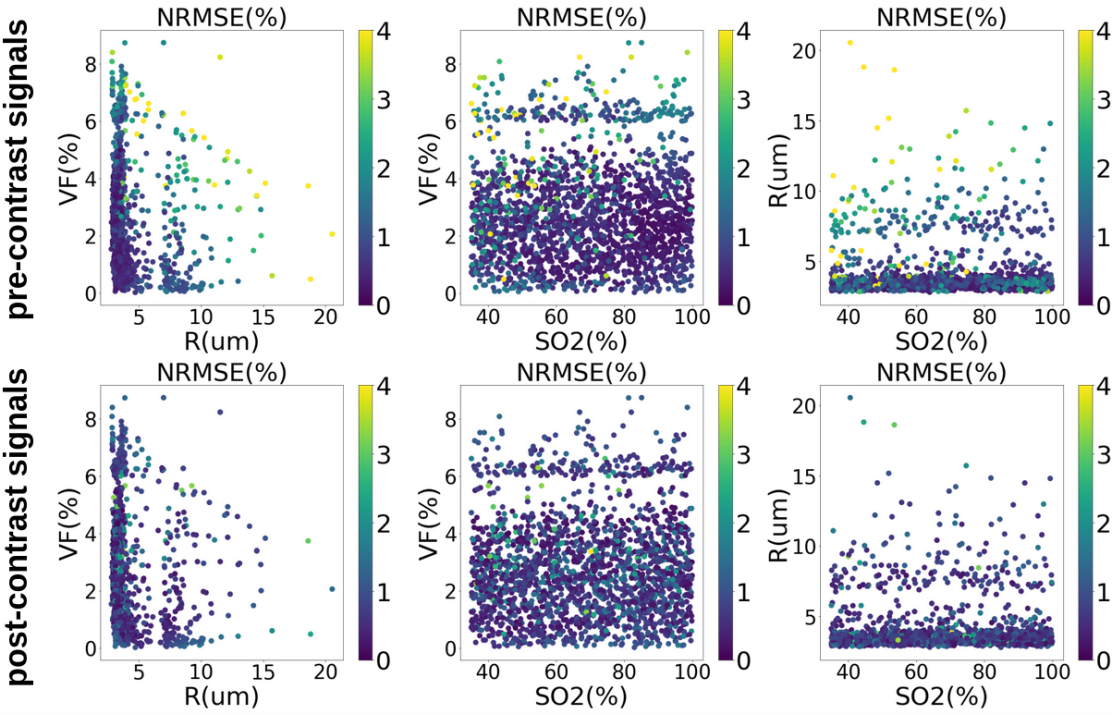


**Figure V.3.5**: NRMSE between prediction (RNN) and ground truth signal (MRVox) for pre and post-CA parts of the signal, plotted across the 3D parameters space (CBV, R, $SO_2$) before adding the $T_2$.

Second, we also used the same computed dictionaries and reconstructed data from stroke animals. In Figure V.3.7, we show an example of the results of one slice from one of the 9

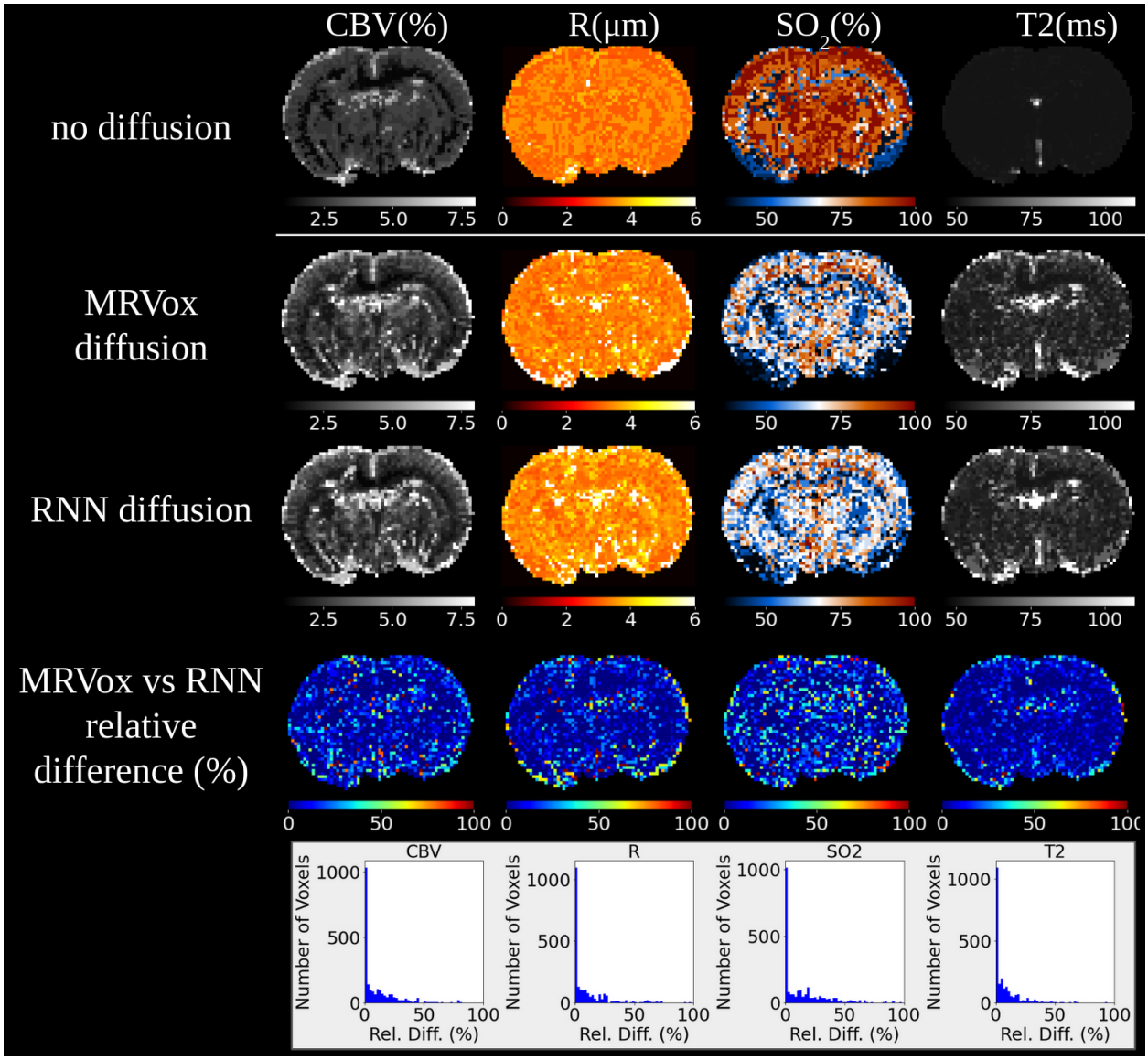


**Figure V.3.6**: Reconstructed maps computed from dictionaries in which the diffusion effects were simulated using MRVox or the proposed RNN model In the last line, relative difference maps are shown in %, threshold below 100%. Below the maps, detailed histograms of the density of relative difference values are shown for each parameter map.

stroke animals. As shown in the bottom lines of Figure V.3.7, the results are visually similar, and the RNN prediction error doesn't seem to disturb the quantitative maps. We effectively see the effect of diffusion compared to a match without diffusion (upper line).

Bland-Atlman plots are shown in Figure V.3.8 for healthy animals, and Figure V.3.9 for stroke animals, for each reconstructed parameter map across the three previously manually drawn ROIs. They show good agreement for all the estimated parameters in the whole brain as well as in the contralateral and the stroke areas separately. It is interesting to note that as expected, mean measurements of CBV, $SO_2$ and $T_2$ are lower in the stroke area than in the contralateral region.

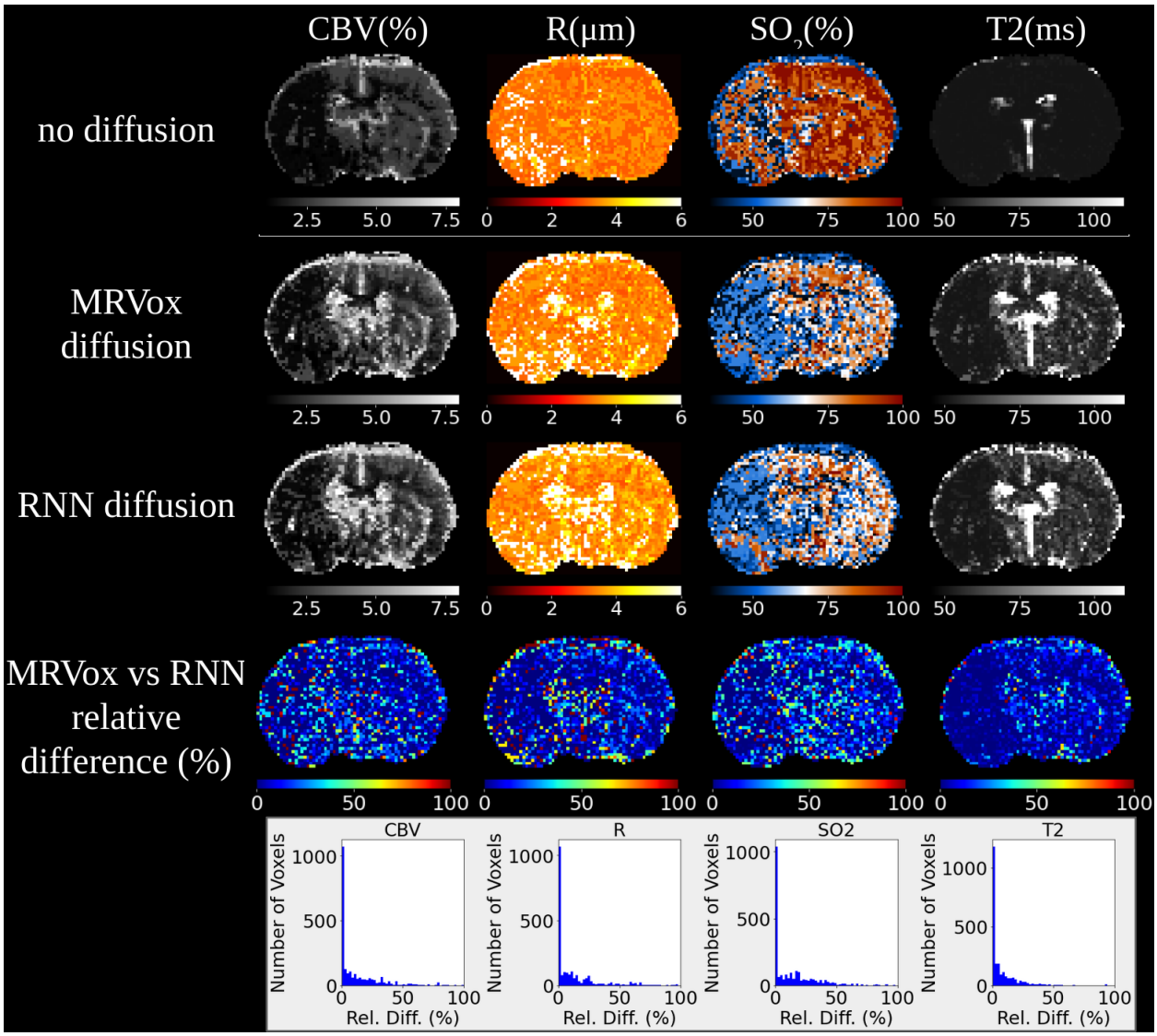


**Figure V.3.7**: Reconstructed maps on one of the stroke animals computed from dictionaries in which the diffusion effects were simulated using MRVox or the proposed RNN model In the last line, relative difference maps are shown in %, threshold below 100%. Below the maps, detailed histograms of the density of relative difference values are shown for each parameter map.

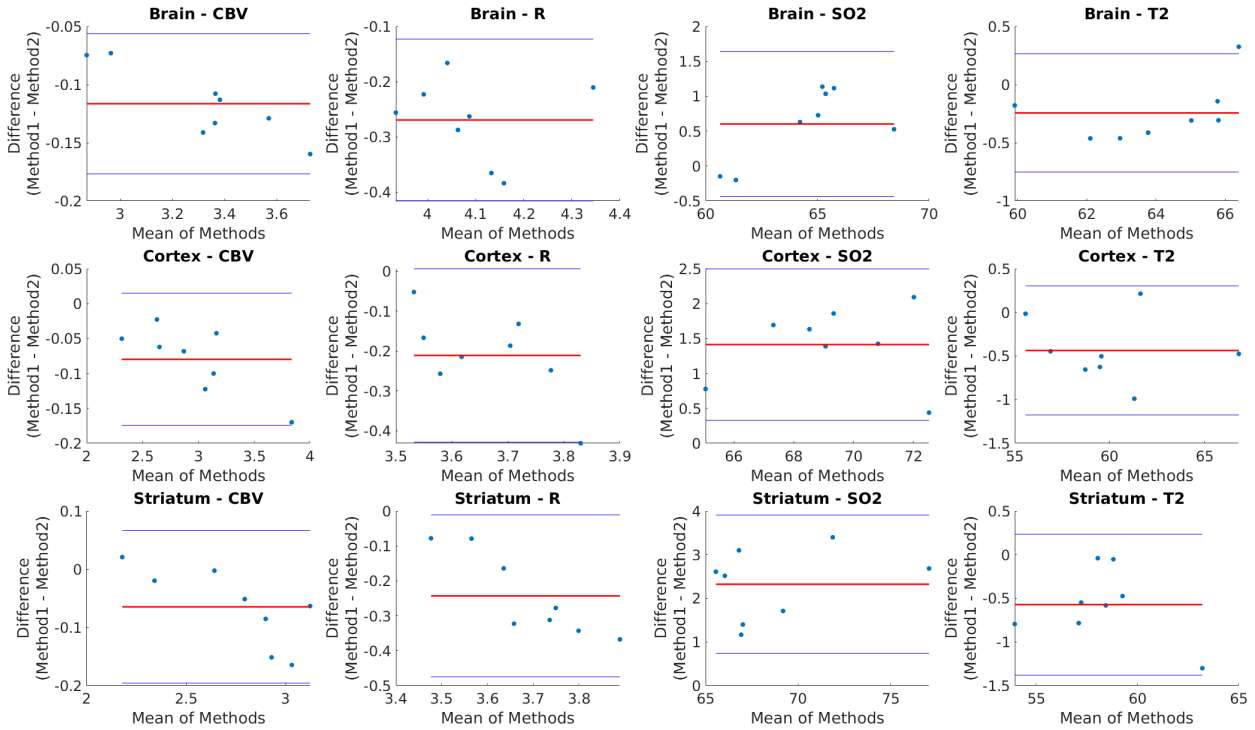


**Figure V.3.8**: Bland-Altman plots assess the differences in CBV, R, $SO_2$ and $T_2$ reconstructed using the MRVox diffusion dictionary and the RNN one, in 8 healthy animals.

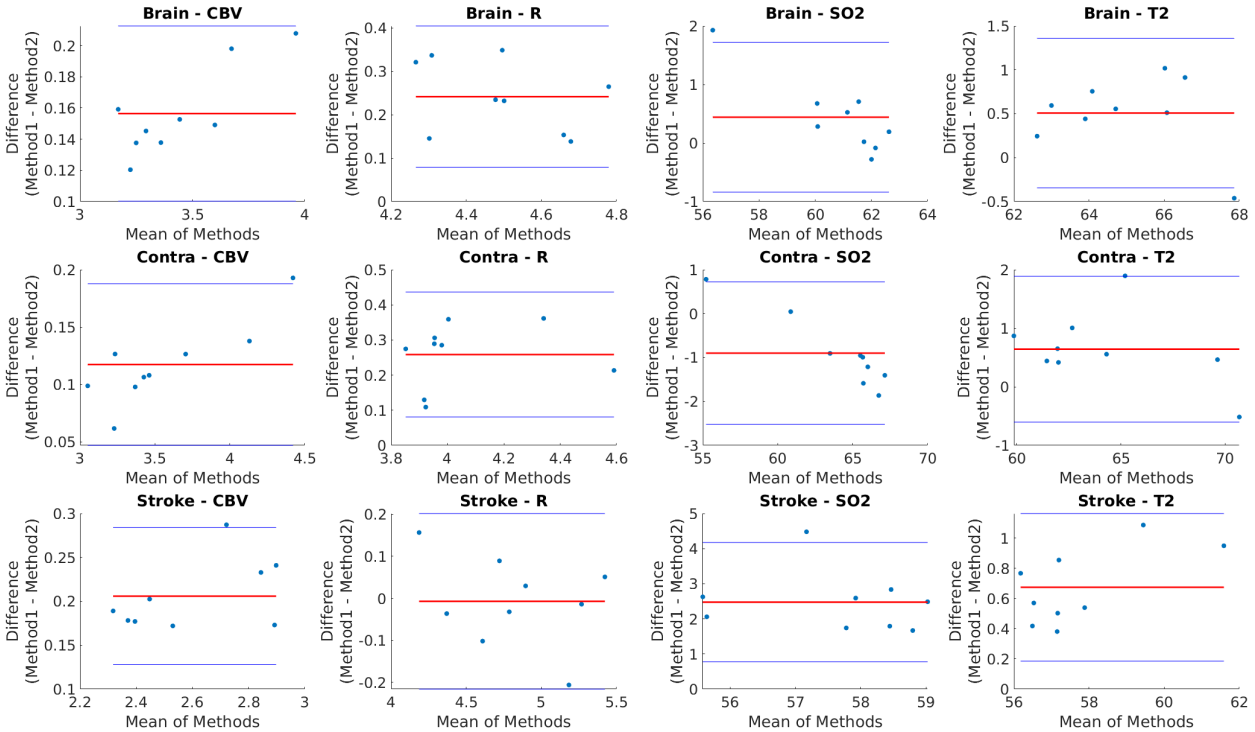


**Figure V.3.9**: Bland-Altman plots assess the differences in CBV, R, $SO_2$ and $T_2$ reconstructed using the MRVox diffusion dictionary and the RNN one, in 9 stroke animals.

### V.3.3 Combining both methods for large MRF dictionaries simulations

#### V.3.3.1 Small validation dictionary

Our first tests focused on reconstructing MRF parameter maps on healthy and stroke animals, using a 2,000-entry MRF dictionary simulated with MR-WAVES. Figure V.3.10a shows the NRMSE (%) computed across the whole parameters space between signals simulated with MRVox on one side and MR-WAVES on the other side. In Figure V.3.10b, examples of simulated signals from MR-WAVES (red) are compared with signals simulated with MRVox (blue).

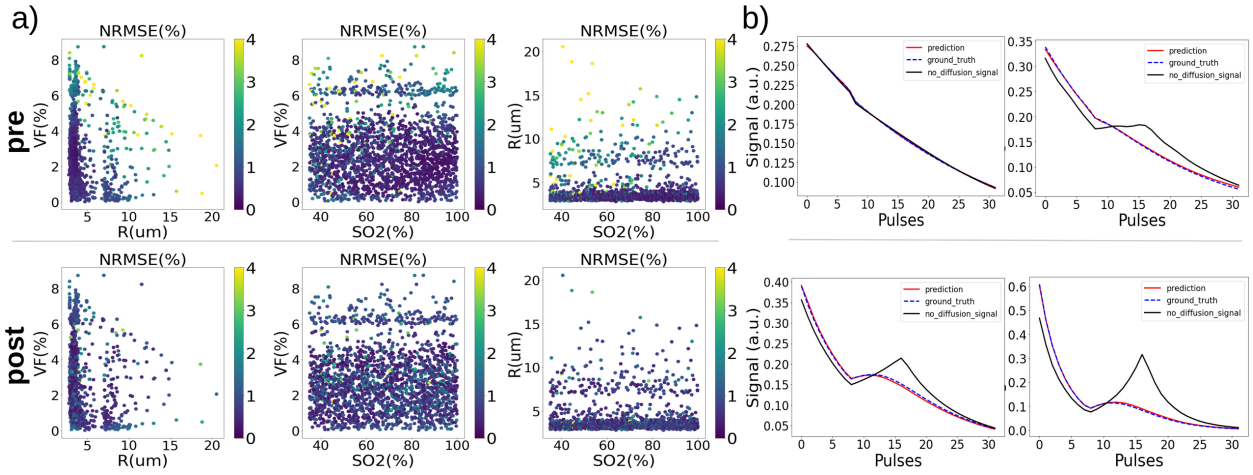


**Figure V.3.10**: a) NRMSE (%) computed across dictionary parameters space between both methods. b) Examples of signal predictions from the MR-WAVES model with the pre (first line) and the post-CA (last line) of the signals. MR-WAVES: red, no diffusion reference: MRVox, ground truth: MRVox. Left column: CBV=1.25%, R=3.60µm, $SO_2$=91.21%. Right column: CBV=2.85%, R=3.18µm, $SO_2$=52.47%. The WAVES simulation is made before $T_2$ relaxation representation, here $T_2$=100ms everywhere.

In Figure V.3.11, we show reconstructed MRF maps of CBV, R, $SO_2$ and $T_2$ computed with a dictionary without diffusion from MRVox; a dictionary with diffusion from MRVox; a dictionary where the diffusion has been added through the RNN after MRVox simulations; and finally the proposed MR-WAVES dictionary combining fast simulations and fast diffusion representation. Maps are shown for single-slice examples of one animal in each group (healthy and stroke). In Figure V.3.12, single-slice examples are shown for two other rats of each group, supplemented with relative difference maps and histogram of values across the voxels of the slice. Times of simulation in seconds are indicated below the description of each simulation method.

Visually, resulting maps computed from the MR-WAVES model are of the same quality as the reference MRVox computed maps. However, some non-negligible differences between the two simulators can be noticed, mainly located in the sinus area or the white matter regions of the rat brain. For the Distribution methods only, the differences were mainly located in these areas and the error in the MR-WAVES simulation could be related to this method more than the RNN prediction. We pursued this analysis through Bland-Atlman plots in the

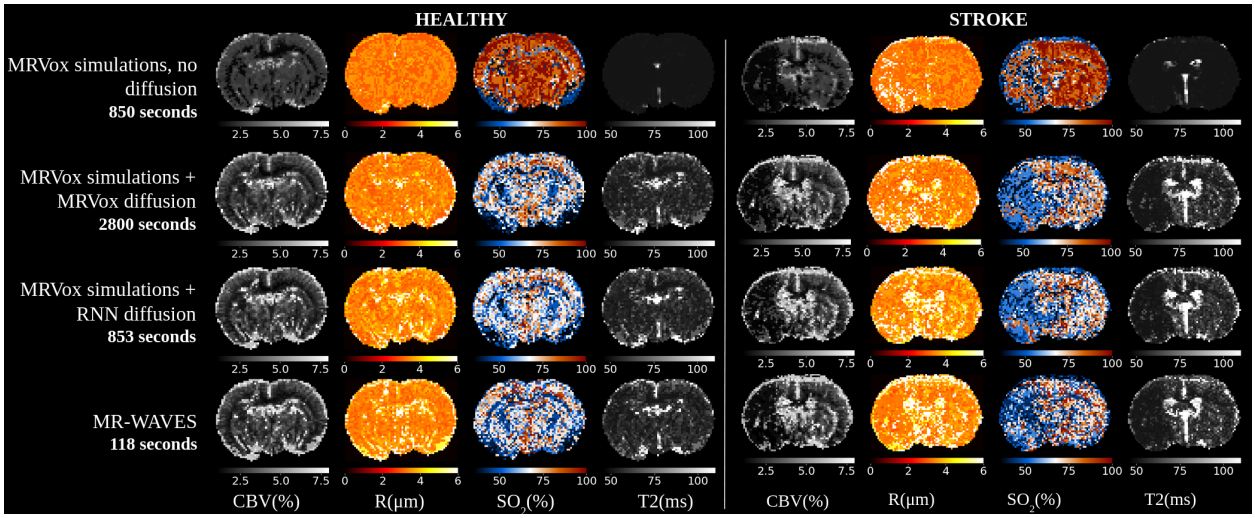


**Figure V.3.11**: Single-slice reconstructed MRF maps from dictionaries computed (from top to bottom line): (1) without diffusion in MRVox (2) with diffusion in MRVox (3) combining MRVox and RNN for the diffusion (4) with the proposed MR-WAVES pipeline. Right panel: healthy animal, left panel: stroke animal.

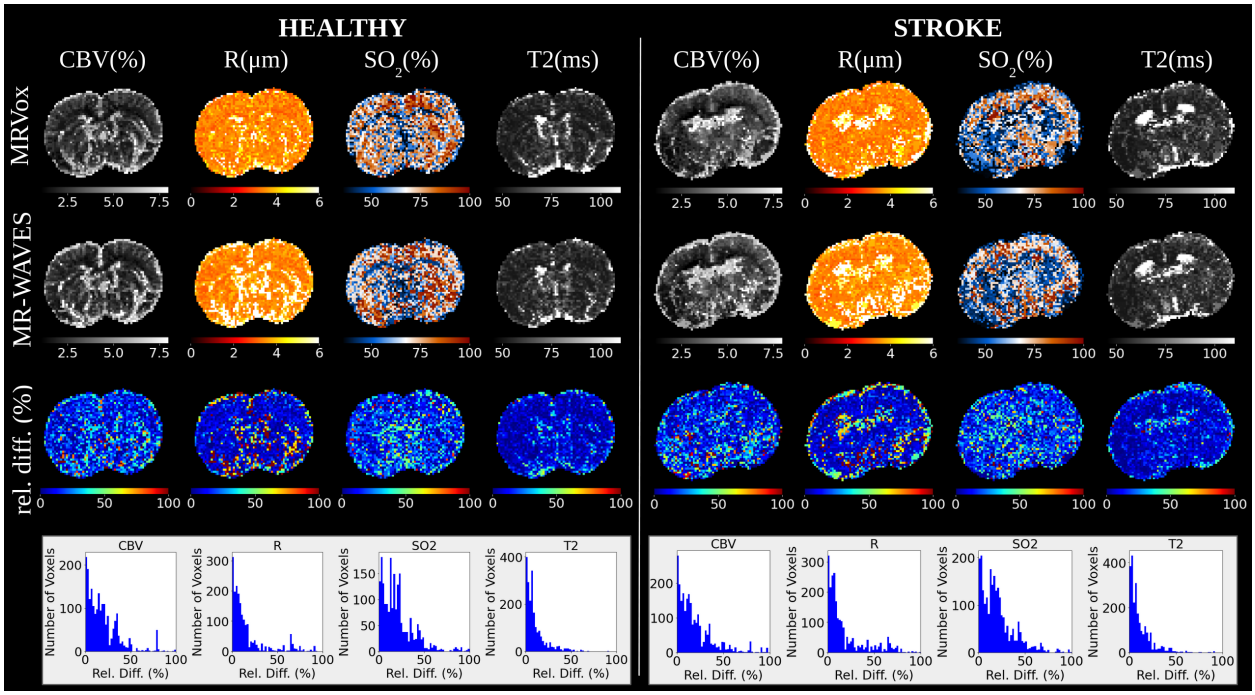


**Figure V.3.12**: Comparison of reconstructed maps matched in dictionaries from MRVox or MR-WAVES. In the last line, relative difference maps are shown in %. Below the maps, detailed histograms of the density of relative difference values are shown for each parameter map.

whole brain for healthy and stroke animal groups. Results are shown in Figure V.3.13 where the first line is focused on the N=8 healthy animals and the second line shows results for the N=9 stroke animals.

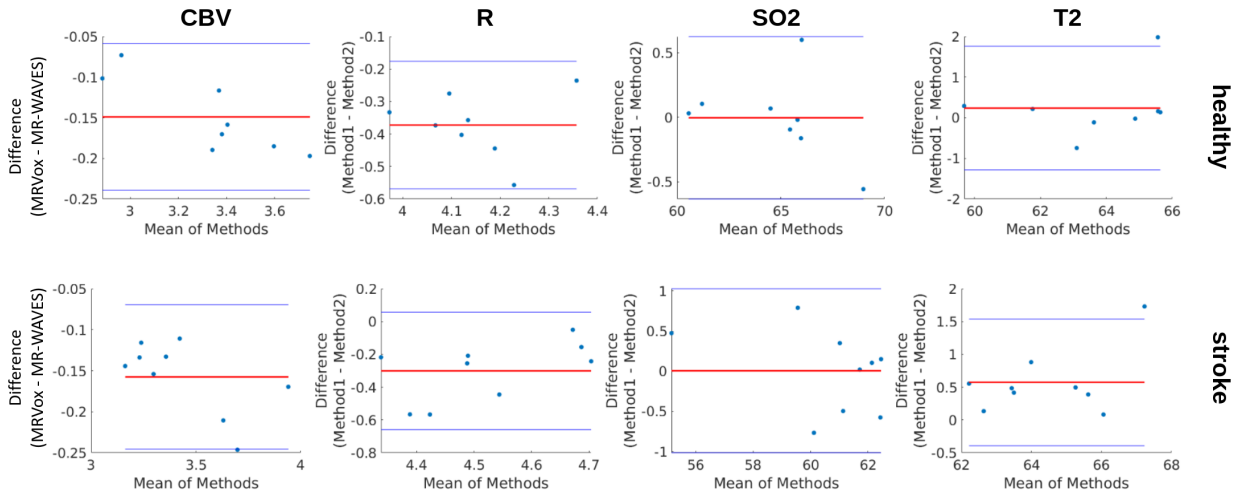


**Figure V.3.13**: Bland-Altman plots of the differences in CBV, R, $SO_2$, and $T_2$ reconstructed using the MRVox diffusion dictionary and the MR-WAVES computed one, in N=8 healthy animals (upper line) and N=9 stroke animals (bottom line).

For the CBV, the plot for healthy individuals shows a small bias of around -0.15, indicating that MR-WAVES tends to slightly overestimate CBV compared to MRVox. All data points fall within the limits of agreement (±1.96 SD), suggesting a good level of agreement between the methods for healthy subjects. A similar trend is observed in stroke patients, although the data points are more scattered, indicating increased variability, possibly due to pathological changes. Despite this, the overall agreement remains reasonable for CBV in stroke cases. For the R estimates, the healthy population plot reveals a larger bias of approximately -0.4, with all data points within the limits of agreement, though some variance is observed. In stroke patients, the spread of data points increases slightly, suggesting that stroke may introduce additional variability in the measurement of R. For the $SO_2$ parameter, healthy subjects exhibit minimal bias and excellent agreement between methods, as the differences hover around zero. However, in stroke patients, there is greater variability, with several points deviating further from the mean difference, suggesting that $SO_2$ measurements may be more affected by pathological conditions.
For $T_2$, the healthy population shows good agreement between methods, with a bias close to zero and minimal spread, indicating consistency. In contrast, for stroke patients, the $T_2$ plot reveals considerable variability, with a significant positive bias and larger scatter, especially near the upper limit of agreement. This suggests that $T_2$ measurements are less consistent between the two methods in the presence of stroke pathology, reflecting the greater complexity and alterations in tissue properties in these patients.
Overall, the Bland-Altman analysis highlights good agreement between MRVox and MR-WAVES in healthy subjects, while stroke conditions introduce more variability, particularly for $SO_2$ and $T_2$, which may be due to underlying physiological changes.

### V.3.3.2 Larger dictionary

Finally, we generated a large MRF dictionary of 90,000 entries. Using MR-WAVES and considering intra-voxel frequency distributions available precomputed in a large database

of tissue parameters, the first generation of the dictionary took 1440 seconds for pre and post-contrast signals inferred in 14 seconds using the RNN model, resulting in a total MR-WAVES simulation time of 1454 seconds. Based on our observation of the simulation time using MRVox linearly increasing with respect to the number of simulated signals (see Figure V.3.14a), the equivalent simulation of an MRF dictionary of 90,000 entries would take $1.26e6$ seconds (*i.e* 350 hours or more than two weeks) in MRVox. Thus, we observed an acceleration factor of 866 with the proposed MR-WAVES method. As shown in Figure V.3.14b, this factor of acceleration increases with the number of simulated signals, and thus MR-WAVES will be even more efficient for high-dimensional MRvF dictionaries generation.

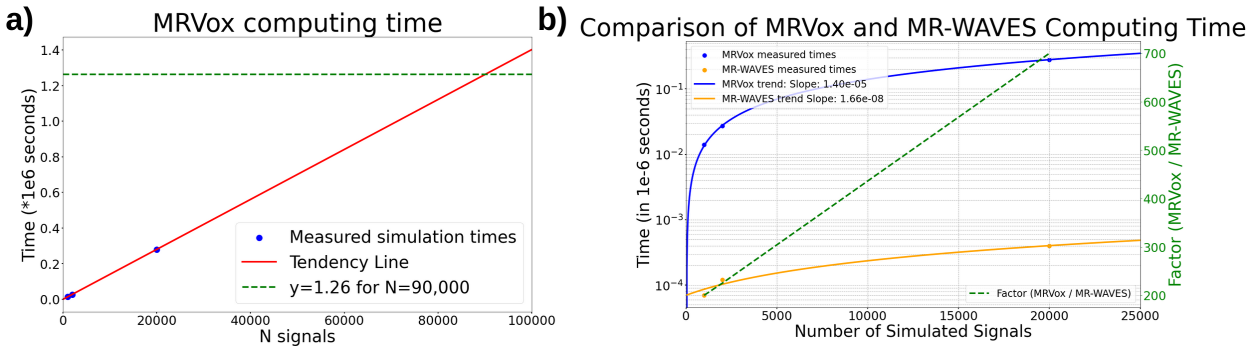


**Figure V.3.14**: a) MRVox simulation times. Blue markers are simulation times measured on simulated dictionaries. The red curve shows the linear tendency and the green dotted line highlights the expected simulation times for a 90,000-entry dictionary. b) MR-WAVES (orange) vs MRVox (blue) measured simulation times. The green line shows the computed acceleration factor between both methods for the measured values.

From this simulated large dictionary, we reconstructed MRF maps of CBV, R, $SO_2$ and $T_2$ on both animal groups. Examples of resulted maps for one slice of each animal are shown in Figure V.3.15 for the healthy group and Figure V.3.16 for the stroke group.

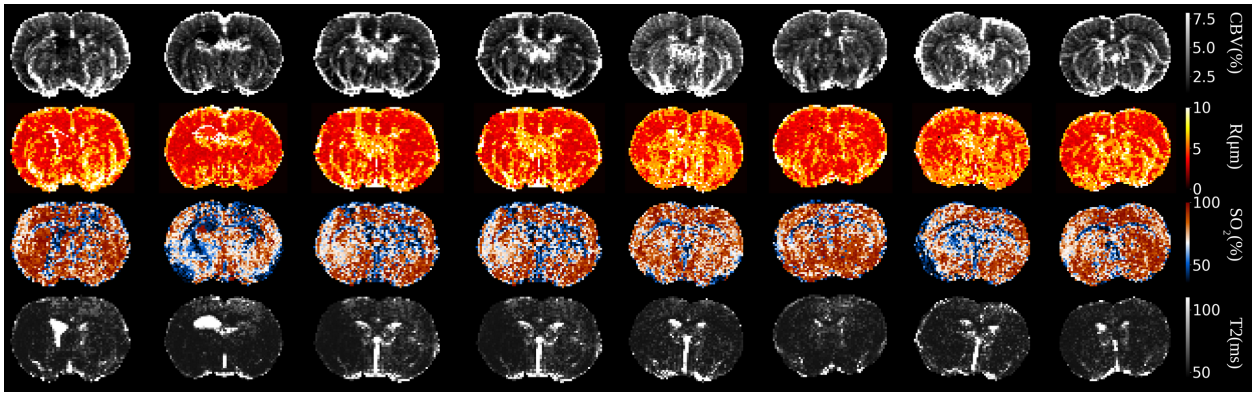


**Figure V.3.15**: MR-WAVES reconstructed maps on the N=8 healthy animals. Please note that R values are plotted between 0 and 10 µm here.

It can be observed that the results are different from those obtained with smaller dictionaries, especially for estimated values of R and $SO_2$ that seem to be increased whereas the CBV and $T_2$ values are consistent with previous observations but smoother because the sampling

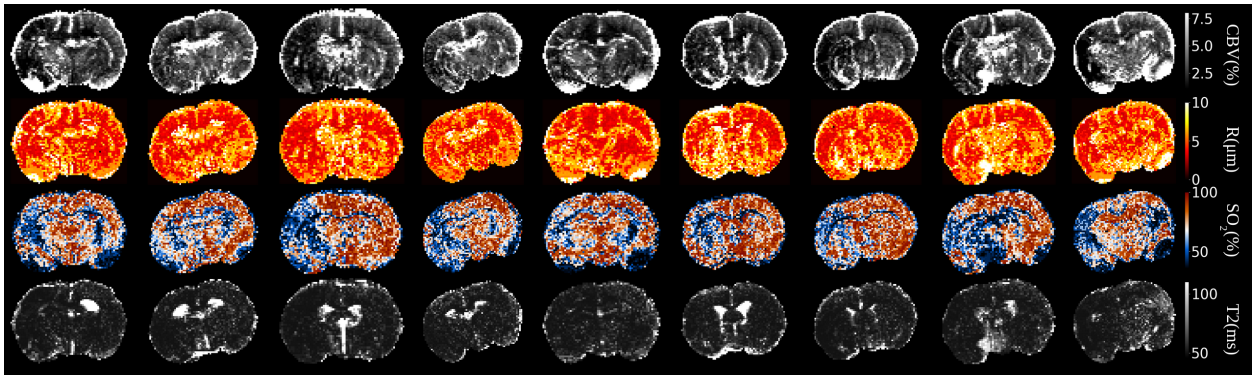


**Figure V.3.16**: MR-WAVES reconstructed maps on the N=9 stroke animals. Please note that R values are plotted between 0 and 10 µm here.

| | CBV (%) | R (µm) | $SO_2$ (%) | $T_2$ (ms) |
|---|---|---|---|---|
| **Healthy: brain** | 4.20±0.48 | 5.13±0.19 | 73.40±3.06 | 58.43±1.72 |
| **Healthy: cortex** | 3.30±0.75 | 4.41±0.33 | 79.28±2.18 | 55.21±1.63 |
| **Healthy: striatum** | 2.94±0.43 | 4.47±0.27 | 79.45±4.13 | 54.25±1.75 |
| **Pathological: brain** | 4.56±0.46 | 5.52±0.19 | 68.72±2.81 | 59.24±1.31 |
| **Pathological: contra** | 4.37±0.87 | 5.25±0.40 | 75.49±5.08 | 56.95±2.01 |
| **Pathological: stroke** | 3.20±0.32 | 5.39±0.27 | 61.31±3.40 | 55.05±1.74 |

**Table V.1**: Region of interest analysis for *in vivo* CBV, R, $SO_2$ and $T_2$ values in each group.

of the parameters in the dictionary is thiner. Table V.1 shows the mean estimated values for each parameter across the healthy and pathological stroke animal groups. In Figure V.3.17, detailed estimates are plotted for both animal groups with the corresponding standard deviation. The mean values observed in the stroke ROIs of the pathological group highlight deoxygenation in the lesion compared with the contralateral ROIs in the same animals and with the healthy group.

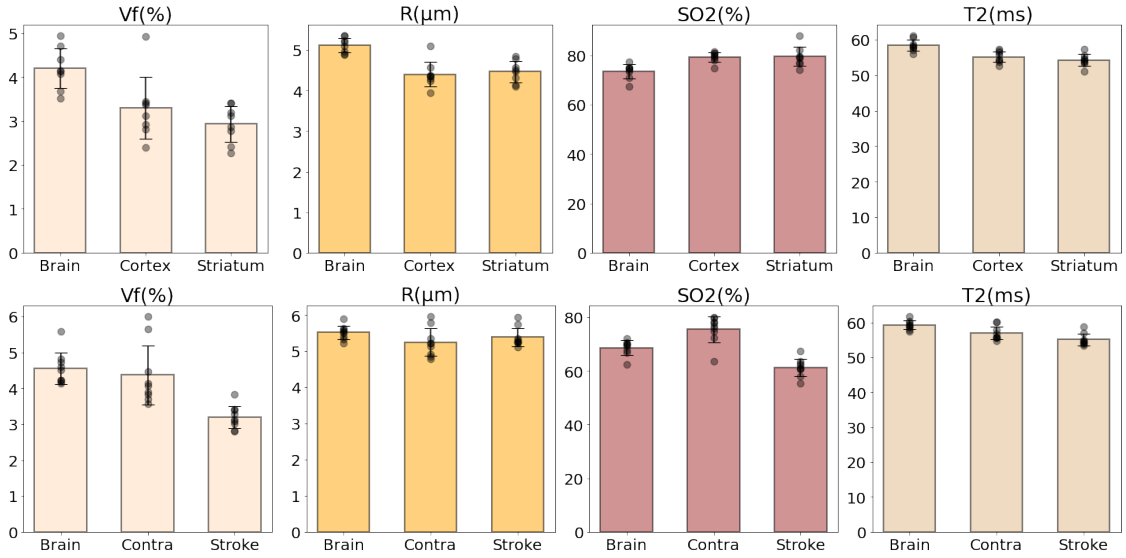


**Figure V.3.17**: MR-WAVES vascular and tissue parameter estimates in healthy (top) and stroke (bottom) animal groups. For the healthy group, comparisons are made across the brain, cortex, and striatum; for the stroke group, across the brain, contralateral (contra), and stroke-affected regions. Error bars indicate standard deviations.

## V.4 Discussion

In this chapter, we introduced MR-WAVES, a novel simulation method for incorporating water-diffusion and vascular effects into MRF dictionaries. By combining a simplified representation of intra-voxel magnetic field inhomogeneities with a recurrent neural network (RNN), MR-WAVES achieves over 800 times the computational speed of the previously proposed MRVox while maintaining comparable estimate quality. This method allows for the computation of parametric maps for CBV, R, $SO_2$, and $T_2$, while accounting for the effects of water diffusion.

Concerning the first fast simulation tools utilizing pre-computed intra-voxel frequency distributions, our results align closely with MRVox outputs, as confirmed by Bland-Altman analyses, although a slight bias exists between the two methods. In certain cases, particularly in animals with larger discrepancies, we suspect that suboptimal shimming during acquisition may have led to these outliers, as visible in the sinus area of Figure V.3.2, right panel. The difference between the two methods could result from their distinct approaches in representing magnetic field inhomogeneities. In our work, intra-voxel magnetic field maps were approximated with a 1Hz frequency step, while MRVox uses a higher-resolution field map. Refining our frequency sampling, particularly near the on-resonance frequency, could be a solution to improve our method's accuracy.

For the RNN implementation, two models were trained on separate datasets for pre-contrast and post-contrast signals, in line with the two-stage acquisition. We believe this approach minimizes errors that might arise from concatenating these signals. While the predicted signals showed an NRMSE of up to 4% compared to MRVox simulations, the reconstruction

remained effective in generating accurate quantitative maps for CBV, R, $SO_2$, and $T_2$. In stroke models, the stroke area showed lower CBV, $SO_2$, and $T_2$ values compared to the contralateral region, validating the method's ability to differentiate affected tissue.
The slight prediction errors appear to have a limited impact on matching, especially given the noise in acquired signals due to undersampling. However, during RNN training, we observed minor overfitting, which likely contributed to prediction errors for data outside the training parameter space. To address this, we propose to further employ data augmentation techniques or add dropout layers to the RNN architecture. Additionally, for longer sequences like MRF-bSSFP, more robust neural networks, such as LSTMs or BiLSTMs, could be considered.

When MR-WAVES was tested against an MRVox diffusion-simulated dictionary of 2,000 entries, as expected, differences in the reconstructed parametric maps were more pronounced. The approximation of intra-voxel inhomogeneities in the first part of MR-WAVES likely contributed to error propagation through the RNN. Specifically, the discrepancy between predicted and simulated $T_2$ maps increased when both methods were combined, likely because relaxation was modeled using a simple exponential form, introducing bias from prior simulation errors. Addressing this by incorporating $T_2$ from the beginning of the Bloch simulations could reduce these errors, although this would extend simulation time. In simulations involving larger dictionaries, R and $SO_2$ values were higher than those observed in the 2,000-entry experiment. This could result from differences in parameter distributions. With the 90,000-entry dictionary, our results are in line with the experiments conducted by Delphin et al. 2024 that have validated their method against histological and analytical estimations. Our $SO_2$ estimates specifically align in cases with a simplified cylindrical vascular model, though they exceed those derived from more realistic microscopy-based structures. This suggests that our non-spatial distribution function for field inhomogeneities might oversimplify the microvasculature representation and it supports the idea of increasing their frequency sampling before signal simulations.

Finally, we observed that our stroke models showed smaller oxygenation variations in pathological tissues compared to the previously studied tumor models (see Figure V.1.1), necessitating enhanced sensitivity to subtle oxygenation changes. MR-WAVES can be extended to accommodate multiple ADCs within the MRF dictionary, and preliminary tests indicate that the RNN successfully learns water-diffusion representations across different ADC values. This extension could enhance oxygenation measurements and enable the simultaneous estimation of ADC maps, crucial for stroke diagnosis.

# General Conclusion

In this thesis, we set out to address the imaging challenges associated with acute stroke patient management by advancing the capabilities of Magnetic Resonance Fingerprinting (MRF) for fast simultaneous multiparametric quantitative MRI. We extended the application of MR vascular Fingerprinting (MRvF) to estimate multiple relaxometry parameters, image contrasts, and microvascular properties in the human brain, with a particular focus on overcoming the reliance on contrast-agent injection—a significant limitation for rapid clinical diagnostics.

Our initial efforts concentrated on implementing novel MRF methods to achieve fast and realistic numerical simulations, efficient acquisition processes, and robust reconstruction of quantitative relaxometry ($T_1$, $T_2$) maps. Leveraging extensive literature on MRF applications, we developed a state-of-the-art pipeline using in-house Matlab/Python code. By combining these simulations and reconstruction tools into the framework, we effectively corrected for scanner imperfections, such as slice profile effects and $B_1$ field inhomogeneities. This pipeline supports the free design of MRF sequences, which can be applied under various acquisition parameters and undersampling schemes at the scanner.
Additionally, low-rank compression methods were employed to reduce the computational load, resulting in a protocol that is both fast and close to clinical applicability. This enhanced protocol extends relaxometry estimates to extract comprehensive information relevant to human stroke imaging, including standard angiographic-like contrast images and blood volume fraction estimates using a new multi-compartment approach that accounts for blood, non-blood, and fluid components. These tools were tested through *in vivo* acquisitions on human volunteers. While this method offered an initial response to the challenges outlined in this thesis, the first results show a limited ability to realistically characterize microstructures based solely on relaxometric measurements.

Building on the conclusions of the first phase of our work, we focused on the design of new sequences that could be more sensitive to microvascular effects. We sought to exploit the sensitivity of MR signals to the BOLD effect, which relies on changes in blood oxygenation levels that directly affect the magnetic properties of the blood and consequently the MRI signal. Traditionally, this effect has been exploited with contrast-agent injection and spoiled GRE sequences to estimate microvascular properties. However, studies have highlighted the inherent sensitivity of balanced GRE sequences to magnetic field inhomogeneities, even without contrast agents. We conducted a detailed analysis of these properties, comparing the behavior of spoiled and balanced sequences in response to magnetic field distributions across various acquisition parameters. This analysis led us to hypothesize that a carefully designed bSSFP sequence, integrated with an appropriate MRF framework, could provide valuable microstructural information without the need for contrast agents. We proceeded to design an optimal bSSFP sequence based on *in silico* simulations and predictions of encoding capabilities using tailored sensitivity evaluation functions.

Following these developments, we tested our hypothesis through an *in vivo* study involving several healthy volunteers. Drawing on previous MRvF studies, where microscopy-segmented voxels in the mouse brain were extended to simulations of magnetic field inhomogeneities in the human brain, we incorporated these insights into our numerical simulations. By combining these simulations with the optimized bSSFP scheme, our preliminary results proposed the simultaneous estimation of ($T_1$, $T_2$, $T_2^*$) relaxometry maps, magnetic fields ($B_1$, $B_0$), and microvascular properties (CBV, R) within a single acquisition, without the use of contrast agents. The first results display a very interesting contrast between grey matter and white matter CBV with a measured ratio of 2 as expected in the literature. Moreover, big vessel areas such as the sagittal sinus region exhibit large CBV and R values. While the relaxometry and magnetic field measurements were properly validated against standard sequences, further validation of CBV and R estimates against traditional contrast-based methods is still necessary to fully establish the efficacy of our approach.

Despite the promising results, the proposed bSSFP MRF method introduces significant technical challenges, particularly in terms of computational complexity. The high-dimensional nature of MR vascular Fingerprinting, coupled with the need for high-resolution acquisitions across numerous parameters, exacerbates the "curse of dimensionality." Given the limited resources available in MRI scanner software and the need for rapid scan times, this poses a challenge. To address this, we adopted a two-pronged approach. First, in collaboration with the INRIA Statify team, we developed a low-rank subspace representation of the MRF dictionary using mixtures of Gaussian distributions, resulting in memory-efficient dictionaries and faster matching times in reduced dimensions. Second, we trained a Bidirectional LSTM neural network to predict quantitative parameter maps directly from MRF acquisitions, eliminating the need for dictionary matching and significantly reducing generation time and memory requirements. We called this approach MARVEL. Both techniques were validated against standard dictionary matching references in *in vivo* acquisitions, each offering unique advantages in reducing computational costs and reconstruction times. Moving forward, we aim to combine these two methods into a single neural network trained on low-rank data, thereby combining the benefits of both approaches. These advances represent a significant step towards bridging the gap between the proposed method and its clinical application.

In the final chapter of this manuscript, we addressed the need for two additional imaging biomarkers critical for stroke imaging that had been previously overlooked: water diffusion and oxygen saturation ($SO_2$). Although earlier MRvF studies already incorporated these effects into MRF dictionaries, the simulation tools used were highly time-consuming, limiting the scope of the computations and the parameter grid sampling, which ultimately reduced the accuracy of the estimates. Our contributions here were twofold: First, using the novel vascular simulation method introduced in Chapter III, we significantly sped up the protocol for simulation without diffusion effects. Second, by employing a deep learning approach using a GRU-RNN, we accelerated the incorporation of water diffusion effects into MRF dictionaries by a factor of over 800. To address the lack of human data, we validated this combined process, named MR-WAVES, through *in vivo* studies on healthy and stroke animal models, benchmarking it against the reference software, MRVox. Our results were very encouraging and several potential optimization steps can already be foreseen. While the retrospective data were acquired using a spoiled-GRE sequence and a contrast agent, the proposed algorithm

has been designed to adapt to any sequence type, facilitating future translation to human data acquired without the use of contrast agents, as proposed in this thesis.

In conclusion, this manuscript presents a first proposition for the contrast-free simultaneous generation of multiparametric maps, including relaxometry characteristics, magnetic fields, and microvascular properties, alongside usual contrast images in the human brain. In Figure V.4.1, the proposed MRF framework is illustrated with the integration of the tools developed during this thesis. As a key contribution to a broader research initiative focused on improving stroke patient management through innovative imaging techniques, this work lays a substantial foundation for the fast, efficient, and robust imaging of cerebrovascular disease pipelines. As a contribution to open science, the code of the tools that have been developed during this thesis is available online:

- MR-WAVES (MR Water-diffusion And Vascular Effects Simulations) allows fast simulations of MR signals accounting microvascular contributions and water-diffusion effect.
- MARVEL (MR Fingerprinting with Additional micRoVascular Estimates using bidirectional LSTMs) allows the simultaneous and fast high-dimensional MRF reconstruction of relaxometry, magnetic field, and microvascular properties maps.

In the near future, we can already foresee two lines of technical development before we can offer our protocol as a clinical tool.
Firstly, by validating the current results. These will be carried out on animals in a controlled environment and on healthy volunteers injected with CA to validate the microvasculature maps and on certain stroke patients to check the relaxometry maps. These latter tests will enable us to determine if it is possible to replace at least a few standard MRI sequences in a protocol that is already time-sensitive.
Secondly, by working on optimizing MRF sequences in terms of acquisition time. This will be done by simultaneously improving the design of the sequences and the way the data is collected in 3D k-space. This step is now feasible thanks to the flexible and fast tools (simulation and reconstruction) that we put in place during the thesis. We have already started to work on an automatic sequence search method based on simulation tools that incorporate spatial gradient configuration (KomaMRI), sequences defined in a vendor-independent language called Pulseq, and automatic optimization algorithms in the form of reinforcement learning. As already mentioned earlier in this manuscript, studies are also being carried out in parallel in the laboratory on the development of synthetic MRI to provide weighted images of clinical utility from our MRF sequence. These developments could also benefit from this automatic optimization pipeline.
Finally, although it has not been developed in this manuscript, the development of a set of MRF tools for correcting patient movement artifacts will be needed before the clinical acceptance of our protocol.

Once validated, the tools and concepts developed in this thesis for the difficult context of stroke should also be transposable to other pathologies such as cancer or neurodegenerative diseases, with the possibility to trade acquisition times for the measurements of new biomarkers.

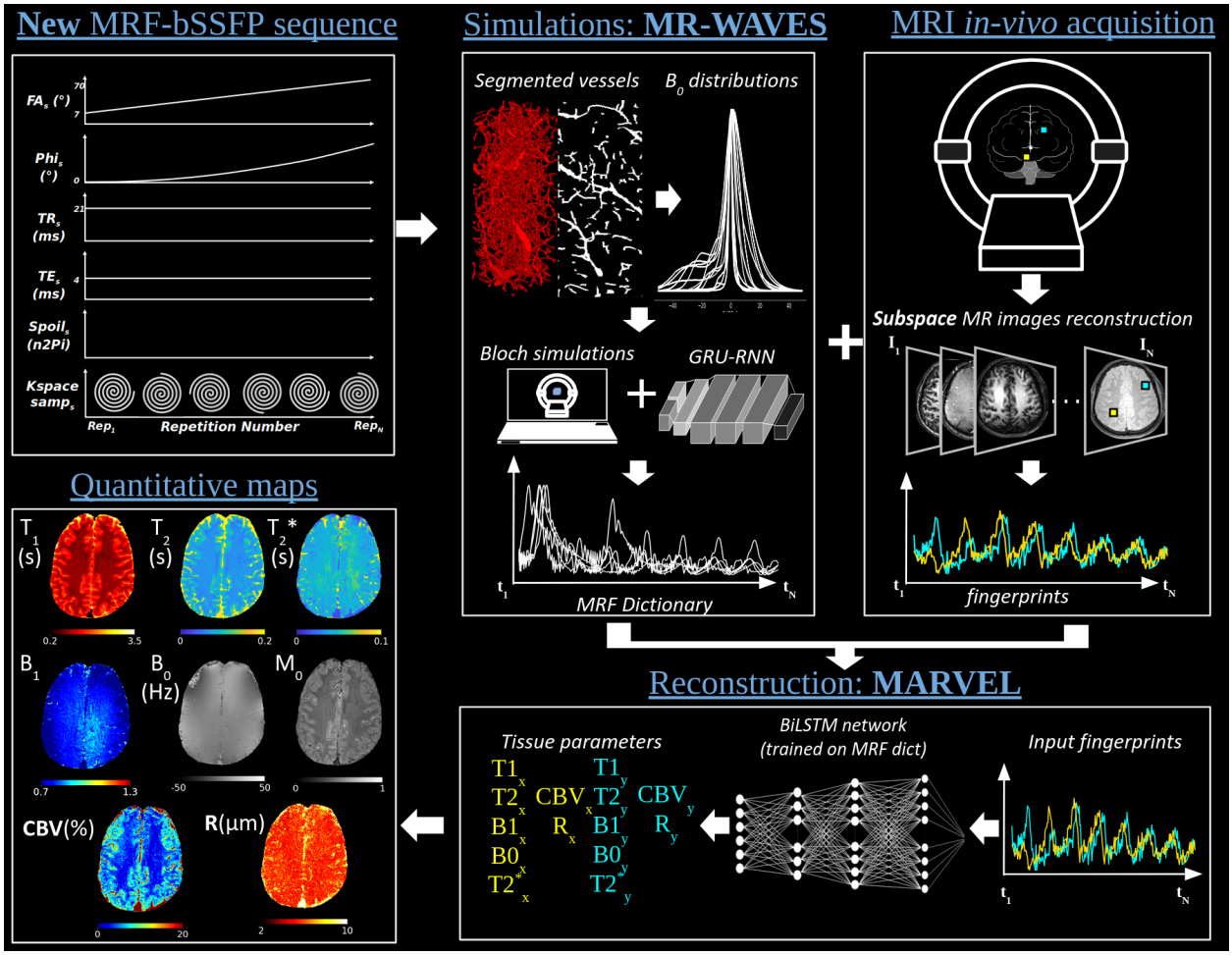


**Figure V.4.1**: Illustration of our proposed MRF framework. Data was obtained at 3T (Philips; IRMaGe) on a healthy volunteer.

# Bibliography


Albers, G. W. et al., Thrombectomy for Stroke at 6 to 16 Hours with Selection by Perfusion Imaging, The New England Journal of Medicine **378**, 708 (2018).

Assländer, J., A perspective on MR fingerprinting, Journal of magnetic resonance imaging : JMRI **53**, 676 (2021).

Assländer, J., M. A. Cloos, F. Knoll, D. K. Sodickson, J. Hennig and R. Lattanzi, Low Rank Alternating Direction Method of Multipliers Reconstruction for MR Fingerprinting, Magnetic Resonance in Medicine **79**, 83 (2018).

Assländer, J., S. J. Glaser and J. Hennig, Pseudo Steady-State Free Precession for MR-Fingerprinting, Magnetic Resonance in Medicine **77**, 1151 (2017).

Balzano, L., Y. Chi and Y. M. Lu, "Streaming PCA and Subspace Tracking: The Missing Data Case", *Proceedings of the IEEE*, (2018).

Barbieri, M., L. Brizi, E. Giampieri, F. Solera, D. N. Manners, G. Castellani, C. Testa and D. Remondini, A deep learning approach for magnetic resonance fingerprinting: Scaling capabilities and good training practices investigated by simulations, Physica medica **89**, 80 (2021).

Barrier, A., T. Coudert, A. Delphin, L. Legris, J. Warnking, E. Barbier and T. Christen, "Reconstructions de cartes multi-paramétriques haute dimension accélérées via LSTM bidirectionnel et IRM Fingerprint.", *IABM2024 conference, March 2024, Grenoble*, (2024).

Barrier, Antoine and Coudert, Thomas, A. Delphin, B. Lemasson and C. Thomas, MARVEL: MR Fingerprinting with Additional micRoVascular Estimates using bidirectional LSTMs, Proceeding of MICCAI 2024 (2024).

Bejot, Y., H. Bailly, J. Durier and M. Giroud, Epidemiology of stroke in Europe and trends for the 21st century, La Presse MÃ©dicale **45**, e391 (2016).

Bellas, A., C. Bouveyron, M. Cottrell and J. Lacaille, Model-based Clustering of High-dimensional Data Streams with Online Mixture of Probabilistic PCA, Advances in Data Analysis and Classification **7**, 281 (2013).

Benkert, T., P. Ehses, M. Blaimer, P. M. Jakob and F. A. Breuer, Dynamically phase-cycled radial balanced SSFP imaging for efficient banding removal, Magnetic Resonance in Medicine **73**, 182 (2015).

Bieri, O. and K. Scheffler, Fundamentals of balanced steady state free precession MRI, Journal of Magnetic Resonance Imaging **38**, 2 (2013).

Biondetti, E., J. Cho and H. Lee, Cerebral oxygen metabolism from MRI susceptibility, NeuroImage **276**, 120189 (2023).

Bjørnerud, A. and K. Emblem, A fully automated method for quantitative cerebral hemodynamic analysis using DSC-MRI, J Cereb Blood Flow Metab **30**, 1066 (2010).

Bloch, F., Nuclear Induction, Phys. Rev. **70**, 460 (1946).

Bobman, S. A., S. J. Riederer, J. N. Lee, S. A. Suddarth, H. Z. Wang, B. P. Drayer and J. R. MacFall, Cerebral magnetic resonance image synthesis, AJNR. American journal of neuroradiology **6**, 265 (1985).

Bouveyron, C. and C. Brunet-Saumard, Model-based clustering of high-dimensional data: A review, Computational Statistics & Data Analysis **71**, 52 (2014).

Bouveyron, C., S. Girard and C. Schmid, High-dimensional data clustering, Computational statistics & data analysis **52**, 502 (2007).

Boux, F., F. Forbes, J. Arbel, B. Lemasson and E. Barbier, Bayesian Inverse Regression for Vascular Magnetic Resonance Fingerprinting, IEEE Transactions on Medical Imaging **40**, 1827 (2021).

Boyacioglu, R., C. Wang, D. Ma, D. McGivney, X. Yu and M. Griswold, 3D magnetic resonance fingerprinting with quadratic RF phase, Magnetic Resonance in Medicine **85** (2020).

Brown, R. W., Y.-C. N. Cheng, E. M. Haacke, M. R. Thompson and R. Venkatesan (2014), "Fast Imaging in the Steady State", *Magnetic Resonance Imaging*, John Wiley & Sons, Ltd, chap. 18, 447.

Buonincontri, G. and S. Sawiak, MR fingerprinting with simultaneous B1 estimation, Magnetic Resonance in Medicine **76**, 1127 (2016).

Buonincontri, G., R. F. Schulte, M. Cosottini and M. Tosetti, Spiral MR fingerprinting at 7T with simultaneous B1 estimation, Magnetic Resonance Imaging **41**, 1 (2017).

Cabini, R. F., L. Barzaghi, D. Cicolari, P. Arosio, S. Carrazza, S. Figini, M. Filibian, A. Gazzano, R. Krause, M. Mariani, et al., Fast deep learning reconstruction techniques for preclinical magnetic resonance fingerprinting, NMR in Biomedicine **37**, e5028 (2024).

Calamante, F., D. Gadian and A. Connelly, Quantification of Perfusion Using Bolus Tracking Magnetic Resonance Imaging in Stroke, Stroke **33**, 1146 (2002).

Cappé, O. and E. Moulines, On-line expectation–maximization algorithm for latent data models, Journal of the Royal Statistical Society Series B: Statistical Methodology **71**, 593 (2009).

Carr, H. Y., Steady-State Free Precession in Nuclear Magnetic Resonance, Physical Review **112**, 1693 (1958).

Cauley, S. F., K. Setsompop, D. Ma, Y. Jiang, H. Ye, E. Adalsteinsson, M. A. Griswold and L. L. Wald, Fast group matching for MR fingerprinting reconstruction, Magnetic resonance in medicine **74**, 523 (2015).

Chen, W., S. Foxley and K. Miller, Detecting microstructural properties of white matter based on compartmentalization of magnetic susceptibility, NeuroImage **70**, 1 (2013).

Chen, Y., M. Chen, K. Baluyot, T. Potts, J. Jimenez, W. Lin and bibinitperiod U. B. C. P. Consortium, MR fingerprinting enables quantitative measures of brain tissue relaxation times and myelin water fraction in the first five years of life, NeuroImage **186**, 782 (2019).

Chen, Y., Y. Jiang, S. Pahwa, D. Ma, L. Lu, M. D. Twieg, K. L. Wright, N. Seiberlich, M. A. Griswold and V. Gulani, MR Fingerprinting for Rapid Quantitative Abdominal Imaging, Radiology **279**, 278 (2016).

Christen, T., D. Bolar and G. Zaharchuk, Imaging Brain Oxygenation with MRI Using Blood Oxygenation Approaches: Methods, Validation, and Clinical Applications, AJNR. American journal of neuroradiology **34** (2012).

Christen, T., P. Bouzat, N. Pannetier, N. Coquery, A. Moisan, B. Lemasson, S. Thomas, E. Grillon, O. Detante, C. Rémy, J.-F. Payen and E. L. Barbier, Tissue Oxygen

Saturation Mapping with Magnetic Resonance Imaging, Journal of Cerebral Blood Flow & Metabolism **34**, 1550 (2014).

Christen, T., H. Jahanian, W. Ni, D. Qiu, M. Moseley and G. Zaharchuk, Noncontrast Mapping of Arterial Delay and Functional Connectivity Using Resting-State Functional MRI: A Study in Moyamoya Patients, Journal of magnetic resonance imaging : JMRI **41** (2015).

Christen, T., B. Lemasson, N. Pannetier, R. Farion, C. Segebarth, C. Rémy and E. Barbier, Evaluation of a quantitative blood oxygenation level-dependent (qBOLD) approach to map local blood oxygen saturation [Internet], NMR in biomedicine **24**, 393 (2010).

Christen, T., N. Pannetier, W. W. Ni, D. Qiu, M. E. Moseley, N. Schuff and G. Zaharchuk, MR vascular fingerprinting: A new approach to compute cerebral blood volume, mean vessel radius, and oxygenation maps in the human brain, Neuroimage **89**, 262 (2014).

Cloos, M. A., F. Knoll, T. Zhao, K. T. Block, M. Bruno, G. C. Wiggins and D. K. Sodickson, Multiparametric imaging with heterogeneous radiofrequency fields, Nature Communications **7**, 12445 (2016).

Cohen, O. and M. S. Rosen, Algorithm comparison for schedule optimization in MR fingerprinting, Magnetic Resonance Imaging **41**, 15 (2017).

Cohen, O., B. Zhu and M. S. Rosen, Deep Learning for Rapid Sparse MR Fingerprinting Reconstruction, CoRR **abs/1710.05267** (2017).

Costelloe, C. M., B. Amini and J. E. Madewell, Risks and Benefits of Gadolinium-Based Contrast-Enhanced MRI, Seminars in ultrasound, CT, and MR **41**, 170 (2020).

Coudert, T., A. Delphin, L. Legris, A. Barrier, J. Warnking, D. Chechin, L. Lamalle, P. Mazurkewitz, P. Koken, E. Barbier, M. Doneva and T. Christen, Contrast-free Blood Volume, Microvascular Properties and Relaxometry mapping using bSSFP MR Fingerprinting ().

Coudert, T., A. Delphin, L. Legris, A. Barrier, J. M. Warnking, D. Chechin, L. Lamalle, P. Mazurkewitz, P. Koken, E. L. Barbier, M. Doneva and T. Christen, "Contrast-free Blood Volume, Microvascular Properties and Relaxometry mapping using bSSFP MR Fingerprinting", *2024 ISMRM Annual Meeting & Exhibition, Singapour*, (2024).

Coudert, T., A. Delphin, J. M.Warnking, E. L. Barbier and T. Christen, "Réseaux de neurones profonds pour la simulation de signaux IRM pour l'IRM Fingerprint vasculaire.", *IABM2023 conference, March 2023, Paris*, (2023).

Coudert, T., A. Delphin, J. M.Warnking, E. L. Barbier and T. Christen, "Utilisation de séquences de type MR Fingerprint bSSFP pour les mesures T2* et la quantification de l'effet BOLD.", *SFRMBM2023 conference, March 2023, Paris*, (2023).

Coudert, T., A. Delphin, J. M. Warnking, B. Lemasson, E. L. Barbier and T. Christen, "Searching for an MR Fingerprinting sequence to measure brain oxygenation without contrast agent", *ISMRM 31st Annual Meeting & Exhibition, May 2022, London, United Kingdom*, (2022).

Coudert, T., A. Delpin, A. Barrier, L. Legris, J. M. Warnking, L. Lamalle, M. Doneva, B. Lemasson, E. L. Barbier and T. Christen, Relaxometry and contrast-free cere-

bral microvascular quantification using balanced Steady-State Free Precession MR Fingerprinting, Submitted to Magnetic Resonance in Medicine (2024).

Çukur, T., M. Lustig and D. G. Nishimura, Multiple-profile homogeneous image combination: Application to phase-cycled SSFP and multicoil imaging ().

Deleforge, A., F. Forbes and R. Horaud, High-Dimensional Regression with Gaussian Mixtures and Partially-Latent Response Variables, Statistics & Computing **25**, 893 (2015).

Delphin, A., F. Boux, C. Brossard, T. Coudert, J. Warnking, B. Lemasson, E. Barbier and T. Christen, Enhancing MR Vascular Fingerprinting through Realistic Microvascular Geometries, Imaging Neuroscience (2024).

Delphin, A., T. Coudert, A. Fan, M. Moseley, G. Zaharchuk and T. Christen, "MR Vascular Fingerprinting with 3D Realistic Blood Vessel Structures and Machine Learning to Assess Oxygenation Changes in Human Volunteers", *2023 ISMRM & ISMRT Annual Meeting & Exhibition*, (2023).

Demeestere, J., A. Wouters, S. Christensen, R. Lemmens and M. G. Lansberg, Review of Perfusion Imaging in Acute Ischemic Stroke, Stroke **51**, 1017 (2020).

Deshmane, A., C. Badve, M. Rogers, A. Yu, D. Ma, J. Sunshine, V. Gulani and M. Griswold, Tissue mapping in brain tumors with partial volume magnetic resonance fingerprinting (PV-MRF). ().

Donahue, M. J. et al., Consensus statement on current and emerging methods for the diagnosis and evaluation of cerebrovascular disease, Journal of Cerebral Blood Flow & Metabolism **38**, 1391 (2018).

Doneva, M., T. Amthor, P. Koken, K. Sommer and P. BÃ¶rnert, Matrix completion-based reconstruction for undersampled magnetic resonance fingerprinting data, Magnetic Resonance Imaging **41**, 41 (2017).

Ebinger, M., P. Brunecker, G. J. JungehÃ¼lsing, U. Malzahn, C. Kunze, M. Endres and J. B. Fiebach, Reliable Perfusion Maps in Stroke MRI Using Arterial Input Functions Derived From Distal Middle Cerebral Artery Branches, Stroke **41**, 95 (2010).

Emblem, K., K. Mouridsen, A. Bjørnerud, C. Farrar, D. Jennings, R. Borra, P. Wen, P. Ivy, T. Batchelor, B. Rosen, R. Jain and A. Sorensen, Vessel Architectural Imaging Identifies Cancer Patient Responders to Anti-angiogenic Therapy, Nature medicine **73** (2013).

Fang, Z., Y. Chen, S.-C. Hung, X. Zhang, W. Lin and D. Shen, Submillimeter MR fingerprinting using deep learning-based tissue quantification, Magnetic Resonance in Medicine **84**, 579 (2020).

Fang, Z., Y. Chen, M. Liu, L. Xiang, Q. Zhang, Q. Wang, W. Lin and D. Shen, Deep Learning for Fast and Spatially Constrained Tissue Quantification From Highly Accelerated Data in Magnetic Resonance Fingerprinting, IEEE transactions on medical imaging **38**, 2364 (2019).

Fort, G., E. Moulines and H. T. Wai, "A stochastic path-integrated differential estimator Expectation Maximization algorithm", *34th Conference on Neural Information Processing Systems (NeurIPS)*, (2020).

Fukunaga, M., T.-Q. Li, P. van Gelderen, J. A. de Zwart, K. Shmueli, B. Yao, J. Lee, D. Maric, M. A. Aronova, G. Zhang, R. D. Leapman, J. F. Schenck, H. Merkle, J. H. Duyn and L. G. Ungerleider, Layer-Specific Variation of Iron Content

in Cerebral Cortex as a Source of MRI Contrast, Proceedings of the National Academy of Sciences of the United States of America **107**, 3834 (2010).

Gelman, N., J. R. Ewing, J. M. Gorell, E. M. Spickler and E. G. Solomon, Interregional Variation of Longitudinal Relaxation Rates in Human Brain at 3.0 T: Relation to Estimated Iron and Water Contents, Magnetic Resonance in Medicine **45**, 71 (2001).

Gilman, K., D. Hong, J. A. Fessler and L. Balzano, Streaming Probabilistic PCA for Missing Data with Heteroscedastic Noise, arXiv preprint arXiv:2310.06277 (2023).

GJ, S., O. EE, P. J, E. M, G. SJ, B. MJ and H. RM, T1, T2 relaxation and magnetization transfer in tissue at 3T, Magnetic Resonance in Medicine **54**, 507 (2005).

Golbabaee, M., D. Chen, P. A. Gómez, M. I. Menzel and M. E. Davies, "Geometry of deep learning for magnetic resonance fingerprinting", *ICASSP 2019-2019 IEEE International Conference on Acoustics, Speech and Signal Processing (ICASSP)*, (2019).

Gómez, P. A., M. Molina-Romero, G. Buonincontri, M. I. Menzel and B. H. Menze, Designing contrasts for rapid, simultaneous parameter quantification and flow visualization with quantitative transient-state imaging, Scientific Reports **9**, 8468 (2019).

Graves, A., S. FernÃ¡ndez and J. Schmidhuber, "Bidirectional LSTM Networks for Improved Phoneme Classification and Recognition", *Artificial Neural Networks: Formal Models and Their Applications â€“ ICANN 2005*, (2005).

Graves, A. and J. Schmidhuber, Framewise Phoneme Classification with Bidirectional LSTM and other Neural Network Architectures, Neural Networks **18**, 602 (2005).

Guo, S. and D. C. Noll, Oscillating steady-state imaging (OSSI): A novel method for functional MRI, Magnetic Resonance in Medicine **84**, 698 (2020).

Hagiwara, A., M. Warntjes, M. Hori, C. Andica, M. Nakazawa, K. K. Kumamaru, O. Abe and S. Aoki, SyMRI of the Brain: Rapid Quantification of Relaxation Rates and Proton Density, With Synthetic MRI, Automatic Brain Segmentation, and Myelin Measurement, Investigative Radiology **52**, 647 (2017).

Hamilton, J. I., Y. Jiang, Y. Chen, D. Ma, W.-C. Lo, M. Griswold and N. Seiberlich, MR fingerprinting for rapid quantification of myocardial T1 , T2 , and proton spin density, Magnetic Resonance in Medicine **77**, 1446 (2017).

Hasan, K. M., I. S. Walimuni, L. A. Kramer and P. A. Narayana, Human Brain Iron Mapping using Atlas-Based $T_2$ Relaxometry, Magnetic Resonance in Medicine **67**, 731 (2012).

He, X. and D. Yablonskiy, Quantitative BOLD: Mapping of Human Cerebral Deoxygenated Blood Volume and Oxygen Extraction Fraction: Default State, Magnetic resonance in medicine : official journal of the Society of Magnetic Resonance in Medicine / Society of Magnetic Resonance in Medicine **57**, 115 (2007).

Heckel, R., M. Jacob, A. Chaudhari, O. Perlman and E. Shimron, Deep Learning for Accelerated and Robust MRI Reconstruction: a Review, PrePrint arXiv (2024).

Hoff, M. N., J. B. Andre and Q.-S. Xiang, Combined geometric and algebraic solutions for removal of bSSFP banding artifacts with performance comparisons ().

Hong, D., K. Gilman, L. Balzano and J. A. Fessler, HePPCAT: Probabilistic PCA for data with heteroscedastic noise, IEEE Transactions on Signal Processing **69**, 4819 (2021).

Hong, T., D. Han, M.-O. Kim and D.-H. Kim, RF slice profile effects in magnetic resonance fingerprinting, Magnetic Resonance Imaging **41**, 73 (2017).

Hoppe, E., G. Körzdörfer, M. Nittka, T. Wür, J. Wetzl, F. Lugauer, M. Schneider, J. Pfeu and A. Maier, Deep Learning for Magnetic Resonance Fingerprinting: Accelerating the Reconstruction of Quantitative Relaxation Maps, Studies in Health Technology and Informatics **243**, 202 (2018).

Hoppe, E., F. Thamm, G. Körzdörfer, C. Syben, F. Schirrmacher, M. Nittka, J. Pfeuffer, H. Meyer and A. Maier, "RinQ Fingerprinting: Recurrence-Informed Quantile Networks for Magnetic Resonance Fingerprinting", *International Conference on Medical Image Computing and Computer-Assisted Intervention*, (2019).

Ito, H., I. Kanno, C. Kato, T. Sasaki, K. Ishii, Y. Ouchi, A. Iida, H. Okazawa, K. Hayashida, N. Tsuyuguchi, K. Ishii, Y. Kuwabara and M. Senda, Database of Normal Human Cerebral Blood Flow, Cerebral Blood Volume, Cerebral Oxygen Extraction Fraction and Cerebral Metabolic Rate of Oxygen Measured by Positron Emission Tomography with $^{15}$O-Labelled Carbon Dioxide or Water, Carbon Monoxide and Oxygen: a Multicentre Study in Japan, European Journal of Nuclear Medicine and Molecular Imaging **31**, 635 (2004).

Iyad, N., S. M. Ahmad, S. G. Alkhatib and M. Hjouj, Gadolinium contrast agents- challenges and opportunities of a multidisciplinary approach: Literature review, European Journal of Radiology Open **11**, 100503 (2023).

Jespersen, S. N. and L. Østergaard, The Roles of Cerebral Blood Flow, Capillary Transit Time Heterogeneity, and Oxygen Tension in Brain Oxygenation and Metabolism, Journal of Cerebral Blood Flow & Metabolism **32**, 264 (2012).

Ji, S., D. Yang, J. Lee, S. H. Choi, H. Kim and K. M. Kang, Synthetic MRI: Technologies and Applications in Neuroradiology, Journal of Magnetic Resonance Imaging **55**, 1013 (2022).

Jiang, Y., D. Ma, N. Seiberlich, V. Gulani and M. Griswold, MR Fingerprinting using Fast Imaging with Steady State Precession (FISP) with Spiral Readout, Magnetic Resonance in Medicine **74**, 1621 (2015).

Jiang, Y., R. Zhu, B. Zhao and N. Seiberlich, The Feasibility of 3D MR Fingerprinting using Cartesian sampling for isotropic 1mm3 resolution at 0.55T ().

Jordan, S. P., S. Hu, I. Rozada, D. F. McGivney, R. Boyacioglu, D. C. Jacob, S. Huang, M. Beverland, H. G. Katzgraber, M. Troyer, M. A. Griswold and D. Ma, Automated Design of Pulse Sequences for Magnetic Resonance Fingerprinting using Physics-Inspired Optimization, Proceedings of the National Academy of Sciences **118**, e2020516118 (2021).

Kang, B., M. Singh, H. Park and H.-Y. Heo, Only-train-once MR fingerprinting for B0 and B1 inhomogeneity correction in quantitative magnetization-transfer contrast, Magnetic Resonance in Medicine **90**, 90 (2023).

Knutsson, L., E. Lindgren, A. Ahlgren, M. van Osch, K. Bloch, Y. Surova, F. hlberg, D. van Westen and R. Wirestam, Dynamic susceptibility contrast MRI with a prebolus contrast agent administration design for improved absolute quantification of perfusion, Magn Reson Med **72**, 996 (2014).

Lee, P., L. Watkins, T. Anderson, G. Buonincontri and B. Hargreaves, Flexible and efficient optimization of quantitative sequences using automatic differentiation of Bloch simulations, Magnetic Resonance in Medicine **82**, 1438 (2019).

Leenders, K., D. Perani, A. Lammertsma, J. Heather, P. Buckingham, M. Healy, J. Gibbs, R. Wise, J. Hatazawa and S. Herold, Cerebral blood flow, blood volume and oxygen utilization. Normal values and effect of age, Brain **113 ( Pt 1)**, 27 (1990).

Lemasson, B., N. Pannetier, N. Coquery, L. Boisserand, N. Collomb, N. Schuff, M. Moseley, G. Zaharchuk, E. Barbier and T. Christen, MR Vascular Fingerprinting in Stroke and Brain Tumors Models, Scientific Reports **6** (2016).

Leupold, J., Steady-state free precession signals of arbitrary dephasing order and their sensitivity to T2*, Concepts in Magnetic Resonance Part A **46**, e21435 (2018).

Li, P. and Y. Hu, Learned Tensor Low-CP-Rank and Bloch Response Manifold Priors for Non-Cartesian MRF Reconstruction, IEEE Transactions on Medical Imaging (2023).

Liu, D., F. Xu, D. Lin, P. van Zijl and Q. Qin, Quantitative measurement of cerebral blood volume using velocity-selective pulse trains, Magn Reson Med **77**, 92 (2017).

Liu, H., O. van der Heide, C. A. T. v. d. Berg and A. Sbrizzi, Fast and Accurate Modeling of Transient-State Gradient-Spoiled Sequences by Recurrent Neural Networks, NMR in Biomedicine **34** (2021).

Lu, H., L. Nagae-Poetscher, X. Golay, D. Lin, M. Pomper and P. van Zijl, Routine clinical brain MRI sequences for use at 3.0 Tesla, Journal of Magnetic Resonance Imaging **22**, 13 (2005).

Lu, H., H. Ye and B. Zhao, "Improved Balanced Steady-State Free Precession Based MR Fingerprinting with Deep Autoencoders", *Proceedings of the Annual International Conference of the IEEE Engineering in Medicine and Biology Society (EMBC)*, (2022).

M, C., W. Wu, B. Tendler, Z. Nagy, K. Miller and S. Jbabdi, Quantifying myelin in crossing fibers using diffusion-prepared phase imaging: Theory and simulations, Magnetic Resonance in Medicine **86**, 2618 (2021).

Ma, D., S. Coppo, Y. Chen, D. F. McGivney, Y. Jiang, S. Pahwa, V. Gulani and M. A. Griswold, Slice Profile and B_1 Corrections in 2D Magnetic Resonance Fingerprinting, Magnetic Resonance in Medicine **78**, 1781 (2017).

Ma, D., V. Gulani, N. Seiberlich, K. Liu, J. L. Sunshine, J. L. Duerk and M. A. Griswold, Magnetic resonance fingerprinting, Nature **495**, 187 (2013).

Marques, J. and R. Bowtell, Application of a Fourier-based method for rapid calculation of field inhomogeneity due to spatial variation of magnetic susceptibility, Concepts in Magnetic Resonance Part B: Magnetic Resonance Engineering **25B**, 65 (2005).

McGivney, D., A. Deshmane, Y. Jiang, D. Ma, C. Badve, A. Sloan, V. Gulani and M. Griswold, Bayesian estimation of multicomponent relaxation parameters in magnetic resonance fingerprinting, Magnetic Resonance in Medicine **80**, 159 (2018).

McGivney, D. F., E. Pierre, D. Ma, Y. Jiang, H. Saybasili, V. Gulani and M. A. Griswold, SVD compression for magnetic resonance fingerprinting in the time domain, IEEE transactions on medical imaging **33**, 2311 (2014).

McLachlan, G. and T. Krishnan, *The EM Algorithm and Extensions* (Wiley).

McLachlan, G. J., D. Peel and R. Bean, Modelling high-dimensional data by mixtures of factor analyzers, Computational Statistics & Data Analysis **41**, 379 (2003).

Miller, K. L., B. A. Hargreaves, J. Lee, D. Ress, R. Christopher deCharms and J. M. Pauly, Functional brain imaging using a blood oxygenation sensitive steady state, Magnetic Resonance in Medicine **50**, 675 (2003).

Miller, K. L. and P. Jezzard, Modeling SSFP functional MRI contrast in the brain, Magnetic Resonance in Medicine **60**, 661 (2008).

Miller, K., FMRI using balanced steady-state free precession (SSFP), Neuroimage **62**, 713 (2012).

Miller, K., S. Smith and P. Jezzard, Asymmetries of the balanced SSFP profile. Part II: white matter, Magnetic Resonance in Medicine **63**, 396 (2010).

Moya-Saez, E., Ã. PeÃ±a-Nogales, R. d. Luis-GarcÃa and C. Alberola-LÃ³pez, A deep learning approach for synthetic MRI based on two routine sequences and training with synthetic data, Computer Methods and Programs in Biomedicine **210**, 106371 (2021).

Nagaraja, N., Diffusion weighted imaging in acute ischemic stroke: A review of its interpretation pitfalls and advanced diffusion imaging application, Journal of the Neurological Sciences **425**, 117435 (2021).

Nagtegaal, M., E. Hartsema, K. Koolstra and F. Vos, Multicomponent MR fingerprinting reconstruction using joint-sparsity and low-rank constraints, Magnetic Resonance in Medicine **89**, 286 (2023).

Nehrke, K. and P. Börnert, DREAM - A Novel Approach for Robust, Ultrafast, Multislice $B_1$ Mapping, Magnetic Resonance in Medicine **68**, 1517 (2012).

Nguyen, H. D., F. Forbes and G. J. McLachlan, Mini-batch learning of exponential family finite mixture models, Statistics and Computing **30**, 731 (2020).

Ni, W., T. Christen, Z. Zun and G. Zaharchuk, Comparison of R2' measurement methods in the normal brain at 3 Tesla, Magnetic Resonance in Medicine **73**, 1228 (2015).

Oksuz, I., G. Cruz, J. Clough, A. Bustin, N. Fuin, R. Botnar, C. Prieto, A. King and J. Schnabel, *Magnetic Resonance Fingerprinting using Recurrent Neural Networks* ().

Otsu, N., A Threshold Selection Method from Gray-Level Histograms, IEEE Transactions on Systems, Man, and Cybernetics **9**, 62 (1979).

Oudoumanessah, G., T. Coudert, C. Lartizien, M. Dojat, T. Christen and F. Forbes, Scalable magnetic resonance fingerprinting: Incremental inference of high dimensional elliptical mixtures from large data volumes, Submitted (2024).

Oudoumanessah, G., C. Lartizien, M. Dojat and F. Forbes, "Towards frugal unsupervised detection of subtle abnormalities in medical imaging", *International Conference on Medical Image Computing and Computer-Assisted Intervention*, (2023).

Pannetier, N., C. Debacker, F. Mauconduit, T. Christen and E. Barbier, Correction: A Simulation Tool for Dynamic Contrast Enhanced MRI, PloS one **8**, e57636 (2013).

Peretti, L., G. Donatelli, M. Cencini, P. Cecchi, G. Buonincontri, M. Cosottini, M. Tosetti and M. Costagli, Generating Synthetic Radiological Images with PySynthMRI: An Open-Source Cross-Platform Tool, Tomography (Ann Arbor, Mich.) **9**, 1723 (2023).

Perlman, O., B. Zhu, M. Zaiss, M. S. Rosen and C. T. Farrar, An end-to-end AI-based framework for automated discovery of rapid CEST/MT MRI acquisition protocols

and molecular parameter quantification (AutoCEST), Magnetic Resonance in Medicine **87**, 2792 (2022).

Peters, A., M. Brookes, F. Hoogenraad, P. Gowland, S. Francis, P. Morris and R. Bowtell, T2* measurements in human brain at 1.5, 3 and 7 T, Magn Reson Imaging **25**, 748 (2007).

Plähn, N., S. Poli, E. Peper, B. Acikgoz, R. Kreis, C. Ganter and J. Bastiaansen, Getting the phase consistent: The importance of phase description in balanced steady-state free precession MRI of multi-compartment systems, Magnetic Resonance in Medicine **92** (2024).

Preetha, C. J. et al., Deep-learning-based synthesis of post-contrast T1-weighted MRI for tumour response assessment in neuro-oncology: a multicentre, retrospective cohort study, The Lancet Digital Health **3**, e784 (2021).

Provost, C., M. Soudant, L. Legrand, W. Ben Hassen, Y. Xie, S. Soize, R. Bourcier, J. Benzakoun, M. Edjlali, G. Boulouis, H. Raoult, F. Guillemin, O. Naggara, S. Bracard and C. Oppenheim, Magnetic Resonance Imaging or Computed Tomography Before Treatment in Acute Ischemic Stroke, Stroke **50**, 659 (2019).

Sakai, F., K. Nakazawa, Y. Tazaki, K. Ishii, H. Hino, H. Igarashi and T. Kanda, Regional cerebral blood volume and hematocrit measured in normal human volunteers by single-photon emission computed tomography, J Cereb Blood Flow Metab **5**, 207 (1985).

Salomir, R., B. D. de Senneville and C. T. Moonen, A fast calculation method for magnetic field inhomogeneity due to an arbitrary distribution of bulk susceptibility, Concepts in Magnetic Resonance Part B: Magnetic Resonance Engineering **19B**, 26 (2003).

Schäper, J., G. Bauman, C. Ganter and O. Bieri, Pure balanced steady-state free precession imaging (pure bSSFP), Magnetic Resonance in Medicine **87**, 1886 (2022).

Schauman, S., S. S. Iyer, M. Yurt, X. Cao, C. Liao, Z. Zhong, G. Wang, G. Zaharchuk, S. Vasanawala and K. Setsompop, "(ISMRM 2022) Toward a 1-minute high-resolution brain exam - MR Fingerprinting with fast reconstruction and ML-synthesized contrasts", *2022 ISMRM & ISMRT Annual Meeting & Exhibition*, (2022).

Scheffler, K. and J. Hennig, Is TrueFISP a gradient-echo or a spin-echo sequence?, Magnetic Resonance in Medicine **49**, 395 (2003).

Scheffler, K. and S. Lehnhardt, Principles and applications of balanced SSFP techniques, European Radiology **13**, 2409 (2003).

Schwarz, G., Estimating the dimension of a model, The Annals of Statistics 461 (1978).

Scope Crafts, E., H. Lu, H. Ye, L. L. Wald and B. Zhao, An efficient approach to optimal experimental design for magnetic resonance fingerprinting with B-splines, Magnetic Resonance in Medicine **n/a** (2022).

Sedlacik, J. and J. R. Reichenbach, Validation of quantitative estimation of tissue oxygen extraction fraction and deoxygenated blood volume fraction in phantom and in vivo experiments by using MRI, Magnetic Resonance in Medicine **63**, 910 (2010).

Shiroishi, M. S., G. Castellazzi, J. L. Boxerman, F. D'Amore, M. Essig, T. B. Nguyen, J. M. Provenzale, D. S. Enterline, N. Anzalone, A. DÃ¶rfler, Ã. Rovira, M. Wintermark and M. Law, Principles of T2*-weighted dynamic susceptibility

contrast MRI technique in brain tumor imaging, Journal of Magnetic Resonance Imaging **41**, 296 (2015).

Siami-Namini, S., N. Tavakoli and A. S. Namin, "The Performance of LSTM and BiLSTM in Forecasting Time Series", *2019 IEEE International Conference on Big Data (Big Data)*, (2019).

Sobol', I. M., Distribution of Points in a Cube and the Approximate Evaluation of Integrals (in Russian), Zhurnal Vychislitel'noi Matematiki i Matematicheskoi Fiziki **7**, 784 (1967).

Sommer, K., T. Amthor, M. Doneva, P. Koken, J. Meineke and P. Börnert, Towards predicting the encoding capability of MR fingerprinting sequences, Magnetic Resonance Imaging **41**, 7 (2017).

Soyak, R., E. Navruz, E. O. Ersoy, G. Cruz, C. Prieto, A. P. King, D. Unay and I. Oksuz, Channel attention networks for robust MR fingerprint matching, IEEE Transactions on Biomedical Engineering **69**, 1398 (2021).

Spangenberg, P. et al., Rapid and fully automated blood vasculature analysis in 3D light-sheet image volumes of different organs, Cell Reports Methods **3** (2023).

Stadlbauer, A., M. Zimmermann, S. Oberndorfer, A. Doerfler, M. Buchfelder, G. Heinz and K. Roessler, Vascular Hysteresis Loops and Vascular Architecture Mapping in Patients with Glioblastoma treated with Antiangiogenic Therapy, Scientific Reports **7** (2017).

Staehle, F., J. Leupold, J. Hennig and M. Markl, Off-resonance-dependent slice profile effects in balanced steady-state free precession imaging, Magnetic Resonance in Medicine **59**, 1197 (2008).

Stikov, N., M. Boudreau, I. R. Levesque, C. L. Tardif, J. K. Barral and G. B. Pike, On the Accuracy of $T_1$ Mapping: Searching for Common Ground, Magnetic Resonance in Medicine **73**, 514 (2015).

Su, P., H. Fan, P. Liu, Y. Li, Y. Qiao, J. Hua, D. Lin, D. Jiang, J. Pillai, A. Hillis and H. Lu, MR fingerprinting ASL: Sequence characterization and comparison with dynamic susceptibility contrast (DSC) MRI, NMR in Biomedicine **33** (2019).

Tang, S., C. Fernandez-Granda, S. Lannuzel, B. Bernstein, R. Lattanzi, M. Cloos, F. Knoll and J. AsslÃ¤nder, Multicompartment Magnetic Resonance Fingerprinting, Inverse problems **34** (2018).

Tchamedeu, L. D. T. M., B. Lambert, T. Coudert, E. M. Cohen-Jonathan, S. Ken, G. L. Duc, M. Dojat, F. Boux and B. Lemasson, "Segmentation d'IRM multimodales par réseaux de neurones : Stratégies de transfert d'apprentissage pour des ensembles de données de taille limitée", *IABM2024 conference, March 2024, Grenoble*, (2024).

Thomson, E. L., E. Powell, C. A. M. G. Wheeler-Kingshott and G. J. M. Parker (2023), *Quantification of water exchange across the blood-brain barrier using non-contrast MR fingerprinting*, preprint, Neuroscience.

Tipping, M. E. and C. M. Bishop, Mixtures of probabilistic principal component analyzers, Neural computation **11**, 443 (1999).

Triantafyllou, C., R. D. Hoge, G. Krueger, C. J. Wiggins, A. Potthast, G. C. Wiggins and L. L. Wald, Comparison of physiological noise at 1.5 T, 3 T and 7 T and optimization of fMRI acquisition parameters, NeuroImage **26**, 243 (2005).

Troprès, I., N. Pannetier, S. Grand, B. Lemasson, A. Moisan, M. Péoc'h, C. Rémy and E. Barbier, Imaging the microvessel caliber and density: Principles and applications of microvascular MRI, Magnetic Resonance in Medicine **73**, 325 (2015).

Tsivgoulis, G., A. H. Katsanos, P. D. Schellinger, M. Köhrmann, V. Caso, L. Palaiodimou, G. Magoufis, A. Arthur, U. Fischer and A. V. Alexandrov, Advanced Neuroimaging in Stroke Patient Selection for Mechanical Thrombectomy, Stroke **49**, 3067 (2018).

Uh, J., K. Lewis-Amezcua, R. Varghese and H. Lu, On the measurement of absolute cerebral blood volume (CBV) using vascular-space-occupancy (VASO) MRI, Magn Reson Med **61**, 659 (2009).

Ullah, I., A. M. Hassan, R. M. Saad and H. Omer, GPU accelerated grouped magnetic resonance fingerprinting using clustering techniques, Magnetic Resonance Imaging **97**, 13 (2023).

Valable, S., B. Lemasson, R. Farion, M. Beaumont, C. Segebarth, C. Remy and E. L. Barbier, Assessment of blood volume, vessel size, and the expression of angiogenic factors in two rat glioma models: a longitudinal in vivo and ex vivo study, NMR Biomed. **21**, 1043 (2008).

van Dijken, B., P. van Laar, G. Holtman and A. van der Hoorn, Diagnostic accuracy of magnetic resonance imaging techniques for treatment response evaluation in patients with high-grade glioma, a systematic review and meta-analysis, European Radiology **27**, 4129 (2017).

Vasanawala, S. S., J. M. Pauly and D. G. Nishimura, Linear combination steady-state free precession MRI, Magnetic Resonance in Medicine **43**, 82 (2000).

Wang, C. Y., S. Coppo, B. B. Mehta, N. Seiberlich, X. Yu and M. A. Griswold, Magnetic resonance fingerprinting with quadratic RF phase for measurement of $T_2^*$ simultaneously with $\delta_f$, $T_1$, and $T_2$, Magnetic Resonance in Medicine **81**, 1849 (2019).

Wang, K., M. Doneva, J. Meineke, T. Amthor, E. Karasan, F. Tan, J. I. Tamir, S. X. Yu and M. Lustig, High-fidelity direct contrast synthesis from magnetic resonance fingerprinting, Magnetic Resonance in Medicine **90**, 2116 (2022).

Wansapura, J., S. Holland, R. Dunn and W. J. Ball, NMR Relaxation Times in the Human Brain at 3.0 Tesla, Journal of Magnetic Resonance Imaging **9**, 531 (1999).

Warach, S. J. et al., Acute Stroke Imaging Research Roadmap III Imaging Selection and Outcomes in Acute Stroke Reperfusion Clinical Trials: Consensus Recommendations and Further Research Priorities, Stroke **47**, 1389 (2016).

Weigel, M., Extended phase graphs: Dephasing, RF pulses, and echoes - pure and simple: Extended Phase Graphs, Journal of Magnetic Resonance Imaging **41**, 266 (2015).

Welvaert, M. and Y. Rosseel, On the Definition of Signal-To-Noise Ratio and Contrast-To-Noise Ratio for fMRI Data, PLOS ONE **8**, e77089 (2013).

Wilkins, E., L. Wilson, K. Wickramasinghe, P. Bhatnagar, J. Leal, R. Luengo-Fernandez, R. Burns, M. Rayner and N. Townsend, *European Cardiovascular Disease Statistics 2017* (European Heart Network).

Willats, L. and F. Calamante, The 39 steps: evading error and deciphering the secrets for accurate dynamic susceptibility contrast MRI, NMR in Biomedicine **26**, 913 (2013).

Wirestam, R., O. Thilmann, L. Knutsson, I. Björkman-Burtscher, E. Larsson and F. Ståhlberg, Comparison of quantitative dynamic susceptibility-contrast MRI perfusion estimates obtained using different contrast-agent administration schemes at 3T, European Journal of Radiology **75**, e86 (2010).

Yang, M., D. Ma, Y. Jiang, J. Hamilton, N. Seiberlich, M. A. Griswold and D. McGivney, Low rank approximation methods for MR fingerprinting with large scale dictionaries, Magnetic resonance in medicine **79**, 2392 (2018).

Zhao, B., K. Setsompop, E. Adalsteinsson, B. Gagoski, H. Ye, D. Ma, Y. Jiang, P. Ellen Grant, M. A. Griswold and L. Wald, Improved magnetic resonance fingerprinting reconstruction with low-rank and subspace modeling, Magnetic Resonance in Medicine **79**, 933 (2018).

# List of Figures

# List of Tables

# Published work & CV

### Articles

- T. Coudert, A. Delpin, A. Barrier, L. Legris, J. M. Warnking, L. Lamalle, M. Doneva, B. Lemasson, E. L. Barbier and T. Christen, Relaxometry and contrast-free cerebral microvascular quantification using balanced Steady-State Free Precession MR Fingerprinting, Submitted to Magnetic Resonance in Medicine (2024)
- G. Oudoumanessah, T. Coudert, C. Lartizien, M. Dojat, T. Christen and F. Forbes, Scalable magnetic resonance fingerprinting: Incremental inference of high dimensional elliptical mixtures from large data volumes, Submitted (2024)
- Barrier, Antoine and Coudert, Thomas, A. Delphin, B. Lemasson and C. Thomas, MARVEL: MR Fingerprinting with Additional micRoVascular Estimates using bidirectional LSTMs, Proceeding of MICCAI 2024 (2024)
- A. Delphin, F. Boux, C. Brossard, T. Coudert, J. Warnking, B. Lemasson, E. Barbier and T. Christen, Enhancing MR Vascular Fingerprinting through Realistic Microvascular Geometries, Imaging Neuroscience (2024)

### Conference abstracts

- T. Coudert, A. Delphin, L. Legris, A. Barrier, J. M. Warnking, D. Chechin, L. Lamalle, P. Mazurkewitz, P. Koken, E. L. Barbier, M. Doneva and T. Christen, "Contrast-free Blood Volume, Microvascular Properties and Relaxometry mapping using bSSFP MR Fingerprinting", *2024 ISMRM Annual Meeting & Exhibition, Singapour*, (2024) - **Power pitch oral**
- L. D. T. M. Tchamedeu, B. Lambert, T. Coudert, E. M. Cohen-Jonathan, S. Ken, G. L. Duc, M. Dojat, F. Boux and B. Lemasson, "Segmentation d'IRM multimodales par réseaux de neurones : Stratégies de transfert d'apprentissage pour des ensembles de données de taille limitée", *IABM2024 conference, March 2024, Grenoble*, (2024) - **Poster presentation**
- A. Barrier, T. Coudert, A. Delphin, L. Legris, J. Warnking, E. Barbier and T. Christen, "Reconstructions de cartes multi-paramétriques haute dimension accélérées via LSTM bidirectionnel et IRM Fingerprint.", *IABM2024 conference, March 2024, Grenoble*, (2024) - **Poster presentation**
- A. Delphin, T. Coudert, A. Fan, M. Moseley, G. Zaharchuk and T. Christen, "MR Vascular Fingerprinting with 3D Realistic Blood Vessel Structures and Machine Learning to Assess Oxygenation Changes in Human Volunteers", *2023 ISMRM & ISMRT Annual Meeting & Exhibition*, (2023) - **Poster presentation**
- T. Coudert, A. Delphin, J. M.Warnking, E. L. Barbier and T. Christen, "Utilisation de séquences de type MR Fingerprint bSSFP pour les mesures T2* et la quantification de l'effet BOLD.", *SFRMBM2023 conference, March 2023, Paris*, (2023) - **Poster presentation**
- T. Coudert, A. Delphin, J. M.Warnking, E. L. Barbier and T. Christen, "Réseaux

de neurones profonds pour la simulation de signaux IRM pour l'IRM Fingerprint vasculaire.", *IABM2023 conference, March 2023, Paris*, (2023) - **Poster presentation**

- T. Coudert, A. Delphin, J. M. Warnking, B. Lemasson, E. L. Barbier and T. Christen, "Searching for an MR Fingerprinting sequence to measure brain oxygenation without contrast agent", *ISMRM 31st Annual Meeting & Exhibition, May 2022, London, United Kingdom*, (2022) - **Poster presentation**

# Résumé français - French Summary

## Introduction

### L'Accident Vasculaire Cérébral à l'ère de la thrombectomie

L'accident vasculaire cérébrale (AVC) est une pathologie neurologique caractérisée par une interruption soudaine de la circulation sanguine dans le cerveau, entraînant des déficits neurologiques aigus. Cette interruption peut être due soit à une ischémie, causée par une obstruction ou un rétrécissement des vaisseaux sanguins, soit à une hémorragie, résultant d'un saignement à l'intérieur du cerveau. Les conséquences immédiates d'un accident vasculaire cérébral peuvent être la perte des fonctions motrices et sensorielles, des difficultés d'élocution, des troubles cognitifs et, dans les cas les plus graves, la mort. Dans l'Union européenne, 1,1 million de personnes sont victimes d'un accident vasculaire cérébral chaque année, ce qui représente environ 9% de l'ensemble des décès. En termes de prévalence, près de 12 millions de personnes en Europe vivent avec les effets à long terme d'un accident vasculaire cérébral, qui comprennent souvent des handicaps importants tels que l'hémiplégie, des difficultés d'élocution et des troubles cognitifs. Les effets à long terme de l'AVC sont directement liés à la durée pendant laquelle les tissus sont privés d'oxygène.

Étant donné le besoin urgent d'un diagnostic et d'une intervention rapides, l'AVC représente un défi important pour les systèmes de santé, exigeant non seulement des stratégies de traitement efficaces, mais aussi des techniques d'imagerie sophistiquées pour guider la prise en charge et porter un diagnostic. Depuis 2015, plusieurs études cliniques (Warach et al. 2016), ont montré l'efficacité des nouvelles thérapies endovasculaires (EVT) sur l'évaluation et le traitement des lésions de l'AVC. L'une des principales conclusions de ces études a mis en évidence le rôle essentiel des techniques d'imagerie cérébrale dans l'identification des patients les plus susceptibles de bénéficier d'un traitement. Cependant, cette amélioration majeure des soins a été atténuée par le faible nombre de patients (environ 10,5 %) qui pouvaient recevoir le traitement. Ce faible taux s'explique en grande partie par le fait que les patients soient arrivés à l'hôpital en dehors de la période d'éligibilité recommandée par les lignes directrices pour recevoir le traitement. L'imagerie dans la phase aiguë de l'AVC doit être réalisée rapidement, car l'efficacité du traitement est maximale dans une courte fenêtre temporelle, généralement moins de six heures après l'apparition des symptômes. Cette situation a commencé à changer en 2018 lorsque plusieurs essais cliniques ont montré que la thrombectomie endovasculaire et la thrombolyse intraveineuse pouvaient également être efficaces dans les 24 heures suivant l'apparition de l'AVC si des protocoles d'imagerie avancés étaient utilisés pour l'orientation des patients (Albers et al. 2018). Ces résultats soutiennent l'idée selon laquelle la physiologie cérébrale peut être un meilleur indicateur pronostique de l'issue de l'AVC que l'attente observatoire, et laissent espérer une augmentation significative

du nombre de patients (environ 30 % des patients dont l'heure d'apparition des symptômes est inconnue), une meilleure sélection des thérapies et une meilleure prédiction de l'issue de l'AVC.

## Stratégies d'imagerie

Alors que des essais récents ont souligné la nécessité d'examens d'imagerie robustes, rapides et multiparamétriques dans les urgences d'AVC (Tsivgoulis et al. 2018), il a également été noté les limites (nécessité d'une injection de produit de contraste, faible sensibilité et reproductibilité, manque de consensus) des outils d'imagerie actuels pour la détection du tissu cérébral qui peut être sauvé si le flux sanguin est rétabli (*i.e.* la pénombre ischémique). Cependant, la question de l'imagerie la mieux adaptée aux urgences de l'AVC n'est toujours pas résolue. En effet, la première modalité d'imagerie généralement utilisée dans la prise en charge des patients est la tomodensitométrie (TDM), qui est à la fois rapide (protocole d'environ 5 minutes) et largement accessible. Cependant, il est nécessaire d'améliorer la capacité à détecter l'ischémie et les hémorragies afin d'améliorer l'orientation des patients (Donahue et al. 2018). Une évaluation plus précise de la pénombre ischémique est également cruciale car elle pourrait aider à estimer le moment de l'apparition de l'AVC chez les patients qui n'ont pas été témoins de l'accident et potentiellement étendre la fenêtre thérapeutique.

D'autre part, l'IRM permet l'acquisition d'informations quantitatives grâce à des techniques d'imagerie quantitative (IRMq) telles que les images pondérées en diffusion (DWI, Nagaraja 2021) pour détecter le noyau ischémique et l'utilisation de mécanismes de contraste multiples (FLAIR, perfusion (PWI, Demeestere et al. 2020), ou d'éventuels nouveaux contrastes) pour détecter les tissus à risque. En outre, l'imagerie $T_2^*$ aide également à détecter les micro-saignemebts et les changements hémorragiques chroniques qui peuvent influencer la prise en charge et l'issue de l'AVC. En outre, des essais récents ont démontré que ≈90% des patients cliniquement éligibles pour l'EVT peuvent être scannés avec l'IRM (les principales restrictions cliniques restent les patients agités ou instables) et que les temps réel d'exmamens IRM pour l'AVC sont similaires à ceux en tomodensitométrie (Provost et al. 2019).

**Il apparaît donc qu'un examen très efficace pour les urgences liées aux accidents vasculaires cérébraux consisterait en un protocole d'IRM qui (1) réduirait considérablement les temps d'acquisition actuels de l'IRM (environ 20-25 minutes) (2) obtiendrait plus d'informations sur les microstructures tissulaires (3) fournirait des données quantitatives, standardisées et résumées en quelques minutes.**

## Offrir un changement de paradigme en IRM

Répondre à toutes les exigences ci-dessus semble hors de portée avec les outils d'IRM actuels. Les protocoles qui produisent des informations similaires à celles de la tomodensitométrie sont déjà longs pour les urgences liées aux accidents vasculaires cérébraux (protocole d'environ 25 minutes), car chaque estimation implique l'acquisition d'une séquence d'IRM indépendante. Un moyen de gagner du temps est de réduire la résolution spatiale des images acquises, mais au prix d'une dégradation de la qualité du diagnostic clinique. Dans ce contexte, collecter plus d'informations pour imager la pénombre ischémique tout en réduisant le temps d'acquisition

total semble difficile.

Heureusement, deux concepts complémentaires et révolutionnaires sont apparus ces dernières années dans le domaine et pourraient changer radicalement la façon dont nous acquérons et reconstruisons les données d'IRM.

### Le concept d'IRM Fingerprint (MRF)

Introduite par Ma et al. 2013 dans Nature, l'approche IRM Fingerprint a été un grand pas pour la pleine utilisation de toute la puissance de l'IRM en permettant à une séquence unique d'exciter les tissus de manière aléatoire et d'être sensible à plusieurs paramètres en même temps. Le processus MRF implique des acquisitions haute résolution à sous-échantillonnage rapide avec des paramètres variant dans le temps qui définissent la séquence MRF qui produit des évolutions temporelles du signal (ou "*fingerprint*") dans chaque voxel. Ces empreintes *in vivo* sont ensuite comparées à un grand nombre de signaux simulés obtenus à l'aide de combinaisons de paramètres tissulaires *a priori* et stockés dans une base de données queue l'on appelle le "dictionnaire". Les valeurs des paramètres correspondant aux signaux simulés les plus proches sont ensuite attribuées aux voxels associés, ce que l'on appelle le *maching*, ce qui permet de produire simultanément plusieurs cartes quantitatives. La figure .0.2 présente une illustration schématique du cadre MRF standard.

Avec l'IRM Fingerprint, il est déjà possible de cartographier quantitativement 3 paramètres ($T_1$, $T_2$, densité de protons) de l'ensemble du cerveau humain (résolution spatiale de $1mm^3$) dans la minute (Schauman et al. 2022. Il est également possible de corriger les imperfections du système (par exemple les inhomogénéités de champ $B_1$) ainsi que certains mouvements du patient en les incluant dans les simulations numériques et les pipelines de post-traitement. Ces types d'acquisitions ont maintenant atteint la clinique et pourraient être appliqués à plusieurs organes et pathologies, y compris les accidents vasculaires cérébraux.

**Il est cependant important de réaliser que l'IRM Fingerprint n'est pas limité à un seul schéma d'excitation (1 seule séquence MRF), ni à l'unique mesure des temps de relaxation transversale ou longitudinale ($T_1$, $T_2$).**

En effet, une caractéristique importante de la méthode MRF est la flexibilité inhérente à la conception des séquences. En IRM généralement, le type de paramètres estimés et la précision avec laquelle ils sont mesurés dépendent fortement du design de la séquence. Les paramètres clés définissant une séquence IRM comprennent l'angle de bascule (FA), qui détermine l'angle de rotation de l'aimantation ; le temps de répétition (TR), le temps entre les impulsions radio-fréquence (RF) successives ; le temps d'écho (TE), l'intervalle entre l'impulsion RF et la mesure du signal ; et la phase RF, qui contrôle la phase des impulsions RF. Le réglage de ces paramètres permet d'optimiser le contraste de l'image et la sensibilité aux paramètres tissulaires. Alors qu'une séquence d'IRM quantitative standard est généralement constituée d'un petit nombre d'impulsions produisant un petit nombre d'images (<20 pour les mesures de relaxométrie), les séquences MRF peuvent être facilement définies par un nombre élevé d'impulsions RF (>200-2000). Les paramètres de la séquence MRF peuvent être variés arbitrairement avec le temps pour augmenter la variance entre les signaux du dictionnaire et

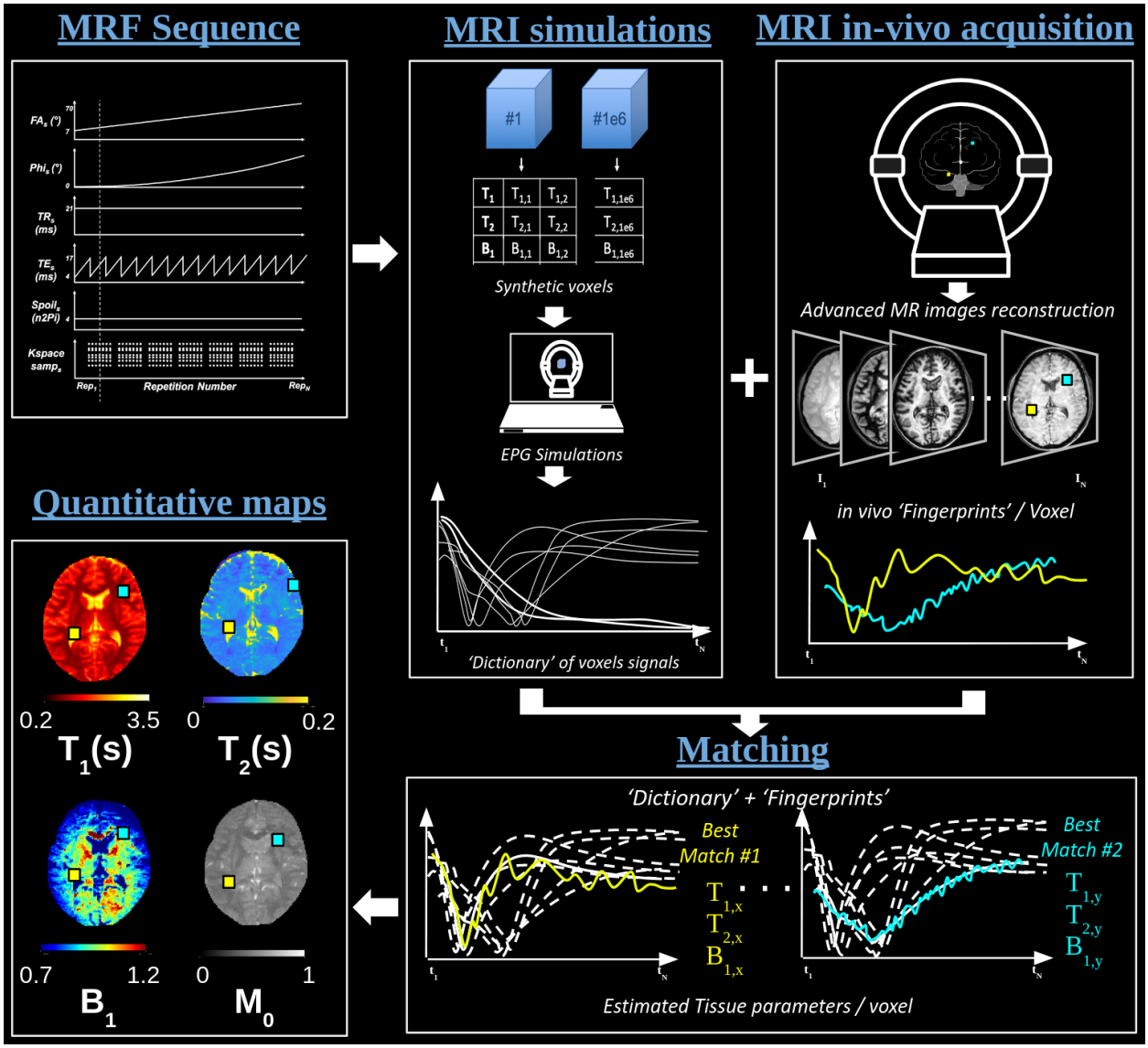


**Figure .0.2**: Illustration du protocole MRF. Les données ont été collectées à 3T (Philips; IRMaGe) chez un volontaire sain.

donc la sensibilité à différents matériaux ou tissus. Tant que la séquence est sensible aux paramètres d'intérêt, qu'elle produit différentes *fingerprints* en réponse à différents types de tissus et que les simulations MRF sont suffisamment réalistes pour capturer ces variations du signal, toutes sortes de design d'acquisition MRF peuvent être proposés (Cohen et al. 2017a).

En suivant cette idée, plusieurs équipes ont proposé d'optimiser les séquences MRF en termes de temps d'acquisition ou de robustesse à plusieurs artefacts ($B_1$ en particulier). Étant donné le très grand espace de recherche pour les séquences MRF, de nombreux algorithmes d'optimisation automatique des séquences ont été proposés. D'autres types de schémas d'acquisition ont également été proposés pour être sensible à d'autres effets tels que les inhomogénéités de champ magnétique $B_0$ et le temps effectif $T_2^*$ en utilisant des variations du signal entre 2 impulsions (Wang et al. 2019). L'utilisation de ces variations de champ

IRM a permis de mesurer le coefficient de diffusion et de quantifier le flux sanguin (CBF) dans les grands vaisseaux sanguins. En utilisant un schéma d'acquisition de marquage de spin artériel couplé à des changements aléatoires dans les temps de marquage, une ASL-MRF a également été proposée pour fournir des cartes quantitatives du CBF et du temps de transit moyen (MTT) (cette méthode est l'MRF-ASL, Su et al. 2019).

Pour toutes ces approches, les modèles numériques pour la génération du dictionnaire MRF ont été largement améliorés par rapport aux simulations classiques de Bloch impliquant un seul isochromat par voxel. Allant encore plus loin, l'équipe MRF de Grenoble a proposé d'utiliser des simulations contenant des représentations virtuelles en 3D des vaisseaux sanguins pour obtenir des cartes paramétriques simultanées représentant les structures géométriques et l'oxygénation du système microvasculaire (voir la figure .0.3). Pour l'instant, les séquences MRF vasculaires (ou MRvF, Christen et al. 2014b) correspondantes sont courtes (<70 impulsions) et simples (principalement des variations de TE), mais des combinaisons d'acquisitions obtenues avant et après l'injection d'un agent de contraste intravasculaire USPIO (Ultrasmall SuperParamagnetic Iron Oxide) ont conduit à des résultats prometteurs à la fois chez les animaux et les volontaires humains (Delphin et al. 2023).

Enfin, il convient de mentionner que l'IRM Fingerprint peut également fournir des images standard pondérées. Des études récentes ont exploré le contraste *intrinsèque* des séries temporelles d'images MRF acquises. Ceci est particulièrement intéressant car des milliers d'images peuvent potentiellement être reconstruites à partir d'une seule acquisition. Par exemple, Gómez et al. 2019 ont soigneusement conçu le schéma des paramètres d'acquisition MRF pour obtenir des images pondérées $T_1$ ou $T_2$ ou des projections de type angiographie. Il est également possible d'utiliser les cartes quantitatives estimées par MRF pour recréer (ou synthétiser) des images pondérées à l'aide de techniques de post-traitement.

### Limites actuelles de l'IRM Fingerprint

En tirant parti de la vitesse de l'approche Fingerprint, combinée à l'acquisition simultanée d'un grand nombre de nouvelles cartes de paramètres et de contrastes, il peut être facile d'imaginer un nouveau type de protocole IRM pour l'imagerie des AVC aigus. Cependant, la combinaison de plusieurs séquences en une seule acquisition n'est pas triviale. L'IRM Fingerprint fonctionne bien lorsque limité à un petit nombre de paramètres à estimer (<3). Mais l'augmentation des dimensions à estimer (>5) pose de nouveaux défis techniques en termes de puissance informatique, de mémoire de stockage (>Téraoctets) et de temps de reconstruction (>jours) qui deviennent irréalistes, même dans un contexte de recherche. Un deuxième défi pour l'examen de l'AVC par MRF est que le cadre MRvF actuel pour les estimations microvasculaires repose sur un agent de contraste spécifique (ferumoxytol) qui ne peut être utilisé pour les études humaines que dans quelques pays, et sous surveillance médicale. Dans tous les cas, le protocole MRvF nécessite l'administration d'un composé à base de métal, même autre que le ferumoxytol, dans la circulation sanguine du patient afin d'améliorer la sensibilité au réseau microvasculaire. Même si l'agent de contraste est utilisé dans les protocoles actuels de l'AVC pour l'imagerie de perfusion, des études ont déjà mis en évidence les risques potentiels de réactions allergiques aux composés de type Gadolinium (voir Costelloe et al. 2020; Iyad et al. 2023). En outre, l'efficacité des agents

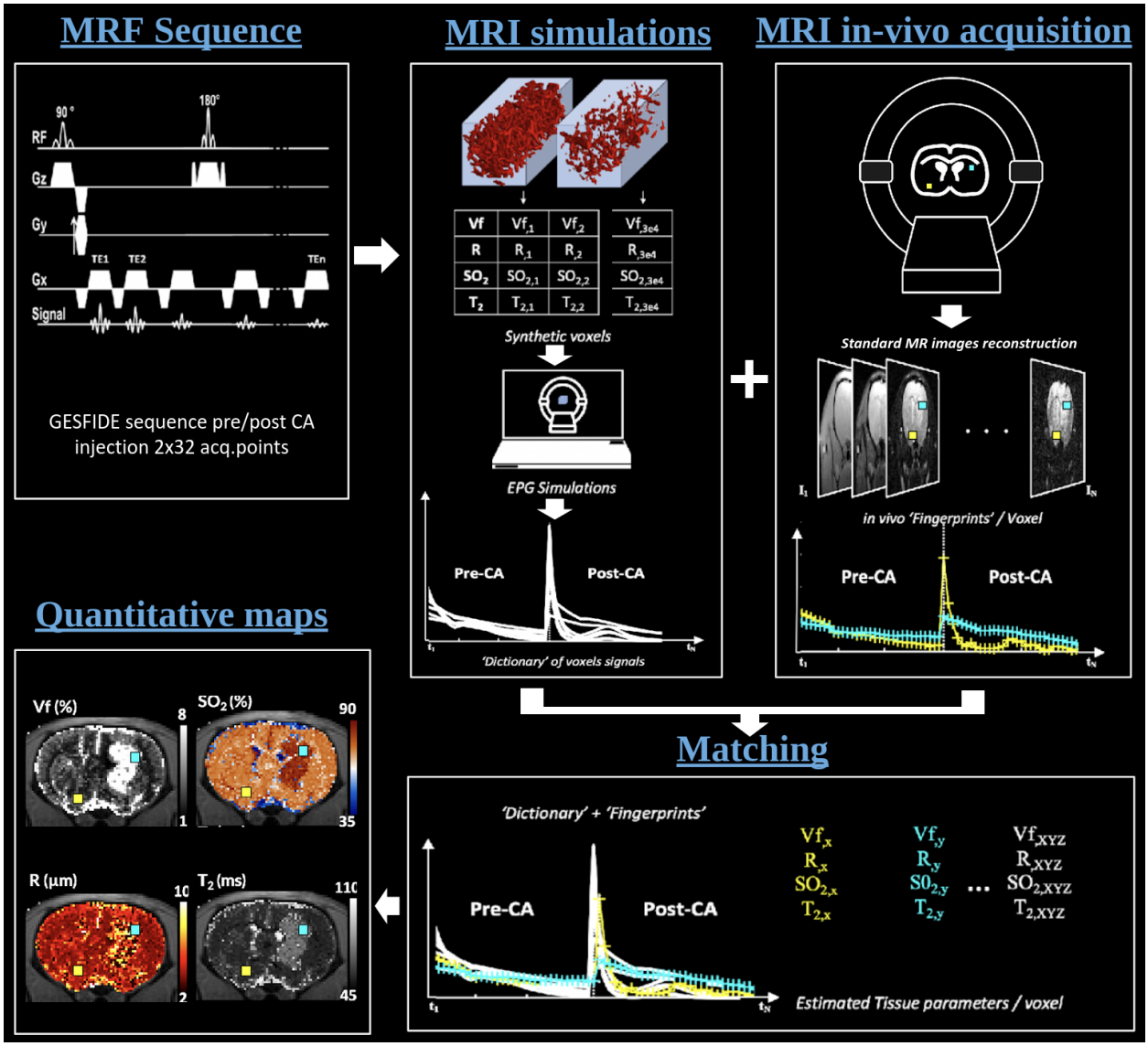


**Figure .0.3**: Illustration du protocole MRvF. Données acquises à 4.7T (Bruker; IRMaGe) sur un rat porteur d'une tumeur.

de contraste pour mettre en évidence le tissu cérébral ischémique peut varier en fonction de facteurs tels que le moment de l'administration et l'état physiologique du patient, ce qui a un impact sur la répétabilité et la précision des mesures quantitatives (Calamante et al. 2002; Ebinger et al. 2010). Enfin, le coût élevé et la disponibilité limitée des agents de contraste peuvent encore restreindre leur application à grande échelle, en particulier dans les contextes où les ressources sont limitées. Surtout, l'injection intraveineuse d'AC pendant le protocole augmente la durée de l'examen. Toutes ces raisons font qu'un examen MRF sans contraste serait donc préférable, mais de nouveaux modèles MRvF doivent être trouvés.

### Émergence des outils d'intelligence artificielle (IA) pour l'IRM

L'intelligence artificielle (IA), par le biais de méthodes d'apprentissage profond (Deep Learning) et d'apprentissage automatique (Machine Learning), a fait progresser de manière significative de multiples aspects de l'IRM en améliorant la reconstruction des images, en réduisant les temps de scan et en optimisant l'analyse des images. Depuis de nombreuses années, de nombreux algorithmes d'apprentissage profond se sont révélés extrêmement efficaces dans différents problèmes inverses de l'imagerie (Heckel et al. 2024). Les réseaux neuronaux convolutifs (CNN) et, plus récemment, les modèles de vision ont eu un impact sur la reconstruction d'images, et apprendre à produire des images à partir d'ensembles de données incomplets est aujourd'hui un point d'intêret majeur en recherche IRM. Dans le domaine de l'IRM Fingerprint, les algorithmes d'IA ont transformé l'approche traditionnelle de la génération de cartes de propriétés tissulaires. Au lieu de s'appuyer uniquement sur le *matching* de dictionnaires à forte coût de calcul, les méthodes pilotées par l'IA peuvent traiter rapidement les données MRF pour produire des cartes précises de plusieurs paramètres tissulaires, tels que les temps de relaxation $T_1$ et $T_2$ (Hoppe et al. 2018; Fang et al. 2019). Alors que certains modèles d'apprentissage automatique ont été appliqués à la simulation des signaux MRF (Boux et al. 2021), les modèles d'apprentissage profond séquentiel ont été principalement utilisés pour apprendre des modèles complexes à partir des signaux MRF déjà simulés, permettant des reconstructions plus rapides et plus efficaces (Oksuz et al. 2018; Hoppe et al. 2019; Kang et al. 2023). En outre, l'IA est désormais utilisée pour optimiser les schémas d'acquisition de l'IRM, ce qui permet d'élaborer des stratégies de sous-échantillonnage plus efficaces qui réduisent encore les temps de scan sans sacrifier la qualité de l'image (Perlman et al. 2022). Enfin, en combinant des données provenant de différentes méthodes d'acquisition, les modèles de DL peuvent également générer des contrastes synthétiques, offrant de nouvelles perspectives sur les caractéristiques des tissus sans nécessiter de scans ou d'agents de contraste supplémentaires (Preetha et al. 2021; Moya-Saez et al. 2021, voir la figure .0.4). Cette intégration de l'IA dans l'IRM, en particulier en MRF, est en train de faire évoluer le domaine, permettant une imagerie plus rapide, plus précise et moins invasive.

## Hypothèse générale du projet

**Nous soutenons la thèse que l'IRM Fingerprint combinée à des solutions d'IA innovantes permettra de créer de véritables examens d'IRM multiparamétriques et intégrés, compatibles avec les besoins exigeants des protocoles d'urgence AVC.**

### Contexte et objectifs de la thèse

L'équipe développe et analyse des méthodes d'imagerie pour l'étude des pathologies cérébrales et possède une expertise internationalement reconnue dans la mesure de la perfusion microvasculaire et l'IRM multiparamétrique quantitative. Le laboratoire fait également partie du projet MIAI Grenoble Alpes 3IA (Multidisciplinary Institute in Artificial Intelligence) qui vise à mener des recherches innovantes en intelligence artificielle. Les IRM sont accessibles sur la plateforme d'imagerie IRMaGe à Grenoble, qui dispose de 2 scanners IRM précliniques ainsi que d'un scanner IRM clinique dédié à la recherche (une approbation éthique pour réaliser des examens sur des volontaires et un partenariat est en cours avec Philips pour

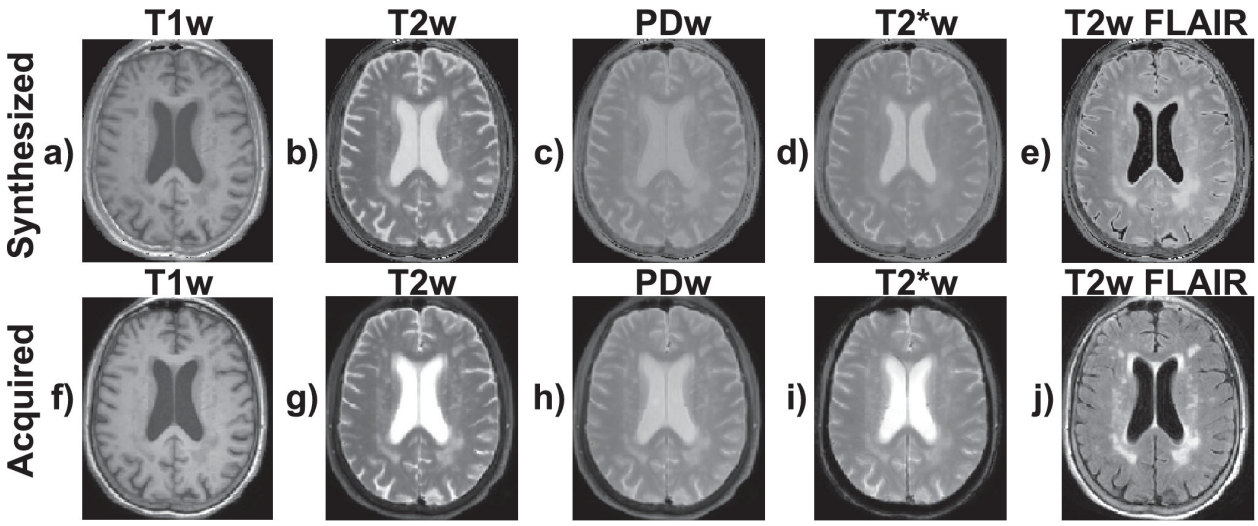


**Figure .0.4**: Tranche axiale d'images pondérées synthétiques générées à partir d'un ensemble de cartes T1, T2 et PD par un CNN et de images acquises correspondantes en références. Adaptée de Moya-Saez et al. 2021

des développements MRF). L'équipe travaille également en étroite collaboration avec des mathématiciens de l'INRIA Grenoble (équipe Statify) et bénéficie de l'expertise des neuroradiologues du CHU de Grenoble et des neurologues de l'unité neurovasculaire spécialisée dans les nouvelles thérapies cellulaires pour les patients victimes d'accidents vasculaires cérébraux.

La présente thèse, financé par le projet ANR "Magnetic Resonance Fingerprinting Unification for Stroke Emergencies (MRFUSE)", vise à développer des outils flexibles d'IA et d' IRM Fingerprint (simulations, acquisition et reconstruction) qui poseraient les bases de la conception de protocoles efficaces pour les accidents vasculaires cérébraux aigus. Ces outils seront testés sur des volontaires humains en vue d'études cliniques ultérieures.

**Nos ojectifs ont été de**

- **(1) créer des schémas d'acquisition MRF rapides (<6min vs 25min actuellement), efficaces (plus de 6 paramètres en une acquisition) et robustes qui pourraient remplacer les solutions d'imagerie actuelles et offrir une meilleure sélection des patients susceptibles de bénéficier des traitements.**
- **(2) proposer des techniques MRF pour des mesures quantitatives de biomarqueurs microvasculaires sans injection d'agent d'agent de contraste, ni temps de scan supplémentaire. Cela pourrait permettre une meilleure évaluation des tissus qui peuvent être sauvés, d'estimer le moment de l'apparition de l'AVC chez les patients qui n'en ont pas été témoins et de mieux individualiser les traitements en dehors de la fenêtre thérapeutique actuelle.**

Le présent manuscrit est organisé en 5 chapitres résumés ci-dessous. Les deux premiers chapitres se concentrent sur des développements techniques et de l'exploration théorique, établissant les concepts fondamentaux et les hypothèses de ce manuscrit. Ces travaux servent

de base aux trois chapitres suivants, qui proposent des études appliquées, fournissant une validation des méthodes par le biais d'une analyse statistique et des résultats *in vivo*.

# Résumé du chapitre I : Implémentation d'une séquence MRF avec spoiler pour des mesures relaxométriques standard et de l'imagerie de contraste

Ce premier chapitre se concentre sur l'utilisation de séquence IRM de type spoilé dans le protocole MRF. Ces séquences comporte un gradient déphaseur appelé spoiler qui se veut détruire l'aimantation transversale résiduelle après chaque excitation. La majeure partie de la communauté MRF utilise ce type de séquence pour des mesures quantitatives des temps de relaxation $T_1$ et $T_2$ car elles ont l'avantage de ne pas être trop sensible aux variations du champ magnétique et donc permettent des acquisitions moins artefactées. Ce sont des séquences très utilisées et pour lesquelles certains outils MRF existent au sein de notre équipe. Nos efforts initiaux se sont concentrés sur l'amélioration de ces outils MRF existants.

## Développement des méthodes état de l'art

Nous avons mis en œuvre de nouvelles méthodes pour réaliser des simulations numériques rapides et réalistes, des processus d'acquisition efficaces et une reconstruction robuste des cartes de relaxométrie quantitative ($T_1$, $T_2$). En tirant parti d'une abondante littérature sur ces applications MRF, nous avons développé un pipeline de pointe en utilisant un code Matlab/Python interne. Ce pipeline permet de concevoir librement des séquences MRF, qui peuvent être utilisées avec différents paramètres d'acquisition et schémas de sous-échantillonnage au niveau de l'aimant. Ainsi, en générant un fichier JSON (JavaScript Object Notation) contenant les paramètres de séquence désirés, on peut en dériver un fichier CSV (Comma-Separated Values) qui sera lu par l'IRM 3T Philips Achieva de la plateforme IRMaGe, mais aussi l'utiliser en entrée de notre code de simulation pour la génération du dictionnaire MRF pour plusieurs combinaisons de paramètres $T_1$, $T_2$ et $B_1$. Une approche de recherche dictionnaire permet ensuite d'identifier les signaux acquis (*fingerprint*) dans la base de données dictionnaire pour reconstruire des cartes $T_1$, $T_2$ et $B_1$.

## Améliorations

En travaillant sur les simulations, et la reconstruction, il est possible de corriger efficacement les imperfections du scanner, telles que les effets de profil de coupe lors d'acquisition en deux dimensions, et les inhomogénéités du champ $B_1$ (voir Ma et al. 2017). En outre, des méthodes de compression de faible rang ont été employées pour réduire la charge de calcul. Une représentation compressé du dictionnaire MRF avec une approche de Décomposition en Valeurs Singulières (SVD) accelère les temps de recherche dictionnaire, réduit le coup en mémoire, ce qui permet de se rapprocher de l'applicabilité clinique (voir McGivney et al. 2014).

### Un premier pas vers l'imagerie de l'AVC

En se basant sur ces estimations relaxométriques, on peut tenter d'obtenir des informations plus pertinentes encore pour le diagnostic de pathologies cérébrovasculaires. En effet, l'IRM Fingerprint multi-compartiments (Deshmane et al. 2015) permet de modéliser des propriétés à l'échelle intra-voxel en s'appuyant sur les propriétes relaxométriques supposées des tissues. À partir de cette méthode, nous avons alors pu produire des premières estimations de la fraction de myéline dans l'eau, ou encore du volume sanguin cérébral, selon les composants choisis. Enfin, en imagerie clinique, les informations issues de l'imagerie de contraste sont aussi importantes que les cartes quantitatives. Comme montré par Gómez et al. 2019, certains design de séquence permettent l'acquisition de contrastes intrinsèques dans les images temporelles IRM. Nous avons reproduit ces résultats dans le protocole MRF, combiné à une nouvelle méthode de SVD pour débruiter les images acquises et ainsi retrouver des contrastes pondérés $T_1$, $T_2$ ou angiographiques. Si l'on souhaite dériver de ce design de séquence bien précis, de récentes avancées en IRM dit synthétique (Hagiwara et al. 2017) permettent la génération d'images de contraste à posteriori à partir des images MRF quantitatives reconstruites. Cela ouvre la porte à un plus grand nombre de contraste générés, soit à partir d'équation bien définie comme proposé dans ce manuscrit, soit grâce à des outils deep learning comme il a été proposé par Wang et al. 2022.

### Conclusion

Ce protocole amélioré étend les estimations de relaxométrie pour extraire des informations complètes pertinentes pour l'imagerie de l'AVC humain, y compris des images de contraste standard de type angiographique et des estimations de la fraction du volume sanguin à l'aide d'un modèle MRF multi-compartiments qui tient compte des composants sanguins, non sanguins et fluides. Ces outils ont été validés par des acquisitions *in vivo* sur des volontaires humains. Bien que cette méthode offre une première réponse aux défis soulignés dans cette thèse, elle reste limitée dans sa capacité à caractériser de manière réaliste les microstructures en se basant uniquement sur des données relaxométriques.

## Résumé du chapitre II : A la recherche de séquence MRF sensible aux paramètres vasculaires

Dans le second chapitre de ce manuscrit, il est proposé d'ouvrir le protocole MRF à l'utilisation de nouvelles séquences. Alors que les séquences spoilées utilisées classiquement sont designées spécialement pour leur insensibilité aux inhomogénéités du champ magnétique, les séquences dites "balancées" ou "équilibrées" y sont particulièrement sensibles (Scheffler et al. 2003b; Miller 2012). En appliquant des gradients équilibrés et symétriques dans les trois directions spatiales, les déphasages induits par l'aimantation à la fin de l'excitation sont annulés et donc la phase du signal mesurée dépend principalement des effets dit d'*off-resonance*, faisant la sensibilité remarquable de ces séquences. En combinant les effets des inhomogénéités de champ sur le signal réponse aux séquences balancées, et l'effet BOLD (Blood Oxygenation Level Dependant) qui établit un lien entre les propriétés magnétiques du sang, donc la structure

vasculaire et les perturbations du champ magnétique, notre hypothèse serait d'utiliser ces séquences pour des estimations microvasculaires via l'IRM Fingerprint.

## Étude des effets des inhomogénéités de champ sur le signal réponse des séquences

Nous avons tout d'abord comparé la sensibilité des séquences spoilées et balancées à des distributions de champ magnétiques intra-voxel qui seraient directement reliées à des structures microvasculaires. Par le biais d'étude *in silico*, nous avons mis en évidence que, sans agent de contraste, seule les séquences balancées sont sensibles aux inhomogénéités du champ magnétique. De plus, il semblerait que les paramètres de la séquence aient un fort impact sur la réponse du signal à ces perturbations. Cela mène à penser qu'une séquence balancée de type bSSFP (balanced Steady State Free Precession) désignée dans une manière MRF où les paramètres varient avec le temps, pourrait être très sensible aux microstructures vasculaires du cerveau humain.

## Design d'une séquence bSSFP optimale

Afin de maximiser la sensibilité de notre séquence aux paramètres d'intérêt et donc la qualité des estimations, nous avons implémenté des métriques pour prédire la performance des séquences à partir de simulations numériques. Ces métriques se basent principalement sur des mesures de la variabilité des signaux dans le dictionaire MRF associé à la séquence évaluée. Nous les avons designé pour être rapides à calculer tout en reflétant tout de même le réaliste des acquisitions. L'une de ces approches est une méthode Monte-Carlo -proposée par Sommer et al. 2017- qui consiste en la simulation d'un dictionnaire MRF, duquel on extrait un nombre fixé de signaux, que l'on bruite avec un bruit gaussien se voulant imiter le bruit de sous-échantillonnage des acquisitions MRF, et que l'on re-match dans le dictionnaire. On répète ensuite cette maneouvre avec un bruit aléatoire et de nouveaux signaux. A chaque itération, l'erreur faite entre les paramètres tissulaires associés au signal initial et ceux associés au nouveau match, nulle dans le cas idéal, représente l'erreur d'estimation attendue avec cette séquence. En utilisant ces métriques dans un processus itératif, nous avons pu définir les paramètres d'acquisition tels que le FA, TR, TE et la phase RF, qui maximisent la discrimination des signals de réponse à une séquence balancée pour des tissues d'intérêt.

## Conclusion

À partir de simulations *in silico*, et de métriques implémentées durant cette thèse, nous avons pu déterminer une séquence bSSFP qui permettrait l'estimation simultanée des temps de relaxation, du champ magnétique et de propriétés microvasculaires. Ces résultats restent maintenant à vérifier dans une étude *in vivo*.

# Résumé du chapitre III : Mesure relaxométrique et quantification microvasculaire sans agent de contraste, utilisant des séquences bSSFP, chez des volontaires humain

Ce chapitre s'appuie sur une étude *in vivo* d'une nouvelle méthode que nous avons proposé durant cette thèse pour des mesures quantitatives de relaxométrie, de champ magnétique et de perfusion sans agent de contraste. Ces travaux font l'objet d'un article soumis à publication dans un journal.

## Nouvelle méthode de simulation

En s'appuyant sur les travaux de Wang et al. 2019 et Delphin et al. 2023, nous avons mis au point une nouvelle méthode de simulation des dictionnaires MRF. On calcule d'une part les inhomogénéités de champ et donc de fréquence dans chaque voxel d'imagerie à partir de microstructures vasculaires dérivées de microscopie sur des souris. A chaque réseau vasculaire défini par une volume sanguin Vf et un rayon moyen R, on peut alors associer une distribution de fréquence. Ensuite, en considérant que dans chaque voxel, le signal mesuré *in vivo* est une moyenne des signaux résultants de chaque contribution intra-voxel à différentes fréquences de résonance, il est possible d'utiliser les distributions de fréquences issues des réseaux vasculaires de souris, pour représenter l'effet des microstructures sur le signal IRM, dans le dictionnaire MRF. On peut alors simuler des signaux pour différentes combinaisons de paramètres $T_1$, $T_2$, $B_1$, $B_0$, Vf (volume sanguin cérébral), et R (rayon moyen des vaisseaux dans le voxel). Face au coût de simulations importants de tels dictionnaires (milliards de signaux), nous avons utilisé une approche "à la volée" qui consiste à simuler le dictionnaire MRF, sous-partie par sous-partie, et de faire la recherche dictionnaire dans chaque sous partie en gardant l'information du score d'identification. Ainsi, on peut réduire le coût en mémoire du stockage du dictionnaire, mais cela impose de simuler les dictionnaires simultanément au processus de reconstruction.

## Application *in vivo*

En utilisant ces simulations avancées, combinées avec la séquence bSSFP MRF désignée dans le précédent chapitre, nous avons alors pu tester notre méthode sur 6 volontaires sains. Toutes les expériences ont été réalisées selon les directives du protocole MAP-IRMaGe (NCT05036629), approuvé par le CHU Grenoble Alpes et coordonné par le Dr. Arnaud Attyé. Les premiers résultats montrent un contraste très intéressant entre le Vf de la matière grise et celui de la matière blanche, avec un rapport mesuré de 2, comme prévu dans la littérature. En outre, les zones de gros vaisseaux telles que la région du sinus sagittal présentent des valeurs de Vf et de R importantes. Alors que les mesures de relaxométrie et de champ magnétique ont été comparées à des séquences standard, une validation plus poussée des estimations du Vf et du R par rapport aux méthodes traditionnelles avec agent de contraste est nécessaire pour établir pleinement l'efficacité de notre approche.

## Conclusion

Dans ce chapitre, nous avons pu exploiter *in vivo* notre méthode pour l'estimation simultanée des cartes de relaxométrie ($T_1$, $T_2$, $T_2^*$), des champs magnétiques ($B_1$, $B_0$) et des propriétés microvasculaires (Vf, R) au cours d'une seule acquisition, sans l'utilisation d'agents de contraste. Les premiers résultats obtenus sont en accord avec la littérature, de futures validations de ces résultats dans des modèles pathologiques ou contre des protocoles standards restent à effectuer pour confirmer le potentiel clinique de notre méthode. On peut aussi soulever des points d'amélioration de cette méthode. Le réalisme des simulations pourraient être amélioré en simulant les imperfections scanner dans nos dictionnaires comme il a été présenté dans le premier chapitre de ce manuscrit. Malheureusement, les temps de calcul déjà importants de notre méthode, et le comportement particulier des effets de profil de coupe pour les séquences de type balancées -comme soulevé par Staehle et al. 2008- nous amène à devoir repenser la stratégie de prise en compte de tels effets.

# Résumé du chapitre IV : Développement de techniques de reconstruction avancées pour l'IRM Fingerprint de haute-dimension

Malgré des premiers résultats prometteurs, il est important de noter que la méthode proposée dans les chapitres précédents apporte son lot de défis techniques, notamment en termes de complexité de calcul. La haute-dimension d'un tel processus MRF -liée au nombre de paramètres à estimer- associée à des acquisitions *in vivo* à haute résolution, nous amènes face au problème de la « malédiction de la dimensionnalité » où la possibilité d'exploration de l'espace paramétrique entre en conflit avec les ressources techniques à notre disposition. Nous avons, dans les chapitres précédents, contourner ce problème en calculant les dictionnaires MRF "à la volée", au fur et à mesure du processus de reconstruction. Sans avoir jamais à stocker le dictionnaire en entier, cela permettait de réduire le coût en mémoire. Cependant, une telle approche impose des simulations constamment faites en parallèles du processus de reconstruction. Cela pose un défi compte tenu des ressources limitées disponibles dans les logiciels des scanners IRM et de la nécessité d'obtenir des temps de scans rapides. Pour tenter d'apporter une meilleure réponse à la malédiction de la dimensionnalité, nous avons adopté une approche à deux volets.

## Compresser les dictionnaires MRF

Premièrement, nous avons collaboré avec l'équipe Statify de l'INRIA, qui développe des modèles statistiques bayésiens et des valeurs extrêmes pour données structurées et de grande dimension. Avec leur aide, nous avons utilisé une représentation de sous-espace de faible rang du dictionnaire MRF en utilisant des mélanges de distributions gaussiennes (High-Dimensional Gaussian Mixture Models). Ces modèles statistiques sont utilisés pour représenter une distribution de données complexe comme étant la combinaison de plusieurs distributions normales (ou gaussiennes) plus simples. Dans notre contexte MRF, cela permet d'obtenir des dictionnaires efficacement compréssés en termes de mémoire et des temps de recherche

plus rapides dans des espaces de dimensions réduites. En plus d'accélérer la reconstruction et faciliter le stockage des dictionnaires, cette méthode permet en fait d'avoir une information de clusterisation des signaux *fingerprints* lors de la compression des données acquises, permettant une approche de recherche dictionnaire hiérarchique, encore moins coûteuse et fournissant une information *a priori* sur les tissues recherchés. Ces travaux ont mené à l'écriture d'un article de recherche qui a été publié lors d'une conférement de biomédicale ainsi que, sous une version plus généralisée de la méthode, dans une revue de statistique.

### Remplacer la recherche dictionnaire classique

Dans un second temps, nous avons entraîné un réseau de neurone LSTM bidirectionnel pour prédire les cartes de paramètres quantitatifs directement à partir des acquisitions MRF. Un réseau LSTM bidirectionnel est une variante des réseaux de neurones récurrents (RNN) qui traite les données dans les deux directions (avant et arrière) pour capturer des dépendances contextuelles dans un signal temporel. Il utilise deux couches LSTM parallèles, une qui lit la séquence dans l'ordre normal et l'autre dans l'ordre inverse, ce qui permet de mieux comprendre le contexte complet des données séquentielles. La prédiction directe du réseau à partir des *fingerprints* élimine la nécessité de la recherche dictionnaire et réduit de manière significative le temps de génération et les besoins en matière de mémoire. Nous avons appelé cette approche MARVEL. C'est le premier réseau de neurone utilisé pour de l'IRM Fingerprint dans un contexte où le nombre de paramètres à estimer est important. Ces travaux proposent une solution globale pour la gestion des hautes dimensions dans les problématiques fingerprint. Ils ont été soumis à une conférence en Intelligence Artificielle (MICCAI) et seront publiés dans un journal après cette conférence.

### Conclusion

Les deux techniques proposées ont été validées par rapport à des cartes reconstruites par recherche dictionnaire standard à partir d'acquisitions *in vivo*, chacune offrant des avantages uniques en termes de réduction des coûts de calcul et des temps de reconstruction. À l'avenir, nous aimerions combiner ces deux méthodes en un seul réseau neuronal que l'on entrainerait sur des données à faible rang,combinant ainsi les avantages des deux approches. Ces progrès représentent une étape importante pour franchir les derniers obstacles entre la méthode proposée dans cette thèse et son application clinique

## Résumé du chapitre V : Intelligence Artificielle pour la simulation rapide des effets de la diffusion et des structures microvasculaires sur le signal IRM

## Accélerer les processus existants

Dans les chapitres précédents, nous avons proposé une nouvelle méthode de MRF utilisant une séquence bSSFP pour la quantification simultanée et rapide des cartes de paramètres tissulaires ($T_1$, $T_2$, R, CBV), essentielles pour l'imagerie de perfusion et le diagnostic des AVC. Cependant, ces paramètres ne suffisent pas à saisir toute la complexité des AVC, où l'oxygenation cérébrale et la diffusion de l'eau jouent un rôle clé. La diffusion de l'eau, quantifiée par le coefficient de diffusion apparent (ADC), est cruciale pour détecter les premières atteintes ischémiques en reflétant l'intégrité cellulaire, tandis que la saturation en oxygène ($SO_2$), via l'effet BOLD, informe sur la viabilité tissulaire. Notre laboratoire a développé une méthode d'IRM Fingerprint vasculaire (MRvF) permettant de quantifier CBV, R, $T_2$ et $SO_2$ avec l'injection d'agent de contraste. Cette méthode, récemment améliorée avec des modèles microvasculaires réalistes, a été appliquée à des modèles tumoraux animaux et validée par des mesures histologiques et $pO_2$ (Delphin et al. 2024). Les simulations prennent en compte les effets de la diffusion de l'eau à l'aide du logiciel MRVox avec une valeur d'ADC de 850 $\mu m^2/s$. Cependant, en raison de la complexité des simulations, les études précédentes ont été limitées à de petis dictionnaires MRF, réduisant ainsi la précision des estimations. L'utilisation de méthodes d'apprentissage machine pour interpoler les dictionnaires, atteint ses limites avec l'augmentation du nombre de paramètres à estimer.

## Méthode proposée : MR-WAVES

Face à cela, nous proposons une méthode efficace pour simuler rapidement de gros dictionnaires MRF qui incluent des paramètres vasculaires tels que le CBV, le R et la $SO_2$ ainsi qu'une prise en compte des effets de la diffusion de l'eau sur les signaux. Pour cela, nous avons combiné la méthode proposée dans le Chapitre III pour la représentation des inhomogénéités de champ intra-voxel, avec une approche deep learning (réseaux de neurone récurrents) pour la diffusion. Nous avons appelé cette méthode MR-WAVES (Water-diffusion And Vascular Effects Simulations). Face aux manques de données pathologiques retrospectives chez l'homme à notre disposition, la validation *in vivo* de notre méthode est faite sur des données pré-clinique chez l'animal, avec un groupe sain et un groupe AVC. Ces données ont été acquises avec une séquence en écho de gradient spoilé, avant et après injection d'un agent de contraste. Nous avons donc concentré notre étude sur ce type de séquence. Les résultats obtenus montre qu'avec des simulations de dictionnaire MRF jusqu'à 800 fois plus rapide qu'avec MRVox, MR-WAVES permet la reconstruction de cartes paramétriques de même qualité.

## Conclusion

La méthode proposée ouvre la voix à la génération de larges dictionnaires MRF sur de grandes grilles de paramètres microvasculaires, ainsi qu'avec une prise en compte des effets de la diffusion de l'eau pour augmenter le réalisme des simulations, et donc la précision des estimations, notamment dans les tissues pathologiques de type ischémiques. Nous proposons également plusieurs voix d'amélioration de la méthode pour accroître la correspondance avec les simulations originales de MRVox. Prochainement, nous pensons à l'extension de cette méthode dans des modèles où l'ADC serait varié dans le dictionnaire MRF pour estimer également des cartes de diffusion en plus des paramètres microvasculaires. De plus, nous

pensons que la méthode proposée peut facilement être étendue à tout type de séquence MRF, comme les séquences bSSFP sans agent de contraste, dès lors que le design est sensible aux paramètres vasculaires désirés et à la diffusion de l'eau.

# Conclusion Générale

Dans cette thèse, nous avons cherché à relever les défis associé aux méthodes d'imagerie pour la gestion des patients victimes d'accidents vasculaires cérébraux (AVC) en utilisant et améliorant la technique d'IRM Fingerprint (MRF) pour l'estimation quantitative multiparamétrique. Nous avons étendu l'application l'IRM Fingerprint vasculaire (MRvF) permettant l'estimation des propriétés microvasculaires dans le cerveau humain, en nous attachant particulièrement à s'affranchir de l'injection d'un agent de contraste - une limitation importante pour les diagnostics cliniques rapides. Le travail proposé dans ce manuscrit permet l'estimation de propriétés microvasculaires sans injection d'agent de contraste, ce qui constitue une étape clé vers la transition clinique des méthodes MRvF.

Nos efforts initiaux se sont concentrés sur l'amélioration des outils MRF existants et préalablement développés dans notre laboratoire. Nous avons mis en œuvre de nouvelles méthodes pour réaliser des simulations numériques rapides et réalistes, des acquisitions efficaces et une reconstruction robuste des cartes de temps de relaxation ($T_1$, $T_2$). En tirant parti d'une abondante littérature sur les applications MRF en relaxométrie, nous avons développé un pipeline de pointe en implémentant notre propre code Matlab/Python. Ce pipeline permet de concevoir avec une grande liberté des séquences MRF, qui peuvent être appliquées selon divers paramètres d'acquisition et schémas de sous-échantillonnage au scanner. En combinant ces simulations et ces outils de reconstruction dans le cadre, nous avons également montré comment corriger efficacement les imperfections du scanner, telles que les effets du profil de coupe et les inhomogénéités du champ $B_1$.
En outre, des méthodes de compression de faible rang ont été employées pour réduire la charge de calcul et le coût en mémoire du MRF, ce qui a permis d'obtenir un protocole à la fois rapide et proche de l'applicabilité clinique. Par la suite, ce protocole amélioré étend les estimations de relaxométrie pour extraire des informations complètes pertinentes pour l'imagerie de l'AVC humain, comme par exemple des images de contraste standard de type angiographique et des estimations de la fraction du volume sanguin à l'aide d'un modèle MRF multi-compartiments qui tient compte des composants sanguins, non sanguins et fluides. Ces outils ont été ensuite validés par des acquisitions *in vivo* sur des volontaires humains. Bien que cette méthode offre une première réponse aux défis décrits dans cette thèse, elle reste limitée dans sa capacité à caractériser de manière réaliste les microstructures en se basant uniquement sur des mesures relaxométriques.

S'appuyant sur les conclusions de la première phase de nos travaux, la deuxième phase s'est concentrée sur la conception de séquences plus sensibles aux effets microvasculaires. En utilisant les avancées techniques et les connaissances acquises lors des premières expériences utilisant la méthode MRvF, nous avons cherché à exploiter la sensibilité des signaux IRM à l'effet BOLD, qui repose sur des changements dans les niveaux d'oxygénation du sang

qui affectent directement les propriétés magnétiques du sang et, par conséquent, le signal IRM. Dans les premiers travaux MRvF, cet effet est exploité avec l'injection d'un agent de contraste et des séquences GRE spoilées pour estimer les propriétés microvasculaires et la saturation en oxygène dans le cerveau. Cependant, des études ont mis en évidence la sensibilité des séquences GRE "balancées", aux inhomogénéités du champ magnétique, même en l'absence d'agents de contraste. Nous avons effectué une analyse détaillée de ces propriétés, en comparant le comportement des séquences spoilées et balancées en réponse aux distributions de champ magnétique pour différents paramètres d'acquisition. Cette analyse nous a conduits à émettre l'hypothèse qu'une séquence bSSFP soigneusement designée, intégrée à un processus de simulation MRF approprié, pourrait fournir des informations microstructurelles précieuses sans qu'il soit nécessaire d'utiliser un agent de contraste. Nous avons donc procédé à la conception d'une séquence bSSFP optimale basée sur des simulations *in silico* et des prédictions de la capacité d'encodage à l'aide de fonctions d'évaluation de la sensibilité.

Suite à ce travail, nous avons validé notre hypothèse par une étude *in vivo* impliquant plusieurs volontaires sains. En nous inspirant d'études MRvF antérieures, où des voxels segmentés par microscopie dans le cerveau de souris ont été étendus à des simulations d'inhomogénéités de champ magnétique dans le cerveau humain, nous avons incorporé ces connaissances dans nos simulations numériques. En combinant ces simulations avec notre séquence bSSFP optimisée, nos résultats préliminaires proposent l'estimation simultanée de cartes de relaxométrie ($T_1$, $T_2$, $T_2^*$), de champs magnétiques ($B_1$, $B_0$) et des propriétés microvasculaires (Vf, R) en une seule acquisition, sans l'utilisation d'agents de contraste. Les premiers résultats obtenus montrent un contraste très intéressant entre le Vf de la matière grise et celui de la matière blanche, avec un rapport mesuré de 2, comme prévu dans la littérature. En outre, les zones de gros vaisseaux, comme la région du sinus sagittal, présentent des valeurs de Vf et de R élevées. Alors que les mesures de relaxométrie et de champ magnétique ont été correctement validées par rapport à des séquences standard, une validation plus poussée des estimations du Vf et du R par rapport aux méthodes traditionnelles, basées sur l'injection d'agents de contraste, est nécessaire pour confirmer pleinement l'efficacité de notre approche.

Malgré les résultats prometteurs, la méthode MRF bSSFP proposée présente des défis techniques importants, notamment en termes de complexité de calcul. La nature hautement dimensionnelle des méthodes MRF, associée à la nécessité d'acquisitions à haute résolution pour de nombreux paramètres, exacerbe la "malédiction de la dimensionnalité". Cela pose un défi compte tenu des ressources limitées disponibles dans les logiciels des scanners IRM et de la nécessité d'obtenir des temps de scan rapides. Pour relever ces défis, nous avons adopté une approche à deux volets. Premièrement, en collaboration avec l'équipe Statify de l'INRIA, nous avons développé une représentation de sous-espace de faible rang du dictionnaire MRF en utilisant des mélanges de distributions gaussiennes, ce qui permet d'obtenir des dictionnaires peu coûteux en termes de mémoire et des temps de recherche plus rapides dans des dimensions réduites. En parallèle, nous avons entrainé un réseau neuronal LSTM bidirectionnel pour prédire les cartes de paramètres quantitatifs directement à partir des acquisitions MRF, ce qui élimine la nécessité de la recherche dictionnaire et réduit de manière significative le temps de reconstruction et les exigences en matière de mémoire. Les deux techniques ont été validées par rapport à des références standard de recherche dictionnaires dans des acquisitions *in*

*vivo*, chacune offrant des avantages uniques en termes de réduction des coûts de calcul et des temps de reconstruction. À l'avenir, nous souhaitons combiner ces deux méthodes en un seul réseau neuronal entraîné sur un dictionnaire MRF dans un sous-espace de faible rang, combinant ainsi les avantages des deux approches. Ces progrès représentent une étape importante pour combler le fossé entre la méthode proposée et son application clinique.

Dans le dernier chapitre de ce manuscrit, nous avons abordé le besoin de deux biomarqueurs d'imagerie supplémentaires essentiels pour l'imagerie de l'AVC qui avaient été précédemment négligés : la diffusion de l'eau et la saturation en oxygène ($SO_2$). Bien que des études MRvF antérieures aient déjà intégré ces effets dans les dictionnaires MRF, les outils de simulation utilisés prenaient beaucoup de temps, limitant la portée des calculs et l'échantillonnage de la grille de paramètres, ce qui réduisait en fin de compte la précision des estimations. Notre contribution ici est double : Premièrement, en utilisant la nouvelle méthode de simulation vasculaire présentée au Chapitre III, nous avons considérablement accéléré le protocole de simulation sans effets de diffusion. Deuxièmement, en employant une approche d'apprentissage profond à l'aide d'un réseau type GRU-RNN, nous avons accéléré l'incorporation des effets de diffusion de l'eau dans les dictionnaires MRF par un facteur de plus de 800. Pour pallier le manque de données humaines, nous avons validé ce processus combiné, appelé MR-WAVES, par des études *in vivo* sur des modèles animaux sains et victimes d'AVC, en le comparant à un logiciel de référence pour les simulations, MRVox. Nos résultats sont très encourageants et plusieurs étapes d'optimisation potentielles peuvent déjà être envisagées. Bien que les données rétrospectives aient été acquises à l'aide d'une séquence GRE spoilée et d'un agent de contraste, l'algorithme proposé a été conçu pour s'adapter à n'importe quel type de séquence, facilitant ainsi l'application future aux données humaines acquises sans l'utilisation d'agents de contraste et avec des séquences GRE balancées, comme proposé dans cette thèse.

En conclusion, ce manuscrit présente une première proposition pour la génération simultanée et sans contraste de cartes multiparamétriques, incluant des estimations relaxométriques, de champs magnétiques et des propriétés microvasculaires dans le cerveau humain, en plus d'images de contraste habituelles. Dans la figure .0.5, le protocole MRF proposé est illustré avec l'intégration des outils développés au cours de cette thèse. En tant que contribution clé à une initiative de recherche plus large axée sur l'amélioration de la prise en charge des patients victimes d'accidents vasculaires cérébraux grâce à des techniques d'imagerie innovantes, ce travail fonde les bases d'une imagerie rapide, efficace et robuste des maladies cérébrovasculaires.

Dans un avenir proche, nous pouvons d'ores et déjà prévoir deux axes de développement technique avant de pouvoir proposer notre protocole en tant qu'outil clinique.
Tout d'abord, la validation des résultats actuels. Ceux-ci seront réalisés sur des animaux en environnement contrôlé et sur des volontaires sains ayant reçu une injection de CA pour valider les cartes de microvasculature, et sur certains patients ayant subi un accident vasculaire cérébral pour vérifier les cartes de relaxométrie. Ces derniers tests nous permettront de déterminer s'il est possible de remplacer au moins quelques séquences d'IRM standard dans un protocole déjà sensible au temps.
Deuxièmement, en travaillant sur l'optimisation des séquences MRF en termes de temps d'acquisition. Cela se fera en améliorant simultanément la conception des séquences et la

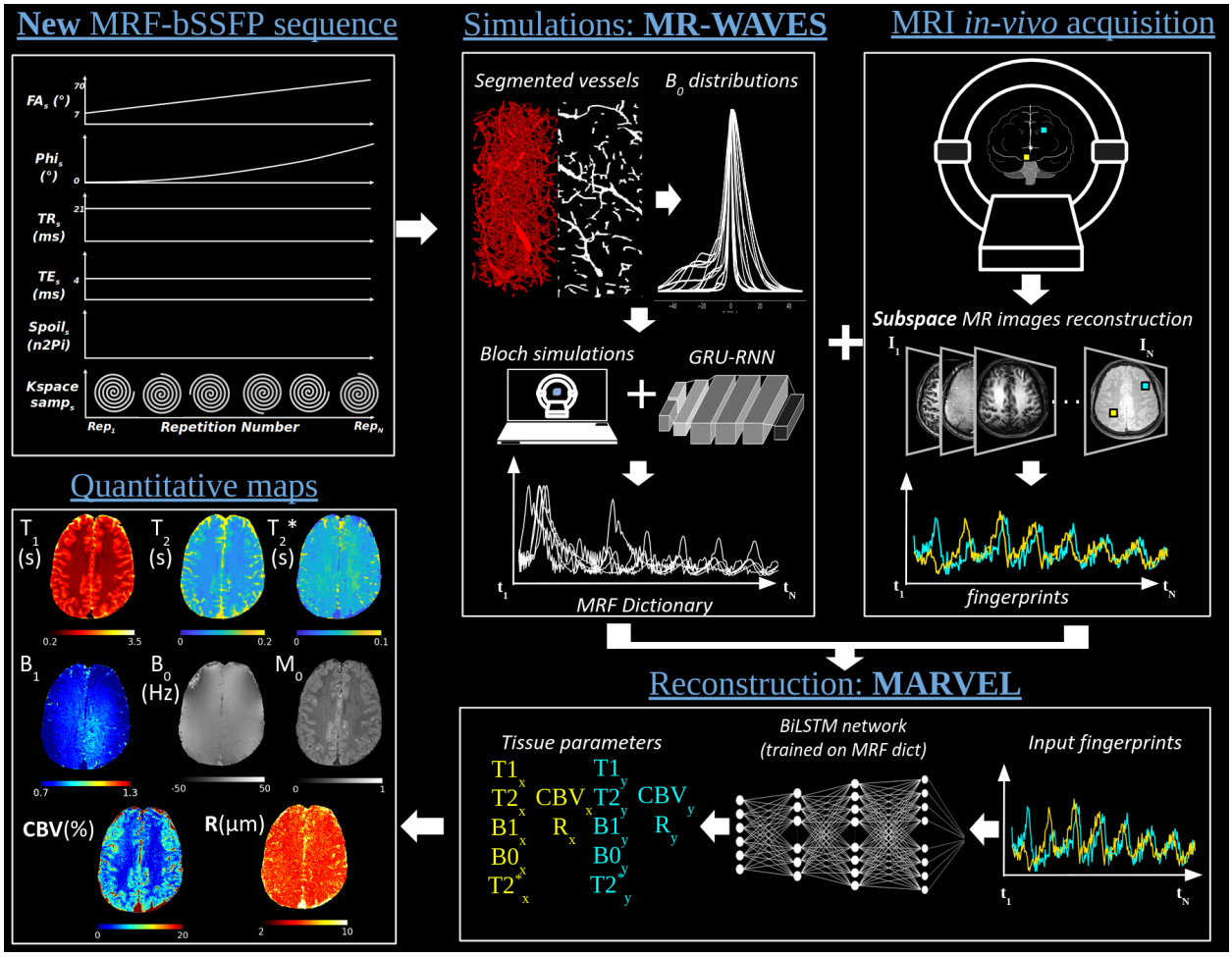


**Figure .0.5**: Illustration du protocole MRF proposé. Données acquises à 3T (Philips;IRMaGe) sur un volontaire sain.

façon dont les données sont collectées dans le k-space en 3D. Cette étape est maintenant réalisable grâce aux outils flexibles et rapides (simulation et reconstruction) que nous avons mis en place pendant la thèse. Nous avons déjà commencé à travailler sur une méthode de recherche automatique de séquences basée sur des outils de simulation qui intègrent la configuration de gradients spatiaux (KomaMRI), des séquences définies dans un langage "constructeur-indépendant" appelé Pulseq, et des algorithmes d'optimisation automatique sous la forme d'apprentissage par renforcement. Comme nous l'avons déjà mentionné plus haut dans ce manuscrit, des études sont également menées en parallèle dans le laboratoire sur le développement de l'IRM synthétique pour fournir des images pondérées d'utilité clinique à partir de notre séquence MRF. Ces développements pourraient également bénéficier de ce pipeline d'optimisation automatique.
Enfin, bien qu'il n'ait pas été développé dans ce manuscrit, le développement d'un ensemble d'outils MRF pour corriger les artefacts de mouvement du patient sera nécessaire avant l'acceptation clinique de notre protocole.

Une fois validés, les outils et concepts développés dans cette thèse pour le contexte difficile de

l'AVC devraient également être transposables à d'autres pathologies telles que le cancer ou les maladies neurodégénératives, avec la possibilité de sacrifier un peu de temps d'acquisition pour mesurer de nouveaux biomarqueurs.

## Abstract

Stroke, a major cause of mortality and long-term disability worldwide, necessitates rapid and accurate diagnosis to optimize treatment outcomes. Current imaging techniques, particularly MRI, are critical for assessing the extent of brain injury and guiding therapeutic interventions. However, traditional MRI protocols are often time-consuming and may lack the precision required for detailed analysis of ischemic brain tissue, limiting their utility in acute stroke settings where time is of the essence.

Magnetic Resonance Fingerprinting (MRF) is a relatively new solution to simultaneously map several brain quantitative parameters from fast, high-resolution acquisitions using a dictionary search approach. However, its extension for microvascular (*e.g.* cerebral blood volume (CBV) or blood vessel diameter (R)) and brain oxygenation estimates currently relies on the injection of exogenous contrast agents (CA) that limit the clinical application and acquisition speed. In this thesis, we aimed to address these limitations by developing a novel and integrated, artificial intelligence (AI) augmented contrast-free MRF technique tailored for stroke emergencies.

First, we developed and adapted standard multiparametric MRF techniques based on spoiled gradient echo MRI sequences. Using scanner artifacts corrections, dictionary compression, and subspace reconstruction, we were able to generate fast relaxometry ($T_1$,$T_2$) maps and standard MRI contrasts from a single MRF sequence. However, the microvascular information provided by our new multi-compartment MRF model in human volunteers suffered from a low signal-to-noise ratio.
We thus focused on a new MRF sequence design based on balanced GRE sequences and their remarkable sensitivity to magnetic field inhomogeneities. After a theoretical and *in-silico* study on general sequences sensitivities to the Blood Oxygen Level Dependent (BOLD) effect and the impact of MRF acquisition parameters, we designed a new MRF-bSSFP sequence that simultaneously estimate relaxometry ($T_1$,$T_2$,$T_2^*$, $M_0$), magnetic fields ($B_1$,$B_0$), and microvascular properties (CBV,R) without the need for CA injection. Using a new pipeline for MRF simulations, the proposed method was tested in a cohort of human volunteers.
Our method was further refined by developing advanced reconstruction methods for high dimensional MRF acquisitions relying on low-rank models and deep neural networks. We finally used our simulation framework combined with Recurrent Neural Networks to fasten our computation times by a factor of 800 and allow the inclusion of water-diffusion effects. This approach was tested in retrospective preclinical data including healthy and stroke animals and the results suggested that additional estimates of ADC or blood oxygenation could be measured with our new bSSFP MRF sequence.

After careful validation and optimization, this methodological work could provide an efficient imaging solution that aligns with the critical time constraints of acute stroke care. Our general framework for high dimensional MRF acquisitions that include microstructure effects could also be used in various other pathologies.



**Keywords:** MR Fingerprinting, AI, Brain, Vascularization, Simulations, Contrast



## Résumé

Les accidents vasculaires cérébraux (AVC), cause majeure de mortalité et d'invalidité à long terme dans le monde, nécessitent un diagnostic rapide et précis pour optimiser les résultats du traitement. Les techniques d'imagerie actuelles, en particulier l'IRM, sont essentielles pour évaluer l'étendue des lésions cérébrales et guider les interventions thérapeutiques. Toutefois, les protocoles IRM traditionnels prennent souvent beaucoup de temps et peuvent manquer de la précision requise pour une analyse détaillée du tissu cérébral ischémique, ce qui limite leur utilité dans les situations d'AVC aiguës où le temps est un facteur essentiel.

L'IRM Fingerprint (MRF) est une solution relativement nouvelle qui permet d'estimer simultanément plusieurs paramètres quantitatifs cérébraux à partir d'acquisitions rapides haute résolution en utilisant une approche de recherche par dictionnaire. Cependant, son extension pour les estimations microvasculaires (*e.g.* volume sanguin cérébral (CBV) ou diamètre des vaisseaux sanguins (R)) et d'oxygénation du cerveau repose actuellement sur l'injection d'agents de contraste exogènes (CA) qui limitent l'application clinique et la vitesse d'acquisition. Dans cette thèse, nous avons cherché à résoudre ces limitations en développant une nouvelle technique intégrée d'IRM Fingerprint sans agent de contraste, améliorée par intelligence artificielle (IA) et adaptée aux urgences des AVC.

Tout d'abord, nous avons développé et adapté des techniques MRF multiparamétriques standard basées sur des séquences à écho de gradient spoilé. En implémentant dans ces outils des corrections d'artefacts du scanner, la compression des dictionnaires et des reconstructions en espace réduit, nous avons pu générer des cartes de relaxométrie ($T_1$,$T_2$) et des contrastes d'IRM standard à partir d'une seule séquence MRF. Cependant, les informations microvasculaires fournies par notre nouveau modèle MRF multi-compartiments chez les volontaires humains souffraient d'un faible rapport signal/bruit.
Nous nous sommes donc concentrés sur un nouveau design de séquence MRF basée sur des séquences GRE équilibrées et leur remarquable sensibilité aux inhomogénéités du champ magnétique. Après une étude théorique et *in-silico* sur les sensibilités des séquences générales à l'effet BOLD (Blood Oxygen Level Dependent) et l'impact des paramètres d'acquisition MRF, nous avons conçu une nouvelle séquence MRF-bSSFP qui estime simultanément des cartes de relaxométrie ($T_1$,$T_2$,$T_2^*$, $M_0$), de champs magnétiques ($B_1$,$B_0$) et de propriétés microvasculaires (CBV,R) sans qu'il soit nécessaire d'injecter un produit de contraste. En utilisant un nouveau pipeline pour ces simulations MRF, nous avons testé notre méthode sur une cohorte de volontaires humains.
Nous avons ensuite développé des méthodes de reconstruction avancées pour les acquisitions MRF à haute dimension en s'appuyant sur des modèles de faible rang et des réseaux neuronaux profonds. Enfin, nous avons utilisé notre pipeline de simulation combiné à des réseaux neuronaux récurrents pour accélérer nos temps de calcul d'un facteur 800 et permettre l'inclusion des effets de diffusion de l'eau. Cette approche a été testée sur des données précliniques rétrospectives comprenant des animaux sains et des animaux ayant subi un AVC et les résultats ont suggéré que des estimations supplémentaires de l'ADC ou de l'oxygénation sanguine pouvaient être mesurées avec notre nouvelle séquence MRF bSSFP.

Après une validation et une optimisation minutieuses, ce travail méthodologique fournira une solution d'imagerie efficace, alignée sur les contraintes de temps critiques des soins de l'AVC en phase aigu. Notre protocole général pour les acquisitions MRF à haute dimension incluant les effets des microvascularités pourrait également être utilisé dans diverses autres pathologies cérébrales.



**Mots-clés :** IRM Fingerprint, IA, Cerveau, Vasculature, Simulations, Contraste